Environmental and Engineering Geophysical Studies for Sinkhole Problems Using Seismic Reflection, Refraction Tomography, Electrical Resistivity Imaging, and Joint Inversions

der Naturwissenschaftlichen Fakultät

der Gottfried Wilhelm Leibniz Universität Hannover

zur Erlangung des akademischen Grades

Doktor der Naturwissenschaften

Dr. rer. nat.

genehmigte Dissertation

von

M.Sc. Berhanu Gebregziabher Gared

geboren am 19.02.1977 in Äthiopien

2011

Referent: Prof. Dr. Hans-Joachim Kümpel
Korreferentin: Prof. Dr. Jutta Winsemann
Tag der Promotion: 01/02/2011

``Imagination is more important than knowledge! ``

Albert Einstein

ACKNOWLEDGMENTS

All of this work was performed in Leibniz Institute for Applied Geophysics (LIAG) under the support of Deutscher Akademischer Austausch Dienst (DAAD) and LIAG. During this work vital assistance was provided by my Professors, senior scientists, institutions and colleagues whose help is acknowledged with utmost gratitude as follows.

- Many thanks to my supervisor Prof. Dr. Hans-Joachim Kümpel (President of BGR) not only for suggesting the topic, careful supervising, helpful advices and constant encouragements in all stages of this study but also in helping me to win the DAAD scholarship and to see the world outside my home country.

- Many thanks to my coordinator and immediate advisor Dr. Helga Wiederhold, the indefatigable senior scientist who has taught me how to think as a geophysicist and directed me to the world of seismic imaging, international conferences and of course the backbone of the whole dissertation.

- Many thanks to Dr. Thomas Günther, the perspicacious young scientist, for leading me to the world of inverse modeling especially in processing of the joint inversion data and also for his encouragements and valuable comments after reviewing the electrical resistivity and joint inversion parts of my thesis.

- Many thanks to Mr. France Binot, the bridge between geophysicists and geologists in LIAG, for his help to understand the geology of north Germany and for his valuable comments after reviewing the geology section of my thesis.

- Many thanks to the LIAG (Section-1) seismic crews S. Cramm, E. Grossmann, S. Grueneberg, W. Rode, and D. Vogel for the successful and fruitful seismic data acquisition during our seismic field surveys.

- Many thanks to Mr. Michael Grinat and Mr. Wolfgang Südekum from LIAG (Section-2) for the geoelectric data acquisitions during the field work.

- Many thanks to the Germany government and Germany people in general and particularly to the German Academic Exchange Service - DAAD for being a very good daddy during my stay in Hannover near to the heaven place, Herrenhäuser Gärten.

- Many thanks to LIAG, the real place for exploration Geophysicists with full instrumentation, comfortable office free of noises, and full of friendly and talented senior Geoscientists. It is often difficult to remember who taught me what, but it is not difficult to remember that I have learned much of what I know from conversations, discussions, correspondence, and arguments with the researchers and senior scientists in LIAG particularly my convivial colleagues from sections S-1 and S-2.

- Many thanks to Professor Dr. Jutta Winsemann and Professor Dr. Jörg Bachmann for their interest and willingness to supervise my Ph.D.

- Many thanks to the Geological survey of Schleswig-Holstein (LLUR) particularly to Dr. Reinhard Kirsch for reporting us the research problems (since a research without a problem is unthinkable) and also for providing us some previous works and borehole data.

Last but not least, I would like to express my deep gratitude to my family and friends (in Ethiopia, Germany, and the Netherlands) and my wife Sinit who gave me care and encouragements with great love in everyday of my life. Oh God thanks for giving me not only success for the Ph.D. from Niedersachsen-Hannover but also the most beautiful and sweet daughter Hyab from the Nederland-Amsterdam in the same period of time.

Abstract

The subsurface of Münsterdorf in North Germany has been intruded by a Permian salt dome, called Krempe-Lägerdorf; its top is at about 600 to 800 m depth. Due to uplifting by the salt dome, upper Cretaceous chalk layers that are normally seated at about 1000 meters were uplifted to a near-surface position of up to 20 meters depth and are covered with Quaternary sediments. This water-soluble stone in the bedrock is being gradually dissolved by the groundwater and can produce holes and cavities. If the sediment layers above them collapse, a sudden depression at the surface, called a sinkhole, occurs. Such types of sinkholes are observed almost linearly aligned in the study area, specifically at the southwestern part of Münsterdorf, close to a football field. The stratigraphy of the Quaternary section consists of sand and till layers of Pleistocene glaciations.

Integrated geophysical investigation using multiple geophysical methods is usually used in order to reduce the limitations and ambiguity of individual techniques. Accordingly, seismic reflection with P- and S-waves, refraction tomography, and DC resistivity data were collected to 1) detect faults, fracture zones, and karstic features that may lead to the formation of the linearly aligned sinkholes, 2) locate the depth to carbonate layers and the salt dome, and 3) to determine the lateral and vertical situation of the leachable horizons that lead to sinkhole collapse. Moreover, a joint inversion of the seismic refraction with P- and S-waves and DC resistivity data was carried out along two selected profiles in order to yield structurally similar results.

Based on the results from 2D seismic reflection sections, no major fault zones were identified in the depth range down to 800 m except for a few discontinuities on top of the upper Cretaceous chalk layer. The discontinuities were detected at about 20 m depth beneath the observed sinkholes and some are away but still aligned linearly with the location of the sinkholes. From the P-wave seismic reflection method information about the Quaternary sediments in the very near surface shallower than 20 meters depth is scarce. To remediate this, on one hand a shear wave seismic reflection survey was added and on the other hand first break arrivals of the seismic waves and the DC resistivity data were used for separate and joint inversions of 2D seismic refraction tomography and electrical resistivity imaging, respectively. The results of the 2D seismic refraction tomography are compared with results of the 2D electrical resistivity tomography and show good compatibility down to about 20

meters. Moreover, clay-filled chalk dissolution zones below 20 m depth and a shallow geological boundary at 3 to 6 m depth (trending almost E-W) between fluvioglacial sand and glacial till/clay layers are interpreted from the electrical resistivity imaging. All of the seismic reflection discontinuities (for both P- and S-waves), clay-filled dissolution zones from the resistivity results, and the observed sinkholes are aligned to this geological boundary. Moreover, an irregularly discontinuous aquiclude of marly to clayey glacial till layer at 12 to 18 meters depth just over the chalk layer is interpreted from both the resistivity and refraction tomographies. The geologic boundary is not only a lithologic boundary but also a hydrogeologic boundary between confined and unconfined sand aquifers from about 6 to 12 meters depth.

The integrated geophysical methods we used in our study area are effective to investigate the causes and zones of sinkholes and give reliable results. Thus, the occurrences of the sinkholes at Münsterdorf may be mainly dependent on 1) the presence of permeable sand on top of the chalk due to erosion of the impermeable glacial till layer at 12 to 18 meters depth and 2) the presence of adjacent impermeable till/clay to the permeable sand layers at the surface, whereas groundwater flow through the chalk is strongly influenced by the geological boundary or contact zones. In other words, in areas of concentrated groundwater recharge along the geological boundary, large conduits or dissolution zones will develop. Moreover, the shallow glacial till/clay layer at 3 to 6 meters depth might cause geotechnical problems at the adjacent margin with the sand by swelling and shrinking when the surface water level fluctuates. This is because the clay minerals are capable of absorbing water between silicate layers held by weak bonds and increase its volume. Therefore, the discontinuous till/clay impermeable margins on top of the chalk and/or contact zones between the permeable sand and adjacent impermeable till/clay layers are the reason for the potential sinkhole hazards in the study area.

Keywords: Sinkholes, Geophysics, Germany

Zusammenfassung

Der Untergrund Norddeutschlands ist durch Salzbewegung geprägt. Die in Perm und Trias gebildeten mächtigen Salzlagerstätten neigen mit wachsender Sedimentbedeckung im Meso- und Känozoikum zur Mobilität. Unterhalb der schleswig-holsteinischen Ortschaft Münsterdorf ist der Salzstock Krempe-Lägerdorf bis auf 600 bis 800 m unter der Erdoberfläche aufgestiegen. Durch den Salzaufstieg sind Kalksteine aus der Oberkreide, die normalerweise in 1000 m Tiefe liegen, bis auf 20 m unter Gelände gehoben worden und sind heute direkt mit quartären Sedimenten bedeckt. Diese wasserlöslichen Kalksteine im Untergrund können durch Grundwasser allmählich gelöst werden und so können Löcher und Hohlräume entstehen. Wenn die darüber liegenden Sedimentschichten einbrechen, entsteht plötzlich eine Bodensenke auch Erdfall genannt. Solche Erdfälle, mehr oder weniger auf einer Linie ausgerichtet, werden im Untersuchungsgebiet beobachtet und zwar im südwestlichen Teil des Ortes Münsterdorf nahe bei einem Sportplatz. Die quartären Schichten bestehen aus Sand und Geschiebemergellagen der pleistozänen Eiszeiten.

Um die Begrenztheit und Uneindeutigkeit einzelner geophysikalischer Methoden gering zu halten, wird üblicherweise eine kombinierte Untersuchung mit verschiedenen geophysikalischen Methoden angewendet. Dementsprechend wurden reflexionsseismische Daten mit P- und S-Wellen, Daten für Refraktionstomographie sowie Gleichstromgeoelektrik erfasst mit den Zielen 1) Störungen, Bruchzonen oder Karstmerkmale, die die Ursache der linear aufgereihten Erdfälle sein könnten, zu detektieren 2) die Tiefenlage der Karbonatgesteine und des Salzstocks zu lokalisieren und 3) die laterale und vertikale Situation der lösbaren Horizonte zu bestimmen, die zu dem Einbruch der Erdfälle führen. Außerdem wurde auf zwei ausgewählten Profilen eine gemeinsame Inversion von Refraktionsseismik mit P- und S-Wellen und Gleichstromgeoelektrik durchgeführt, um strukturell vergleichbare Ergebnisse zu erhalten.

Die Ergebnisse der reflexionsseismischen 2D Sektionen lassen außer einigen Diskontinuitäten in der Oberkante des stratigraphisch als Oberkreide anzusprechenden Kalks keine größeren Störungszonen bis 800 m Tiefe erkennen. Die Diskontinuitäten treten in etwa 20 m Tiefe unterhalb der beobachteten Erdfälle auf und einige auch abseits aber auf einer Linie mit den Erdfällen. Die reflexionsseismischen P-Wellen Sektionen liefern für den oberflächennahen Bereich bis 20 m Tiefe nur spärliche Informationen. Dieser Bereich wird deshalb durch

Reflexionsseismik mit Scherwellen ergänzt. Und, auf der anderen Seite, werden auch die Ersteinsätze der Seismik und die Daten der Gleichstromgeoelektrik invertiert und zwar sowohl einzeln als auch gemeinsam. Die Ergebnisse der seismischen 2D Refraktionstomographie werden mit den Ergebnissen der 2D elektrischen Widerstandstomographie verglichen, und es zeigt sich für den Tiefenbereich bis 20 m Tiefe eine gute Übereinstimmung. Aus der elektrischen Widerstandstomographie ergeben sich im Tiefenbereich unterhalb 20 m, also im Kalk, Lösungszonen, die mit Ton gefüllt sind. Und im flacheren Bereich wird in etwa 3 bis 6 m Tiefe eine annähernd Ost-West verlaufende geologische Grenze zwischen fluvioglazialem Sand und glazialem Geschiebemergel bzw. Ton interpretiert. Entlang dieser Grenze finden sich auch die Diskontinuitäten in den seismischen Reflexionen (bei P- und S-Wellen), die aus der Widerstandstomographie ermittelten mit Ton gefüllten Lösungszonen und die aufgetretenen Erdfälle. Darüber hinaus wird sowohl nach elektrischer Widerstandstomographie als auch seismischer Refraktionstomographie im Tiefenbereich 12 bis 18 m, also direkt oberhalb des Kalks, ein irregulär unterbrochener Grundwassernichtleiter (Aquiclude) bestehend aus mergeligem bis tonigem glazialem Geschiebemergel interpretiert. Die oben genannte geologische Grenze ist nicht nur eine lithologische Grenze sondern auch eine hydrogeologische Grenze zwischen gespannten und nicht gespannten sandigen Grundwasserleitern (Aquifer) in 6 bis 12 m Tiefe.

Die verwendeten kombinierten geophysikalischen Methoden haben sich als effektiv für die Untersuchung der Erdfallgebiete und deren Ursachenforschung erwiesen und geben glaubwürdige Ergebnisse. Demnach ist das Auftreten von Erdfällen bei Münsterdorf im Wesentlichen abhängig von 1) im Tiefenbereich Grenzfläche Quartär zu Oberkreide: dem Vorhandensein von wasserdurchlässigem Sand oberhalb des Kalks in Bereichen wo der gering durchlässige glaziale Geschiebemergel fehlt oder erodiert ist und 2) im oberflächennahen Bereich: dem Aufeinandertreffen von gering durchlässigem Geschiebemergel oder Ton und durchlässigen Sanden. Diese geologische Grenze oder Kontaktzone beeinflusst stark den Untergrundabfluss im Kalk. In anderen Worten, in Gebieten konzentrierter Grundwasserneubildung entlang der geologischen Grenze können sich große Strömungs- oder Lösungszonen entwickeln. Darüber hinaus könnte die in 3-6 m liegende, glaziale Geschiebemergel-/Tonschicht an der Grenzfläche zum Sand geotechnische Probleme verursachen durch Aufquellen und Schrumpfen als Folge von Schwankungen des Oberflächenwasserspiegels. Dies ist möglich, weil die Tonminerale in der Lage sind zwischen den Silikatschichten Wasser in schwacher Bindung einzulagern und dadurch ihr Volumen zu

vergrößern. Deshalb sind die unterbrochene, gering durchlässige Geschiebemergel-/Tonschicht oberhalb des Kalks und/oder die Kontaktzonen zwischen permeablem Sand und angrenzender impermeabler Geschiebemergel-/Tonschicht der Grund für mögliche weitere Erdfallrisiken im Untersuchungsgebiet.

Schlüsselwörter: Erdfällen, Geophysik, Deutschland

CONTENTS

LIST OF FIGURES

LIST OF TABLES

1 INTRODUCTION

1.1 Motivation

Sinkholes are common hazards to human safety and property over the world. They can form naturally from dissolution of carbonate rocks (such as limestone, chalk, and dolomite), evaporite rocks (gypsum, rock salt, and anhydrites), or anthropogenically from mine (tunnel) collapse in former mining areas, and in regions where large quantities of ground water are pumped from the subsurface.

The underground of north Germany is dominated in certain regions by salt domes (Baldschuhn et al., 2001). Due to uplifting of the salt domes carbonate or gypsum layers normally deep seated were uplifted to a near surface position. These water-soluble stones in the bed rock are gradually dissolved by the groundwater and produce holes and cavities. If the soil layers above them collapse, a sudden depression on the surface occurs. This event cannot be predicted until now and it may cause serious damage to buildings, roads and general development in the area.

Over the last years, sinkholes have been observed in northern Germany at several locations, for example, around Münsterdorf, Hamburg, Lüneburg, Stipsdorf, Segeberg and Lieth (Kirsch et al., 2004). The size and number of the sinkholes vary from place to place and most of them occurred in places where salt domes are located. Published papers are rare about the investigation of these sinkholes in north Germany except for some unpublished reports, for example, from the Geological Survey of Schleswig-Holstein (LLUR). Specifically, the problem area proposed for this study is at Lägerdorf-Münsterdorf, over which sinkholes have occurred suddenly in 2004, 2006 and 2007 almost linearly aligned in the south-western part of the town near a football field.

From previous studies, it is known that the area is dominated by chalk layers (upper Cretaceous) uplifted to near surface depths by salt domes (Permian). The predominant hypothesis in recent times connects the sinkhole formations to the chalk and/or the salt dissolution when soft groundwater comes into contact with such rocks.

Since the risk of sinkhole damage to future development of the town is considered to be high, conducting geophysical surveys (e.g., seismic reflection, refraction tomography, and electrical resistivity imaging) around the observed sinkholes is necessary for a detailed investigation of the subsurface and to understand the nature and causes of the sinkholes.

1.2 Sinkholes and the engineering and environmental impacts of karsts

In this section of my thesis the causes, types and investigations of sinkholes in different environmental and engineering issues will be explained briefly. Most of this theoretical part is adopted from different books and published papers such as Beck and Herring (2001), Beck (2003), Waltham et al. (2005).

1.2.1 Occurrence and the origin of sinkholes and karsts

Sinkholes are common where the bed rock below the land surface is carbonate rocks, evaporite rocks, or rocks that can naturally be dissolved by ground water circulating through them. The natural process of dissolution of rocks due to chemical reaction is a slow one. However, mechanical erosion is greater by a factor of approximately 10 depending on the geologic nature of the site (Benson et al., 2003). Thus, dissolution of soluble rocks commonly occurs along secondary porosity pathways, including bedding planes, joints or other structural features. Surface subsidence due to karst occurs as a result of erosion of overlying unconsolidated materials or collapse of rock into a cavity system that has developed over long periods of time.

Carbonate rocks and their sinkholes

Carbonate rocks are defined as those containing more than 50% by weight of carbonate minerals such as calcite ($CaCO_3$) and dolomite ($MgCa(CO_3)_2$), although the proportion commonly exceeds 90% (Waltham et al., 2005). Limestone and chalk are carbonate rocks dominated with calcite minerals. Rocks known as dolomites contain high proportions of dolomite mineral, but are very similar to limestones with respect to their karst and their sinkhole hazards. Although there are different dissolution rates determining mechanisms between limestone and dolomite, from experiment and theoretical analysis under similar conditions the initial dissolution rates of dolomite are lowered by a factor of 3 to 60 compared

to those of limestone (Liu et al., 2005). Limestone is one of the world's most widespread sedimentary rocks (Ford and Williams, 2007), and karst is developed to some degree in almost every country of the world. Major karst terrains lie on limestones that are Proterozoic in Brazil, Ordovician in Pennsylvania, Carboniferous in Great Britain, Permian in China, Mesozoic in Europe and Tertiary in Malaysia (Waltham et al., 2005).

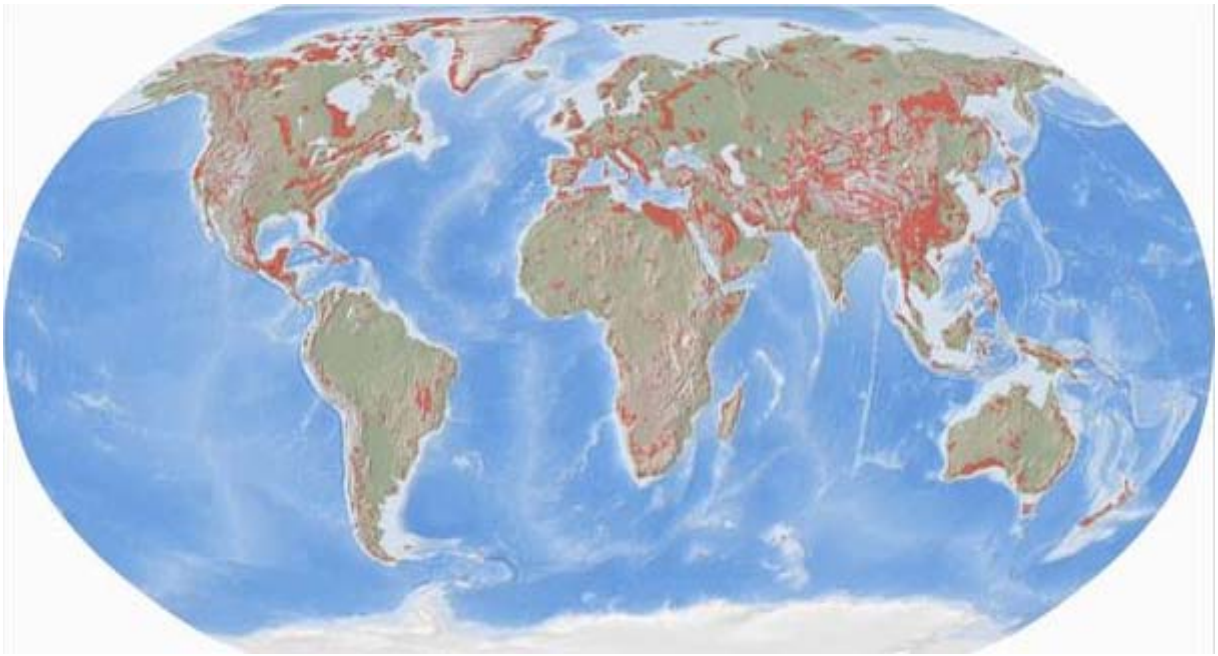

Figure 1.1 *Global distributions of major outcrops of carbonate rocks (red shaded, after Ford and Williams, 2007). Source: http://pubs.usgs.gov/sir/2008/5023/06hollings.htm.*

The solubility of limestone in pure water is extremely low. The key factor is therefore carbon dioxide, as aqueous solutions of this gas with limestone produce the bicarbonate radical, which is greatly soluble. The gross over reaction of the very complex dissolution process is (Waltham et al. 2005)

$$CaCO_3 + CO_2 + H_2O = Ca^{2+} + 2HCO_3^-$$

Dissolution aggressiveness of water to calcium carbonate relates to the content of dissolved carbon dioxide. Direct rainfall has only about 0.03% CO_2 in the open atmosphere. But, most carbon dioxide is biogenic, derived from organic activity within soils. The natural acidic water in equilibrium with the soil atmosphere that contains 1-10% CO_2 has the highest chemical aggressivity towards carbonate rocks. Its aggressiveness may be enhanced by humic acids that are formed by the decay of humus in the soil which can create groundwater with pH

values of 4.5-5.0 or in some extreme cases even less than 4.0 (Waltham et al., 2005). The degree of aggressiveness of water to limestone can be accessed on the basis of the relationship between the dissolved carbonate content, the pH value and the temperature of the water (Bell, 2007). Limestone karst is better developed in humid temperate and tropical regions, due to both the greater availability of carbon dioxide in the soil and also the higher amounts of rainfall (Drew, 1985; Waltham et al., 2005). This slightly acidic water begins to dissolve the surface along any fractures or bedding planes in the carbonate bedrock. Over time, these fractures enlarge as the bed rock continues to dissolve. Openings in the rock increase in size, and an underground drainage system begins to develop, allowing more water to pass through the area, and accelerating the formation of underground karst features.

Chalk, being a carbonate rock, is subject to dissolution along discontinuities and solution pipes may develop at the intersection of discontinuities. Buried sinkholes and solution pipes frequently are found near the contact of the chalk and the overlying Tertiary and superficial deposits (Bell, 2007). Chalk is often described incorrectly as being non-cavernous, but small cave conduits are frequently encountered in deep excavations and in well drilling (Waltham et al., 2005). Coastal cliff sections also expose caves on England's south coast, having 350 m of mapped passages (Waltham et al., 1997). A small area between Chichester and Arundel in West Sussex, southern England, provides several examples of ground subsidence related to dissolution of chalk (McDowell, 1989). The denser and stronger chalk of the Paris basin in France has at least four cave systems each with 1-2 km of mapped passages (Chabert, 1981 and Waltham et al., 2005). It is reasonable to assume that caves too small to be explored by man are probably much more common in chalk than previously has been appreciated (Lowe, 1992).

Evaporite rocks and their sinkholes

The most common evaporite rocks are the sulphates (gypsum, $CaSO4.2H2O$, and anhydrite, $CaSO4$) and rock salt (halite, $NaCl$). Karstic conditions on both gypsum and salt create extensive areas of difficult ground for construction engineers (Johnson and Neal, 2003). These rocks present more than 20% of the world's land surface (Kozary et al., 1968). Gypsum and salt are, respectively, 150 and 7500 times more soluble than limestone (Martinez et al., 1998). Sinkholes and caverns therefore can develop in beds of evaporites more rapidly than they can in carbonates. In the U.S.A., sinkholes have been known to form within a few years

where beds of gypsum are located beneath dams, and extensive surface subsidence has occurred in Oklahoma and New Mexico due to the collapse of cavernous gypsum (Brune, 1965). Many sinkholes have occurred also due to salt dissolution, for example, along the Dead Sea (Legchenko et al., 2008), in the United States (Johnson and Neal, 2003), in England (Bell 1992), in Spain (Gutierrez and Cooper, 2002), etc.

Man's influence on dissolution and sinkholes

Formation of sinkholes often depends on changes in hydraulic and mechanical stresses that may occur naturally or as the result of human activity. The vast majority of sinkholes are induced or accelerated by man's own activities (Newton, 1987). For example, of an estimated 4,000 sinkholes formed in Alabama between 1900 and 1976, only 50 were natural collapses (Newton, 1976). Sinkholes are induced by increased drainage flows that washes any soil cover down into cavernous karst, and that is induced either by pumped declines in groundwater level, by redirected and concentrated flows of storm-water run-off, or by leaking pipelines (Waltham et al., 2005). Rapid declines in groundwater level, due to aggressive pumping or droughts, can cause a loss of fluid pressure support which brings more weight to soils and rocks spanning buried voids. As the stresses on these supporting materials increase, the roof may fail and the cavity may collapse. A good example of sinkhole development by dewatering from an underground limestone quarry occurred in the Hershey Valley, Pennsylvania (Foose, 1969; Foose and Humphreville, 1979), created a cone of depression covering 600 hectares. Nearly 100 subsidence sinkholes formed above the cone of depression within three months of the increased pumping. This sinkhole development ceased after the dewatering stopped and the water table returned to normal (Langer, 2001). China has a record of more than 30,000 sinkholes induced by mine dewatering notably in the provinces of Hunan and Guangdong (Yuan, 1987; Xu and Zhao, 1988). Tunneling structures in old mining areas can also induce sinkhole problems. For example, in Germany at Staßfurt sinkholes have occurred at an old Potash mining area (Gerardi, 2009).

1.2.2 Classification of sinkholes and nomenclature

Sinkholes can be classified on a basis of origin into dissolutional, collapse, caprock, dropout, suffusion and buried sinkholes (Bell, 2007; Waltham et al., 2005). Dissolutional sinkholes form on outcrops of soluble rocks, without significant soil cover, when drainage takes place

through caverns and micro-caverns in the underlying bed rock. Collapse sinkholes are steep-sided and formed by the collapse of roofs of caverns, which have become unstable due to removal of support associated with solution erosion. Caprock sinkholes involve undermining and collapse of an insoluble caprock over a cavity in underlying soluble rock. Dropout sinkholes are formed in cohesive cover soils, for example clay, overlying bedrock fissures. Suffusion sinkholes are developed in non-cohesive soils where the down-washing of soils percolates into cavities in the carbonate or evaporite rocks below. Buried sinkholes occur in carbonate or evaporite rock head and later are filled or buried with sediment deposits.

1.2.3 Geophysical methods to investigate sinkholes and karsts

During the 1960´s and 1970´s, detection of subsurface karst conditions was regarded as a very difficult technical problem to solve and sinkholes were considered acts of God, and beyond our ability to deal with (Benson et al., 2003). The multidisciplinary conferences on sinkholes and karst started at Florida in 1984 (Beck, 1984) and have been an on-going opportunity for engineers and geoscientists to share experiences of karst related problems. Sinkholes in a karst environment can be a dream, or nightmare. Most professionals know that geophysics can help, but the geophysical method and parameters that may be best suited for the problem at hand are a less certain choice (Hoover, 2003). One of the major advantages of geophysical investigations of subsurface explorations over drilling is that information is obtained for much larger volumes of ground at lower cost (McDowell et al., 2002).

According to the British Standards and American Society for Testing and Materials (ASTM, 1999), the most useful geophysical methods applicable in karst are cross-hole seismic, microgravity, resistivity or conductivity profiling and ground penetrating radar (e.g., Hoover, 2003).

Seismic reflection for both P- and S-wave methods that use a high frequency source may detect cavities at greater depths. A direct detection of shallow subsurface voids using high resolution seismic reflection has been done, for example, by Steeples and Miller (1987), and Miller and Xia (2002). Seismic refraction tomography has a potential in identifying areas at risk for sinkhole developments and imaging of high permeability zones (e.g., Carpenter et al., 2003; Hiltunen et al., 2007; Osazuwa and Chinedu, 2008). Shear wave velocity is an important physical parameter that can be used as a tool to characterize stiffness changes with

depth. Characterization of karst with spectral analysis of surface waves has been done by Harrison and Hiltunen (2003).

Multielectrode resistivity, referred to variously as electrical resistivity imaging (ERI) and electrical resistivity tomography (ERT), is increasingly used because modern, automated multi-electrode control units simplify the acquisition of high quality data (Smith, 2005). The presence of a void in the subsurface represents an infinite resistivity, and will increase the apparent bedrock resistivity; while mud filled voids will lower the apparent bedrock resistivity. Therefore, changes or anomalous apparent resistivity values are usually the feature of interest and excellent examples are readily available in the works of Roth et al. (2002), Van Schoor (2002), Al-Zoubi et al. (2007), and Ezersky et al. (2008). A paper of Deceuster et al. (2006) also demonstrates the efficiency of 2D cross-borehole resistivity tomography as a tool to delineate complex covered karst structures beneath building foundations that is essential for civil engineers to design and conduct remedial actions properly which cannot be done by 2D surface data.

The application of GPR involves the transmission of short pulses of high-frequency electromagnetic energy (25-1,000 MHz) into the ground through an antenna. Variations in the ground's electrical impedance due to variations in the dielectric constant of the ground produce reflections that are detected at the surface by the same or another antenna (Waltham et al., 2005). The main limitation of GPR is that the depth of penetration is limited by shallow clays or high conductivity pore fluids due to the attenuation of the radar signal in wet materials that has higher conductivity. Therefore, this method has best application mostly in dry sandy soil conditions. However, GPR units are continually improved, and find wide application in karst investigations, particularly in settings like Florida where the limestone is horizontally stratified and the overburden dry sand soils do not severely attenuate the signals (Smith, 2005). Case histories and developments are regularly reported in annual international conferences devoted to this method (e.g., Benson and Yuhr, 1987).

Gravity and microgravity involves the measurement of small changes in the earth's gravitational field that are caused by localized changes in soil and rock mass and density. They are valuable investigations for karst, because negative anomalies represent `missing mass` which can then be interpreted either as open or water-filled ground cavities or as caves or sinkholes filled with soils of lower density than the surrounding rocks (Waltham et al.,

2005). Early gravity surveys had rather low resolution and were only applicable to large structures (for example; Kleywegt and Enslin, 1973). But these days, due to the presence of extremely sensitive modern gravimeters and data processing softwares, microgravity surveying is possible with station spacing as closely as 1.5 or 2.0 m (Waltham et al., 2005). Such surveys can be carried out inside or outside buildings, and also in areas where electric cables and metal conductors limit the use of electrical and electromagnetic surveys. Tedious field work, involving careful surveying and tie points, has limited its use. New generations of automated digital-output gravity meters attain 5 μgals accuracy, which is sufficient to detect shallow voids and absolute gravity meters with 10 μgals accuracy are now available which eliminate the need to tie into an established benchmark (Smith, 2005). Thus, microgravity is one of the main techniques applied in karst investigations mainly in search of voids and caverns (for example; Patterson et al., 1995; Bishop et al., 1997; Eppelbaum et al., 2008; etc).

These days, more emphasis is being placed on integrated surveys, in which two or more complementary methods are combined to constrain an interpretation. For example, seismic refraction tomography was used with ERT and GPR to identify loosened rock around a cave at an archaeological site (e.g. Leucci, 2003). Microgravity in conjunction with multichannel analysis of surface waves (MASW) has been performed by Debeglia et al. (2006) for karst investigations in Orleans, France. High-resolution magnetic survey, electrical resistivity profiling and microgravity profiling were used by Xia and Miller (2007) to delineate a subsidence feature in Kansas, USA.

1.3 Problem definition and research aims

A sudden sinkhole event occurred in September 2004 in the village of Münsterdorf near a football field resulting in an about 5 x 2 m wide and 2 m deep hole in the ground. One year later the second sinkhole occurred on the other side of the football field. In November 2007 when the geophysical survey was conducted a third sinkhole 2 x 2 m wide and 2 m deep occurred in between the previous sinkholes.

The definition of regions with potential sinkhole hazards is a challenge for geophysics. It is clear that the cause for the source of the sinkholes in the study area is unknown. Some of the relevant questions raised after the observations of the sinkholes are:

- Is the salt dome directly involved in the generation of the sinkhole?
- What is the role of the chalk layer and the Quaternary sediments covering it?
- How is the nature of the groundwater circulation?
- Why did the observed sinkholes occurre along linear structures and were concentrated in some parts of the area?
- Are there any geologic structures such as faults that cross the sinkholes?
- What is the extent of the dissolution horizons and the salt dome?
- Can we expect additional sinkholes in the area? Where?

Since the main aim of this research is to delineate the subsurface expression of this growing chalk dissolution causing sinkholes and asses their risk to the town's stability, to achieve this aim, the study is built upon the following specific objectives:

1. Detecting faults, fracture zones, and karstic features that may lead to the formation of the linearly aligned sinkholes;
2. Locating the depth to the carbonate/chalk layer and a known salt dome called Krempe-Lägerdorf;
3. Understanding the nature of the Quaternary sediments and the groundwater on top of the carbonate layer.
4. Determining the lateral and vertical situation of the leachable horizons that lead to hazards of sinkhole collapses; and
5. Producing a zonation map that shows the vulnerability of the area to hazards of sinkhole collapse.

1.4 Scope of the thesis

The thesis discusses integrated geophysical methods applied in 2007 and 2008 to study the sinkhole problems in the Lägerdorf-Münsterdorf area, North Germany. It concentrates on the processing results and interpretation of seismic reflection for P- and S-wave data, P- and S-wave refraction tomography, and inversion of DC resistivity imaging. Moreover, a joint inversion of the seismic refraction and DC resistivity data has been done for the investigation of common structures or anomalies. Finally, the integrated results are presented and after detailed discussions final conclusions have been made following the major findings.

Thus, in chapter 2 the general and local geologic settings are explained according to its location from previous works. Chapter 3 presents the results and interpretation of the P- and S-wave seismic reflection data following the short review of a seismic theory and the processing techniques. Chapter 4 provides the P- and S-wave seismic refraction tomography and velocity inversion results of the study area after introducing the basic inverse theory. In chapter 5 the results of 2D resistivity imaging have been interpreted after the explanation of basic resistivity theory and inversion techniques of DC resistivity data. In chapter 6 the joint inversion results of both seismic velocity and DC resistivity for two selected survey lines are discussed. Chapter 7 summarizes all the geophysical results and interpretations so that final conclusions can be drawn. Chapter 8 concludes this thesis by highlighting the achievements and their importance and recommending the future research opportunities in the study area.

2 THE STUDY AREA AND ITS GEOLOGY

2.1 Location of the study area

The study area is located in the North German Basin (NGB) at the southern margin of the Gluckstadt Graben (GG) near the south east coast of the North Sea. A village called Münsterdorf is found at a district of Steinburg in Schleswig-Holstein state, which is 3 km SSE of the city Itzehoe over a salt dome called Krempe-Lägerdorf (Fig. 2.1). Geographically it is situated at 53^0 54´ 12” North and 9^0 32´ 27” East. The area lies on an average of 10 meters above sea level and has a population density of 376 per kilometer square (31 December 2006). It has a more or less flat topography with accessible farm lands and forest area.

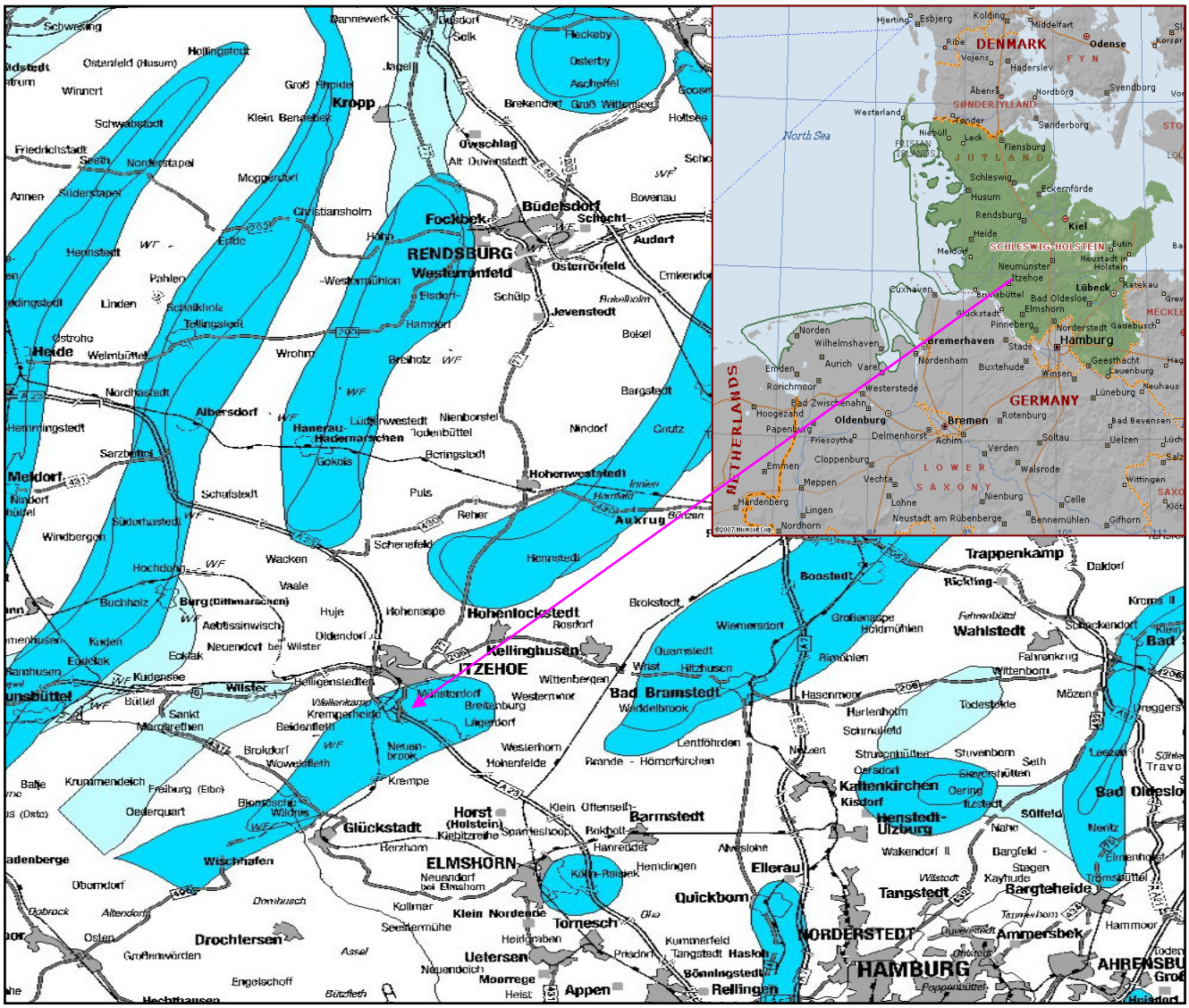

Figure 2.1 *Location of the study area (arrow) and distribution of salt structures (blue) in Schleswig-Holstein (after Baldschuhn et al., 2001).*

The underground of Schleswig-Holstein (North Germany) is dominated in certain regions by salt domes (Baldschuhn et al., 2001). Due to uplifting of the salt domes carbonate or gypsum layers normally deep seated were uplifted to a near surface position. These water-soluble stones in the bed rock are gradually dissolved by the groundwater and produce holes and cavities. If the soil layers above them collapse, a sudden depression on the surface occurs.

A sudden sinkhole event occurred in September 2004 in the village of Münsterdorf near a football field resulting in an about 5 x 2 m wide and 2 m deep hole in the ground. One year and half later a second sinkhole occurred on the other side of the football field. In November 2007, when the geophysical survey was conducted, a third sinkhole 2 x 2 m wide and 2 m deep occurred in between the previous sinkholes (Fig. 2.2).

Figure 2.2 *Photo of sinkholes that occurred in 2004 (left) and in 2007 (right).*

2.2 Geologic Settings

2.2.1 Regional geology and geologic history of the study area

Since the study area is located in the North German Basin at the south-eastern coast of the North Sea I try to asses the regional geological history of the study area starting from the basement formations of the North Sea, which were roughly formed during the Caledonian geosynclinals stage of the Cambrian-Devonian periods.

Much of the younger history of the North Sea and surrounding areas can be considered under the Caledonian (Iapetus), the Variscan (Rheic), and post Permian basin developments and tectonic events (Ziegler, 1975).

In the late Ordovician epoch, the Tornquist Sea between Baltica and Avalonia continents closed first and Avalonia collided with Baltica creating the suture of the north German-Polish Caledonides (Glennie and Underhill, 1998). This was followed by the closure of the main branch of Iapetus Ocean between the Baltica-Avalonia and the Laurentia continents and form the Laurussia (Euramerica) plate in the late Silurian (Fig.2.3). During the closure of the Iapetus Ocean when the continents and terranes of Laurentia, Baltica and Avalonia collided, metamorphic and intrusive rocks of Caledonian Orogeny formed the basement complex for much of the North Sea area (Ziegler, 1975).

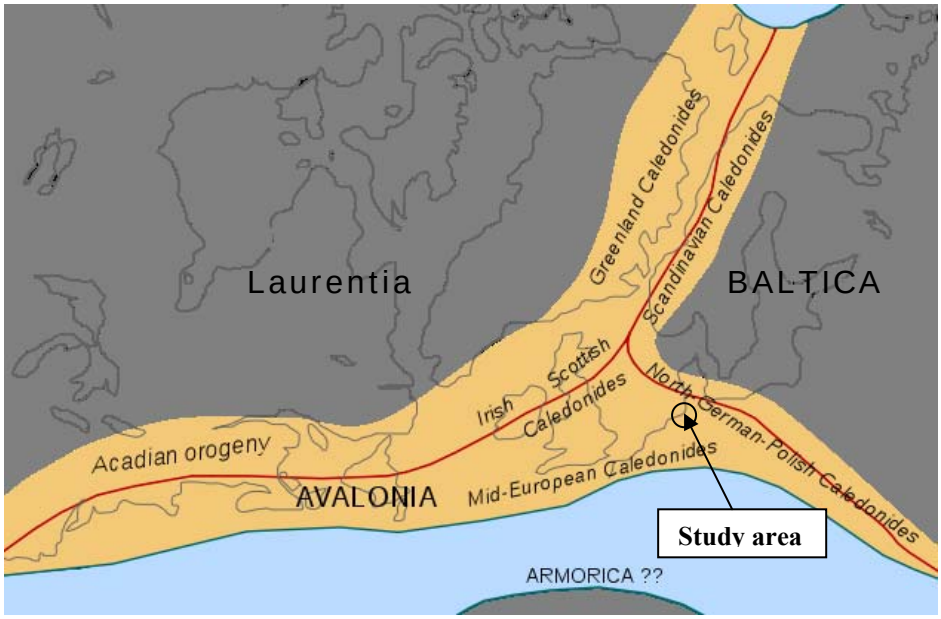

Figure 2.3 *Location of the Caledonian/Acadian mountain chains in the Early Devonian Period. Present day coastlines are shown for reference. Red lines are sutures; capitalized names are the different continents that joined during the Caledonian orogeny. (Source: http://en.wikipedia.org/wiki/File:Caledonides_EN.svg).*

Direct evidence of the extent of the Caledonian orogenic event across central Europe is limited because of the lack of outcrops. However, deep seismic and potential field studies have provided some of the best constraints on the subsurface location of the structure and relationships between these terranes (Krawczyk et al., 2008).

The oldest known sediments (called the Old Red Sandstones) from the German part of the North Sea are of Devonian age, which overlies the Caledonian crystalline basement. During the late Devonian, the North Sea and the British Isles were dominated by Old Red Sandstone (ORS) deposits, mainly sand deposited in fluvial, lacustrine and aeolian systems (Torsvik et al., 2002; Belka and Narkiewicz, 2008). The depositional environment of the North Sea and

NE Germany is characterized by a predominantly erosional regime where deposition was often intermittent and confined to narrow depocentres. Although the early Devonian sedimentation was predominantly continental (Fig. 2.5*l*), the late Devonian is influenced by a marine environment (Belka and Narkiewicz, 2008). Devonian and Carboniferous deposition transgressed from the south over the eroded Caledonides and reached maximum thickness in the southern North Sea, an area which formed part of the Variscan fore deep (Ziegler, 1975).

The Variscan (Rheic) plate cycle resulted in the formation of the supercontinent called Pangea when Gondwana and Laurussia (Euramerica) collided in the late Carboniferous. The elimination of the Rheic Ocean caused the formation of a massive mountain range through the border countries of the present day North Sea (Glennie and Underhill, 1998), which is extended along Spain, Brittany, central Germany, and into Poland. In this period the area now named the North Sea was in the subtropics and was central to the continental Pangaea with a non-marine arid environment (Torsvik et al., 2002, Kroner et al., 2008).

During latest Carboniferous to Early Permian times, magmatism affected large areas of the North Sea, the British Isles, Germany and SW Sweden (Fig. 2.5k) where vast amounts of NW-SE trending dikes intruded parallel to the Tornquist Margin (Torsvik et al., 2002). Then, two major intracontinental sedimentary basins generally referred to as the northern and southern Permian basins (Fig. 2.5j) began to subside within western and central Europe in response to thermal contraction of the lithosphere (e.g., Wilson et al., 2004). Within these basins a thick sequence of clastic and evaporite sediments (called the Rotliegend continental successions) were deposited (McCann et al., 2008). The early Permian sedimentation was predominantly fluvial changing later to aeolian. But by the end of the early Permian the extensive dune fields occupied the basin margins with saline lakes (playas) in the basin depocenters (Verdier, 1996).

The progressive subsidence of the Norwegian-Greenland Sea Rift, combined with a glacio-eustatic sea-level rise due to deglaciation in Gondwana, resulted in the flooding of these intracontinental depressions by forming a huge Zechstein inland sea during the late Permian. An arid climate combined with repeated restriction of the sea water invasion into the basin gave rise to the cyclical Zechstein deposition of carbonate, sulphate, and halite series. Seven evaporitic cycles have been recognized in the axial parts of the North German Basin, which

suggests phases of progressively greater evaporation and the shallowing of the basin or its margins (McCann et al., 2008).

The sedimentary successions of the Triassic facies reflect a long term transgressive evolution following a global sea-level low-stand at the end of the Permian, and a recovery of marine and terrestrial ecosystems (Feist-Burkhardt et al., 2008). The marine incursions were controlled by connecting sea ways between the Germanic Basin and the NW Tethys shelf. The Triassic facies include from the oldest to the youngest clastic red-beds (Buntsandstein), carbonate and evaporites (Muschelkalk), and clay or sandstone (Keuper) deposits, respectively (Fig. 2.5i).

A principal rift systems which had been initiated during the early Triassic, remained active during the early Jurassic (Ziegler, 1990). According to Ziegler (1990), the Triassic corresponds to a period of global plate boundary and plate kinematics reorganization that marks the beginning of the break-up of Pangea. Many Triassic subsidences occurred within the Central European Basin such as the Gluckstadt Graben, the Horn Graben, the Danish Basin, and the Polish Trough (Fig. 2.4). The thickest Triassic succession is observed in the Gluckstadt Graben where it reaches up to 9000 meters (Maystrenko et al., 2006).

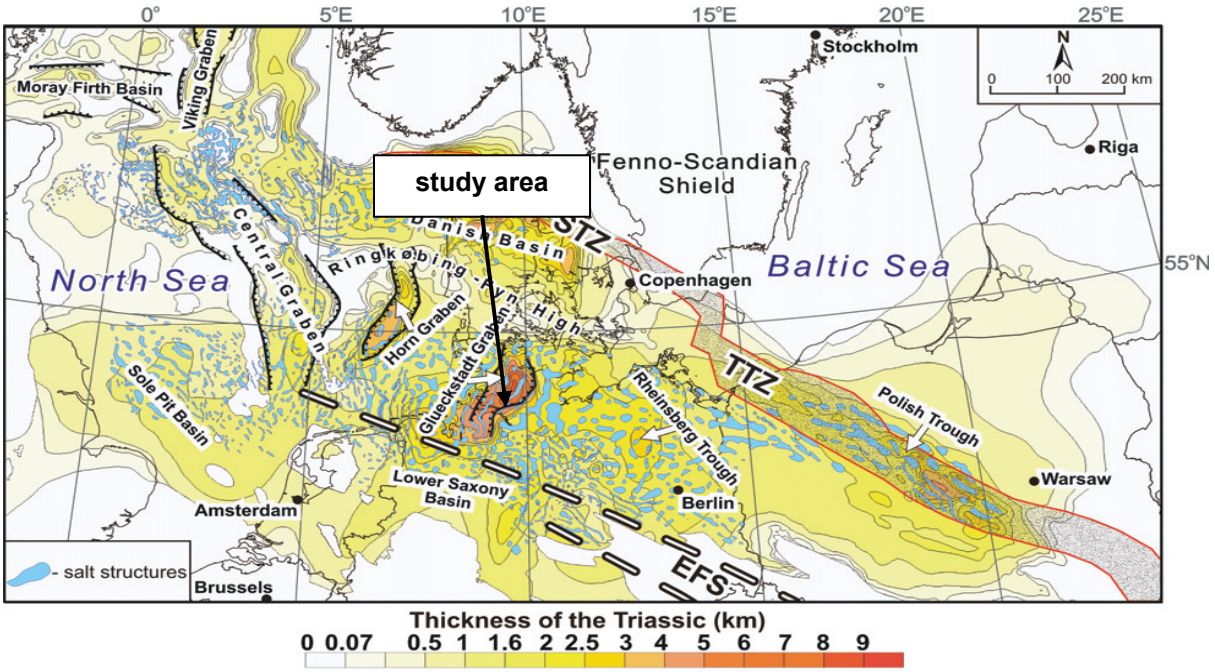

Figure 2.4 *Map showing the major Triassic subsidence centres within the Central European Basin System (after Maystrenko et al., 2006). Major structural elements – EFS: Elbe Fault System, STZ: Sorgenfrei-Tornquist Zone, TTZ: Teysseyre-Tornquist Zone.*

From Triassic times on vertical flow of salt (halokinese) was triggered during the periods of changing tectonic stress and led to the formation of several salt walls and diapirs, often along the strike direction of deeper faults (Scheck-Wenderoth et al., 2008).

During the Middle Jurassic (Fig. 2.5h) the uplift of the North Sea rift dome, which separates the Arctic Sea and Tethys (Pienkowski et al., 2008), acted as a major sediment source shedding material both to the north (to the Viking Graben) and to the south (to northern Germany and the Netherlands). This uplifting was also accompanied by extensive volcanic activity. The Iapetus suture was believed the major weakness creating a volcanic fault in the central North Sea during the later Jurassic period.

Taphrogenesis of the Central Graben, block faulting and general uplift of its eastern shoulder as well as deep erosion continued during the upper Jurassic (Jaritz, 1969). Due to this general uplift and erosion, stratiform salt layers within the Triassic sediments approached the land surface and were leached (Kockel, 1995). Above them, subrosion sinks originated, which were filled later by marine transgressive sediments of lower Cretaceous age.

The Jurassic shelf, lagoonal and lacustrine sediments show with an intercalation of limestone and marl, carbonate-rich and -poor mud rocks, or more silty and clayey (organic-rich) laminae. These are the most economically important units of rocks in the whole of Europe, being the major source for oil fields in the North Sea hydrocarbon province. Jurassic outcrops occur in several countries of central Europe with large areas. But in northern Germany outcrops are smaller and more scattered.

The Cretaceous evolution of sedimentary basins in central Europe was influenced by the interplay of plate tectonics and eustatic sea-level change (Voigt et al., 2008). During this period, central Europe was part of the European continental plate, which was bordered by the north Atlantic Ocean and the Arctic Sea to the NW and north, the Bay of Biscay to SW, the northern branch of the Tethys Ocean to the south, and by the east European platform to the east (Figs. 2.5, e-g).

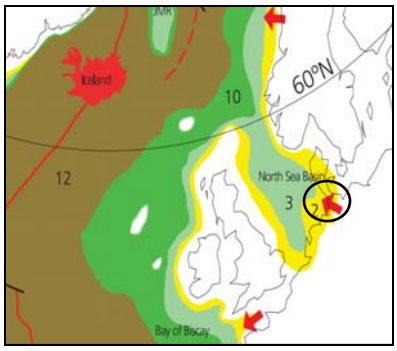

a) Pliocene (3 Ma)

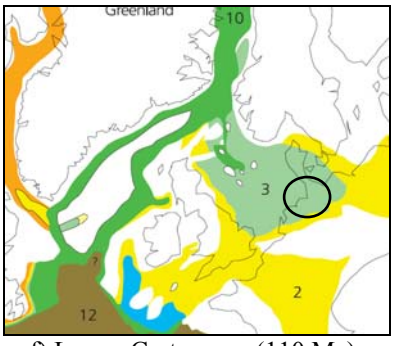

f) Lower Cretaceous (110 Ma)

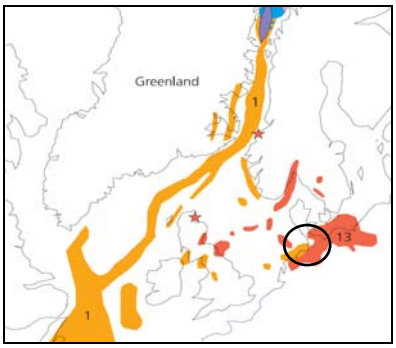

k) Lower Permian (290 Ma)

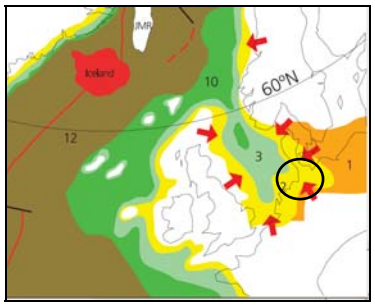

b) Middle Miocene (15 Ma)

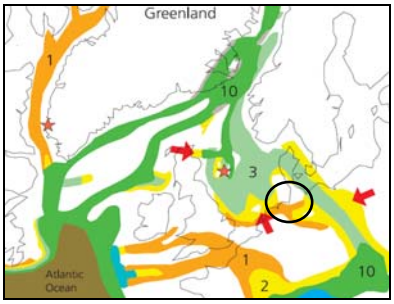

g) Lower Cretaceous (130 Ma)

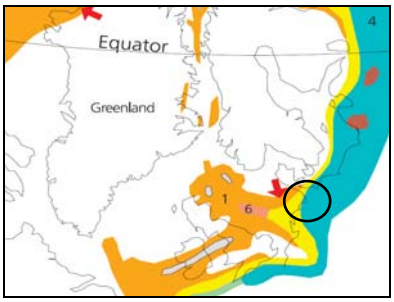

l) Late Devonian (360 Ma)

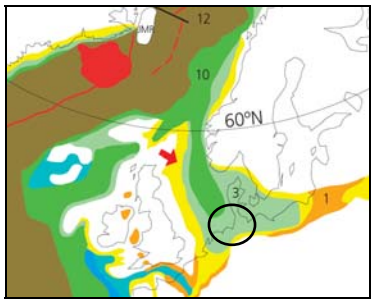

c) Late Oligocene (25 Ma)

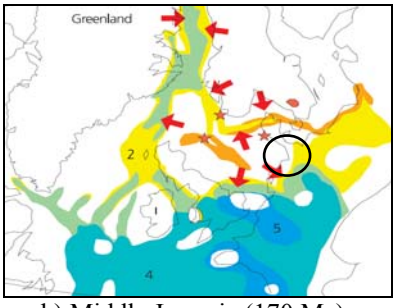

h) Middle Jurassic (170 Ma)

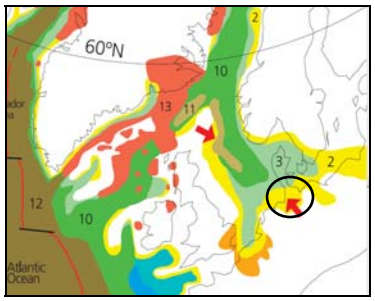

d) Paleocene (60 Ma)

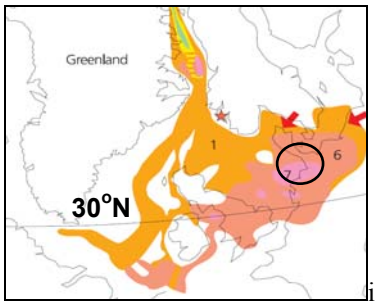

i) Upper Triassic (220 Ma)

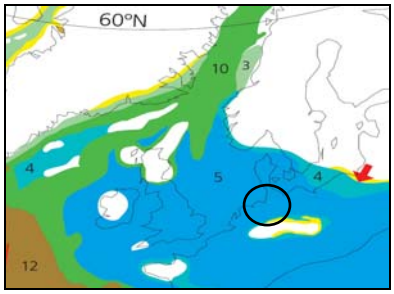

e) Upper Cretaceous (80 Ma)

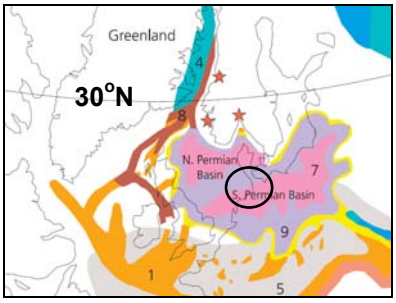

j) Upper Permian (250 Ma)

Figure 2.5 *Main geological activities of the study area and its surroundings from Late Devonian (l) to the Late Tertiary (a). Modified after Torsvik et al. (2002). Center of the circle indicates the study area.*

During the lower Cretaceous, rifting changed from E-W to NW-SE orientation, and rapid post-rift subsidence occurred in the North Sea, the Norwegian-Greenland Sea rift, and on the Barents Shelf (Torsvik et al., 2002). In the rapidly subsiding graben systems of the North Sea (Central Graben, Danish Basin, and Mid-Polish Trough), thick open-marine mudstones and shales were deposited in the basin centers whilst towards the flanks, shallow-marine sands became common (Fig. 2.5f).

The eustatic long-term sea level rise started in the lower cretaceous, achieved its maximum rate during the beginning of upper Cretaceous, and was superimposed by several short-term transgressions (Voigt et al., 2008). During the upper Cretaceous, the Atlantic rift propagated northwards and sea-floor spreading was initiated and caused a tectonically-induced sea-level rise, probably 100 - 300 m above the present sea level (Torsvik et al., 2002), and connected the Arctic oceans with the southern Tethys ocean as shown in Fig. 2.5e. In the North Sea, rifting and transgression had flooded most of the low-lying areas, cutting off clastic input, and leading to the deposition of pelagic chalky limestones. Sea-level rise peaked until the end of the upper Cretaceous times when only the Scottish and Norwegian Highlands and Greenland remained emergent (Fig. 2.5e).

Cenozoic times were characterized by a gradual long-term fall in global sea levels (Rasser et al., 2008). The Alpine compressive tectonics caused a general uplift of Europe during the Cenozoic due to the collision between Africa and the Eurasia plates (Reicherter et al., 2008). The Cenozoic succession consists mainly of clastics with some marls (Fig. 2.5, a-d).

During the Tertiary, there were repeated alternating regressions (lower and middle Palaeocene) and transgressions (upper Palaeocene and Eocene). In the early Eocene, the North Sea Basin was at its most extensive, which covered the present-day North Sea, southern and eastern England, eastern Scotland, Belgium, the Netherlands, northern and eastern Germany, southern Sweden, Denmark, and northern Poland (Rasser et al., 2008).

The most extensive transgression occurred during the early Oligocene in the Rupelian age and resulted in the deposition of marine Rupelian clays. The Rupelian clays serve as a basin-wide marker horizon for the differential subsidence and uplift in the north German basin (Reicherter et al., 2008). A broad zone of subsidence stretches from Hamburg through Berlin

to Wroclaw (Poland) and is delineated by the elevation of the base of the Rupelian (Garetzky et al., 2001).

There were repeated sea-level fluctuations throughout the North Sea during the Miocene, continuing up to Pleistocene and deltaic conditions dominated much of the area. The main lignite deposits of northern Germany are of middle Miocene age. The Pliocene marine transgression extended only as far east as Hamburg and the remainder of the north German basin area was characterized by fluvial sediments (Fig. 2.5a).

The Quaternary (Pleistocene and Holocene), traditionally considered to be the Ice Age, is an interval of oscillating climate extremes between glacial and interglacial stages. In this period northern Germany had been affected by three main glaciations (Litt et al., 2008); namely the Elsterian (middle Pleistocene), Saalian (late of middle Pleistocene), and Weichselian (upper Pleistocene) glacial stages (Fig. 2.6). The lower Pleistocene is characterized by alternating cold and warm stages. However, the north-central European lowland was not affected by inland ice, but permafrost conditions may have occurred in some of the cold phases (Litt et al., 2008).

The oldest glaciation, represented by widespread till sheets throughout north-central Europe, is the Elsterian glaciation. The Saalian was a complex period including several cold and warm fluctuations and it corresponds to the lower Saalian and the upper Saalian glaciations. In the upper Saalian two major glaciations (Drenthe and Warthe) occurred. In northern Germany, the maximum extent of the Weichselian glaciation reached up to the Brandenburg area in the east; further west it extended as far as the northern parts of Hamburg and the eastern part of Schleswig-Holstein (Litt et al., 2008).

The Holsteinian interglacial stage, between the Elsterian and Saalian tills, corresponds to a warm climate stage of fine-grained gravel and sand with some lacustrine sediments (Eissmann, 1995). Similarly, the Eemian interglacial stage describes sediments deposited during a warm period between the Saalian and Weichselian glacial stages in the upper Pleistocene.

Figure 2.6 *Ice age map of Europe, red line maximum limit of Weichselian ice age, yellow Saalian ice age at maximum (Drenthe stage), blue the Elsterian ice age maximum glaciation. (Source: http://en.wikipedia.org/wiki/File:EisrandlagenNorddeutschland.png).*

The Holocene, as an interglacial stage, is strongly influenced by human impact. The most established zonation scheme of the Holocene in north-central Europe is based on vegetational development reflecting climatic changes (Litt et al., 2008).

Repeated glaciation/deglaciation processes during the Pleistocene also impacted on the landscape of northern Germany. Presently, the isostatic rebound of the Fenno-Scandian shield has the greatest influence on the stress field in northern Germany (Kaiser et al., 2005). The Scandinavian landmass continued to experience postglacial uplift up to the present as a result of isostatic response due to lithospheric unloading, causing erosion and deposition of thick sediments into the NW Atlantic margin (Torsvik et al., 2002). From 1 to 5 cm of uplift have been recorded, mainly in present-day Norway, but recent uplift rates decrease to the south of the Scandinavian Shield, with subsidence predominating in the area of Hamburg 1-2 mm/year. In contrast, salt diapirs are rising from 1-1.2 mm/year (e.g. the Kalkberg, Bad Segeberg, Schleswig-Holstein, Lüneburg, Niedersachsen, Sperenberg, south of Berlin) accompanied by dissolution and subrosion processes and the formation of rim syncline lakes in the Holocene (Reicherter et al., 2008).

2.2.2 Local Geology

The area is covered mainly by Quaternary (Pleistocene and Holocene) sediments, which overlay unconformbly on the upper Cretaceous (chalky limestone). The main Pleistocene sediments exposed in the study area from the oldest to the youngest are: Saalian glacial sediments (Saalekaltzeit glazial), Saalian glaciofluvial sediments (Saalekaltzeit glazifluviatil), and aeolian sand (Flugsand) sediments. The Saalian glaciofluvial sediments are dominated by sand and gravels with 10% of tills, whereas, the Saalian glacial sediments are dominated by till with some sands and gravels. The Aeolian sand layer (on the western part of the study area) is a sand layer deposited by wind and overlies both the glaciofluvial sand and the glacial till (Fig. 2.7). The Holocene sediments which are the tidal flat sediments dominated by very fine sand, silt and mixtures of clay with silt. They contain also peats especially at the contact boundary with the Pleistocene sediments.

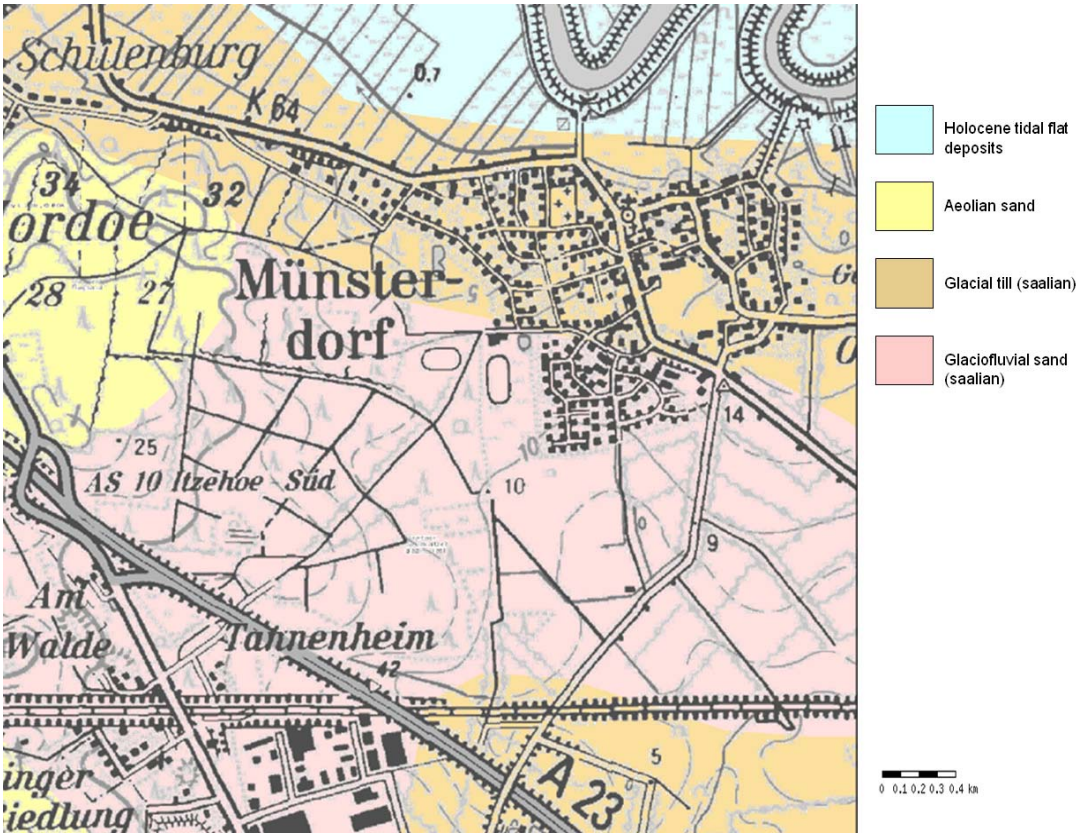

Figure 2.7 *Geologic map around the study area (Source: https://www.gga-hannover.de/app/fis_gp/index.htm).*

The upper Cretaceous chalk is usually found in Schleswig-Holstein from 500 m to 1000 m depth, but with the rise of the Permian salt dome called Krempe-Lägerdorf, it uplifted to near

surface around 20 m depth in the study area (Fig. 2.8) and is found exposed on the south-eastern part of the study area at Lägerdorf quarry site.

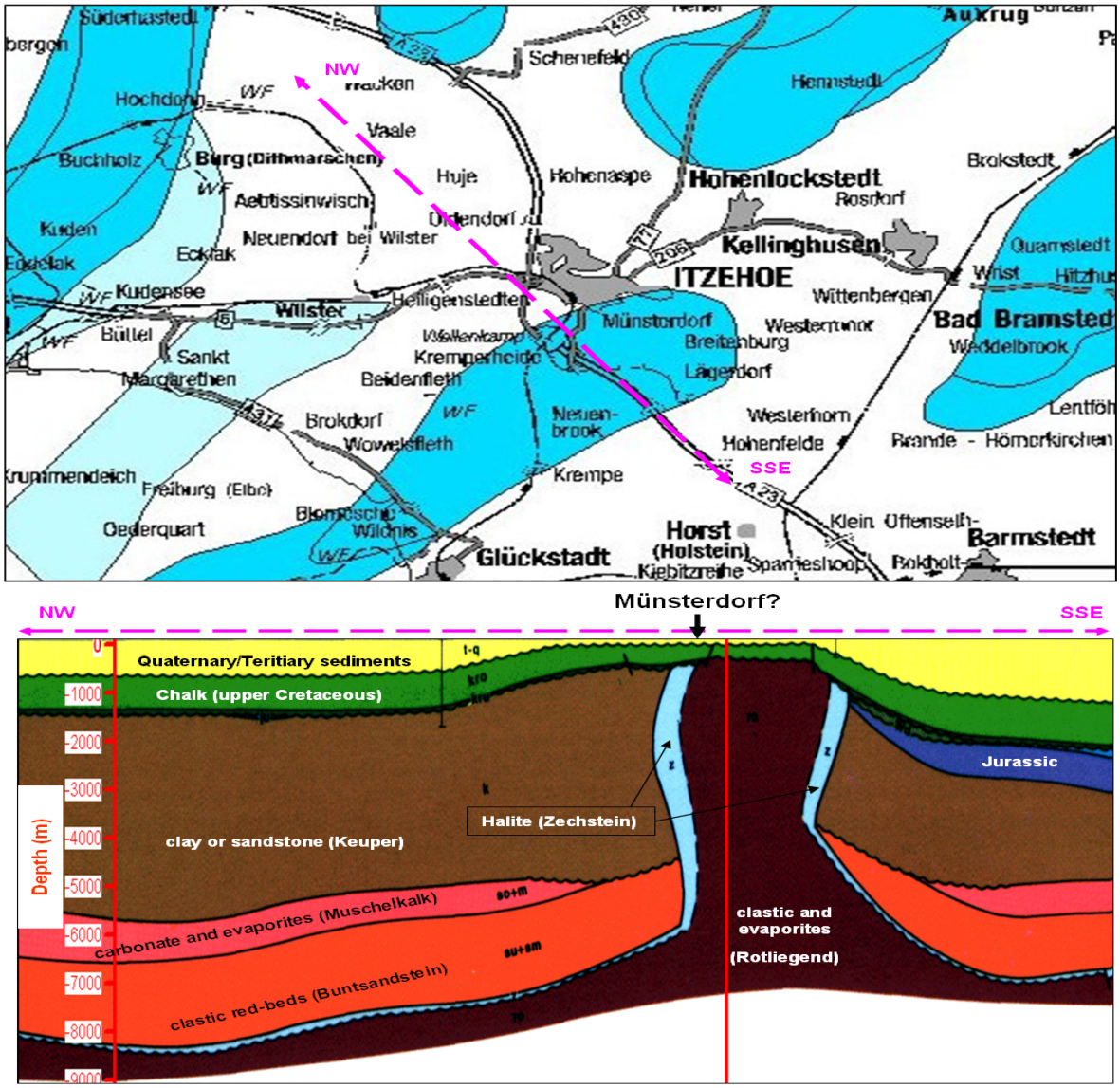

Figure 2.8 *Regional cross-sectional maps across the Krempe-Lägerdorf salt dome southwest of the study area (after Baldschuhn et al., 2001).*

There is no tertiary sediment layer in the study area because of erosion before deposition of the Quaternary sediments. Therefore, the quaternary sediments are underlain by the upper Cretaceous chalky limestone unconformably (Fig. 2.9). The chalk in Lägerdorf formation contains between 97 and 98% of $CaCO_3$ (Ehrmann, 1986) and its upper layer is dominant with black colour flints. The Lägerdorf salt dome in the study area is characterized by parallel elongated salt structures in north to northeast direction (Jaritz, 1987).

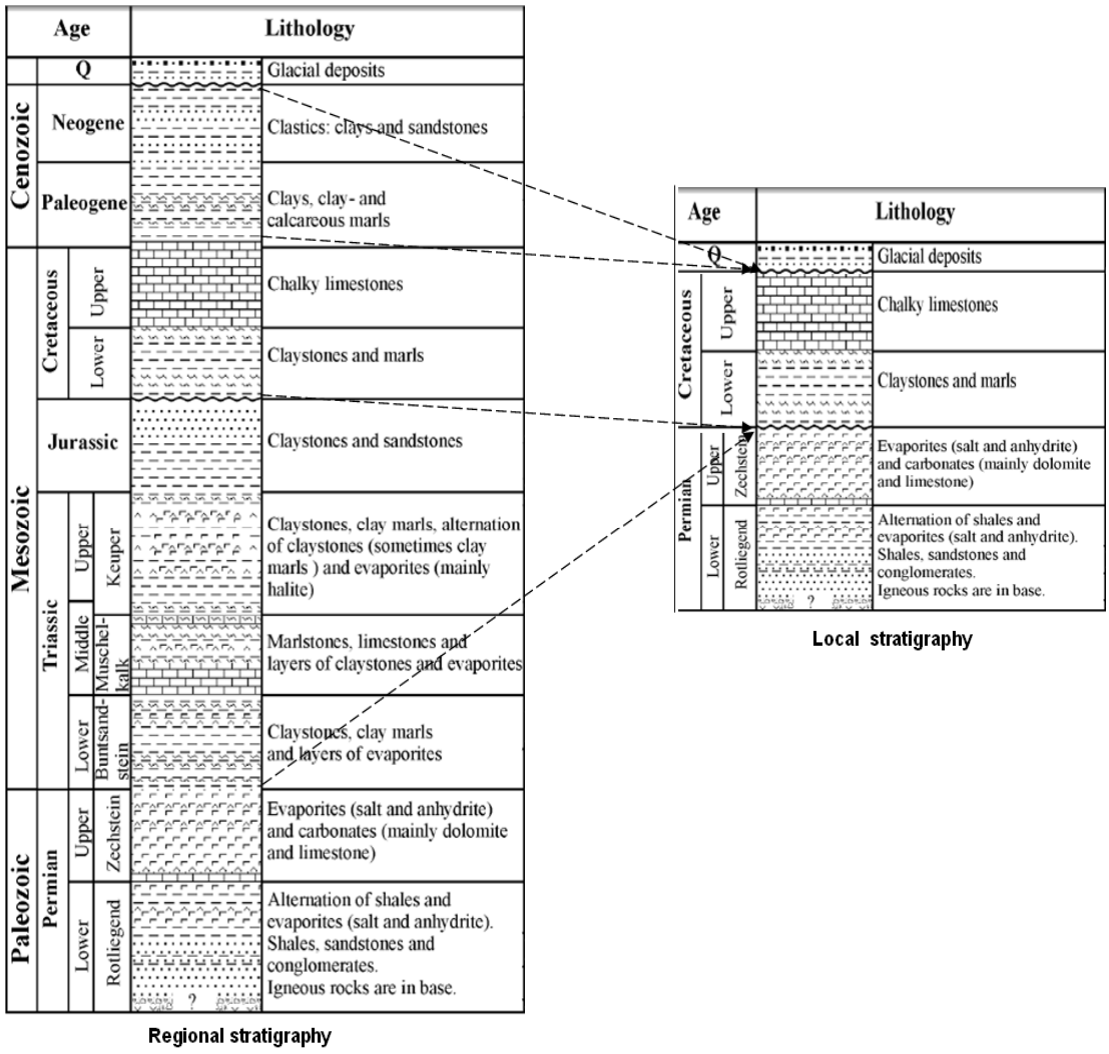

Figure 2.9 *Lithostratigraphic correlation of the regional and local geology (modified after Maystrenko et al., 2006).*

2.2.3 Groundwater situation

Since aggressive pumping can induce sinkholes by abruptly changing groundwater levels and disturbing the equilibrium between a buried cavity and the overlying earth materials, I will try to assess briefly the groundwater situation of the study area in this section.

About a kilometer in southeastern direction of the study area, mining is occurring for cement and lime factories in the area of Lägerdorf (Fig. 2.10a). According to Iwanoff (1998), in three pits with depths of nearly 100 m, mine pumping affects deeper aquifers and sometimes shallow ones as well. The total amount of mine water pumped ranges up to $6*10^6$ m^3/year and due to the relief of hydraulic pressure, saline water is ascending from deeper parts of the chalk and infiltrating into the pits with the minefloor. Although the water table in the study area is

found at 5 m above sea level, the water surface of the pit lakes lies about 70 m below the surface or 63 m below sea level, due to dewatering associated with the mines (Iwanoff, 1998). The water is pumped from basins or lakes in the deepest parts of the quarries directly into a river.

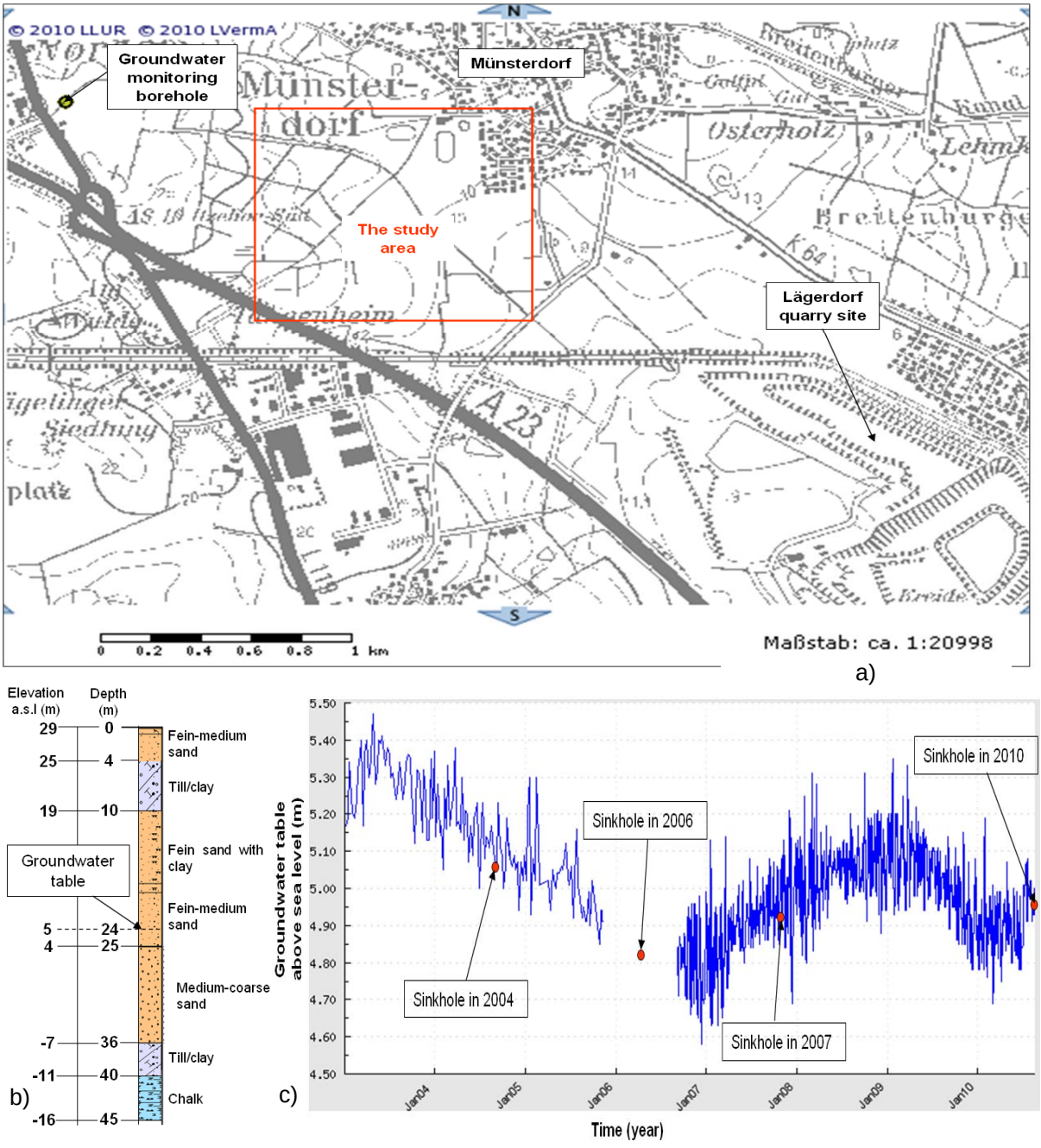

Figure 2.10 *a) Location map of groundwater monitoring well and the Lägerdorf quarry site, b) the borehole lithology, and c) the groundwater table from 2003 to 2010 (modified from LLUR http://www.umweltdaten.landsh.de/atlas/script/index.php).*

The annual recharge of the shallow aquifers ranges between 30 and 130 mm/year. The groundwater shows high concentration of calcium and bicarbonates and has a pH values between 6.1 and 7.8 (Iwanoff, 1998). A groundwater monitoring well located on the northwestern part of the study area indicates that the groundwater table fluctuates between 4.5 and 5.5 m above sea level from year to year as shown in Fig. 2.10c.

3 SEISMIC REFLECTION METHOD

3.1 Fundamentals of seismic waves

Although the theoretical developments are not the subject of this thesis, it is important to introduce some basic concepts before discussing the seismic methods. The seismic method is rather simple in concept. An energy source (for example dynamite or vibrator) is used to produce seismic waves (similar to sound) that travel through the earth and that are detected by geophones (on land) or hydrophones (at sea). The detectors convert the motion or pressure variations to electric signals that are recorded by electronic instruments. Two paths between source and receiver are of particular interest – reflection and refraction. In this section, some basic concepts of seismic methods which are relevant to my work are briefly reviewed. The theoretical background is mainly adapted and summarized from a number of publications (e.g., Yilmaz, 1987; Robinson and Coruh, 1988; Garotta, 1999; Kearey et al., 2002; Steeples, 2005; Rabbel, 2006; Veeken, 2007; Gadallah and Fisher, 2009).

3.1.1 Seismic wave propagation

The seismic method utilizes the propagation of energy waves through the earth. The propagation of seismic waves is described by the wave equation. Deriving the wave equation means getting over three essential steps: expressing the stability of a small element in the elastic medium; linking stresses and strains with elastic constants by applying Hooke's law; and equating inertial force to the surrounding stresses by applying Newton's second law of motion (Robinson and Coruh, 1988; Lay and Wallace, 1995; Garotta, 1999).

The wave equation

An object can be deformed (strained) in different ways by applying force (stress) on the sides of the object. The stress deforms that object by changing its shape and size. When the stress is applied suddenly, energy is released and produces vibrations, which are called seismic (elastic) waves. Although there are different kinds of strain that can be produced depending on the strength and direction of stress and the nature of the substance being deformed, in seismic wave propagation the most interesting is the elastic strain. A perfectly elastic body is

the one that recovers completely after being deformed. Solid substances ordinarily respond elastically to relatively weak, short-term stresses, and exhibit plastic strain if stronger or more prolonged stress is applied. For small magnitude, short duration stresses as in the case of seismic (elastic) wave propagations, almost all earth materials display a linear proportionality between stress and strain.

For a three dimensional wave propagation in homogeneous, isotropic, and elastic media, the wave equation can be written in the form of the equation of motion for the displacement vector U = (u, v, w):

$$\rho\frac{\partial^2 U}{\partial t^2}=(\lambda+\mu)\nabla\theta+\mu\nabla^2 U \quad \text{or} \quad \rho\frac{\partial^2 U}{\partial t^2}=(\lambda+\mu)\nabla(\nabla.U)+\mu\nabla^2 U \tag{3.1}$$

where u, v, and w are displacements along x, y, and z directions, λ and μ are called Lamés constants, ρ is density of the medium, ∇^2 is the Laplacian operator, and

$$\nabla=i\frac{\partial}{\partial x}+j\frac{\partial}{\partial y}+k\frac{\partial}{\partial z} \qquad \nabla^2=\frac{\partial^2}{\partial x^2}+\frac{\partial^2}{\partial y^2}+\frac{\partial^2}{\partial z^2} \qquad \theta=\nabla.U=\frac{\partial u}{\partial x}+\frac{\partial v}{\partial y}+\frac{\partial w}{\partial z}$$

Using the vector identity, $\nabla^2 U=\nabla(\nabla.U)-\nabla\times\nabla\times U$ the wave equation can be written as

$$\rho\frac{\partial^2 U}{\partial t^2}=(\lambda+2\mu)\nabla(\nabla.U)-\mu\nabla\times\nabla\times U \tag{3.2}$$

By making use of the vector identities $\nabla.(\nabla\times U)=\nabla\times(\nabla.U)=0$, for any vector U, we can derive the following two equations from a scalar and vectorial components of the above wave equation.

1) The scalar component

$$\nabla.\rho\frac{\partial^2 U}{\partial t^2}=\nabla.((\lambda+2\mu)\nabla(\nabla.U)-\mu\nabla\times\nabla\times U)$$

$$\rho\frac{\partial^2 \nabla.U}{\partial t^2}=(\lambda+2\mu)\nabla^2(\nabla.U)$$

Replacing $\nabla.U=\theta$ we obtain

$$\rho \frac{\partial^2 \theta}{\partial t^2} = (\lambda + 2\mu)\nabla^2 \theta \quad \text{or} \quad \frac{1}{\alpha^2}\frac{\partial^2 \theta}{\partial t^2} = \nabla^2 \theta \tag{3.3}$$

The scalar component yields a particle motion perpendicular to the wavefront and a propagation velocity V_p,

$$V_p = \sqrt{\frac{\lambda + 2\mu}{\rho}} \tag{3.4}$$

which is the propagation velocity (speed) of the compressional or P-waves.

2) The vectorial component

$$\nabla \times \rho \frac{\partial^2 U}{\partial t^2} = \nabla \times ((\lambda + 2\mu)\nabla(\nabla . U) - \mu \nabla \times \nabla \times U)$$

$$\rho \frac{\partial^2 (\nabla \times U)}{\partial t^2} = -\mu \nabla \times \nabla \times (\nabla \times U)$$

Replacing $\omega = \nabla \times U$ we obtain

$$\rho \frac{\partial^2 \omega}{\partial t^2} = -\mu \nabla \times \nabla \times \omega$$

using the vector identity, $\nabla^2 \omega = \nabla(\nabla . \omega) - \nabla \times \nabla \times \omega = -\nabla \times \nabla \times \omega$, it can be written as

$$\rho \frac{\partial^2 \omega}{\partial t^2} = \mu \nabla^2 \omega \tag{3.5}$$

where ω is called the rotation which is an essential feature of S-waves. The vectorial component has a particle motion tangential to the wavefront and a propagation velocity V_s,

$$V_s = \sqrt{\frac{\mu}{\rho}} \tag{3.6}$$

which is the propagation velocity of the shear mode or S-waves.

The seismic waves, which are composed of both the compression and shear waves, are propagating in the earth materials at different velocities depending on the elastic properties of

that material. That means different rock layers can be identified based on the different velocities of the seismic waves that propagate through them.

Seismic waves and their velocities

Seismic waves occur as compressional (P) waves, shear (S) waves, and surface waves also called ground rolls of the Rayleigh (R) and Love (L) wave types. P- and S-waves (called body waves) are usually of greatest interest. Surface waves may be recorded on land seismic records as ground roll, an undesirable event in seismic reflection surveys and, hence referred to as "noise". P-waves propagate in solids, liquids and gases. S-waves propagate only in solids. According to Eqs.3.4 and 3.6, P-waves always have higher propagation velocities than S-waves, in the same medium or material (Table 3.1). The P-waves have only one oscillation direction that is, parallel to the propagation direction. On the other hand, for the S-waves, there are countless oscillation planes around the propagation direction axis. From all the possible polarization planes, by considering only the vertical and horizontal oscillation planes to the earth's surface, the S-waves can be subdivided into SV-waves (vertically polarized) and SH-waves (horizontally polarized).

The compressional modulus, k is defined as the ratio between pressure and volume deformation connected with the passage of a P-wave. The shear modulus, μ is correspondingly defined as the ratio of shear stress to shear deformation. It can be shown that $\lambda + 2\mu$ equals $k + 4\mu/3$. In contrast to the P-wave movement, no volume change occurs in the rock during S-wave propagation (except at interfaces). Therefore, the S-wave velocity V_s depends mainly on the properties of the rock matrix and is nearly independent of the pore fill whereas the P-wave velocity V_p depends on both matrix and pore fill. In particular, P-waves are sensitive to rock porosity and fluid saturation making them a suitable tool for groundwater exploration (e.g., Kirsch, 2006). S-waves can be used to obtain more detailed or special information in geotechnical engineering projects, particularly between boreholes, to establish the shear modulus of soils and foundation materials. For more comprehensive lithological investigation of the subsurface advantage can be taken of combined P- and S-wave surveys and thus of the relations (3.4) and (3.6).

On a seismogram, surface waves usually produce the largest amplitudes. Rayleigh waves exhibit a retrograde elliptical particle motion. Love waves are S-waves that are reflected

multiple times while trapped in a surface layer, and they require a low-velocity layer at the earth's surface in which to propagate. Interference from Love waves can be a major source of difficulties when data from shallow S-wave reflection surveys are being analyzed.

Material	**Velocity v_p** [m s^{-1}]	**Velocity v_s** [m s^{-1}]	**Bulk density ρ** [g cm^{-3}]
clay	500 - 2800	110 - 1500	1.25 - 2.32
-sandy clay	2000 - 2750		
-loamy clay	500 - 1900	440 - 1080	0.76 - 1.57
sand	100 - 2000	100 - 500	1.80 - 2.05
-dry	100 - 600		2.33 - 2.80
-wet	200 - 2000		1.50 - 2.00
-saturated	1300 - 1800		1.80 - 2.05
-coarse	1835		2.03
-fine grained	1740		1.98
gravel	180 - 1250		1.95 - 2.20
-wet	750 - 1250		1.95 - 2.20
weathering layer	100 - 500		1.20 - 1.80
marly limestone	3200 - 3800		2.65 - 2.73
marlstone	1300 - 4500	715 - 2250	
siltstone	1900 - 2000		2.35 - 2.73
sandstone	800 - 4500	320 - 2700	2.30 - 2.55
-loose	1500 - 2500	575 - 1101	1.80 - 2.40
-compacted	1800 - 4300	672 - 1023	2.22 - 2.69
-siliceous	2200 - 2400		
quartzite	5800		2.64
schistose quartzite	5500		2.65
lime	3000 - 6000		
-chalky	3560		
-fine grained	4680		
-crystalline	5500		2.67
marble	5100		2.66 - 2.70
chalk	1800 - 3500		2.00 - 2.57
limestone	2000 - 6250	1800 - 3800	1.75 - 2.88
dolomite	2000 - 6250	2900 - 3740	1.75 - 2.88
gypsum	1500 - 4600	750 - 2760	2.31 - 2.33
anhydrite	4500 - 6500	750 - 3600	2.15 - 2.44
halite	4500 - 6500	2250 - 3300	2.15 - 2.44
bituminous coal	1600 - 1900	800 - 1140	1.25 - 1.84
brown coal	500 - 1800		1.20 - 1.50
air (depending on temperature)	310 - 360		$1.29 \cdot 10^{-3}$
petroleum	1035 - 1370		0.92 - 1.07
water	1430 - 1590		0.98 - 1.01
saltwater (seawater)	1400 - 1600		1.01

Table 3.1 *Seismic velocities for some common rocks and fluids after Fertig (2005).*

3.1.2 Reflection, transmission and conversion of seismic waves

When an incident seismic wave strikes a boundary between two media with different velocities of wave propagation and/or different densities, part of the energy is reflected from the boundary and the rest is transmitted into the next layer (Fig. 3.1). The sum of the reflected (A_r) and transmitted (A_t) amplitudes is equal to the incident amplitude (A_i).

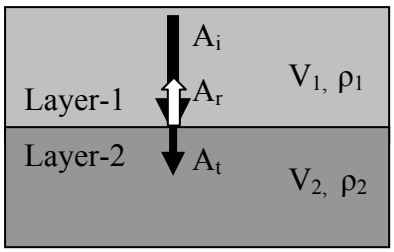

Figure 3.1 *Normal reflection and transmission.*

The reflection coefficient R is the ratio of the amplitude A_r of the reflected ray to the amplitude A_i of the incident ray. Similarly, the transmission coefficient T is the ratio of the transmitted amplitude A_t to the incident amplitude. Accordingly, we have

$$R = \frac{A_r}{A_i} \tag{3.7}$$

and

$$T = \frac{A_t}{A_i} = 1 - R \tag{3.8}$$

The relative sizes of the transmitted and reflected amplitudes depend on the contrast in acoustic impedances of the rocks on each side of the interface. The acoustic impedance Z of a rock is defined as product of its density and its P-wave velocity. The magnitude and polarity of the reflection coefficient depends on the difference between seismic impedances of layers 1 and 2, Z_1 and Z_2. It can be show that

$$R = \frac{Z_2 - Z_1}{Z_2 + Z_1} = \frac{\rho_2 V_2 - \rho_1 V_1}{\rho_2 V_2 + \rho_1 V_1} \tag{3.9}$$

and

$$T = \frac{2 Z_1}{Z_2 + Z_1} = \frac{2 \rho_1 V_1}{\rho_2 V_2 + \rho_1 V_1} \tag{3.10}$$

Large differences ($Z_2 - Z_1$) in seismic impedances result in relatively large reflection coefficients. If the seismic impedance of layer 1 is larger than that of layer 2, the reflection coefficient is negative and the polarity of the reflected wave is reversed.

For a given incident mode, a partition also occurs by conversion, generating different reflected and transmitted modes in which the directions of the reflected or transmitted waves obey Snell's law. For example, when a P-ray strikes an interface at an angle other than 90^0, reflected and transmitted P-rays are generated as in the case of normal incidence. In such cases, however, some of the incident P-wave energy is converted into reflected and transmitted SV-waves (Fig. 3.2). The SV- waves, which are polarized in the vertical plane, can also be reflected and transmitted as P-waves at boundaries. Only those SH-waves whose direction of polarization is parallel to the reflection plane will be reflected and refracted as pure SH-waves. Because of this reason, near-surface applications of SH-waves receive increasing attention by developers of new sources and receivers (see section 3.3.2). Using this technique can reduce the noise effect of the converted waves such as the P- and SV-waves as only the SH-waves are recorded.

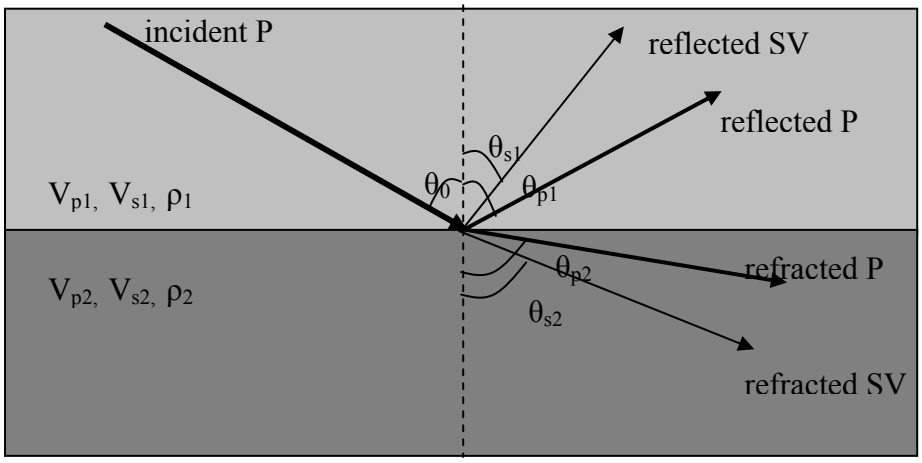

Figure 3.2 *Partitioning at an interface showing refracted, reflected and converted waves.*

The major application of Snell's law is to determine angles of reflection and refraction from the incidence of seismic waves on layer boundaries at angles other than 90^0. Snell's law of reflection states that the angle at which a ray is reflected is equal to the angle of incidence (i.e. $\theta_0=\theta_{p1}$). Both the angle of incidence and the angle of reflection are measured from the normal to the boundary between two layers having different seismic impedances. The portion of incident energy that is transmitted through the boundary and into the second layer with changed direction of propagation is called a refracted ray. The direction of the refracted ray

depends upon the ratio of the velocities in the two layers. If the velocity in layer 2 is faster than that of layer 1, the refracted ray is bent away from the normal ($\theta_{p2} > \theta_0$). If the velocity in layer 2 is slower than that of layer 1, the refracted ray is bent toward the normal. The angle of incidence is called critical angle (θ_c) when $\theta_{p2} = 90^0$ and the refracted (called head) waves are generated and travel along the interface. Refracted waves form the basics of the seismic refraction method and will be presented in chapter four of my thesis.

Snell's law governs these situations at the interface of Fig. 3.2 in the following way:

$$\frac{\sin\theta_{p1}}{V_{p1}} = \frac{\sin\theta_{s1}}{V_{s1}} = \frac{\sin\theta_{p2}}{V_{p2}} = \frac{\sin\theta_{s2}}{V_{s2}} \tag{3.11}$$

In Fig. 3.2 the relationships among the various velocities are: $V_{P2} > V_{S2} > V_{P1} > V_{S1}$. As a result the angles of refraction for both P- and S-waves are greater than the angle of incidence. There are, however, three other possible relationships (Table 3.2). Since the S-wave velocity is always slower than the P-wave velocity the reflected S-wave always reflects at an angle less than that of the P-wave (i.e., $\theta_{p1} > \theta_{s1}$).

Velocity relationship	Angle relationship
$V_{P2} > V_{S2} > V_{P1} > V_{S1}$	$\theta_{p2} > \theta_{s2} > \theta_{p1} > \theta_{s1}$
$V_{P2} > V_{P1} > V_{S2} > V_{S1}$	$\theta_{p2} > \theta_{p1} > \theta_{s2} > \theta_{s1}$
$V_{P1} > V_{P2} > V_{S1} > V_{S2}$	$\theta_{p1} > \theta_{p2} > \theta_{s1} > \theta_{s2}$
$V_{P1} > V_{S1} > V_{P2} > V_{S2}$	$\theta_{p1} > \theta_{s1} > \theta_{p2} > \theta_{s2}$

Table 3.2 *Snell's law relationships.*

The partition of the energy between the different modes of the reflected, converted or transmitted waves is given by the Zoeppritz` equations, which express the continuity of the displacement on two sides of the boundary. These equations are a relatively complex set of equations that allow calculation of the amplitudes of the two reflected and the two transmitted waves as functions of the angle of incidence. The calculations require the knowledge of P- and S-wave velocities plus that of the densities on both sides of the boundary. The Zoeppritz equations describe the variation of the P wave reflectivity as a function of the incident angle and they are the basis of AVO (Amplitude Versus Offset) studies (Garrota, 1999). These equations can be found, along with relevant mathematical and technical discussions, in many

advanced seismology textbooks (e.g., Lay and Wallace, 1995). There is no converted wave at zero offset i.e. when $\theta_0 = 0$ (Aki and Richards, 1980).

3.1.3 Attenuation of seismic waves

As seismic waves propagate over greater and greater distances the amplitudes become smaller and smaller. That is, seismic waves are attenuated with the distance traveled. After the initial wavelet leaves the source zone, it receives no more energy. But an advancing wavelet has a continually expanding spherical shell called wave front when it propagates in a homogeneous material. As the wave front expands, the same quantity of energy must be distributed over a larger spherical surface. Therefore, particles farther from the source vibrate at smaller amplitudes than particles closer to the source. This effect is called geometrical spreading or spherical divergence.

If the radius of the wavefront is r and the original energy transmitted from the source is E, the amount of energy contained within a unit area of the shell is $E/4\pi r^2$. With increasing distance along a ray path, the energy contained in the ray falls off as $1/r^2$ due to the effect of the geometrical spreading of the energy. The wave amplitude, which is proportional to the square root of the wave energy, therefore falls off as 1/r, or

$$A_r = A_o/r \qquad (3.12)$$

where A_o and A_r are amplitudes of the wavelet at the source and at a distance r, respectively.

In the case of surface waves, geometrical spreading is analogous to the rock-in-the-water wavefront rather than to the wavefront in a three-dimensional earth volume. Because the loss occurs in two dimensions rather than three, surface-wave energy decreases proportionally to 1/r instead of $1/r^2$. The effect in terms of wave amplitude is a decrease as $1/r^{1/2}$. This gives surface waves an advantage over body waves with increasing distance, in terms of relative amplitude.

Due to internal friction of the vibrating particles, some of the energy of a seismic wave is converted into heat. This effect, called absorption, also causes the amplitude of vibration to decrease with distance from the source, given by

$$A_r = A_o/e^{\alpha r} \tag{3.13}$$

where α is called the absorption coefficient, and e = 2.71828 is the mathematical constant called Euler's number which is the base of natural logarithm.

Attenuation is frequency-dependent; therefore, it is often expressed in terms of wave length λ. Using the so called quality factor Q, we have:

$$Q = \pi/ \alpha \lambda \quad \text{or} \quad 1/ Q = \log (A_o\lambda/A_r r) \tag{3.14}$$

The dimensionless number Q is sometimes called the absorption constant. The reciprocal of Q represents the fraction of energy dissipated during propagation over a distance of one wavelength. For example, soil or loose sand could have a Q value of 10 (Table 3.3). This means that 10% of the energy is lost for each wavelength of propagation. That is, for each successive wavelength of propagation, 10% of the remainder energy disappears.

Clay and sand	5–25
Sandstone	10–50
Shale	25–75
Granite	55–130
Limestone	50–180

Table 3.3 *Typical Q-Values (after Steeples, 2005)*

At higher frequencies, wavelengths are shorter; thus, higher frequencies become attenuated more quickly over distance. The rapid loss of high frequencies in near-surface earth materials is considered to be the barrier to the widespread use of seismic methods as effective tools in the search for submeter-scale anomalies in near surface materials.

3.1.4 Seismic resolution

The resolution of the conventional reflection seismic method is poorer than that of a standard well logging method. Only under favourable circumstances individual beds of thickness 10

metres or less are resolved. In contrast, a resolution of 30 cm is generally achieved by the standard well logging methods and sometimes it is even better (Veeken, 2007).

Vertical resolution

The vertical resolution is a measure of the ability to recognize individual, closely spaced reflectors and is determined by the pulse length on the recorded seismic section. For a reflected pulse represented by a simple wavelet, the maximum resolution possible is between one-quarter and one-eighth of the dominant wavelength of the pulse (Widess, 1973). Therefore, the vertical resolution of seismic data is determined by the frequency of the seismic signal, its bandwidth, the interval velocity of the rock layers and the acoustic impedance contrast (Veeken, 2007).

Special high resolution surveys (100 MHz input signals with boomers as a sound source) have an increased vertical resolution of up to 10 cm, but here the penetration depth of the signal is much reduced (10 metres). The Ground Penetrating Radar (GPR) technique, using an electromagnetic signal as input, has also a resolution down to 5 cm (Veeken et al., 1999) and the display of GPR sections resembles that of reflection seismic data and similar interpretation techniques can be applied. But the penetration depth is usually very limited.

The seismic resolution depends also on the vertical spacing between the layers (bed thickness). If the layers are too closely spaced, the reflected seismic energy from both interfaces give rise to interference patterns (Sheriff, 1977). In such situations the two-way time interval between two interfaces becomes too narrow, the reflected wavelets will overlap in time and a complex composite waveform is recorded. It also occurs that the signal's amplitude is boosted when the interference is positive (constructive interference) and decreases when the interference is negative (destructive interference).

The bed-thickness resolution power normally decreases with increasing depth (e.g. Widess, 1973, Sheriff, 1977). Since deeper travelling seismic waves tend to have a lower dominant frequency due to the progressive loss of higher frequencies by absorption (Section 3.1.3) and higher velocity due to the effects of sediment compaction, vertical resolution decreases as a function of depth.

Lateral resolution

There are two main controls on the lateral resolution of a reflection survey, one being determined by the receiver spacing and the other being fundamental to the physical process of reflection.

The horizontal resolution is clearly determined by the spacing of the individual depth estimates from which the reflector geometry is reconstructed. From Fig. 3.3 (a), it can be seen that, for a flat-lying reflector, the horizontal sampling is equal to half the receiver spacing. In areas of complex geology, the spacing of receivers must be kept sufficiently small to ensure that reflections from the same interface can be correlated reliably from trace to trace. Note, also, that for a single shot point the length of a reflector sampled by any receiver spread is half the spread length.

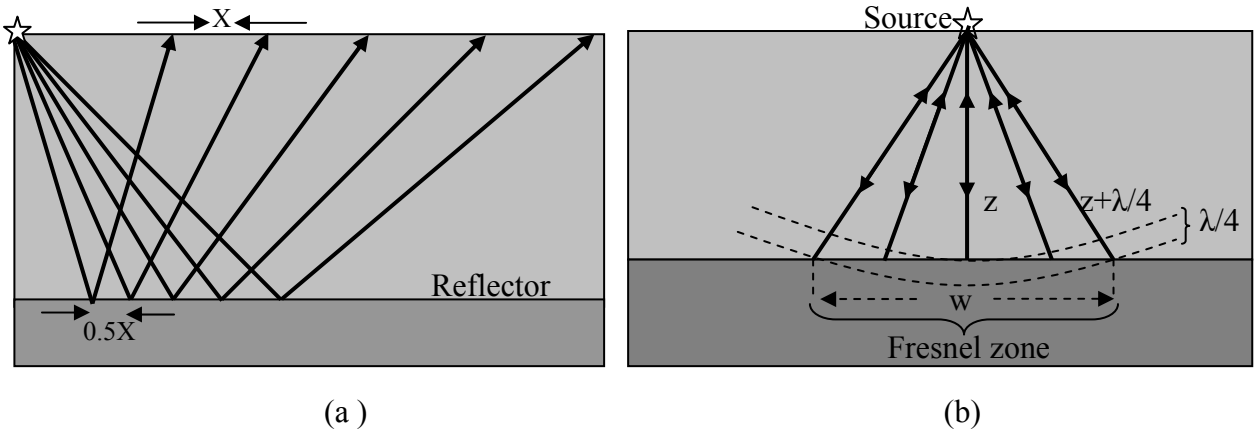

Figure 3.3 *(a) The horizontal sampling of a seismic reflection survey and (b) the Fresnel zone.*

Reflected energy, detected by the geophones at the surface, travels in the earth using the so-called 'Fermat path'. The Fermat path is 'the path for which the traveltime between two points in the medium is at a minimum'. If there are velocity changes in the subsurface, this path will not be straight. It is curved in such a way that the overall traveltime is minimized. The recorded signal on stacked seismic sections is not only composed of the reflected signal, travelling along the Fermat path between the shot locations, the reflector point, and the receiver position at the surface; but also neighboring interception points on the reflector may contribute to the received signal in the geophone (Hubral et al., 1993). This area, contributing to the energy of the reflected wavefront, is known as the Fresnel zone (Fig. 3.3b). The radius

of the Fresnel zone depends on the wavelength of the acoustic signal and also on the depth of the reflector as the wavefront gets wider with increasing depth.

The width of the Fresnel zone represents an absolute limit on the horizontal resolution of a reflection survey since reflectors separated by a distance smaller than this cannot be distinguished. The width w of the Fresnel zone is related to the dominant wavelength λ of the seismic signal and the reflector depth z by

$$w = (2z\,\lambda)^{1/2} \quad \text{for } z >> \lambda \tag{3.15}$$

The size of the Fresnel zone increases as a function of reflector depth. Also, as noted in Section 3.1.3, deeper travelling reflected energy tends to have a lower dominant frequency due to the effects of absorption. The lower dominant frequency is often coupled with an increase in interval velocity, and both lead to an increase in the wavelength. For both these reasons the horizontal resolution, like the vertical resolution, reduces with increasing reflector depth.

3.2 Basic principles of the seismic reflection method

The seismic reflection method creates a geophysically sampled 2D or 3D picture of the subsurface, which has to be interpreted in a geologically meaningful manner. This technique has been proven to be a useful tool for imaging subsurface structures from small to large scale investigations.

Previously, reflection surveying was concerned almost exclusively with the search for hydrocarbons and coal, down to depths of a few kilometers. Now, the method is increasingly applied for high-resolution mapping of shallow and ultra-shallow reflectors to depths less than or equal to 200 m or 20 m for engineering, environmental, and groundwater problems (e.g., Steeples and Miller, 1990; Wiederhold et al., 1998; Miller and Xia, 2002; Pugin et al., 2009; Sloan et al., 2009). In this thesis, the 2D reflection seismic method of both P- and S-waves is applied for near surface sinkhole problems targeting from 20 to 800 meters depth.

In seismic reflection surveys seismic energy pulses are reflected from subsurface interfaces and recorded at near-normal incidence at the surface. The travel times are measured and can be converted into estimates of depths to the interfaces.

For a single horizontal reflector lying at a depth z beneath a homogeneous top layer of velocity V, the equation for the travel time t of the reflected ray from a shot point to a receiver at a horizontal offset, or shot–receiver separation, x is given by

$$t = \frac{\sqrt{x^2 + 4z^2}}{V} \tag{3.16}$$

For a vertically reflected ray, at zero-offset, the two way travel time, t_0, is obtained by substituting $x = 0$ in equation (3.16) as,

$$t_0 = \frac{\sqrt{4z^2}}{V} = \frac{2z}{V} \tag{3.17}$$

The zero-offset time, t_0, is thus defined as the time required for a vertical reflection from the source to the base of the layer and back. The ordinary reflection time at any offset, t, is greater than t_0. Thus, the difference can be expressed as

$$t - t_0 \approx \frac{x^2}{2V^2 t_0} = \Delta t_{NMO} \tag{3.18}$$

The quantity Δt_{NMO} is called normal moveout or NMO. It depends on the offset, x, the velocity V and reflector depth z (since $z = Vt_0/2$). The concept of moveout, which has a hyperbolic shape, is fundamental to the recognition, correlation and enhancement of reflection events, and to the calculation of velocities using reflection data. One important seismic data processing step is the correction for NMO (see section 3.4).

In a multilayered ground, the travel-time curve is still essentially hyperbolic but the homogeneous top layer velocity V in equations (3.16) and (3.18) is replaced by the root-mean-square velocity V_{rms} of the layers overlying the n^{th} reflector.

The V_{rms} of the n^{th} reflector is given by

$$V_{rms,n} = \sqrt{\frac{\sum_{i=1}^{n} V_i^2 t_i}{\sum_{i=1}^{n} t_i}} \tag{3.19}$$

where V_i is the interval velocity of the ith layer and t_i is the one-way travel time of the reflected ray through the ith layer.

Thus at small offsets x ($x << z$), the total travel time t_n of the ray reflected from the nth interface at depth z is given to a close approximation by

$$t_n = \frac{\sqrt{x^2 + 4z^2}}{V_{rms}} \tag{3.20}$$

and the NMO for the nth reflector is given by

$$\Delta t_{NMO,n} = \frac{x^2}{2V_{rms,n}^2 t_0} \tag{3.21}$$

The individual NMO value associated with each reflection event may therefore be used to derive a root-mean-square velocity value for the layers above the reflector. Values of V_{rms} down to different reflectors can then be used to compute interval velocities using the Dix formula (Dix, 1955). Thus, the interval velocity V_{n} for the nth interval is given as

$$V_n = \sqrt{\frac{V_{rms,n}^2 t_n - V_{rms,n-1}^2 t_{n-1}}{t_n - t_{n-1}}} \tag{3.22}$$

where $V_{rms,n-1}$, t_{n-1} and $V_{rms,n}$, t_n are, respectively, the root-mean-square velocity and the reflected ray travel times to the (n-1)th and nth reflectors.

In the case of a dipping reflector (Fig. 3.4), with dipping angle θ, the travel time for a reflected ray is

$$t = \frac{\sqrt{x^2 + 4z^2 + 4xz\sin\theta}}{V} \tag{3.23}$$

Using binomial expansion equation (3.23) can be derived as

$$t \approx t_0 + \frac{(x^2 + 4xz\sin\theta)}{2V^2 t_0} \tag{3.24}$$

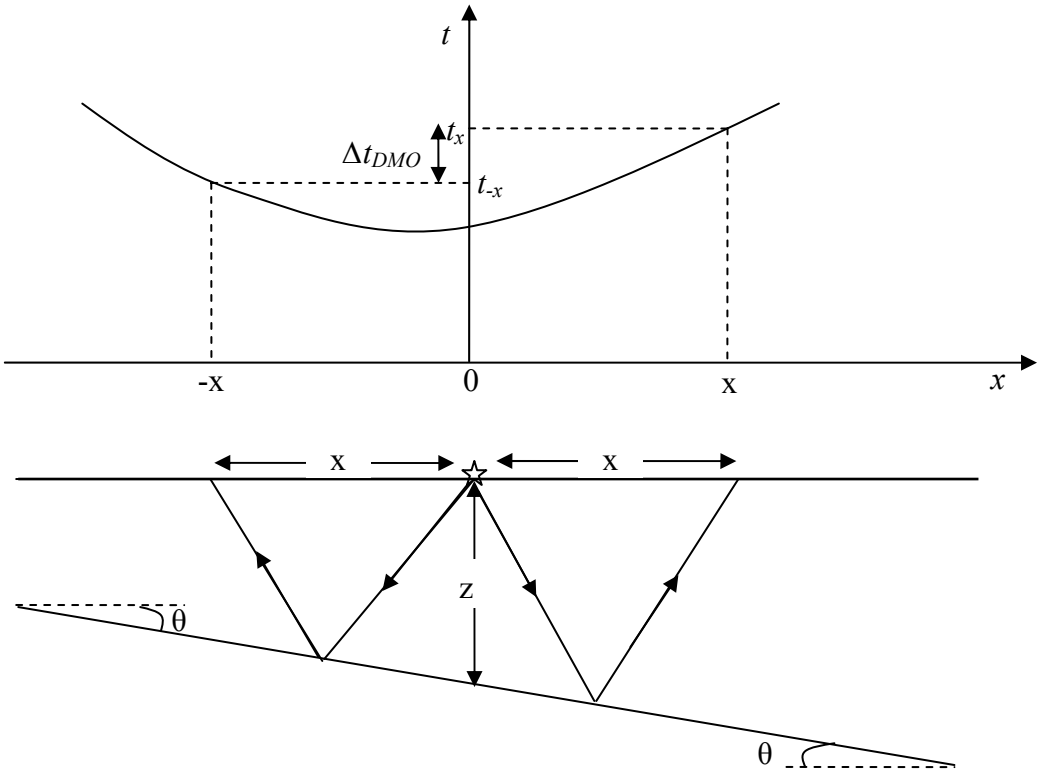

Figure 3.4 *Travel time curve (top) and ray paths (bottom) for a dipping layer.*

Because of the dip of the reflector, the reflected ray paths of equal offsets along the updip and downdip from a central source point are of different length. The two rays will therefore have different travel times. The difference in travel times t_x and t_{-x} of rays reflected from the dipping interface to receivers at equal and opposite offsets x and –x is called dip moveout (DMO). Thus, the dip moveout, Δt_{DMO} is

$$\Delta t_{DMO} = t_x - t_{-x}$$

or, using equation (3.24),

$$\Delta t_{DMO} = \frac{2x\sin\theta}{V} \tag{3.25}$$

3.3 Seismic data acquisition

Seismic survey data acquisition may constitute up to 80% of the total budget allocated for both the fieldwork and data processing (Gadallah and Fisher, 2009). Collecting shallow seismic data requires the use of high frequencies, and therefore, appropriate seismic sources and high-frequency geophones are needed (Knapp and Steeples, 1986; Schuck and Lange, 2007).

P- and S-wave reflection surveys have been conducted at Münsterdorf (Fig. 3.5) in 2007 with the aim to detect fault zones and karst features that may have initiated the observed sinkholes and to determine the depth to the carbonate and salt layers.

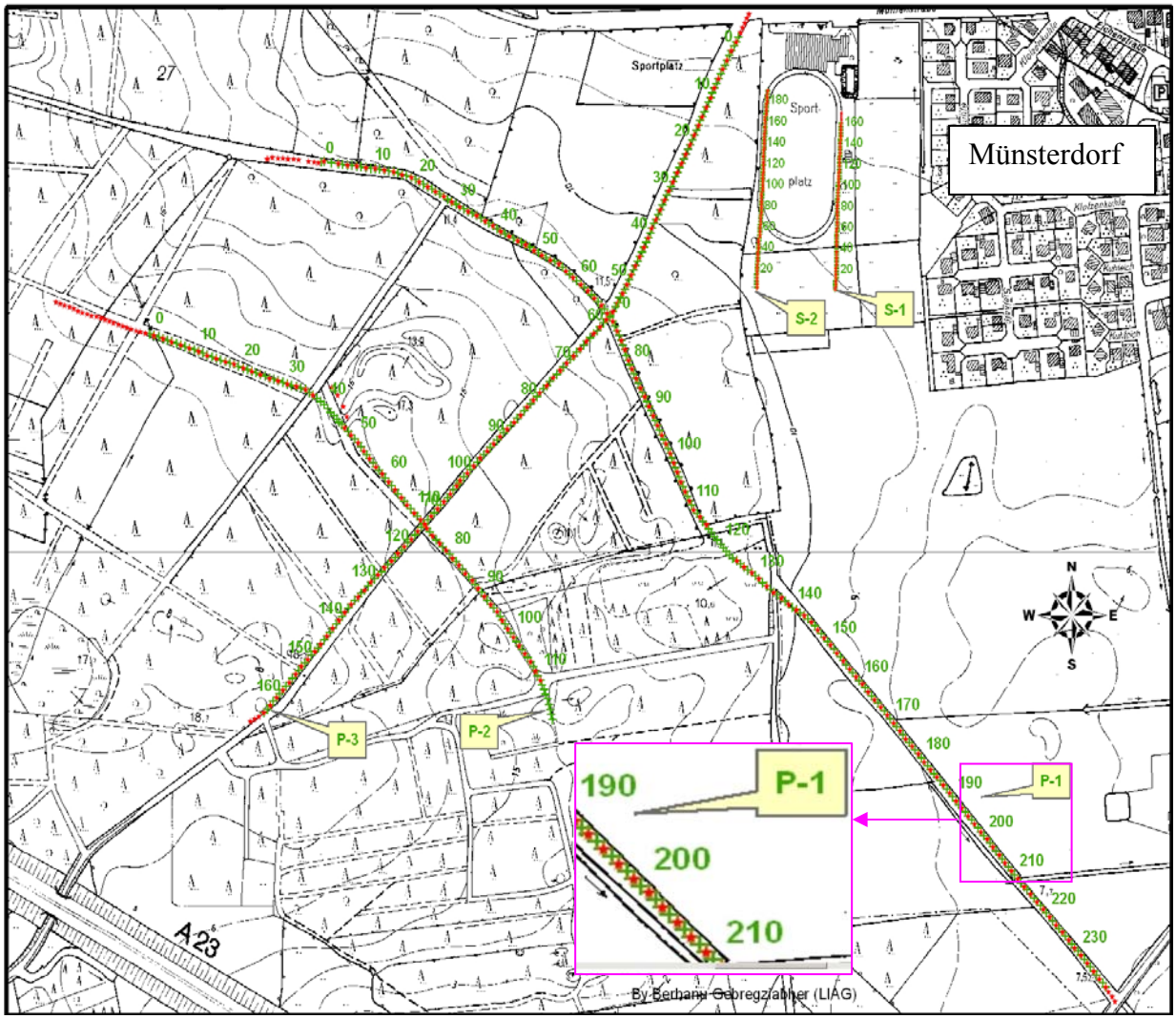

Figure 3.5 *Seismic survey lines with source (red stars) and geophone (green crosses) locations. Notions P-n and S-n refer to the P-wave and S-wave survey lines, respectively. Numbers indicate geophone positions.*

3.3.1 P-wave data acquisition

A seismic reflection survey was conducted from September 10-14, 2007 using a P-wave vibroseis source along three profiles with a primary target to asses a deep tectonic structure that may be related to the salt dome known as Krempe-Lägerdorf and with a secondary target to assess the boundary between the upper Cretaceous and the Quaternary sediments within about 20 meters depth. Three lines with in total 2.7 km length were recorded using 317 seismic source locations and a maximum of 240 channel acquisition system (Fig. 3.5).

Instruments

Instruments for a seismic reflection data acquisition system include energy sources (impulsive or vibroseis) to generate seismic waves with appropriate amplitudes and frequency spectra, receivers (geophones or hydrophones) to detect the propagated waves and to convert them into electrical signals, a navigation system (GPS) for a precise location of source and receiver positions, cables for transmitting signal outputs from the receivers to the recording system, and a recording instrument (seismograph).

The impulsive sources (such as sledgehammer, weight drop, rifle sources, or explosives) provide impulse type signals from the outset by a sudden release of energy. In contrast, vibration sources stretch the signal input over a few seconds by radiating a controlled low energy wavetrain (sweep) generated during sinusoidal vibration of continuously varying frequency (Fig. 3.6b). The Vibroseis technique reconstructs an impulse type signal only after cross-correlating the seismograms with the source signal or sweep (Fig. 3.6c).

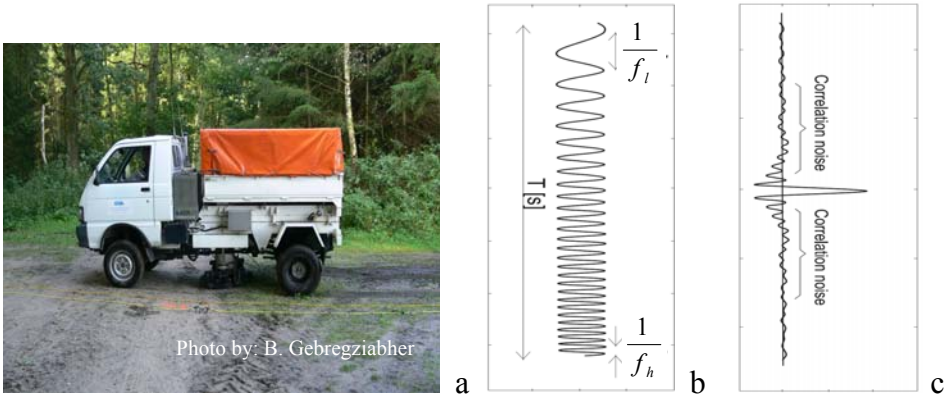

Figure 3.6 *a) LIAG P-wave Vibroseis system (MHV 2.7); b) sweep generated (f_l and f_h are lower and higher frequencies respectively; T sweep length); c) reconstructed impulse type signal from auto-correlation of the sweep.*

The sharpness of both impact and cross-correlated vibration signals depends on the width of the frequency spectrum of the signal and on its extent towards high frequencies. Closely situated reflectors can be resolved only with increasingly broader bandwidth (Yilmaz, 2001).

In this project, the P-wave seismic signals are induced using a small vibrator MHV 2.7 (Fig. 3.6a) that was developed by LIAG and PRAKLA Bohrtechnik GmH Company. This vibroseis source can generate signals between 16-500 Hz. Our data is collected with a sweep of 50-200 Hz main frequency that corresponds to signal lengths of 5-20 ms per cycle.

The vibrator is a 181 kg vehicle-mounted energy source that converts hydraulic energy into mechanical energy to produce the sweep. When the vibrator sends its sweep signal into the ground the receivers begin recording simultaneously and continue for the 10 seconds of the sweep length plus 2 seconds listening time.

At each shot point location, four records are stacked vertically in order to attenuate noise and to increase the signal strength relative to random noise. The stacked record is then cross-correlated with the sweep, producing a single output record with zero-phase correlated traces (Fig. 3.7), the length of which is equal to the listening time of 2000 ms. Although precorrelation processing could achieve enhancement of the signals and some improvement in bandwidth, storing data uncorrelated and unstacked requires 30 times more storage space, about 50 percent more acquisition time, and 5 times more data transfer time (Miller and Xia, 2002).

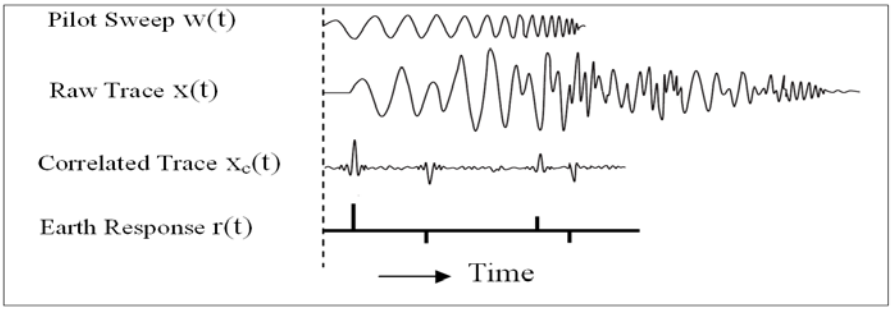

Figure 3.7 *Raw and cross-correlated single vibrator trace with the sweep (after Gadallah and Fisher, 2009).*

The raw trace x(t) is the result of convolution between the source generated sweep w(t) and the earth response r(t). Mathematically, we note

$$x(t) = w(t)^* r(t) \qquad \text{and} \qquad x_c(t) = x(t) \otimes w(t) \tag{3.26}$$

where * and ⊗ are the convolution and cross-correlation operators, respectively, and $x_c(t)$ is the cross-correlated data.

The type of sensor used for P-wave data acquisition is a vertical component SM 4 geophone with 20 Hz natural (resonant) frequency. The geophone converts the seismic energy inputs (movements) into a recordable electrical signal (voltage). It is a moving-coil geophone type, which contains a coil that is suspended by springs inside the magnetic field of a permanent magnet (Fig. 3.8a). The geophone is attached by inserting its spike vertically into the ground. A relative movement between the coil and the permanent magnet generates a voltage in the coil by induction. The voltage induced is proportional to the velocity of the coil motion. The measured quantity is therefore the ground particle velocity, not the amplitude of ground motion (Gadallah and Fisher, 2009).

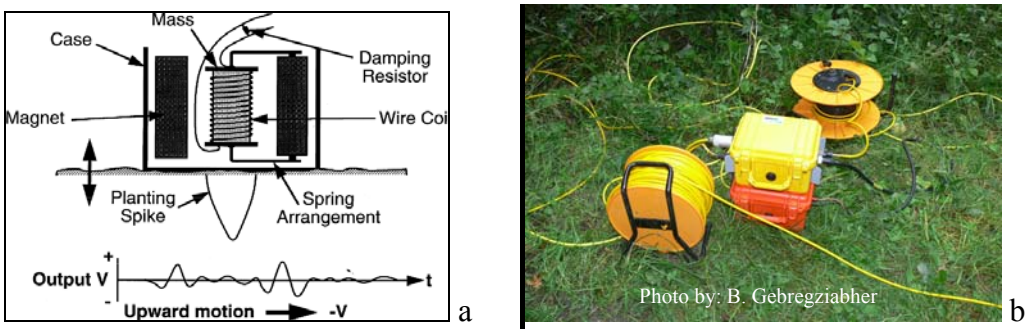

Figure 3.8 *a) Geophone components (Gadallah and Fisher, 2009); b) photo taken in the field that shows the Geode seismograph (yellow box), battery pack (red box), and the network and geophone cables.*

Ten, five, and seven 24-channel seismographs were networked to simultaneously record 240, 120, or 168 channels of input along profiles P-1, P-2 and P-3, respectively. The type of seismograph used is Geode (Fig. 3.8b) made by Geometrics Inc. with a power supply 24 Ah batteries. Geophone cables are connected to the device using LIAG-made adapters (Gisewski G52). Each Geode device is connected with 120 m long network cables.

The data received from 24 geophones in each Geode are amplified with 36 dB of pre-amplifier gain and digitized with a sampling interval of 1 ms in order to preserve a maximum frequency (Nyquist frequency) of 500 Hz in the digitized signal. To avoid aliasing as a source of ambiguity in the signal frequency content and, sometimes giving a false picture of ground motion, the data have to be sampled at sufficiently dense intervals (Steeples and Miller,

1998). Finally, the digitized signals are transported through the network cables and stored on the hard disk of a computer in standard format (SEG 2).

The stations were located using a Trimble 5800 GPS receiver with accuracy of ±30 cm.

Field Array

In two-dimensional reflection surveying all source points and receivers are aligned along preferably straight lines so that the reflected ray paths can be assumed to travel in the profile plane. During the survey the source point and its associated geophone spread are progressively moved forward along the profile line to achieve multi-coverage of the underlying geological section.

Due to the many available channels all three profiles were recorded at fixed spreads with geophone spacing of 5 meters and source spacing of 10 meters (Fig. 3.9).

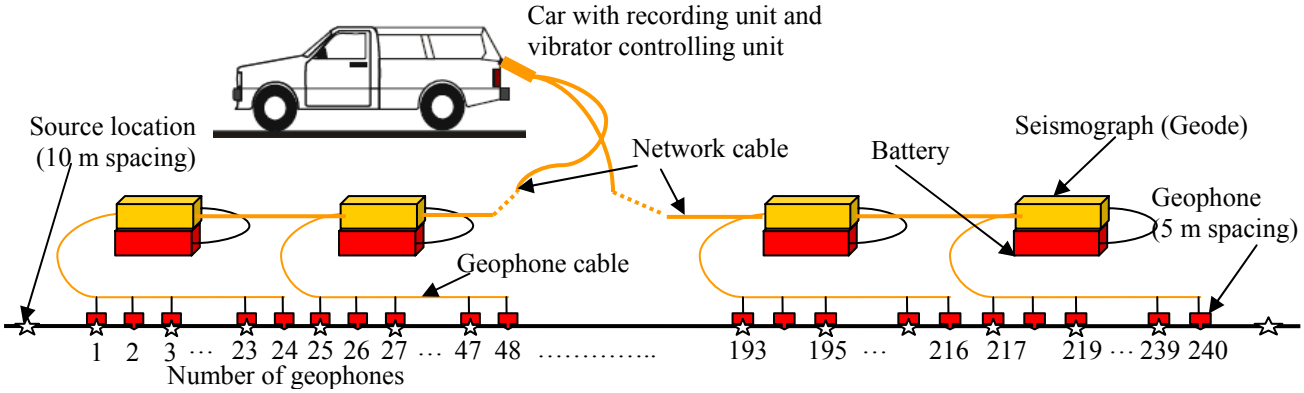

Figure 3.9 *An array of a fixed spread field survey with 5 m geophone and 10 m source spacing.*

Seismic reflection measurements could be performed using the zero-offset (constant-offset) method or the common-midpoint (CMP) method. The first approach provides single-fold coverage of the subsurface by moving along a profile with just one source and one geophone planted near the source each time (Fig. 3.10a). This usually works only in marine seismic surveys or GPR but not with land seismic surveys. Nowadays, the common-midpoint method with multi-fold coverage is a standard practice in reflection seismic surveying by collecting reflection data of the same midpoint reflection part from several seismic shots at different angles of incidence (Fig. 3.10b).

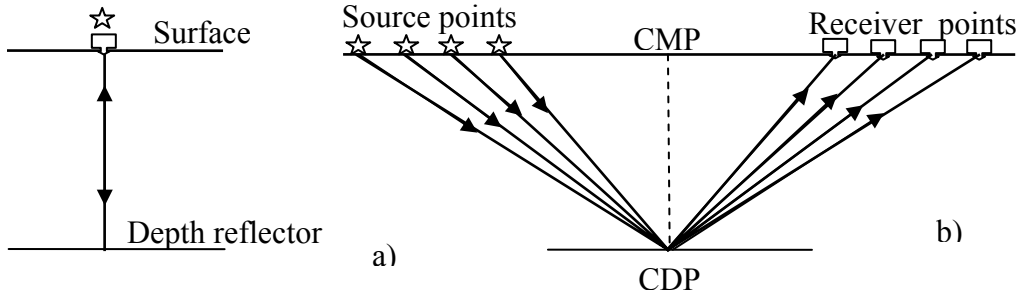

Figure 3.10 *Seismic reflection measurement techniques; a) zero-offset and b) common-midpoint methods. CMP means common midpoint and CDP is common depthpoint, which is equal to CMP only in the case of horizontal layers.*

The number of traces that have a common midpoint (called fold, N_{CMP}) on a 2-D moving spread CMP profile is calculated using the formula

$$N_{CMP} = \frac{N_G . \Delta X_G}{2\Delta X_S} \tag{3.27}$$

with N_G being the number of geophones per spread, ΔX_G the geophone spacing and ΔX_S the distance between the source points. Thus, with 240-, 120-, and 168-channel spread, a geophone spacing of 5 m and a source point distance of 10 m the resulting coverage would be 60-, 30-, and 42-fold for profile-1, -2, and -3, respectively. In fact, due to the additional reverse shots in the fixed spread, the maximum folds are the double of the mentioned values. For near-surface data, the fold commonly ranges between 6 and 60 and the signal-to-noise ratio (S/N) of the reflections increases as the square root of the CMP fold (Steeples, 2005).

The location coordinates of the CMP or CDP (common-depthpoints), X_{CMP}, are given in terms of geophone locations (X_G) and source locations (X_S) as

$$X_{CMP} = \frac{\left| X_S + X_G \right|}{2} \tag{3.28}$$

The spacing of CMP (ΔX_{CMP}) is

$$\Delta X_{CMP} = \min\left\{\Delta X_S/2,\ \Delta X_G/2\right\} \tag{3.29}$$

As ΔX_{CMP} determines the structural sampling of the investigation target, the geophone spacing has to be chosen according to the required resolution. Planting geophones closely together generally increases the cost. Thus shot and geophone intervals must be proportional to the reflector depth of principal interest.

According to Steeples (2005), for a seismograph with n number of channels, the geophone interval would be approximately z/n, and the smallest offset is often less than z/n (where z is the maximum depth of interest). Therefore, at Münsterdorf a maximum number of 240 geophones (profile P-1) are planted with 5 meter spacing on a fixed spread in order to attain a maximum depth of investigation down to 1200 m.

	Profile P-1	**Profile P-2**	**Profile P-3**
Spread type	Fixed	Fixed	Fixed
Source type	Vibrator(MHV2.7)	Vibrator(MHV2.7)	Vibrator (MHV2.7)
Sweep	50-200 Hz	50-200 Hz	50-200 Hz
Sweep length	10 s	10 s	10 s
Source point spacing	10 m	10 m	10 m
No. of source stations	132	77	92
Geophone type	SM4 20Hz vertical	SM4 20Hz vertical	SM4 20Hz vertical
Geophone spacing	5 m	5 m	5 m
No. of geophones	240	120	168
CMP spacing	2.5 m	2.5 m	2.5 m
CMP fold (maximum)	120	60	84
Digitizing time interval	1 ms	1 ms	1 ms
Correlated record length	2 s	2 s	2 s
Length of profiles	1.23 km	0.628 km	0.855 km

Table 3.4 *P-wave data acquisition parameters of the three profiles.*

Another criterion in selecting appropriate geophone spacing is based on the minimum wavelength, which has a particular importance to avoid spatial aliasing of the reflection arrivals during filtering (Rabbel, 2006). That is

$$\Delta X_G < \lambda_{min}/2 = V_{min}.T_{min}/2 = V_{min}/2f_{max} \qquad (3.30)$$

where λ_{min}, V_{min}, T_{min} and f_{max} are the smallest wavelength, propagation velocity, signal period, and maximum frequency to be expected during the survey, respectively. Using 200 Hz

maximum frequency and considering the minimum velocity of the P-waves to be 2000 m/s, the minimum wavelength calculated is 10 m and this will be sampled well with a maximum geophone spacing of 5 m (Table 3.4).

3.3.2 SH-wave data acquisition

After the occurrence of a third sinkhole in November 2007, a high resolution SH-wave vibroseis survey was added along two profiles (S-1 and S-2) near to the observed sinkholes (Fig. 3.5) on December 12 and 13, 2007. The aim was to improve the shallow detection and imaging of fine-scale deformation and stratigraphic features. Using SH-waves, the ability to resolve shallow subsurface structures in a medium is much better than with P-waves, due to the low propagation velocity and thus shorter wavelength of the SH-wave.

Instruments

Every seismic source at the Earth's surface simultaneously generates P- and SV-waves, but only horizontal acting forces generate SH-waves. In this survey the SH-waves are generated using an electrodynamic vibrator system called Elvis-4 SH vibrator (Fig. 3.11), which was developed by LIAG (Rode and Cramm, 2006). Unlike the P-wave vibrator the mass of the SH-vibrator moves horizontally, not vertically.

The vibrator unit is mounted under a wheelbarrow whereas its two 12 V batteries and a controlling electronic unit are installed on top in order to give additional load. During the survey, the load of the vibrator can be further enhanced by a person sitting on the wheelbarrow so as to improve the coupling to the ground. The shear wave source and the wheelbarrow can be disassembled for easy transportation. As shown in Fig. 3.11, the device has permanent magnets and coils for current flow. As the current flows alternating in time through the coils, alternating magnetic fields are induced. As a result, the change in the magnetic field drives the mass and vibrates horizontally along the magnetic field direction.

Elvis-4 produces frequency modulated shear waves preferably in the frequency range of 20-500 Hz from a DC electrical energy source using commercially available 12 V batteries. However, in this survey we use a sweep range of 30-240 Hz for 10 seconds plus 2 seconds listening time. The oscillation direction is perpendicular to the spread line. At each source

station two records are required with reversed polarity. The two records are subtracted from one another later during the data processing to eliminate the P-waves and to amplify the SH-wave arrivals.

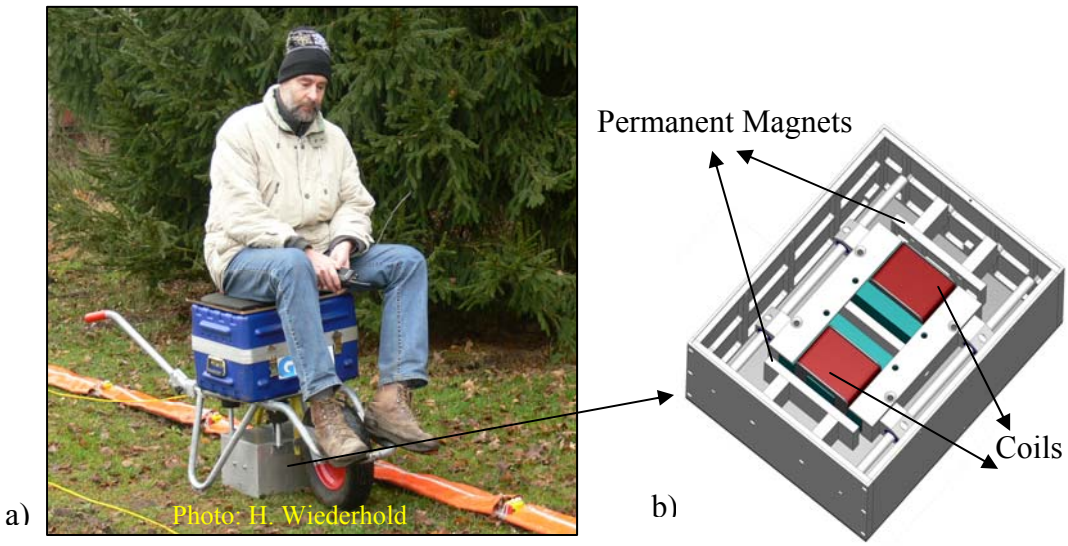

Figure 3.11 *SH-wave electrodynamic vibrator (Elvis-4); a) photo during the fieldwork and b) internal components of the vibrator (after Rode and Cramm, 2006).*

For the SH-wave data acquisition a horizontal component SM 6 geophone with 10 Hz natural (resonant) frequency is used. It is a moving-coil geophone analogue to the geophones for P-waves (Fig. 3.8a) except that the vertical components of the coil system are turned by 90 degrees to detect horizontal movement. S-wave geophones are planted in the same way as conventional geophones, but they require leveling and azimuthal alignment. During this survey, we used a landstreamer where the horizontal component geophones are attached to plates on a belt strap (developed by LIAG, Fig. 3.12a).

Ground coupling is achieved by using abrasion-resistant 3-point bearing feet, which enables the landstreamer measurements to be very efficient on sealed surfaces such as asphalted roads or hard rock terrains. Moreover, paved roads or concrete surfaces suppress Love waves and refracted waves, if the soil layer below them has lower seismic velocity (Polom et al., 2007). The landstreamer can be easily transported by rolling it up on a winder drum as shown in Fig. 3.12b.

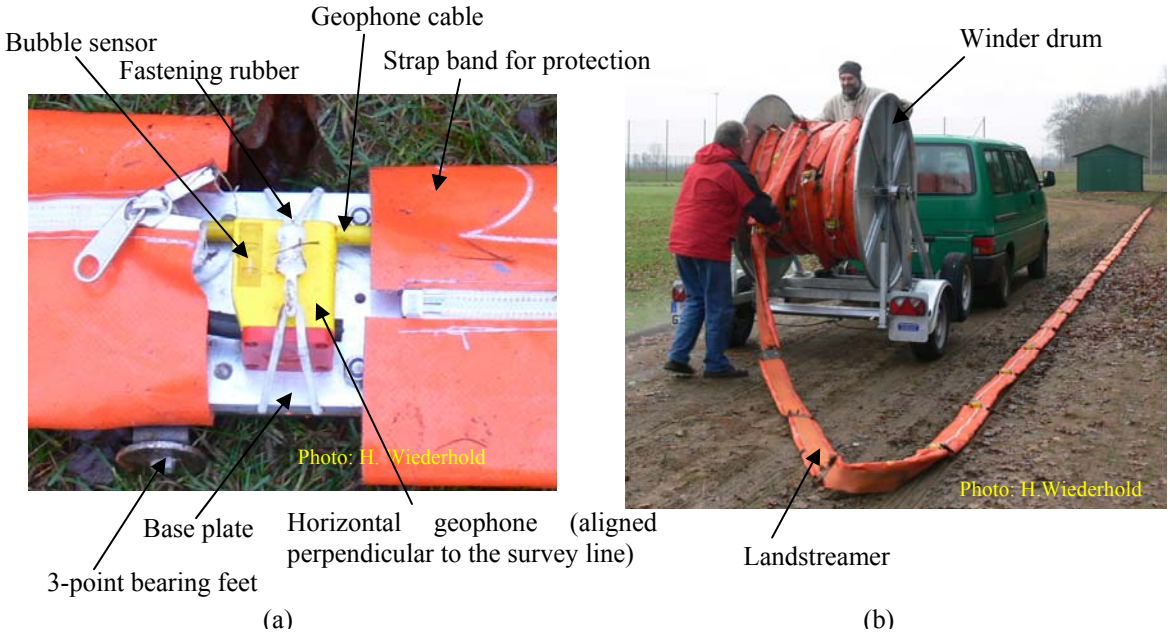

Figure 3.12 *Photo taken during the fieldwork; (a) horizontal geophone and components of the landstreamer; (b) 120 channel landstreamer rolling over the winder drum (geophone spacing 1 m).*

The recorded data is amplified using a 36 dB pre-amplifier gain. The signal is digitized every 1 ms using the 24-channel Geode seismograph (Fig. 3.8b) similar to the P-wave records.

	Profile S-1	**Profile S-2**
Spread type	Moving spread	Moving spread
Source type	Vibrator(Elvis-4)	Vibrator(Elvis-4)
Sweep	30-240 Hz	30-240 Hz
Sweep length	10 s	10 s
Source point spacing	2 m	2 m
No. of source stations	86	98
Geophone type	SM 6 10Hz horizontal	SM 6 10Hz horizontal
Geophone spacing	1 m	1 m
No. of geophones per record	120	120
CMP Spacing	0.5 m	0.5 m
CMP fold (maximum)	46	46
Digitizing time interval	1 ms	1 ms
Correlated record length	2 s	2 s
Length of profiles	170 m	190 m

Table 3.5 *SH-wave data acquisition parameters of the two profiles.*

Field Array

The two shear wave lines (S-1 and S-2 in Fig. 3.5) are recorded by multi fold spreads with 120 geophones spaced 1 meter and the source points spaced 2 meters. During the survey the source point and its associated geophone spread are progressively moved forward along the profile line to achieve lateral coverage of the underlying geological section up to a total length of 170 (profile S-1) and 190 meters (profile S-2). The spreads were moved every 40 shots and the total numbers of source points for S-1 and S-2 are 86 and 98 stations, respectively (Table 3.5).

3.4 Seismic reflection data processing

The goal of seismic reflection data processing is to enhance the signal-to-noise ratio (S/N) of the data, to image a specific structure or stratigraphy of the subsurface by a zero-offset depth section and to derive a velocity model for lithological interpretation. There is no standard or routine processing sequence that will fit for every seismic record acquired except an outline that must be designed according to the area problems and record quality (Baker, 1999; Yilmaz, 2001; Gadallah and Fisher, 2009). Processing shallow seismic reflection data is different from processing done in hydrocarbon exploration.

In this section of my thesis, the basic reflection seismic data processing steps for both the P- and S-wave data are discussed.

3.4.1 P-wave seismic reflection data processing

All the P-wave data were processed using ProMAX^{TM} 2D version 1998.6, a commercial processing software package from Landmark Graphics Corporation.

The processing flows used for these data were consistent with the near-surface seismic reflection processing techniques (Baker, 1999) such as preprocessing data analysis, improving the signal-to-noise ratio, velocity analysis, CMP stacking, post-stack deconvolution, post-stack migration, and time-to-depth conversion (Fig. 3.13).

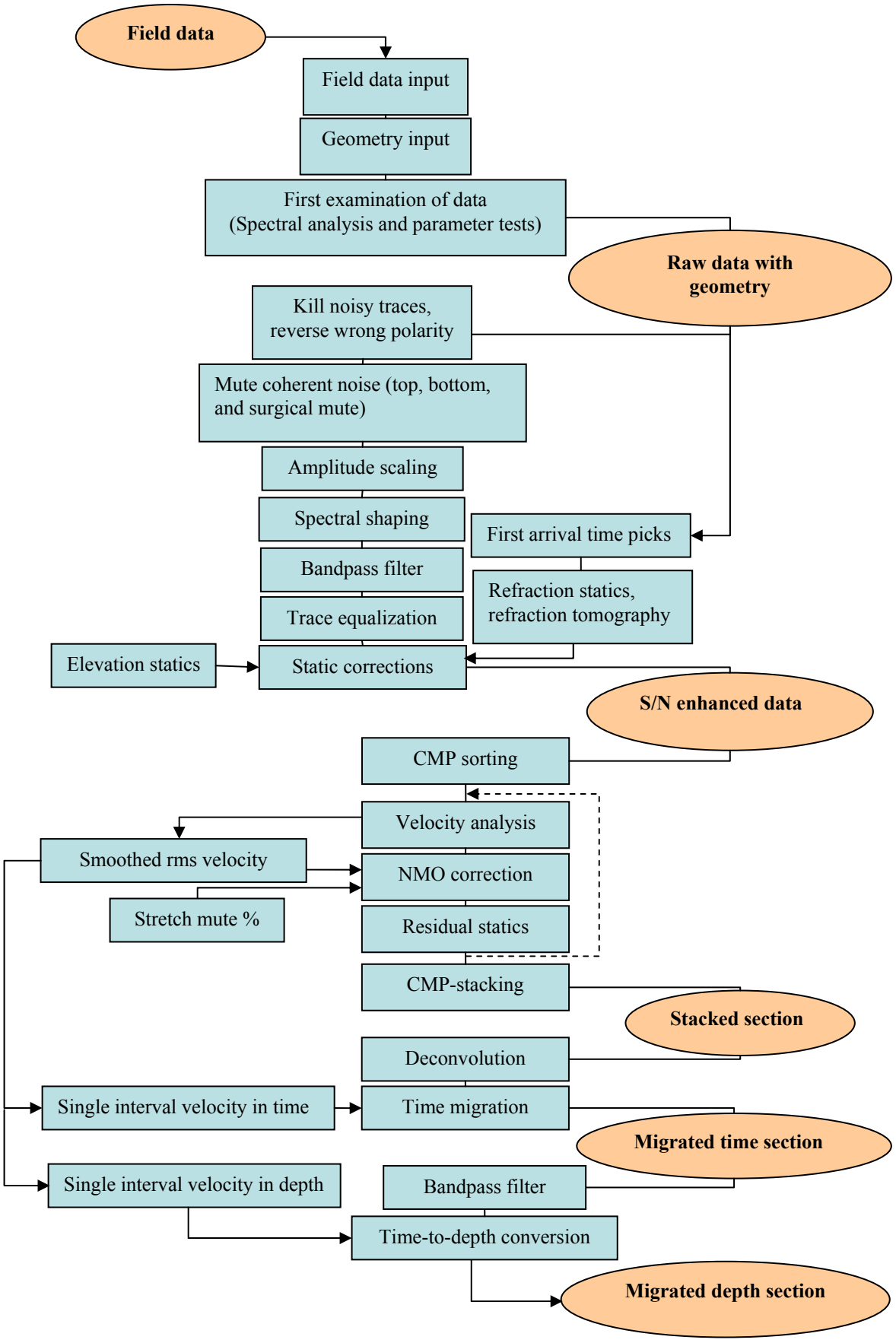

Figure 3.13 *P-wave seismic reflection processing flowchart adapted to the Münsterdorf survey.*

Prestack processing - data analysis

The four recorded shots per station were vertically stacked and correlated with the sweep and saved in SEG-2 format during the field survey. After input of the raw data into the processing system, geometry and trace headers are defined corresponding to the field notes. A first look at typical raw shot gathers up to only 1000 ms is shown in Fig. 3.14. Good reflection hyperbolas, for example, at about 450 and 500 ms of zero offset depth, high amplitude ground rolls, air waves generated from the source's sound, and noisy traces are observed on the raw data from all profiles.

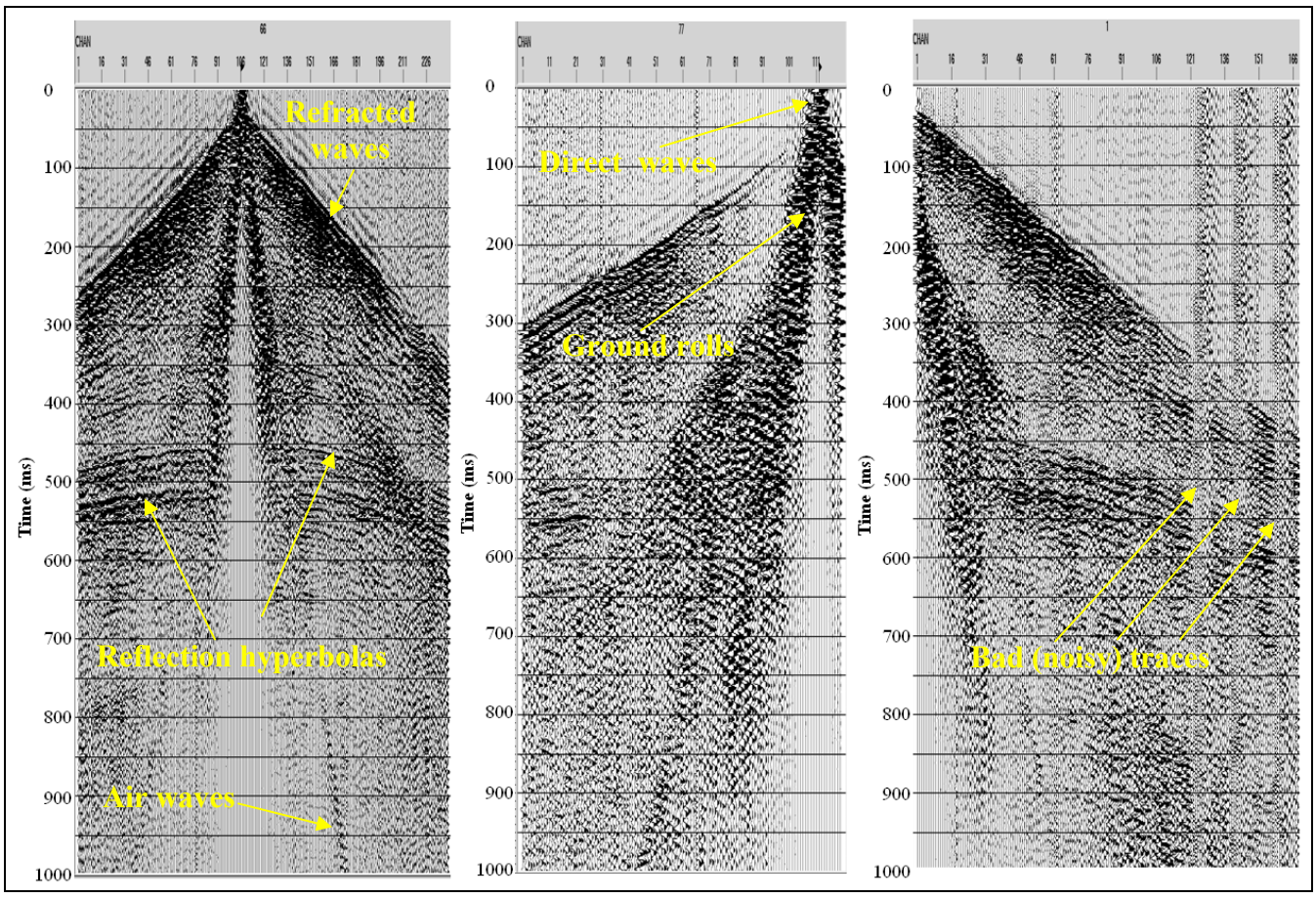

(a) (b) (c)

Figure 3.14 *First examinations of raw data with 5 m spacing between traces. (a) Split spread shot gather from profile P-1, (b) reverse off-end spread shot gather from profile P-2 and (c) forward off-end spread shot gather from Profile P-3.*

During data analysis the frequency content of the data was analyzed and parameters for signal-to-noise ratio (S/N) enhancing processes were chosen. Accordingly, the raw data is

examined using various amplitude gains and filters to see features that might not be obvious on the first look of the data. After parameter test and spectral analysis the processing continues to improve the signal-to-noise ratio.

Improving signal-to-noise ratio

The signal-to-noise ratio of the data is enhanced after killing bad traces, muting coherent noises such as the refracted and surface waves (ground roll), amplitude scaling, spectral shaping, frequency filtering, trace equalization, and statics corrections (Fig. 3.18).

Some noisy traces are removed or killed because of bad connections or bad geophones at particular locations during the data acquisition. Removing any trace with a lower S/N is almost always better than assuming that important information will be lost if the trace is removed (Baker, 1999). A few traces are also reversed because of their opposite polarity to neighboring traces as observed from the raw data (Fig. 3.15a).

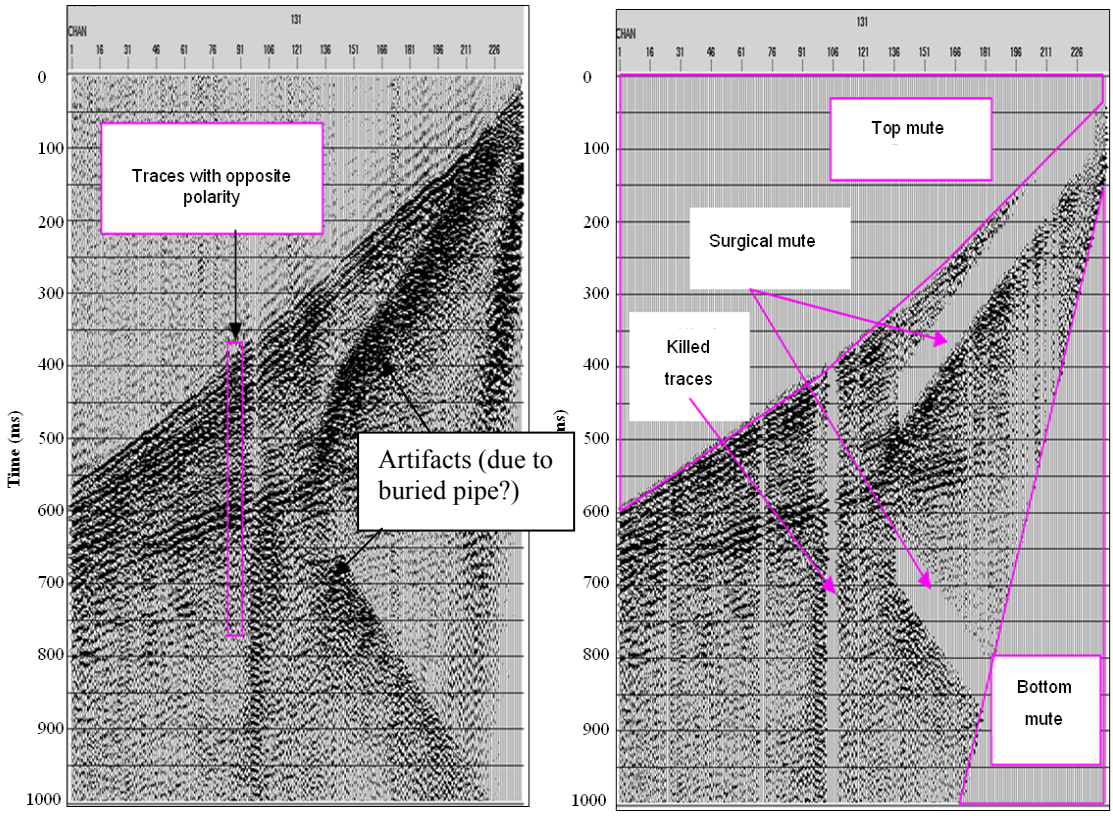

Figure 3.15 *Editing of records and traces. (a) Noisy raw data; (b) after removing bad traces, reversing wrong polarity, and muting (top, bottom, and surgical).*

Muting is applied to avoid all regions with low S/N of the reflection information such as the refracted waves (using top mute and stretch mute), surface waves or the ground roll (using bottom mute), and some ringing or reverberations due to a strong reflector near the surface (using surgical mute). Figure 3.15 illustrates the surgical mute of noise due to a strong reflector of a buried pipe near to the surface mainly at the end of profile P-1.

Amplitude losses due to inelastic attenuation (see section 3.1.3) are scaled or corrected using automatic gain control (AGC). The AGC scale factor is equal to the inverse of the mean (or rms or median) amplitude value of a time window. This scalar is applied to the center sample. The window is moved sample by sample down the trace and the scale factor for each center sample is calculated (Fig. 3.16). The critical parameter in AGC process is the length of the AGC window, within which the amplitudes are normalized (Baker, 1999). If the AGC window is too big (Fig. 3.16c), very little change in the data will be observed; if it is too small (Fig. 3.16b), everything will be changed and strong and weak signals are difficult to distinguish. After checking our seismic data using various lengths of the AGC window, 100 ms is found best for the near surface reflections.

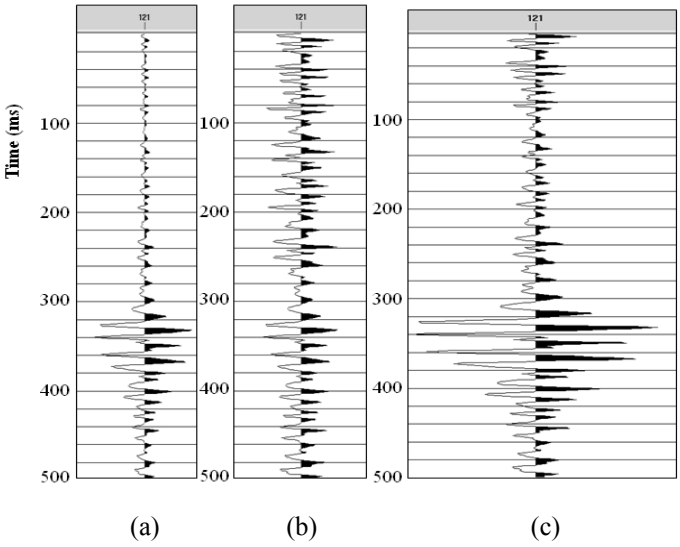

Figure 3.16 *Automatic gain control (AGC); (a) input trace from the field data, (b) and (c) output traces after AGC with 100 and 500 ms operator length, respectively.*

Trace equalization is applied to reduce variations in amplitude between traces of adjacent channels by scaling each trace using the computed mean amplitude values of the adjacent traces.

A frequency domain spectral shaping (Fig. 3.17) has been done using the frequency-amplitude percentage pairs of 50-0, 60-100, 200-100, 220-0. Between 50 and 60 Hz it ramps up from fully attenuated to the 100% level and from 200 to 220 Hz it ramps down from 100% of the maximum amplitude to fully attenuated (0%).

Band-pass filtering discriminates between signal and noise on the basis of frequency by removing undesired frequency ranges. In our data, a band-pass filter of 60-70-200-220 Hz is applied after comparing displays of seismic records with different filter pass bands. The frequency sequence represents the 0% (60 Hz) and 100% (70 Hz) points of the low-cut ramp, and the 100% (200 Hz) and 0% (220 Hz) points of the high-cut ramp. This filter creates a 10 Hz wide low-cut ramp and 20 Hz wide high-cut ramp.

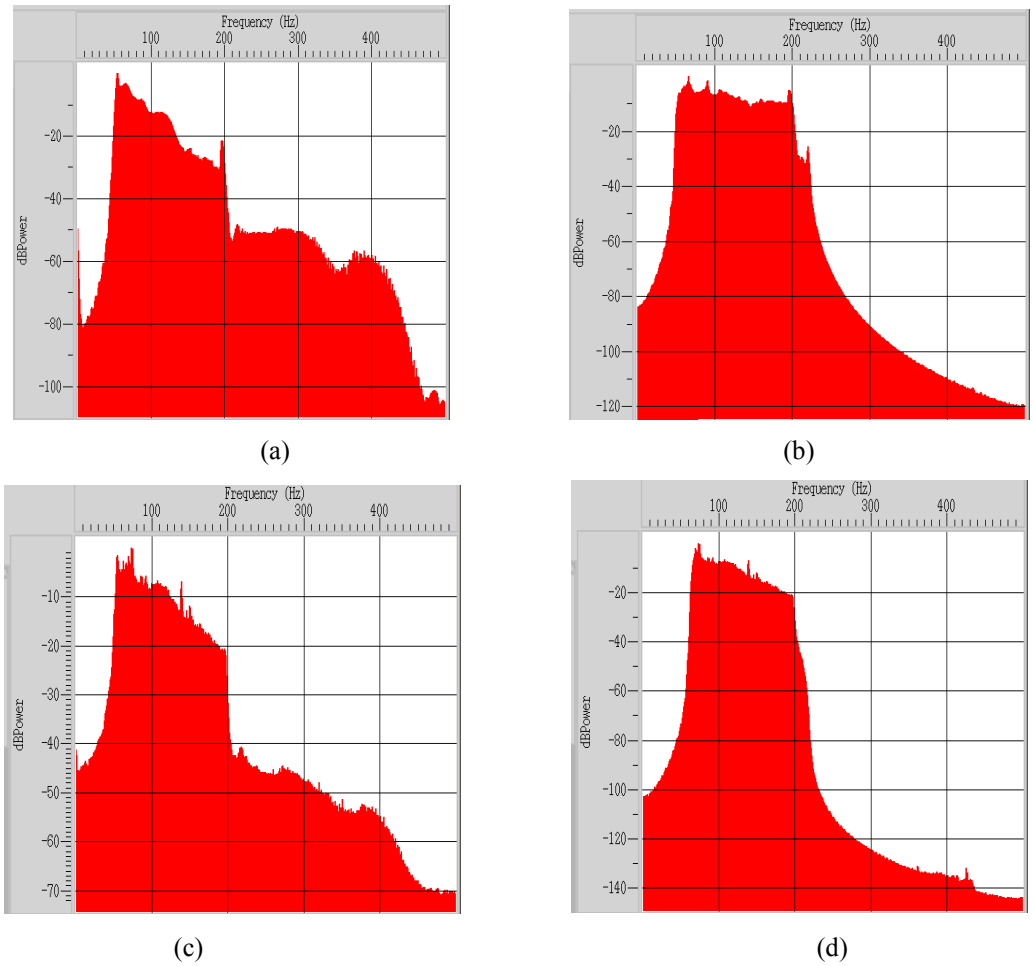

Figure 3.17 *A frequency spectrum of the shot gather in Fig. 3.14 (a); (a) raw data, (b) after spectral shaping, (c) after AGC with 100 ms window length, and (d) after AGC and band-pass filter of 60-70-200-220.*

Elevation and refraction statics are applied to minimize the effect of the surface elevation variations and to solve the velocity and thickness irregularities of the near surface layer, also

called the weathering layer. Our data have only very small elevation changes of 5.2 m, 3.8 m, and 9.1 m along profiles P-1, P-2, and P-3, respectively on a maximum elevation of 20 m above sea level. The elevation changes are corrected by performing a datum static shift, whereby each source and geophone position is shifted in time to a flat datum of 20 m above sea level. By observing changes in the slope of the direct wave arrivals from the data collected using a hammer source, velocity variations between 315-991 m/s, 477-500 m/s, and 480-600 m/s are confirmed easily on the weathering layer of P-1, P-2, and P-3, respectively. Since the velocity of the very-near-surface layer varied over the length of the spreads along all the profiles, refraction statics is applied using a replacement velocity of 1800 m/s. For a detailed theoretical concept of static corrections in seismic reflection surveys, I suggest to refer Cox (1999).

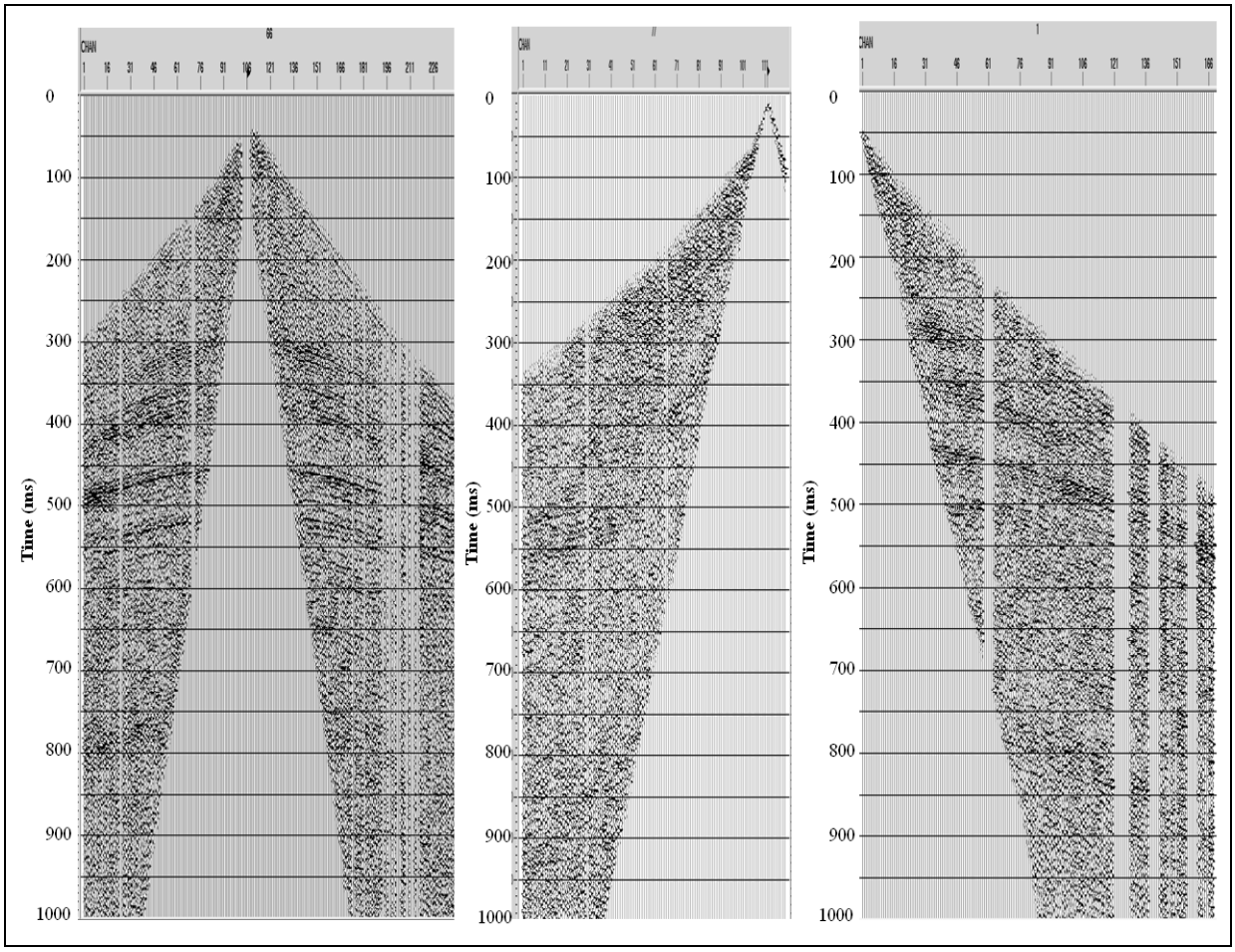

(a) (b) (c)

Figure 3.18 *Signal-to-noise ratio enhanced data corresponding to the raw data in Fig. 3.14: Processing steps applied killing traces, reversing polarity, muting, amplitude scaling, spectral shaping, trace equalization, band-pass filtering, and static corrections. (a) Split spread shot gather from profile P-1, (b) reverse off-end spread shot gather from profile P-2 and (c) forward off-end spread shot gather from Profile P-3.*

Velocity analysis and CMP stacking

After improving the signal-to-noise ratio of the traces in each shot gather, a common-midpoint (CMP) gather is generated to image the same point in the subsurface by traces with different offsets (Fig. 3.10b). Before stacking these traces to set the desired zero-offset trace (Fig. 3.10a), we need information about the seismic velocity to be used for NMO correction. Therefore, before the actual stack, velocity analysis, normal moveout (NMO) and residual static corrections are applied.

There are different ways to determine the stacking velocities of the reflections from the seismic data: for example, by sequentially picking hyperbolas on CMP gathers, by using semblance velocity plots, or by using constant-velocity stacks (Fig. 3.19 a-c). For the velocity analysis of our data we used the constant-velocity stack (CVS) functions by generating 11 CVS plots from 1200 m/s to 3500 m/s of NMO velocity boundaries. After the CVS velocity analysis, the NMO corrected CMP gather is displayed (Fig. 3.19d). The NMO corrections are applied to the CMP gathers to flatten the hyperbolic reflection events that means to get the zero-offset travel times (section 3.2 equation 3.18) using the velocity field generated during the velocity analysis. The velocity analysis was done every 20 CMP´s.

The hyperbolic form is used to define the best stacking path, where the velocity that allows the best fit of the travel time trajectory on a CMP gather to a hyperbola within the spread length is called stacking velocity. Since the NMO is hyperbolic for small-spread and small-dip approximations, the difference between the stacking velocity and the NMO velocity is called spread-length bias (Yilmaz, 2001). The smaller the spread length is, the closer the optimum stacking hyperbola to the moveout hyperbola.

The NMO corrected CMP gathers are stacked resulting into a single trace and each subsequent trace is positioned at their CMP locations. The method of summing the CMP traces is a straight mean stack, which sums the sample values and divides them by the number of samples summed raised to a supplied power scalar of 0.5 for stack normalization. For example, Fig. 3.19(e) shows the stacked trace of the NMO corrected CMP gather of Fig. 3.19(d) together with nine other neighboring CMP stacked traces.

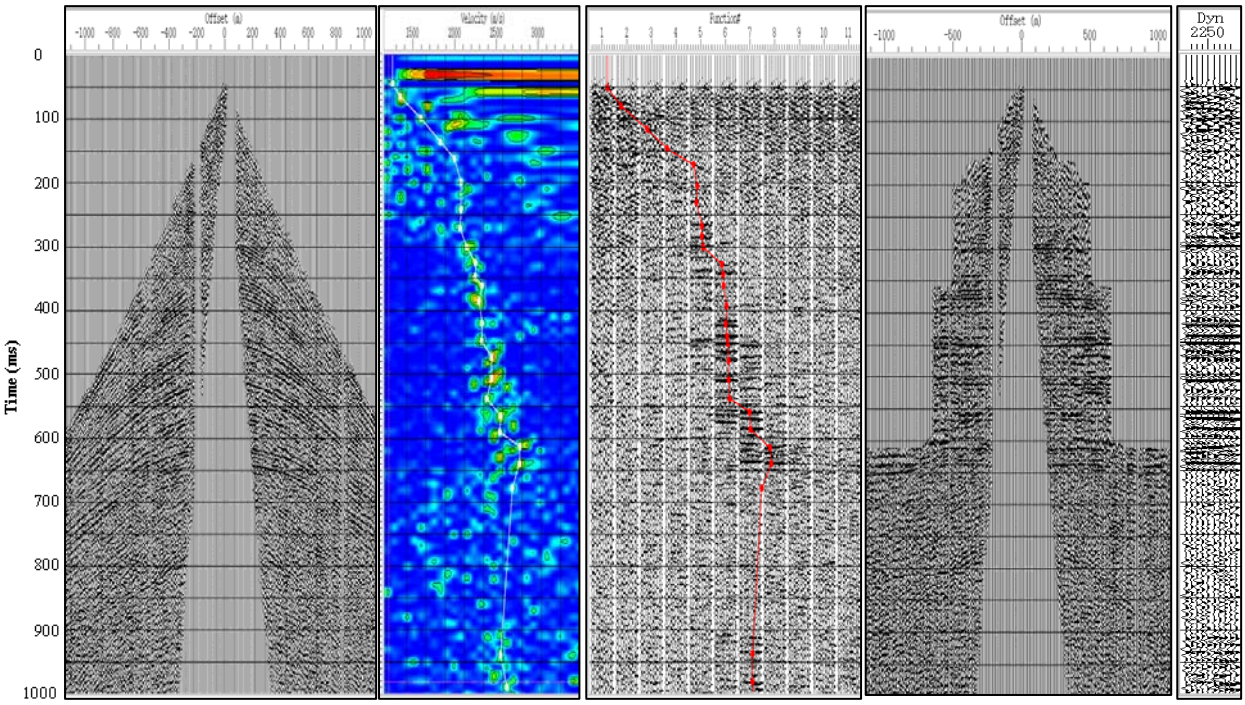

Figure 3.19 *A CMP gather from Profile P-1 and its velocity analysis: (a) CMP gather with fitted hyperbolas, (b) semblance analysis with picked velocity function, (c) constant-velocity stack functions with picked velocity, (d) CMP gather after NMO correction and greater than 100% stretch mute, and (e) a sample of 10 neighboring CMP stacked traces.*

Assuming the horizontally stratified earth, the normal move out velocity is equal to the RMS velocity function provided that the offset is small (Yilmaz, 2001). The individual NMO value associated with each reflection event is therefore used to derive a root-mean-square velocity (V_{rms}) for the layers above the reflector using equation 3.21 (see section 3.2).

Residual-statics-correction is applied to the NMO-corrected CMP gathers to adjust the travel time deviations using small time shifts so as to improve the coherence of existing reflections. The final stacked section can be further improved by performing velocity analysis again after the residual statics are applied. The entire procedures of velocity analysis, NMO correction, and residual statics corrections can be iterated until the improvements become negligible (Fig. 3.13).

Fig. 3.20 shows the stacking (RMS) velocities of the three profiles determined by the velocity analysis. The CMP stacked sections of the three profiles also show sequences of reflected events as displayed in Fig. 3.21.

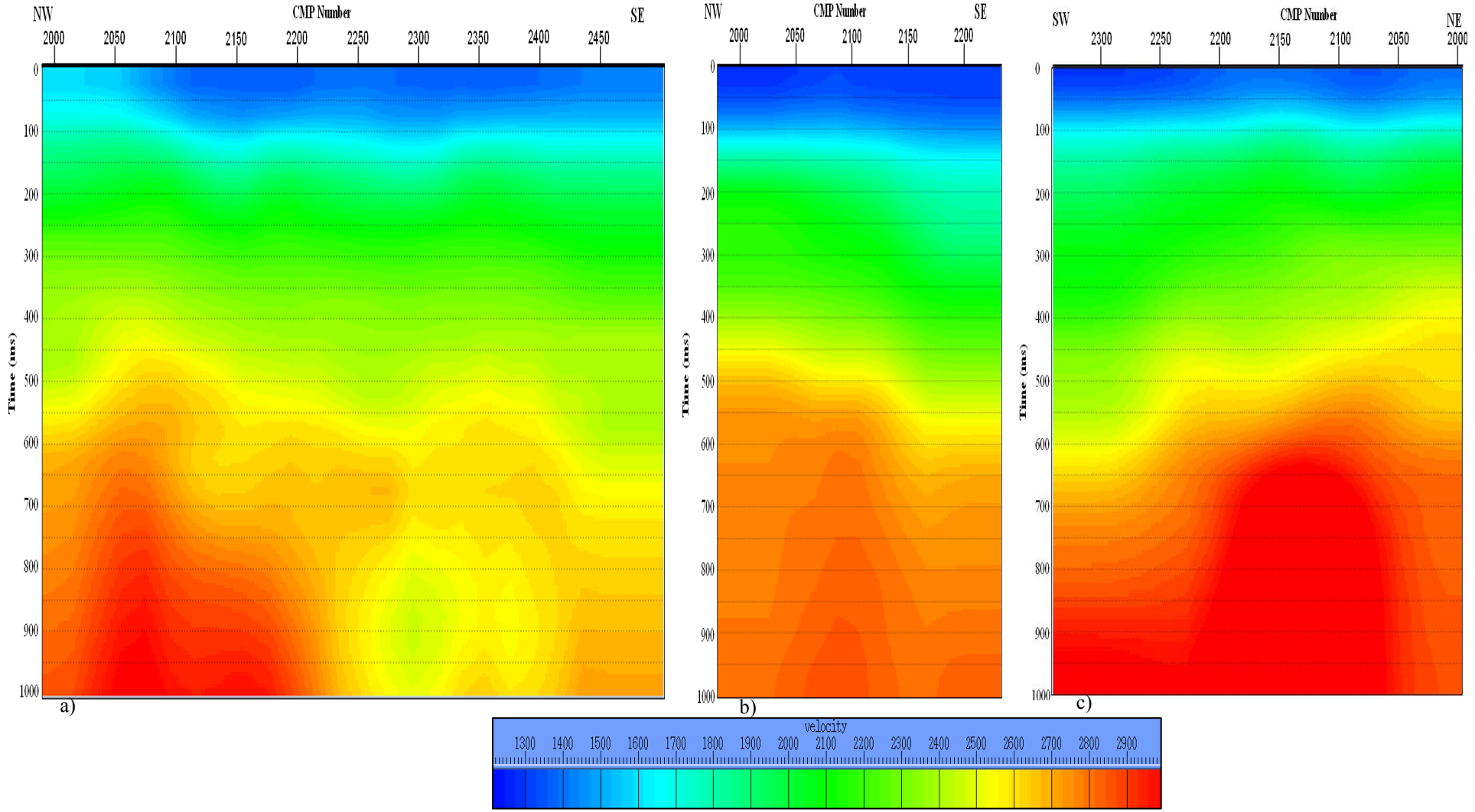

Figure 3.20 *Stacking (RMS) velocity for profile P-1 (a), profile P-2 (b), and profile P-3 (c).*

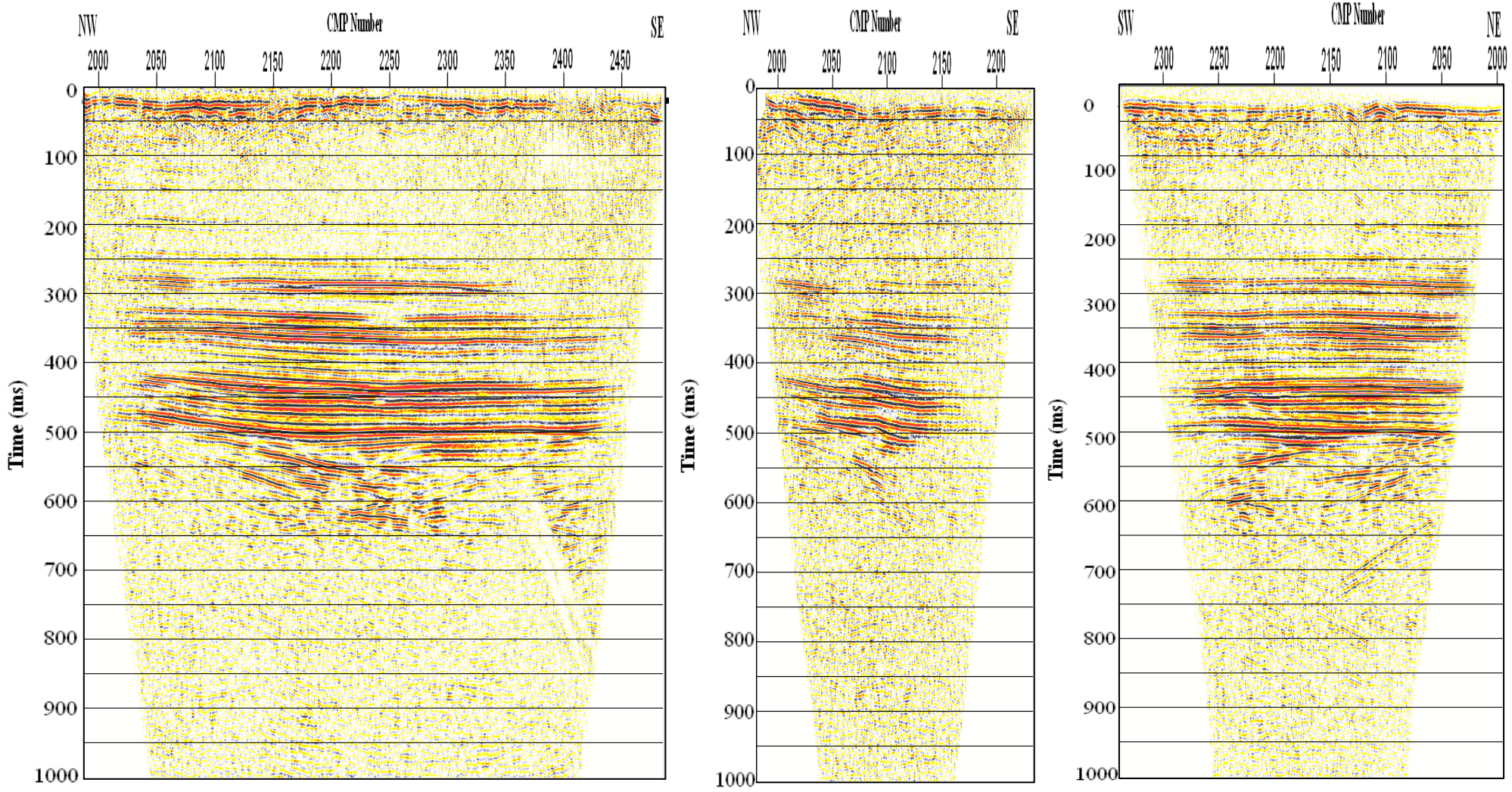

Figure 3.21 *Stacked time sections of P-wave reflections in two-way time and CMP spacing of 5 m for profiles P-1 (a), P-2 (b), and P-3 (c).*

Post-stack deconvolution and migration

Frequency (band-pass) filtering can improve the signal-to-noise ratio but potentially damages the vertical resolution, while deconvolution (also called inverse filtering) improves the resolution, but at the expense of a decrease in the signal-to-noise ratio (Kearey et al., 2002).

Post-stack deconvolution is made to improve the vertical resolution of the seismic section by compressing the basic wavelet, which also increases the bandwidth of the wavelet. Moreover, it is also important to attenuate multiple reflections and reverberations (Yilmaz, 1987; Baker, 1999, Gadallah and Fisher, 2009). We applied F-X deconvolution for our data using the Wiener prediction filter approach. The design of the Wiener filter requires that the difference between the filtered signal and the desired output signal has a minimum mean-squared error. It works in the frequency domain by applying a Fourier transform to each trace of the stacked data. An example of the effect of deconvolution is shown in Fig. 3.22. The coherence of reflection signals is much improved after deconvolution.

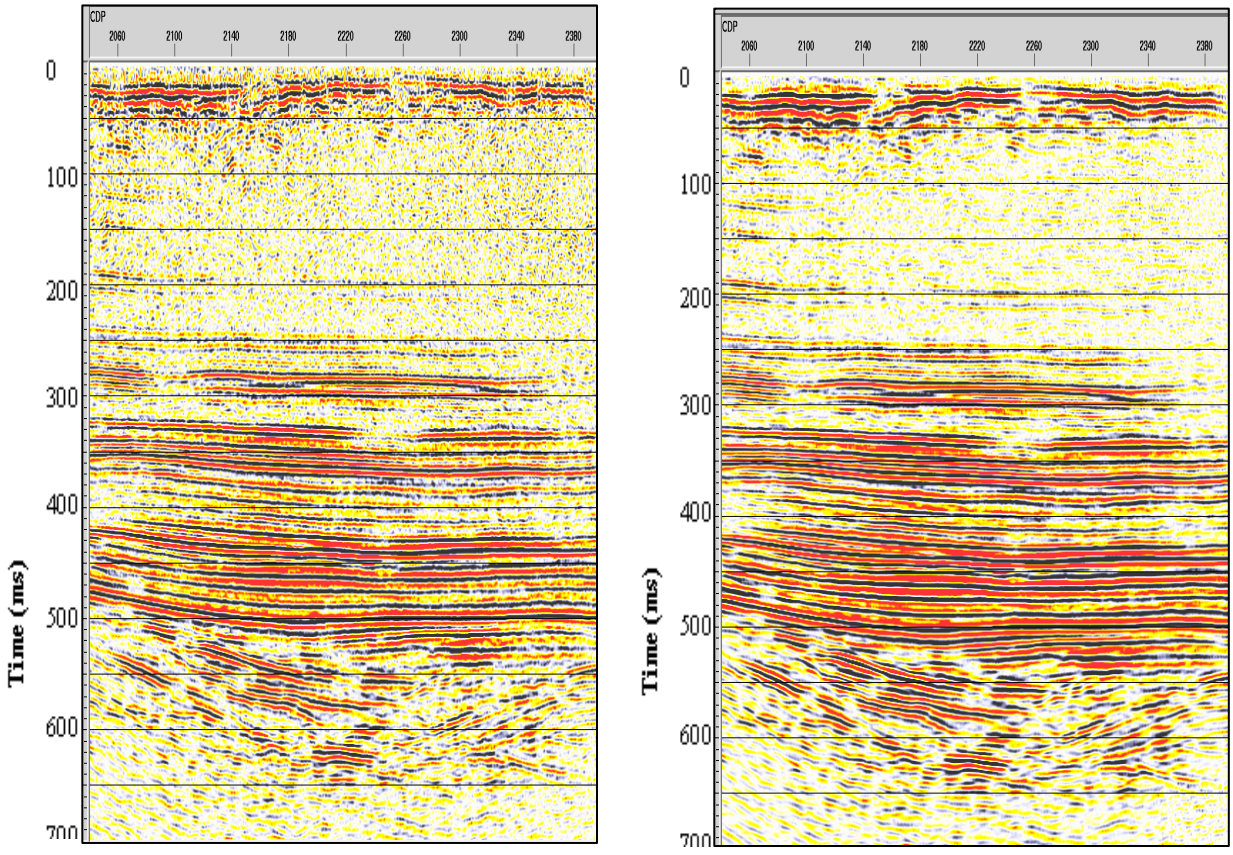

Figure 3.22 *Migrated stacked section; (a) without deconvolution and (b) after F-X deconvolution.*

The use of migration in near-surface data is limited because the depth to the reflector is small compared with the spread length and the propagation velocity is low (Black et al., 1994; Baker, 1999). However, we applied migration after CMP stacking to adjust the apparent angle of dipping reflectors to their true dip angle in the subsurface and to increase the S/N of the stacked section by removing or reducing the effect of diffractions. Implicit FD time migration performs a poststack time migration using a single interval velocity function in time that is estimated from the rms (stacking) velocities. Figs. 3.23 and 3.24 show the single interval velocities and the migrated time section results of the three profiles, respectively.

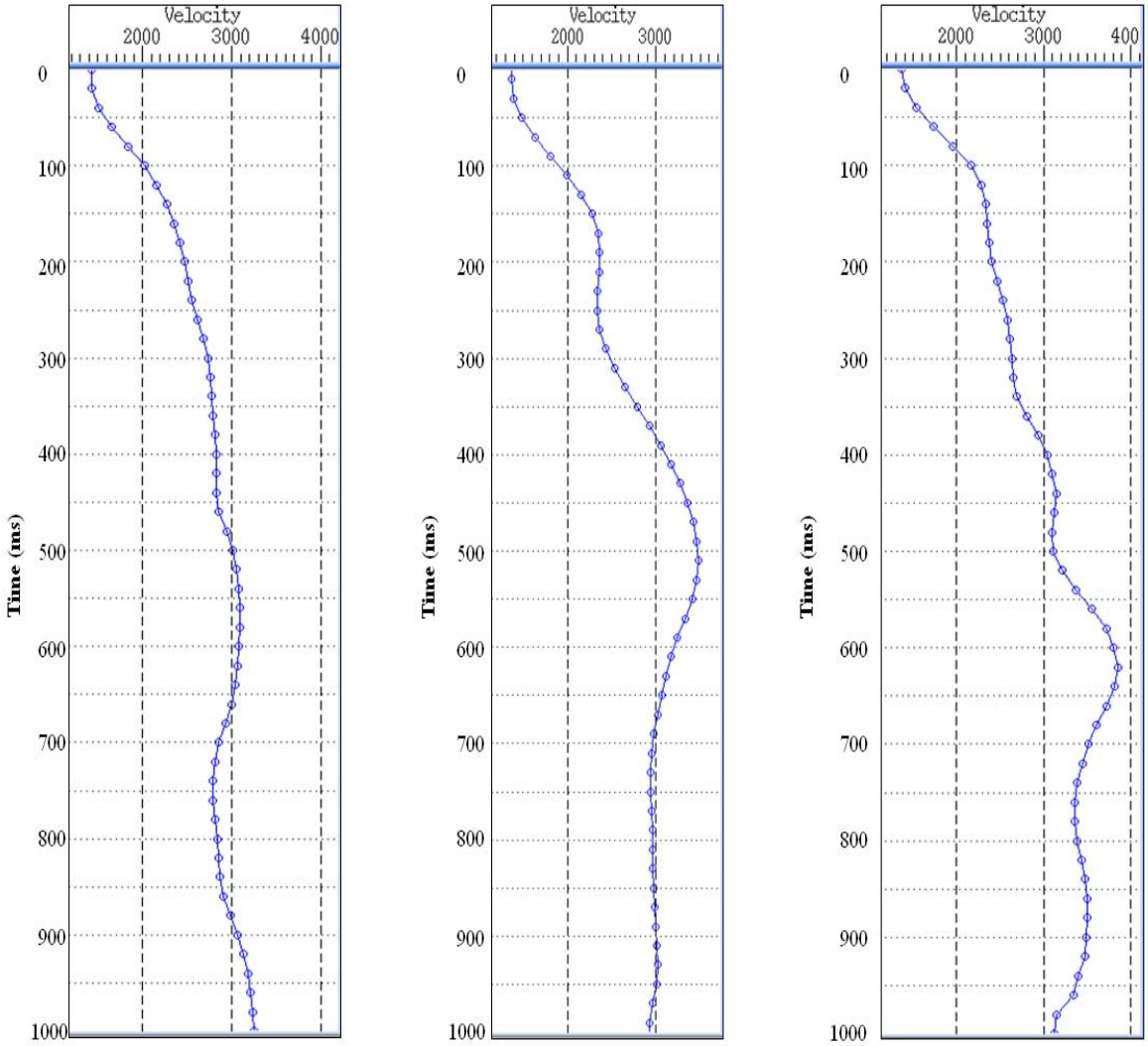

Figure 3.23 *P-wave single interval velocities (in m/s) as a function of two-way time derived from the stacking (rms) velocities: For profiles (a) P-1, (b) P-2, and (c) P-3.*

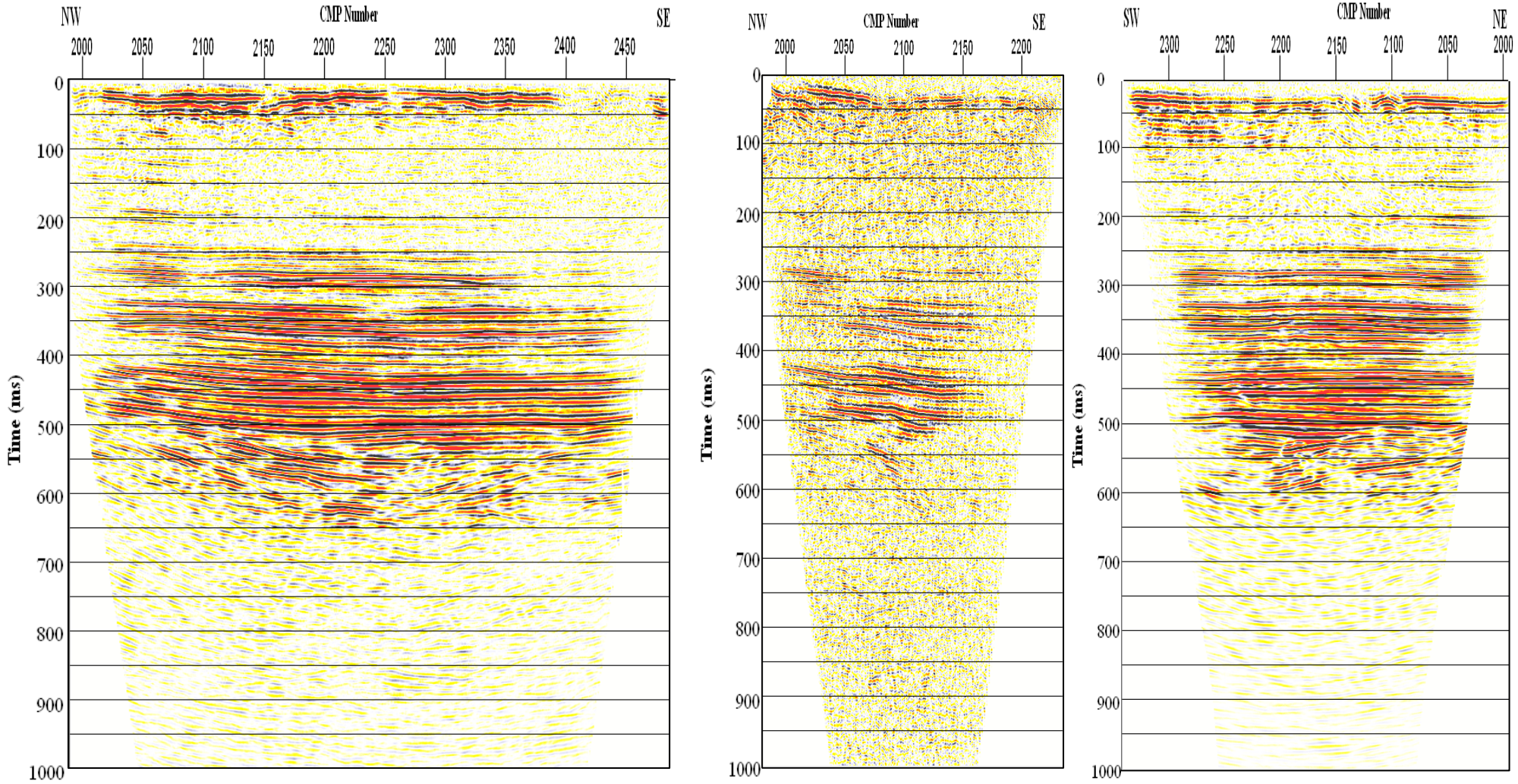

(a) (b) (c)

Figure 3.24 *Migrated time sections of P-wave reflections in two-way time and CMP spacing of 5 m for profiles P-1 (a), P-2 (b), and P-3 (c).*

Time-to-depth conversion

For the interpretation of the data, it is important to prepare seismic depth sections (Fig. 3.26), which display reflector depths that can be explained in terms of geologically meaningful stratigraphic and structural features. To convert the two-way time (TWT) axis to a depth axis, we use interval velocity functions (Fig. 3.25) derived from the rms (stacking) velocities in Fig. 3.20 using the Dix formula (Equation 3.22).

A time section and a depth section from profile P-1 are presented in Fig. 3.27. The differences of these two sections provide evidence of velocity variation within the section.

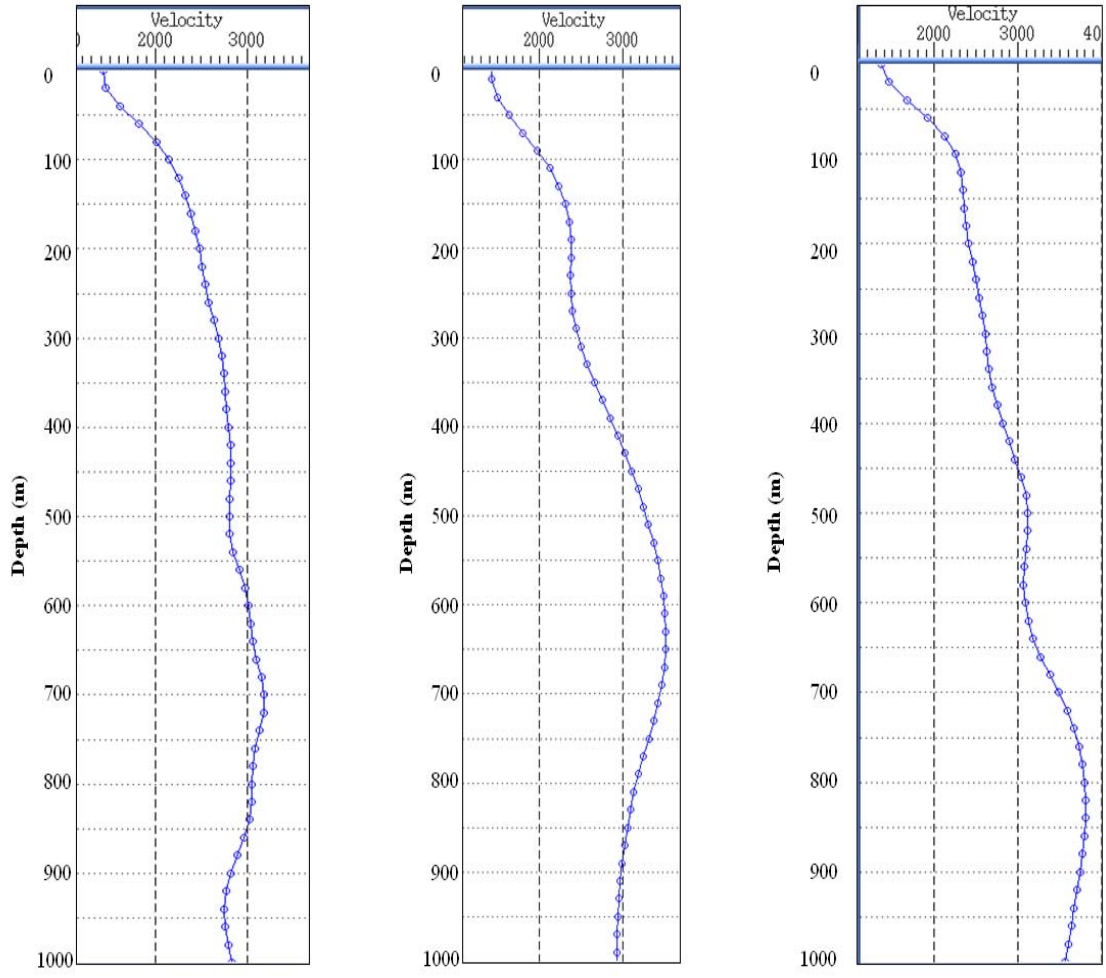

Figure 3.25 *P-wave single interval velocities (in m/s) as a function of depth derived from the stacking (rms) velocities: For profiles (a) P-1, (b) P-2, and (c) P-3.*

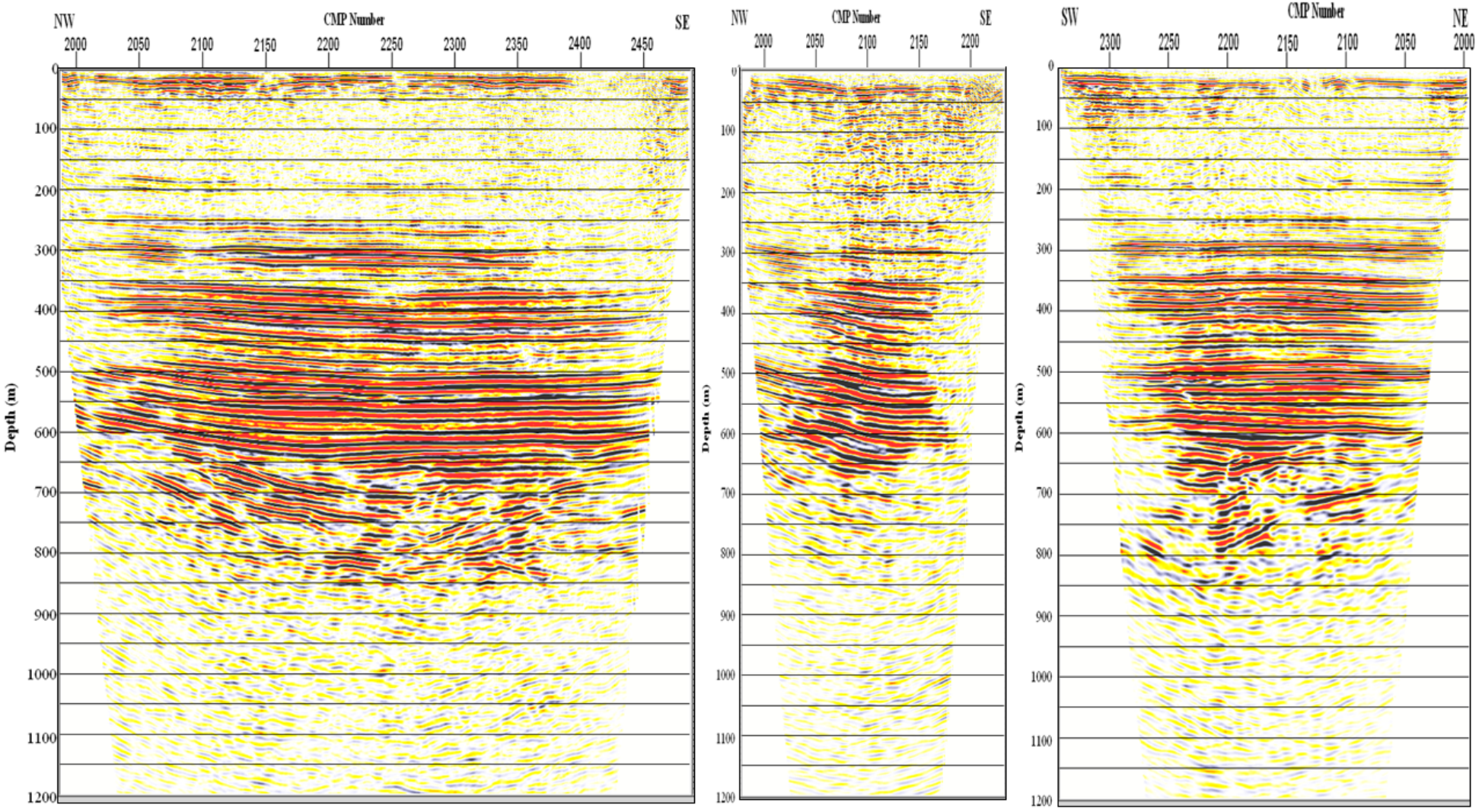

(a) (b) (c)

Figure 3.26 *Migrated depth sections of P-wave reflections for profiles P-1 (a), P-2 (b), and P-3 (c).*

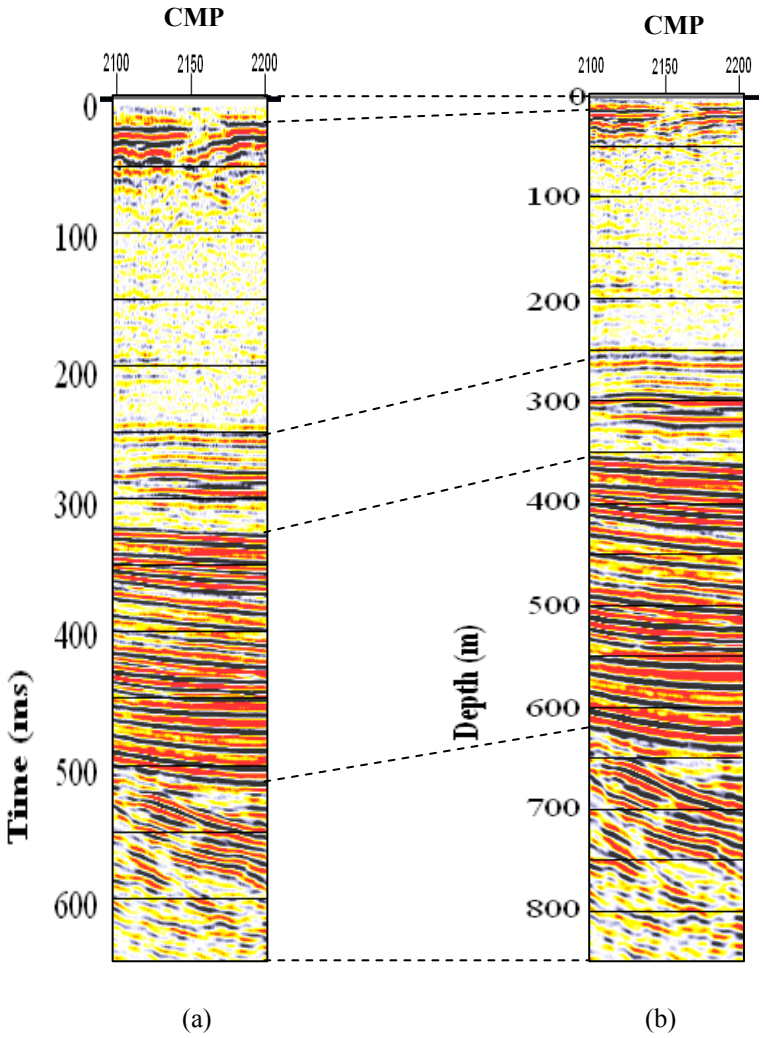

Figure 3.27 *Time-to-depth conversion; (a) time section and (b) depth section*

3.4.2 SH-wave seismic reflection data processing

The SH-wave data were processed using ProMAX^{TM} 2D version 2003.12.1, a commercial processing software package from Landmark Graphics Corporation.

The processing flows used for the shear wave data were more or less similar to the P-wave seismic reflection processing techniques (Fig. 3.13). But the vibroseis correlation and stacking/combining the shot gathers were done after the field work during the data processing stage and additional velocity (f-k) filtering has been applied.

Prestack processing - data analysis

Following the input of the left and right (different polarity of source signal, see section 3.3.2) shot records of each source station into the processing software package, vibroseis (sweep) correlation and ensemble stacking/combining have been done before the geometry and trace headers were defined. Normally, the two records for each source station of opposite polarity should be subtracted from one another to eliminate the P-wave signals and to amplify the SH-wave arrivals before vibroseis correlation. But after correlation with each sweep (since the two sweeps are in opposite directions), the polarity of the SH-waves become the same for both records and they have to be stacked to amplify the SH-wave amplitudes. A first look at typical unprocessed SH-wave records after vibroseis correlation and stacking is given in Fig. 3.28 from the two shear wave profiles (S-1 and S-2). Since the surface (Love type) waves cover most of the reflection arrivals, the data quality is poor to observe reflection arrivals.

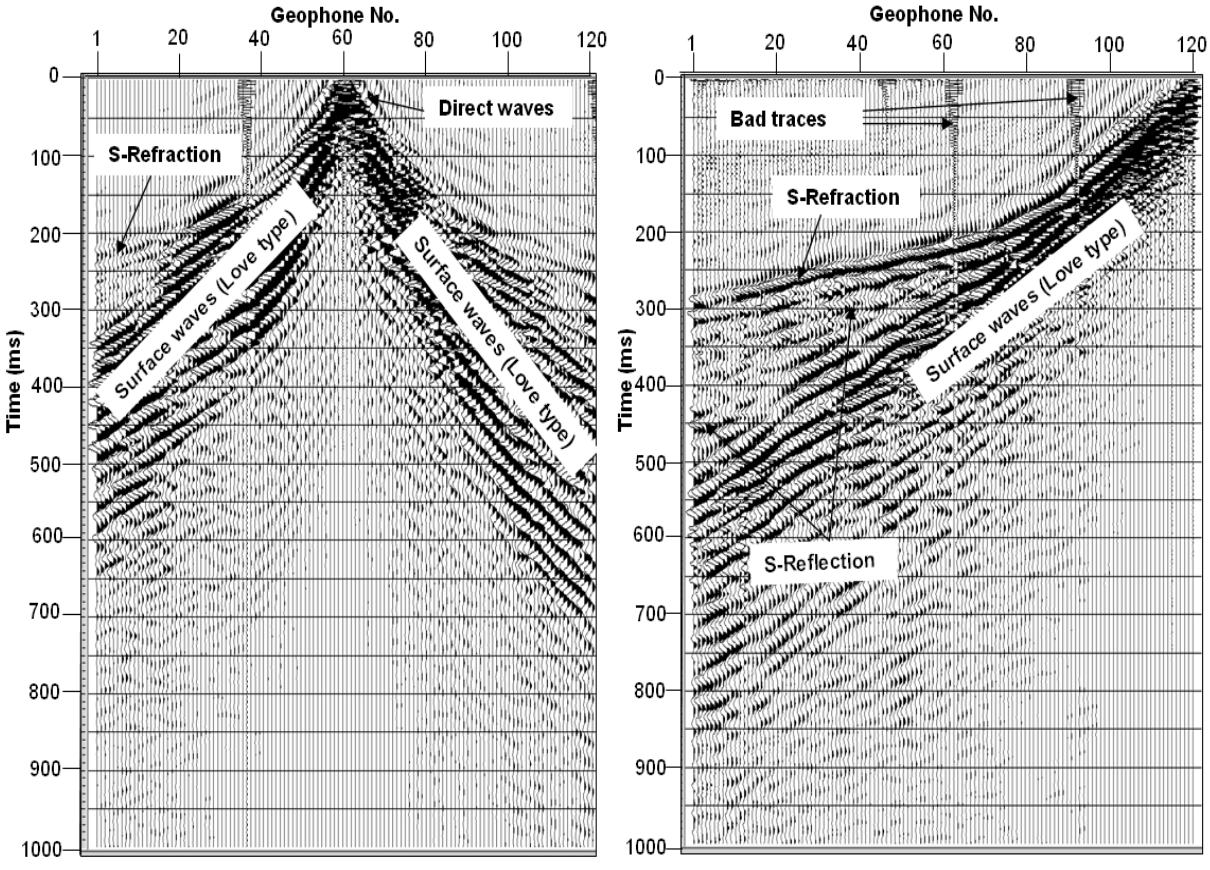

(a) (b)

Figure 3.28 *Shear wave raw data. (a) Mid shot gather from line S-1; (b) end shot gather from line S-2.*

Improving signal-to-noise ratio

For noise attenuation and improvement of the signal-to-noise ratio of the SH-wave data the same measures are available as for the P-wave data and additional true amplitude recovery and f-k (frequency-wavenumber) filtering was applied. In the prestack processing, the signal-to-noise ratio of the SH-wave data is improved by removing bad traces, applying spherical divergence corrections (true amplitude recovery), amplitude scaling (AGC), air blast attenuations, bandpass filtering, trace equalization, f-k filtering, and bottom muting.

The true amplitude recovery (TAR) applies a single time-variant gain function to compensate for loss of amplitude as the propagation distance increases due to wavefront spreading (Section 3.1.3 equation 3.14). The TAR has been done on a function of travel time and velocity of 500 m/s by using 6 dB/sec amplitude corrections. The amplitude losses due to inelastic attenuation are scaled using automatic gain control (AGC) with a window length of 120 ms. Air blast attenuation is applied with an approximate velocity of 50 m/s and 80 m/s and time gate width of 100 ms to attenuate the energy of waves with linear velocity behavior. Then the data is filtered by a bandpass frequency filter of 24-28-135-155 Hz that helps to discriminate the effect of P-waves from the S-wave data. Frequency filtering is more difficult in S-wave processing because the S-wave frequencies are generally a little lower than the P-wave frequencies and consequently differ less from the noise or the surface wave frequencies. Trace equalization is computed using mean amplitude values of adjacent traces to reduce the lateral amplitude variations of adjacent channels up to 500 ms.

The major noises in our data are the surface (Love) waves, which cover almost three-fourth of the data (Fig. 3.28). The Love waves are dispersive surface waves that show no constant period along a seismic trace. Recording the S-wave reflection signals before the arrival of the Love waves is just about impossible as the low frequency phase of the noise with its relatively high velocities hinders the signals. To overcome this short-coming, velocity (f-k) filtering is applied because the dispersion of the Love waves is useful for causing velocity differences at certain points in the seismogram so that to allow the Love waves to be extensively cleared from the seismogram. Fig. 3.29 shows the operating steps of an f-k filter. The initial material is the seismogram presented in distance-time (x-t) domain (Fig. 3.29(a)). The transformation into the frequency-wavenumber (f-k) domain is shown in Fig. 3.29(c). Here, regions associated with the Love waves and the signals are defined. According to the f/k ratio

(velocity), most of the noises are found between -325 m/s and +325 m/s. Fig. 3.29(d) illustrates the f-k spectrum after filtering and finally Fig. 3.29(b) is the seismogram after transformation back into the x-t domain. Fig. 3.30 is an example of the prestack processed (signal-to-noise ratio improved) data of the SH-waves after muting.

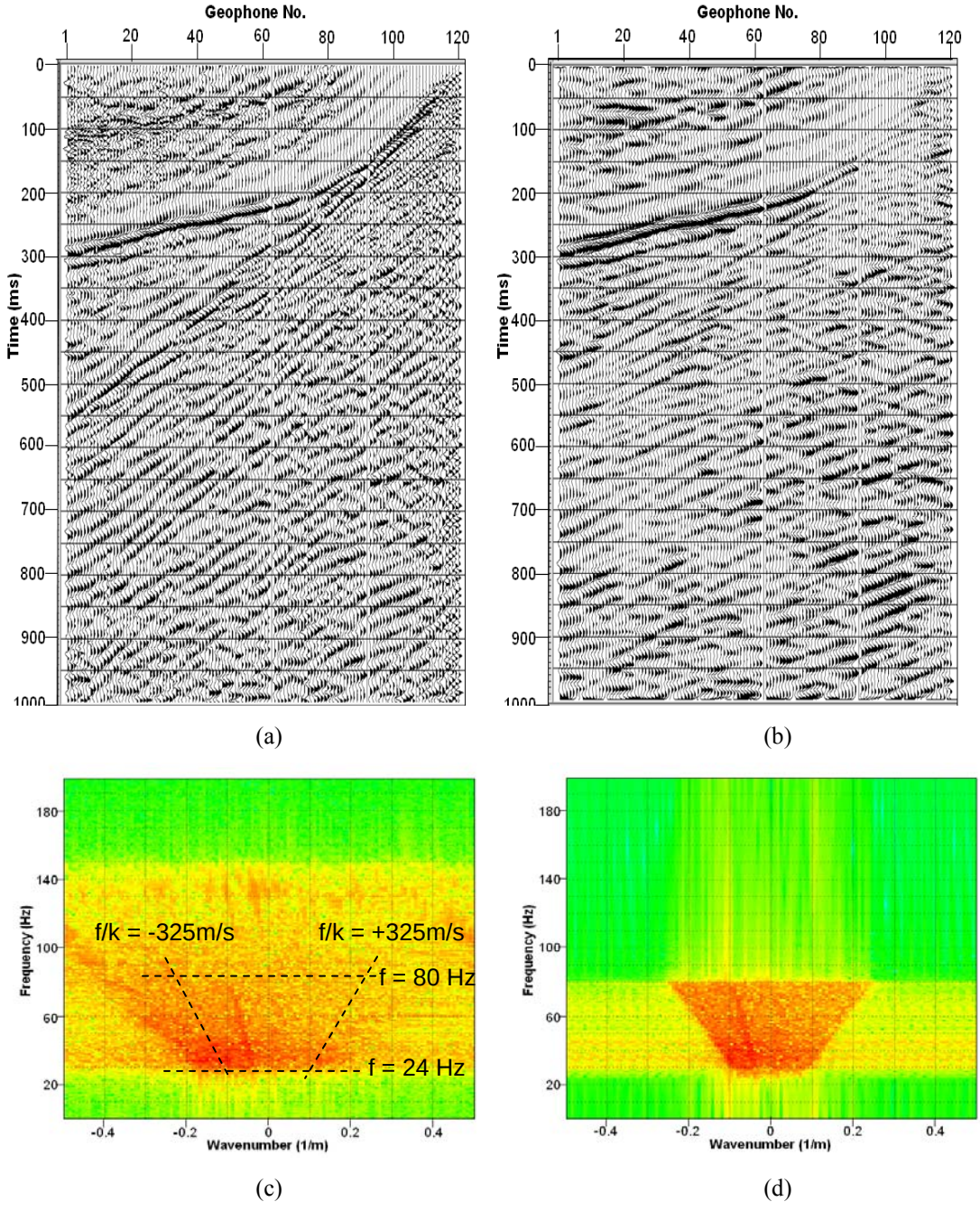

Figure 3.29 *Application of f-k filtering for signal-to-noise ratio enhanced data of the shot gather in Fig. 3.28 (b). (a) The seismogram before f-k filtering, (b) seismogram after f-k filtering, (c) presentation of the frequency content in the (f, k) domain before f-k filtering, and (d) presentation of the frequency content in the (f, k) domain after f-k filtering.*

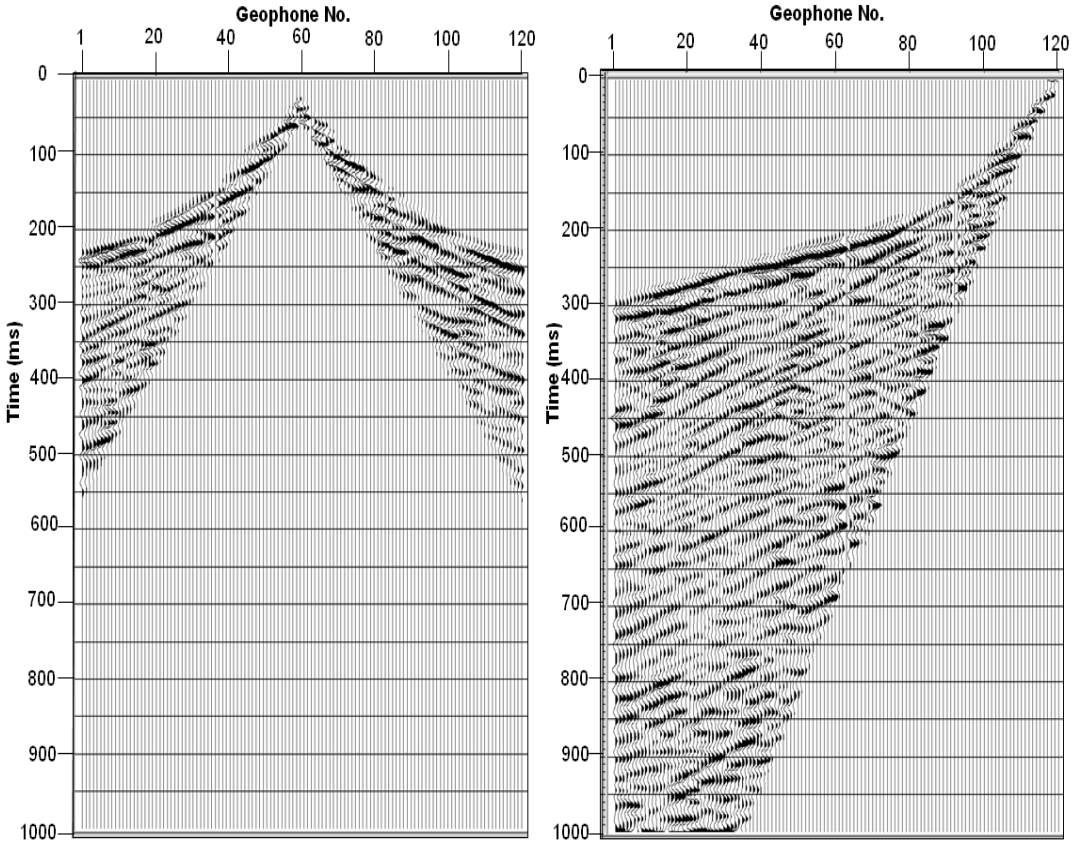

(a) (b)

Figure 3.30 *Shear wave prestack processed (signal-to-noise ratio improved) data. (a) Mid shot gather from line S-1; (b) end shot gather from line S-2.*

Velocity analysis and CMP stacking

In the velocity analysis, the stacking (RMS) velocities of the shear wave reflections are determined by sequentially picking hyperbolas from the CMP gather (Fig. 3.31(a)). This is done using semblance velocity analysis (Fig. 3.31(b)) and constant-velocity stack (Fig. 3.31(c)) methods similar to the P-wave processing. As a result of the lower velocity, S-wave reflections exhibit considerably larger normal moveout times than P-wave reflections and require correspondingly larger dynamic corrections for the stacking procedure. The NMO (dynamic) corrected CMP gather is displayed in Fig. 3.31(d). The NMO corrected CMP gathers are stacked into a single trace as shown in Fig. 3.31(e) together with six other neighboring CMP stacked traces.

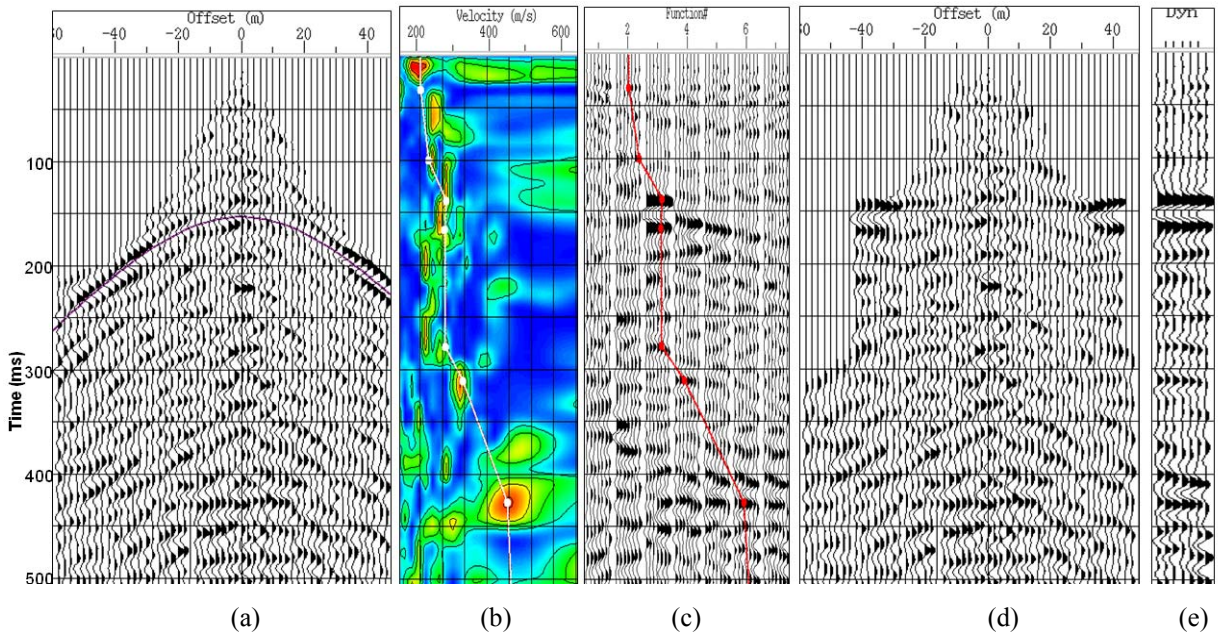

Figure 3.31 *A CMP gather from Profile S-2 and its velocity analysis: (a) hyperbola on CMP gather, (b) NMO velocity picks using semblance analysis, (c) NMO velocity picks using constant-velocity stack functions, (d) CMP gather after NMO correction and greater than 100% stretch mute, and (e) a sample of 7 neighboring CMP stacked traces.*

The stacking (RMS) velocities and CMP stacked sections of the two shear wave profiles (S-1 and S-2) are presented in Figs. 3.32 and 3.33, respectively.

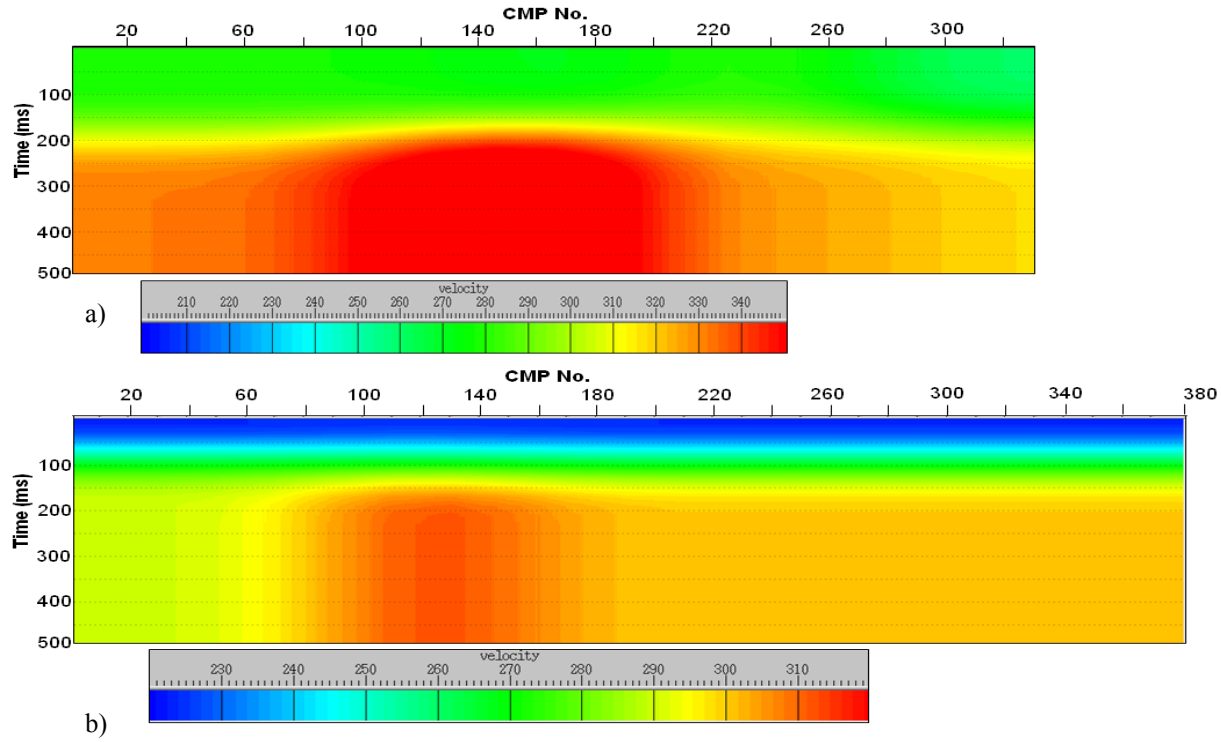

Figure 3.32 *Stacking (RMS) velocity; (a) profile S-1 and (b) profile S-2.*

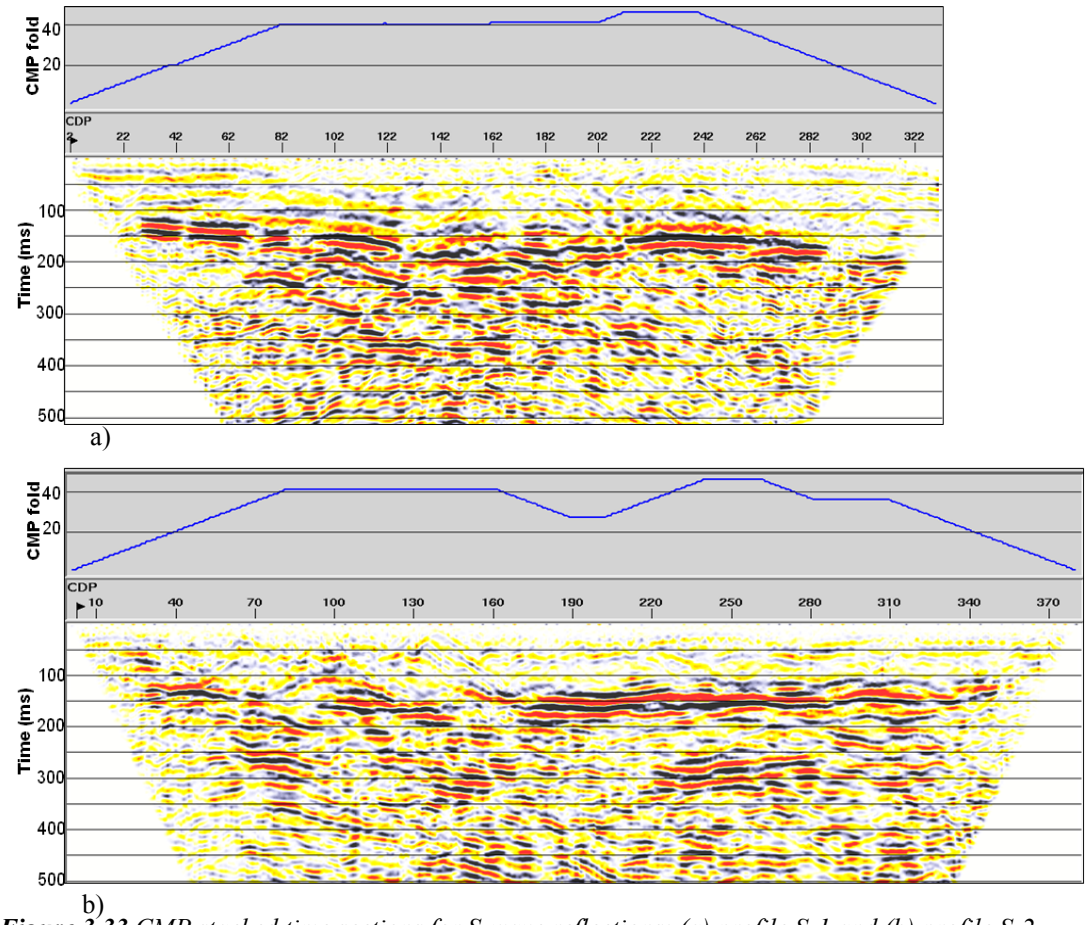

Figure 3.33 *CMP stacked time sections for S-wave reflections; (a) profile S-1 and (b) profile S-2.*

F-X poststack deconvolution using the Wiener prediction filter approach is applied to improve the resolution of the seismic sections before migration. Then implicit frequency domain time migration is applied for the stacked section using a single interval velocity function in time derived from the RMS (stacking) velocities in Fig. 3.32. Figs. 3.34 and 3.35 show the single interval velocities (in m/s) and the sections after deconvolution and time migration for the two shear wave profiles, respectively.

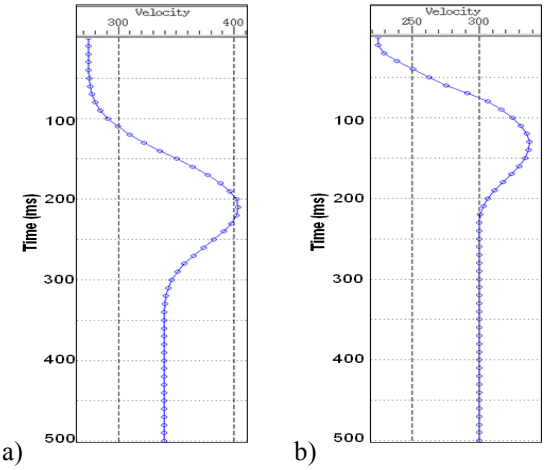

Figure 3.34 *S-wave single interval velocities (in m/s) as a function of time derived from the stacking velocities; (a) for profile S-1 and (b) profile S-2.*

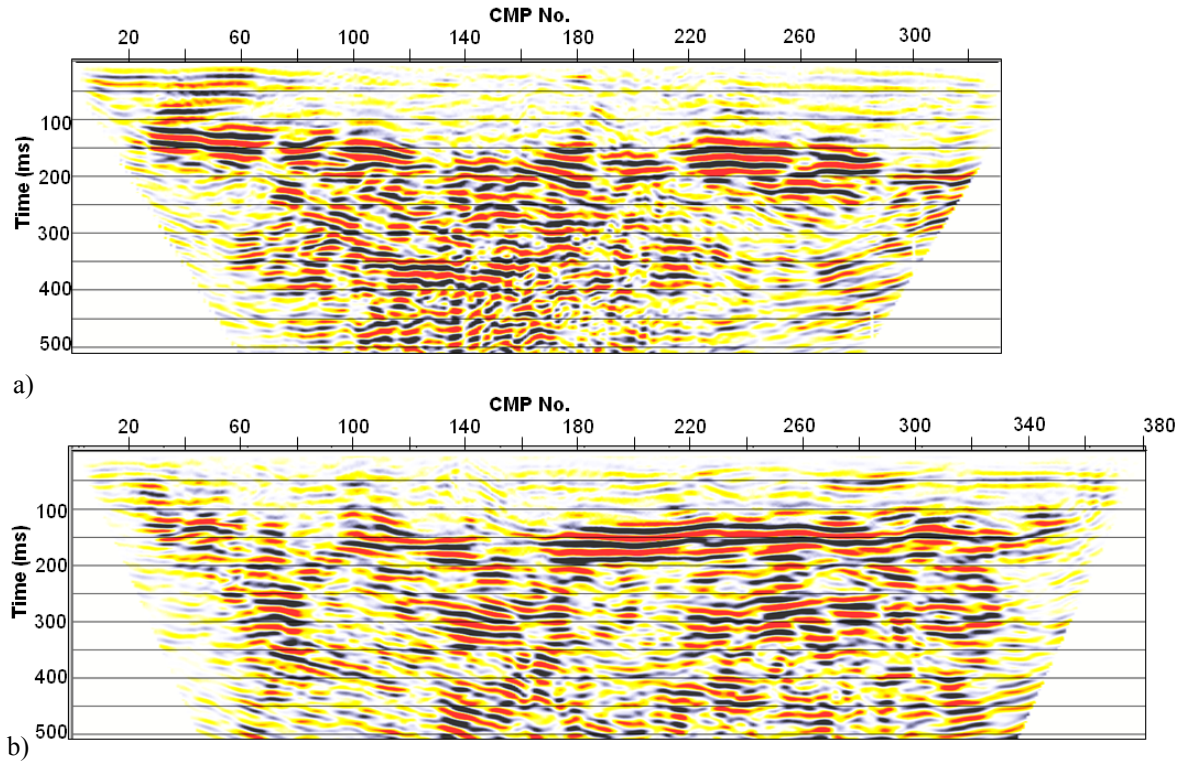

Figure 3.35 *Migrated time sections for S-wave reflections; (a) profile S-1 and (b) profile S-2.*

The migrated CMP stacked time sections are finally converted into depth sections using interval velocity functions in depth derived from the stacking velocities by the Dix formula in equation 3.22. Figs. 3.36 and 3.37 show the single interval velocities as a function of depth and the migrated depth sections for the two shear wave profiles, respectively.

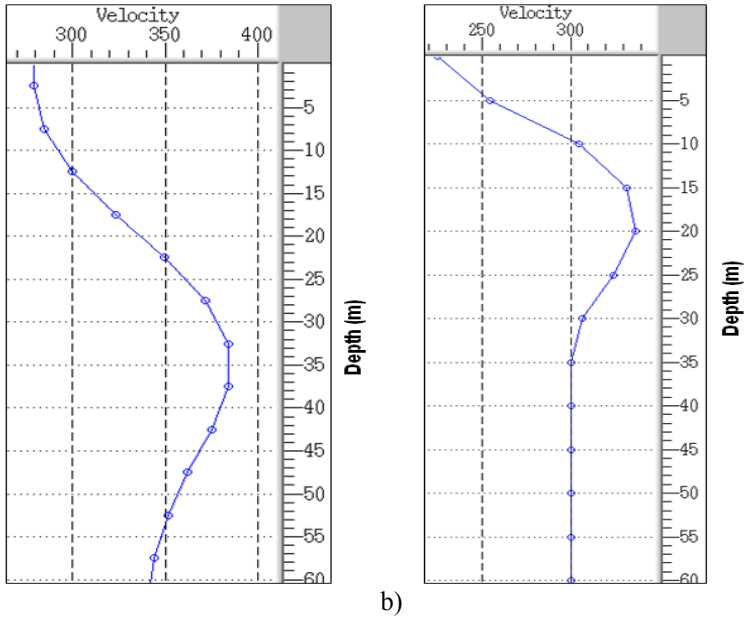

Figure 3.36 *S-wave single interval velocities (in m/s) as a function of depth derived from the stacking velocities; (a) for profile S-1 and (b) profile S-2.*

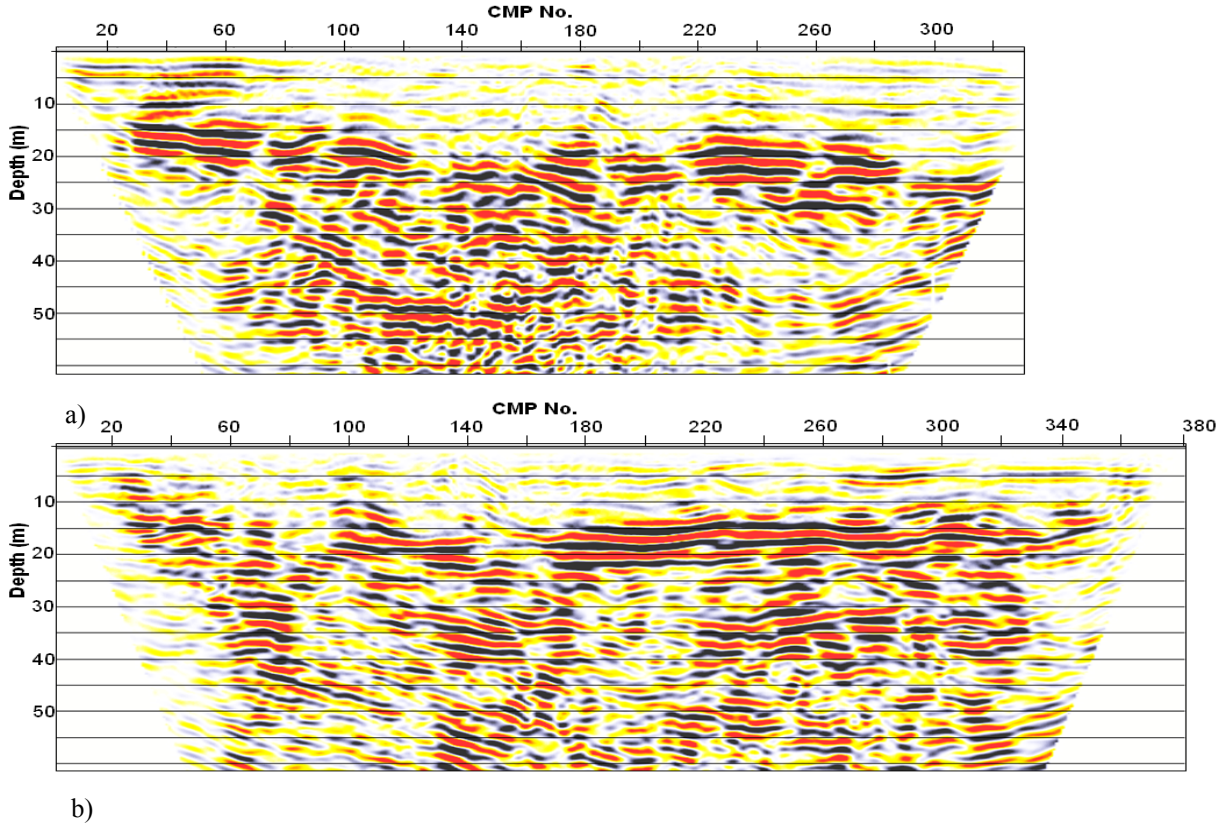

Figure 3.37 *Migrated depth sections for S-wave reflections; (a) profile S-1 and (b) profile S-2.*

3.5 Seismic reflection results and interpretations

The major goal of seismic interpretation is to relate the reflection seismic data to subsurface stratigraphy and depositional facies. Since no borehole data is available below 20 meters depth in the study area, the stratigraphic and lithological conditions that create seismic reflections are identified by correlating with the regional geology. The inclusion of external geological and geophysical constraints is often the key to successful interpretations and the development of a reasonable subsurface geologic image.

According to the results from the 2D seismic sections five geologic layers are interpreted, from the oldest to the youngest, as salt dome (Permian), claystone/ sandstone (Jurassic), claystone/marl (lower Cretaceous), chalky limestone (upper Cretaceous), and the Quaternary sediment layers (Fig. 3.38).

The top of the salt dome is detected at a depth of about 600 meters and is overlain by the horizontally stratified Mesozoic sedimentary rocks. Although, it is not common to find

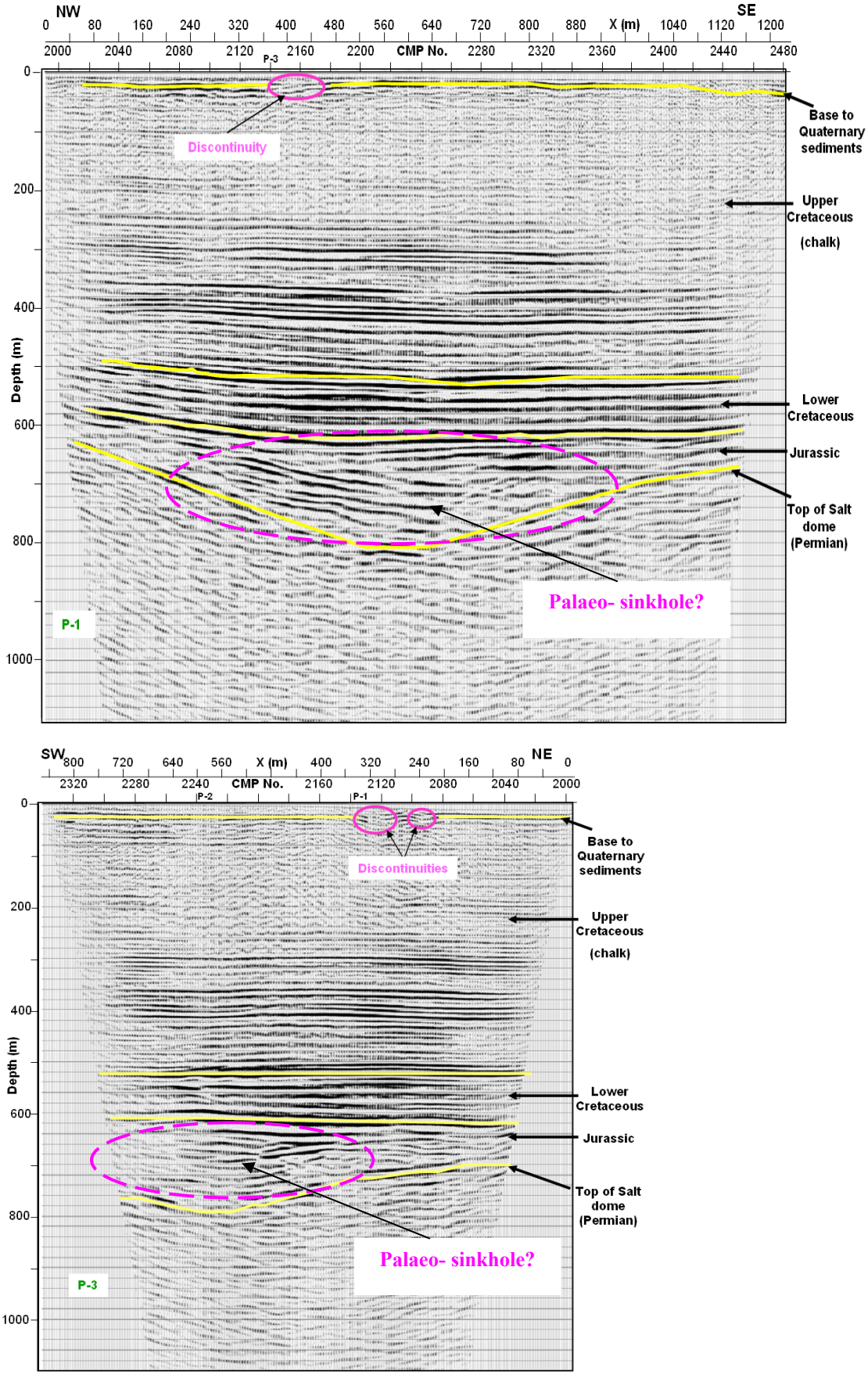

Figure 3.38 *P-wave seismic reflection depth sections with interpretations along profiles P-1 and P-3.*

Jurassic layers on top of the salt domes in north Germany because of erosion (see section 2.2.1 and Fig. 2.9) some Jurassic rock layers are interpreted from the results of the new seismic sections at depths from 600 to 800 meters which might be remnants due to a Paleosinkhole that subsided over the salt layer before the erosion period. The bedding of the Jurassic sedimentary rocks is tilted. This indicates that the subsidence occurred after deposition of the sediments. The thin layer between 500 and 600 meters depth corresponds to the lower Cretaceous claystone-marl intercalations and between 20 and 500 meters depth it is interpreted as the upper Cretaceous chalky limestone. From the seismic reflection method information about the Quaternary sediments in the very near surface that is shallower than 20 meters depth is scarce.

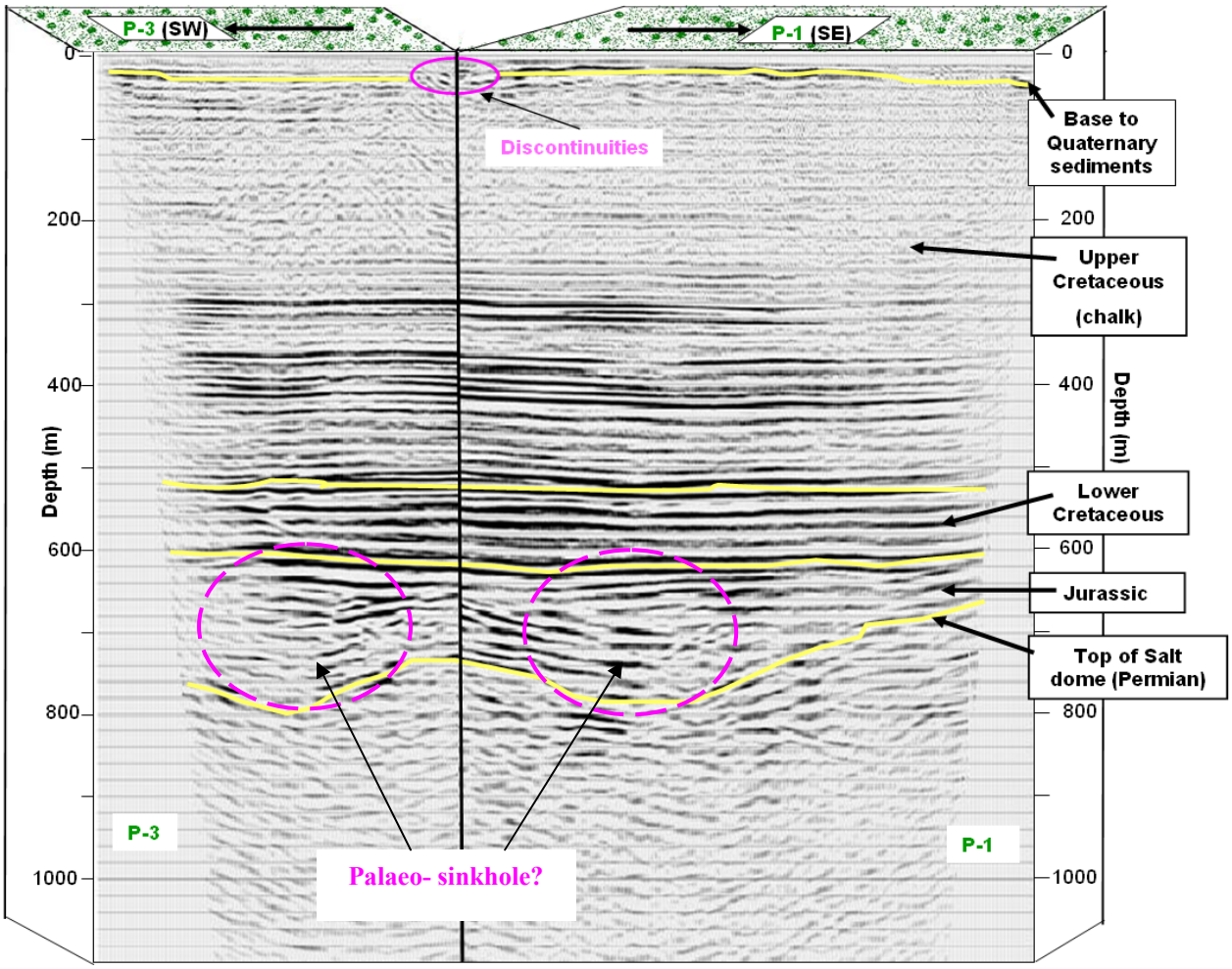

Figure 3.39 *Comparison of seismic reflection interpreted results at the intersection point between profiles P-1 and P-3.*

Although the seismic method can be used to map the geology in 2D imaging with certain degree of success, in this thesis it was initially applied to detect tectonic faults and seismic

discontinuities for the interpretation of sinkholes. Therefore, from the results no major fault zones are identified except for a few discontinuities on top of the upper Cretaceous (chalk) layer. These discontinuities are observed along P-1, P-3, S-1, and S-2 profiles (Figs. 3.38 and 3.40).

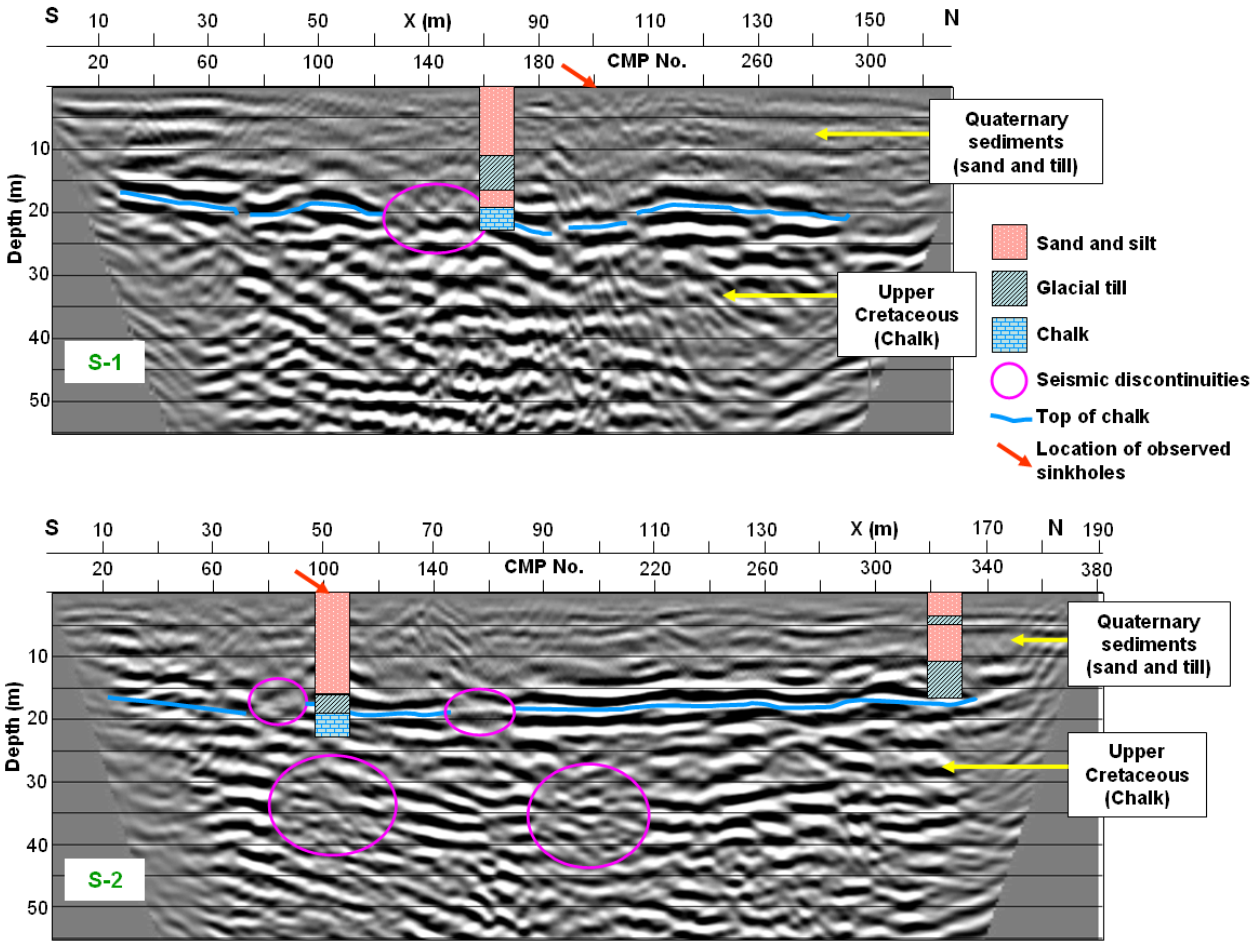

Figure 3.40 *S-wave seismic reflection depth sections with interpretations along profiles S-1 and S-2.*

Some of the seismic reflection discontinuities (at profiles S-1 and S-2) are located close to the observed sinkholes and some of them are away (at the intersection of profiles P-1 and P-3) but still all of them are aligned linearly as shown in Fig. 3.41.

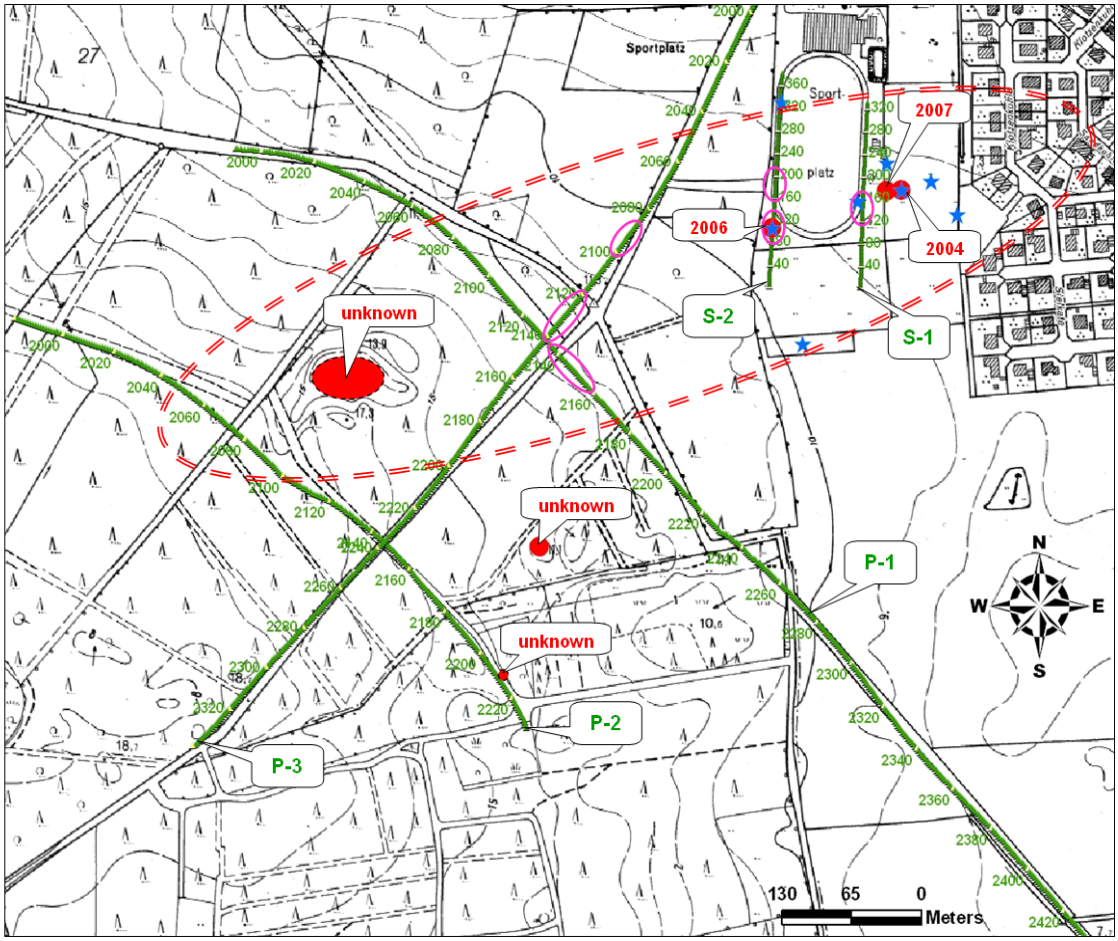

Figure 3.41 *Location of seismic reflection discontinuities (purple ellipses), sinkholes with year of occurrences (red circles), boreholes (blue stars) over the seismic profiles (in CMP number).*

4 SEISMIC REFRACTION TOMOGRAPHY

The principles of tomography are applicable in many ways and on different scales such as, e.g., to investigate internal tissues of human body using x-rays in medicine or to produce velocity models of the earth's subsurface using seismic sources or earthquakes in seismology. In this thesis, 2D seismic refraction tomography is applied using the first break traveltime arrivals of the seismic wave data collected for seismic reflection as already shown in chapter three.

From the seismic reflection results of the study area, information about the Quaternary sediments in the very near surface that is shallower than 20 meters depth is scarce. To fill this lack of information and to image velocity variations of the subsurface the first traveltime arrivals of both the P- and S-wave seismic data were used for 2D velocity modeling.

4.1 Basic principles of seismic refraction tomography

Conventional seismic refraction methods using delay time or generalized reciprocal method analyses make simplifying assumptions about the velocity structure that conflict with heterogeneity, lateral discontinuities, and gradients. But seismic refraction tomography, which is not subject to these constraints, is able to resolve velocity gradients and lateral velocity changes and may be applied in settings where conventional refraction techniques fail such as areas of compaction, karst, and fault zones (Zhang and Toksöz, 1998; Sheehan et al., 2005).

In recent years, many geophysicists have successfully used seismic refraction tomography as method of interpreting seismic refraction data to resolve velocity gradients and lateral velocity changes (e.g., Hiltunen et al., 2007; Osazuwa and Chinedu, 2008; Tamiru, 2009).

Since the tomographic method depends implicitly on the general principles of inverse theory (e.g., Menke, 1989; White, 1989; Parker, 1994; Rawlinson and Sambridge, 2003), the basic principle of inverse theory and traveltime inversion is introduced briefly as follows for better understanding of the techniques.

4.1.1 Introduction to inverse theory

In inverse problems there is a mathematical relationship that links the measured quantities called data with the quantities one really wants to know or being estimated called model parameters.

There are two types of modeling: forward and inverse. Forward modeling makes use of earth models, data acquisition parameters, and theoretical models of physical processes to generate synthetic data that match observed data within some maximum error. Inversion uses data acquisition parameters and theoretical models of physical processes to produce a model of the subsurface that predicts the observed data.

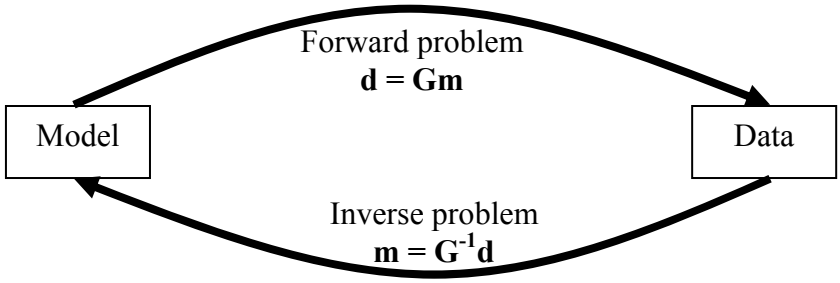

Figure 4.1 *Relationship between forward and inverse modelling.*

The general form of the relationship between data and model parameters can be written as a system of equations:

$$\mathbf{d} = \mathbf{Gm} \tag{4.1}$$

where $\mathbf{d} = (d_1, d_2, d_3, \ldots, d_N)^T$ is the vector of the observation data (in the case of discrete observations), which can also be characterized as a function of the observation data (in the case of continuous observations), $\mathbf{m} = (m_1, m_2, m_3, \ldots, m_M)^T$ is the vector (or some function) containing model parameters, and **G** is the kernel N x M matrix that relates the model to the observed data. The kernel function represents the physics of the problem, including boundary conditions and differential equations.

The main purpose of inverse theory is to provide estimates of model parameters (Fig. 4.1). The inversion process involves computing the inverse of the kernel matrix ($\mathbf{G}^{-1}$) and then multiplying by the data **d** to compute the model **m**.

There are two approaches to solve inverse problems. The first is analytical, just-solve-the-equation approach to find the model from given data using pure mathematics. This works if we plug continuous data points without noise and perfect geometric coverage into the mathematical relationships. Since the mathematical relationship that mathematicians invert this way are very idealized in the real world applications, many geophysical problems are just too unstable for such analytical inversion approaches. A direct inverse solution cannot be found using the traditional mathematical approach because many of the inverse problems in geophysics are non-linear and do not have a unique solution. It is difficult to compute the inverse matrix ($\mathbf{G}^{-1}$) particularly if the matrix is ill posed (mixed-determined), ill-conditioned (small data errors cause large model changes), or large (too many parameters for the available computer memory). Therefore, geophysicists work often with the second much more general approach called optimization-based approach to solve inverse problems. In all optimization methods, an initial model is modified in an iterative manner so that the difference between the model response and the observed data values is reduced.

Inversion requires a forward model with a known response. In the case of a geological model, its geophysical response must be known. The forward problem solution makes it possible to predict geophysical data for specific geological structures. An optimization algorithm is also needed so that parameters of the forward model may be adjusted. The choice of the forward model and the optimization algorithm greatly affects the quality of the inversion.

Part of solving a geophysical inverse problem is to parameterize the continuous function with a finite set of model parameters so that the model is estimated from discrete data points. Since inversion is the estimation of a continuous model function (e.g., 2D image of true velocity, true resistivity, etc) from a set of data points (e.g., first break traveltime arrivals, apparent resistivities, etc), at the end the model parameters are converted back to a continuous model again by smoothing.

The solution of the inverse problem consists in determining a predicted model that generates predicted data called model (forward) responses, **f(m),** that fit well the observed data vector **d**. It is not common to fit the observed data exactly with the predicted data, because they always contain some noise that cannot be fit. Therefore, we have to look for some predicted data that will be close enough to the observed data within the accuracy of our observations.

For linear problems there exists a linear relation between **m** and **f**, which can be expressed by a matrix-vector multiplication

$$\mathbf{f(m) = Gm} \tag{4.2}$$

For non-linear problems the forward operation depends on the model **m** itself. Beginning from a starting model $\mathbf{m^o}$, an iterative process is applied to update the model until data fit or convergence is achieved. In each iteration step *k,* a new model is calculated by adding a model update $\Delta\mathbf{m}^k$

$$\mathbf{m}^{k+1} = \mathbf{m}^k + \Delta\mathbf{m}^k \tag{4.3}$$

under the assumption that **f(m)** is a quasi-linear function of the model parameters **m** and that the estimated solution $\mathbf{m_{est}}$ is close to the true solution. A linear relationship can then be derived using a Taylor series expansion and neglecting high-order terms

$$\mathbf{f}(\mathbf{m}^k + \Delta\mathbf{m}^k) = \mathbf{f}(\mathbf{m}^k) + \frac{\partial \mathbf{f}(\mathbf{m}^k)}{\partial \mathbf{m}}\Delta\mathbf{m}^k + \ldots \approx \mathbf{f}(\mathbf{m}^k) + \mathbf{G}\Delta\mathbf{m}^k$$

where the partial derivative of the model response with respect to the model parameters, G, is called Jacobian or sensitivity or the kernel matrix with the elements

$$\mathbf{G}_{ij}(\mathbf{m}^k) = \frac{\partial \mathbf{f}_i(\mathbf{m}^k)}{\partial \mathbf{m}_j} \tag{4.4}$$

Setting the response of the new model **f(m+Δm)** equal to the data **d** we obtain the non-quadratic equation (Günther, 2004) as

$$\mathbf{G\Delta m = d - f(m)} \tag{4.5}$$

The misfit can be quantified by constructing an objective function **Φ(m)**, consisting of a weighted sum of data misfit $\mathbf{\Phi_d(m)}$ and regularization terms $\mathbf{\Phi_m(m)}$, that is to be minimized. We have to work out the balance between the limited resolution of the continuous function

and the goodness of fit to the noisy data in a process called regularization. A regularization parameter λ is introduced to construct the total functional expression to be minimized as

$$\mathbf{\Phi(m)} = \mathbf{\Phi}_d\mathbf{(m)} + \lambda\, \mathbf{\Phi}_m\mathbf{(m)} \longrightarrow \text{minimum} \tag{4.6}$$

A very important question is how to minimize the difference between the observed and modeled. Choices include least-square error, the least absolute deviation, and min-max methods. A least squares approach is often used to find a solution (Menke, 1989). In the least-squares optimization method, the initial model is modified such that the sum of squares error of the difference between the model response and the observed data values is minimized.

An essential component of the objective function is $\mathbf{\Phi}_d\mathbf{(m)}$ which measures the difference between the observed and predicted data. If it is assumed that the error in the relationship $\mathbf{d}_{obs} \approx \mathbf{f}(\mathbf{m}_{true})$ is Gaussian, then a least squares or L_2 measure of this difference is suitable (Rawlinson and Sambridge, 2003; Günther, 2004):

$$\mathbf{\Phi}_d\mathbf{(m)} = \| \mathbf{d}_{obs} - \mathbf{f(m)} \|^2 \tag{4.7}$$

If uncertainty estimates have been made for the observed data (usually measurement errors, ε_i), then more accurate data are given a greater weight in the objective function using

$$\mathbf{\Phi}_d\mathbf{(m)} = \| \mathbf{D}\,(\mathbf{d}_{obs} - \mathbf{f(m)}) \|^2 = \sum_{i=1}^{N}\left(\frac{d_i - f_i(\mathbf{m})}{\varepsilon_i}\right)^2 \tag{4.8}$$

$$\text{with } \mathbf{D} = \text{diag}\left(\frac{1}{\varepsilon_i}\right)$$

The L_1-norm is particularly advantageous, if the noise has a long-tailed distribution (Günther, 2004). Since it is less sensitive to outliers in the data, an L_1 minimization procedure is often called ``robust inversion`` (Claerbout and Muir, 1973). A major weakness in this definition of data misfit is that the L_2-norm is sensitive to outliers. Despite this weakness, most inversion methods appeal to Gaussian statistics and adopt an L_2-norm (Rawlinson and Sambridge, 2003; Günther, 2004). The functional norm in equation 4.8 can be written as

$$\mathbf{\Phi}_d\mathbf{(m)} = [\mathbf{D}\,(\mathbf{d} - \mathbf{f(m)})]^T\ [\mathbf{D}\,(\mathbf{d} - \mathbf{f(m)})] = (\mathbf{d} - \mathbf{f(m)})^T\mathbf{D}^T\mathbf{D}(\mathbf{d} - \mathbf{f(m)})$$

$$= (\mathbf{d} - \mathbf{f}(\mathbf{m}))^T \mathbf{C}_d^{-1} (\mathbf{d} - \mathbf{f}(\mathbf{m})) \quad (4.9)$$

The product $\mathbf{D}^T\mathbf{D}$ is the inverse of the data covariance matrix $\mathbf{C}_d$ as used by Tarantola (1987) or called data weighting matrix (Rawlinson and Sambridge, 2003).

However, the inverse solution will generally be unstable and the problem must be constrained or regularized by adding a priori information or some measure of the length of the solution. A common problem with tomographic inversion is that not all model parameters will be well constrained by the data alone (i.e. the problem may be under-determined or mixed-determined). A regularization term $\mathbf{\Phi_m(m)}$ is often included in the objective function to provide additional constraints on the model parameters, thereby reducing the non-uniqueness of the solution. The regularization term is typically defined as

$$\mathbf{\Phi_m(m)} = (\mathbf{m} - \mathbf{m}^0)^T \mathbf{C}_m^{-1} (\mathbf{m} - \mathbf{m}^0) \quad (4.10)$$

where $\mathbf{C}_m$ is the a-priori model covariance matrix and also referred as a model weighting matrix. The effect of $\Phi_m\mathbf{(m)}$ is to encourage solution models $\mathbf{m}$ that are near a reference model $\mathbf{m}^0$.

Using the L_2 norm described in equations 4.9 and 4.10, the objective function $\mathbf{\Phi(m)}$ in equation 4.6 can be written as

$$\mathbf{\Phi(m)} = (\mathbf{d} - \mathbf{f}(\mathbf{m}))^T \mathbf{C}_d^{-1} (\mathbf{d} - \mathbf{f}(\mathbf{m})) + \lambda (\mathbf{m} - \mathbf{m_o})^T \mathbf{C}_m^{-1} (\mathbf{m} - \mathbf{m}^0) \longrightarrow \min \quad (4.11)$$

Gradient-based inversion methods make use of the derivatives of $\mathbf{\Phi(m)}$ at a specified point in the model space. The gradient of $\mathbf{\Phi(m)}$ is the weighted sum of the gradients of $\mathbf{\Phi_d(m)}$ and $\mathbf{\Phi_m(m)}$,

$$\frac{\partial \Phi(\mathbf{m})}{\partial \mathbf{m}} = \mathbf{G}^T \mathbf{C_d}^{-1} \left[\mathbf{d} - \mathbf{f}(\mathbf{m})\right] + \lambda \mathbf{C_m}^{-1} \left[\mathbf{m} - \mathbf{m}^0\right] = 0 \quad (4.12)$$

which also holds for the Hessian matrix (Günther, 2004) as

$$\frac{\partial^2 \Phi(\mathbf{m})}{\partial \mathbf{m}^2} = \mathbf{G}^T \mathbf{C_d}^{-1} \mathbf{G} + \frac{\partial \Phi(\mathbf{m})}{\partial \mathbf{m}} \mathbf{G}^T \mathbf{C_d}^{-1} \left[\mathbf{d} - \mathbf{f}(\mathbf{m})\right] + \lambda \mathbf{C_m}^{-1} = 0 \quad (4.13)$$

where $\mathbf{G} = \frac{\partial \mathbf{f(m)}}{\partial \mathbf{m}}$ is the matrix of partial derivatives calculated during the solution of the forward problem. Usually, the second derivative term in the Hessian matrix is neglected since it is time consuming to evaluate, and its effect is small if **d - f(m)** is small. Therefore, Eq. (4.13) can be written as

$$\frac{\partial^2 \Phi(\mathbf{m})}{\partial \mathbf{m}^2} = \mathbf{G}^{\mathrm{T}}\mathbf{C_d}^{-1}\mathbf{G} + \lambda \mathbf{C_m}^{-1} = 0 \tag{4.14}$$

Since **f** is generally non-linear, the minimization of Eq. (4.11) requires an iterative approach:

$$\mathbf{m}^{k+1} = \mathbf{m}^k + \Delta \mathbf{m}^k \tag{4.15}$$

where k is the number of iterations. A Taylor approximation of 1st order yields

$$\mathbf{\Phi}(\mathbf{m}^{k+1}) = \mathbf{\Phi}(\mathbf{m}^k + \Delta \mathbf{m}^k) \approx \Phi(\mathbf{m}^k) + \frac{\partial \Phi(\mathbf{m}^k)}{\partial \mathbf{m}} \Delta \mathbf{m}^k \tag{4.16}$$

The gradient-based inversion methods can be used to determine $\Delta \mathbf{m}^k$ in Eq. (4.15). For example, using the damped-least squares and Gauss-Newton method,

$$\frac{\partial \Phi(\mathbf{m}^{k+1})}{\partial \mathbf{m}} \approx \frac{\partial \Phi(\mathbf{m}^k)}{\partial \mathbf{m}} + \frac{\partial^2 \Phi(\mathbf{m}^k)}{\partial \mathbf{m}^2} \Delta \mathbf{m}^k = 0 \tag{4.17}$$

Substituting Eqs. (4.12 and 4.14) into Eq. (4.17) gives the quasi-Newton solution as,

$$\Delta \mathbf{m}^k = \left[\mathbf{G}^{\mathrm{T}}\mathbf{C_d}^{-1}\mathbf{G} + \lambda \mathbf{C_m}^{-1}\right]^{-1}\left[\mathbf{G}^{\mathrm{T}}\mathbf{C_d}^{-1}\left[\mathbf{d} - \mathbf{f}(\mathbf{m}^k)\right] - \lambda \mathbf{C_m}^{-1}\left[\mathbf{m}^k - \mathbf{m}^0\right]\right] \tag{4.18}$$

If $\mathbf{m}^k = \mathbf{m}^0$ (the starting model), after one iteration the estimated model parameter ($\mathbf{m}^{est}$) is

$$\mathbf{m}^{est} = \mathbf{m}^0 + \left[\mathbf{G}^{\mathrm{T}}\mathbf{C_d}^{-1}\mathbf{G} + \lambda \mathbf{C_m}^{-1}\right]^{-1}\mathbf{G}^{\mathrm{T}}\mathbf{C_d}^{-1}\left[\mathbf{d} - \mathbf{G}\mathbf{m}^0\right] \tag{4.19}$$

where $\mathbf{m}^{est}$ is the best fitting model, $\mathbf{m}^0$ is the starting model, **d** and **G** are the observed data and the kernel/sensitivity matrix, respectively, $\mathbf{C_m}^{-1}$ is the regularization or model weighting

matrix, $\mathbf{C_d}^{-1}$ is the data weighting matrix, and λ is a trade-off or regularization parameter (also called damping factor) that determines how much the data influences the model versus how much the model is constrained by the regularization. For example, for λ = 0 the solution depends only on the data and for large values the solution depends more on the regularization. It adds a constant level to the diagonal elements of the sensitivity matrix product to avoid singularity. The expressions in Eqs.4.18 and 4.19 are often referred to as Damped Least Squares (DLS) solution to the inverse problem.

Various computational methods exist to implement matrix inversions, such as, Algebraic Reconstruction Technique (ART), Simultaneous Iterative Reconstruction Technique (SIRT), Gauss-Newton method, conjugate gradient methods, etc.

A useful measure of data fit is provided by the normalized χ^2*(chi-square) and RMS* misfit functions defined by

$$X^2 = \frac{1}{N}\sum_{i=1}^{N}\left(\frac{d^i{}_{obs} - d^i{}_m}{\varepsilon_i}\right)^2 \qquad (4.20a)$$

$$RMS = \sqrt{\frac{1}{N}\sum_{i=1}^{N}\left(\frac{d^i{}_{obs} - d^i{}_m}{d^i{}_{obs}}\right)^2} \qquad i = 1,2,3,\ldots, N \qquad (4.20b)$$

where $d^i{}_m$ = f(m) is the model response, $d^i{}_{obs}$ is the set of observed data and ε_i are the observed data uncertainties (or weights). An inversion solution fits the data to the level of the noise when $\chi^2 = 1$.

4.1.2 Seismic travel time inversion and tomography

The traveltime of a seismic wave between source and receiver is solely dependent on the velocity structure (slowness) of the medium through which the wave propagates. Seismic tomography is a type of inverse modeling or inversion (Tarantola, 1987; Menke, 1989; Parker, 1994; Rawlinson and Sambridge, 2003) where the data (**d**) are traveltime arrivals and the model parameters (**m**) define velocity (slowness) variations. The two basic parameter types that are normally encountered in traveltime inversion, especially of wide-angle data, are velocity (slowness) and interface depth.

The traveltime of a seismic wave is the integral of slowness (inverse of velocity) along a ray path connecting the source and receiver. Fermat's principle states the correct ray path between two points is the one of least overall traveltime. It is most convenient to develop inversion and tomography formulas in terms of wave slowness models **s(x)**, because the pertinent equations are linear in slowness (Berryman, 1991).

Suppose we have a set of observed traveltimes $\mathbf{t}_i = (t_1, t_2, ..., t_N)$, from N source-receiver pairs in a medium of slowness **s(x)**. Let P_i be the Fermat ray path connecting the i^{th} source-receiver pair. Neglecting observational errors, we can write the traveltime of a ray in a continuous slowness or velocity medium as

$$\mathbf{t}_i = \int_{P_i} \mathbf{s}(\mathbf{x}) d\mathbf{l}^{P_i} \ , \ i = 1, 2, 3 ... N \tag{4.21}$$

Given a block model of slowness with M cells, let $\mathbf{l}_{ij}$ be the length of the i^{th} ray path through the j^{th} cell, Eq. (4.21) can then be written

$$\mathbf{t}_i = \sum_{j=1}^{M} \mathbf{l}_{ij} \mathbf{s}_j \ , \ i = 1, 2, 3, ..., N \tag{4.22}$$

We can rewrite Eq. (4.22) in matrix notation in the form of Eq. (4.1) by defining **s** into **m** and **t** into **d** for the forward modelling as follows,

$$\mathbf{t} = \mathbf{G}\mathbf{s} \tag{4.23}$$

with $\mathbf{t} = \begin{pmatrix} t_1 \\ t_2 \\ . \\ . \\ . \\ t_N \end{pmatrix}$, $\mathbf{s} = \begin{pmatrix} s_1 \\ s_2 \\ . \\ . \\ . \\ s_M \end{pmatrix}$, $\mathbf{G} = \begin{pmatrix} l_{11} l_{12} ... l_{1M} \\ l_{21} l_{22} ... l_{2M} \\ . \\ . \\ . \\ l_{N1} l_{N2} ... l_{NM} \end{pmatrix}$

Implementing a tomographic slowness (velocity) algorithm requires first break traveltime picking, slowness (velocity) model parameterization, ray tracing and segmentation (forward modelling) to produce the predicted traveltimes and the ray paths, computing residual traveltimes (error) which are the deviations between the picked and predicted traveltimes, and

velocity or slowness updating (inverse modelling) to minimize the error by adjusting the slowness (velocity) along the ray paths of the model to reduce the residual traveltimes (Fig. 4.2). Basically, this involves a forward process problem where traveltimes are calculated for any source-receiver pair and an inverse problem where the slowness or velocity is iteratively updated to generate a slowness or velocity model which provides a match with field seismic data.

Model parameterization involves discretizing the 2-D image with a number of pixels, and defining a starting velocity model from prior geological and geophysical information. The number of pixels in the image plane is the number of unknowns in the inverse problem. Choice of the pixel size is subjective. In general, the cell size needs to be small enough to resolve the smallest feature of interest. The number of source-receiver pairs determines the number of known parameters (traveltimes) for the same problem. The choice of the initial model is extremely important. A close guess can result in a good inversion.

Ray tracing and segmentation involve computing traveltimes and ray paths between the source and receiver location as well as obtaining a ray segment in each pixel crossed by a ray. Eq. (4.23) is the basic equation of forward modelling for ray tracing. The segment lengths (l_{ij}) are useful for updating the velocities during the inverse problem and also govern the under-determined or over-determined nature of the problem and image reliability. A ray density plot shows the number of ray segments within each pixel.

In nonlinear tomography or inversion problems, we are given only **t** (along with the source and receiver locations); the aim is to infer **s**, and incidently **G**. In this problem, the dependence of ray paths on the slowness distribution strongly influences the design of the inversion algorithm (Berryman, 1991). The inverse problem is solved using a variety of optimization techniques. In the standard least-squares method (see section 4.1.1 Eq. 4.19), for example, the solution for the best fitting slowness model is expressed using the formula

$$\Delta \mathbf{s}^k = [\mathbf{G}^T \mathbf{C}_d^{-1} \mathbf{G} + \lambda \mathbf{C}_m^{-1}]^{-1} \mathbf{G}^T \mathbf{C}_d^{-1} [\Delta \mathbf{t}^k] \qquad (4.24)$$

where $\Delta \mathbf{s}^k = \mathbf{s}^{k+1} - \mathbf{s}^k$ is the slowness model update; $\Delta \mathbf{t}^k = \mathbf{t} - \mathbf{G}\mathbf{s}^k$ is the deviation between the observed (picked) and the predicted travel time data.

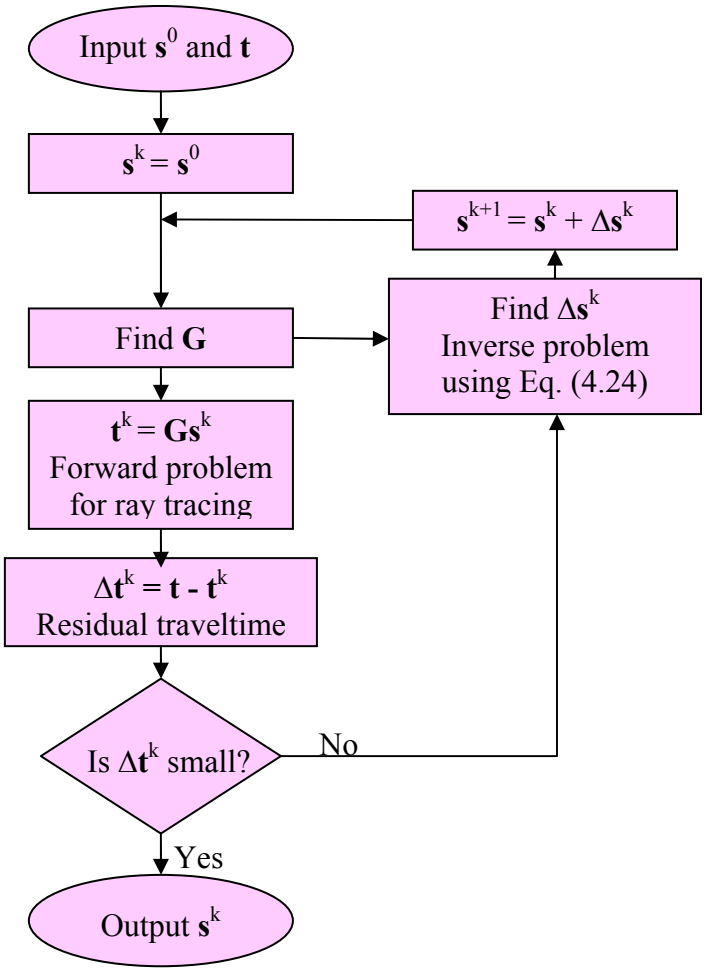

Figure 4.2 *A flowchart of an iterative nonlinear inversion algorithm for seismic traveltime inversion. Where* $\mathbf{t}$ *= set of the observed (picked) traveltime data,* $\mathbf{t}^k$ *= set of predicted traveltime data,* $\Delta\mathbf{t}^k$ *= the set of residual traveltimes (data misfits),* $\mathbf{G}$ *is the sensitivity (kernel) matrix,* $\mathbf{s}^0$ *= a set of the starting slowness model parameters,* $\mathbf{s}^k$ *= a set of the inverted slowness model estimates,* $\Delta\mathbf{s}^k = \mathbf{s}^{k+1} - \mathbf{s}^k$ *is the slowness update for every iteration and k is the number of iterations.*

4.2 Seismic refraction tomography data processing

The field data are processed using ProMAX^{TM} 2D version 1998.6 (for P-wave data) and version 2003.12.1 (for the S-wave data), a commercial processing software package from Landmark Graphics Corporation. The software applies a turning ray tomography (TRT) algorithm technique that is a velocity inversion procedure which uses turning rays (diving rays or continuously refracted direct rays) from any acquisition geometry to iteratively solve for velocity in the near surface between source and receivers (Brzostowski and McMechan, 1992; Stefani, 1995). When an area does not have well defined refractors but has a general increase of velocity with depth, many depths will be sampled by the rays and the TRT is more likely to be effective than the conventional seismic refraction method.

4.2.1 P-wave data processing

Travel time first arrival picking was performed manually for about 56376 traces of the P-wave data for the three seismic profiles along P-1, P-2, and P-3 as already shown in Fig. 3.5. Since the type of seismic data was collected using vibroseis and correlated with the sweep (see section 3.3), determining the first arrival time picks was difficult. To avoid such difficulty, we mix with a sample of traces collected using hammer sources at the same location. Accordingly, time picking was made at the positive peak of the first arrival for each trace. Fig. 4.3 shows an example of shot gathers with the picked first arrivals from the three P-wave survey lines.

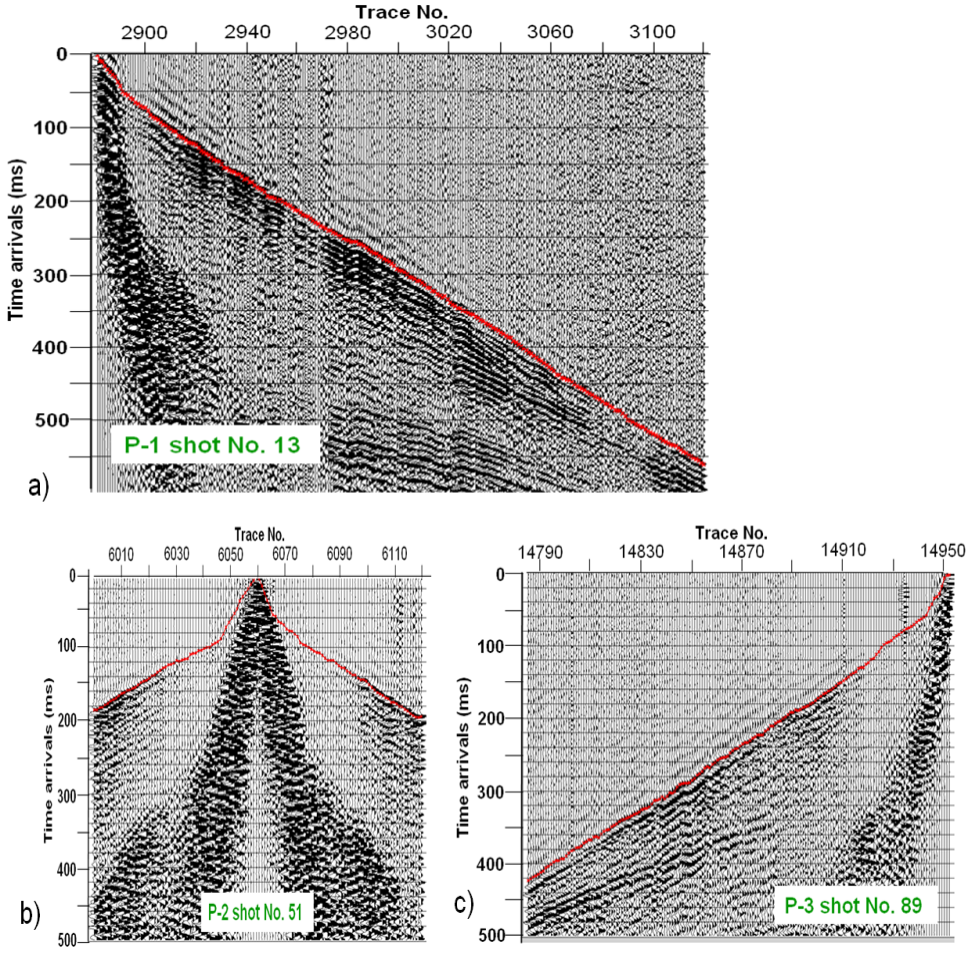

Figure 4.3 *Examples of P-wave shot gathers with picked first arrivals from profiles; a) P-1, b) P-2, and c) P-3.*

A starting interval velocity model is first produced using the `create turning ray velocity´ from the actual picked first arrival times using the flat layer theory of refracted arrivals known as slope/intercept method. Then, the velocity field is smoothed to have gradients with no constant velocity refractors. After some inversions, another starting velocity model is updated again to re-trace rays through a smoothed inverted velocity model only up to 120 m maximum

depth (Fig. 4.4) so that to give more emphasis to the shallow anomalies. The output velocity field function is edited by adding an artificial velocity below the actual last point to create a gradual gradient in the lower section of the model. This helps to stabilize the ray tracing by turning rays to the surface that go deeper than the last actual depth of the velocity field. The turning ray tomography (TRT) approach works by tracing the turning rays through an approximate starting model and more emphasis is given to the shallow part up to a maximum depth of 120 m.

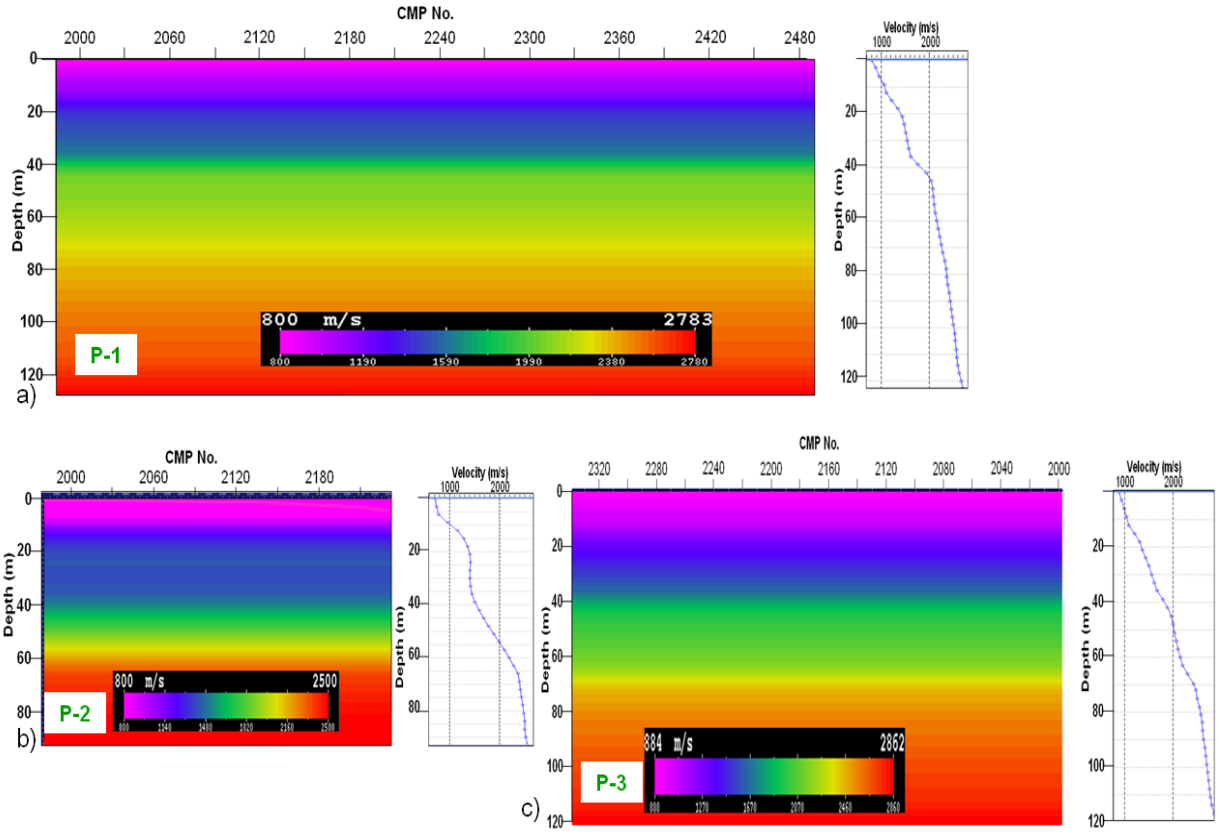

Figure 4.4 *P-wave velocity model prepared for ray tracing after some inversions; a) for P-1, b) P-2, and c) P-3.*

Rays are traced by shooting methods from the source to the receivers through a gridded starting velocity model. Since the spacing between the traces (geophones) was 5 m, the horizontal and vertical cell sizes used for the ray tracing are 5 m by 3 m to resolve the smallest feature of interest. The starting velocity or slowness model produces predicted travel time arrivals and ray paths using Eq. (4.23). Some rays fail to find a receiver as shown in Fig. 4.5. This could be possible if the velocity model is not deep enough, if the model has a negative velocity gradient, if the receiver is too close to the edge of the velocity model or if there is a shadow zone due to sharp velocity variations.

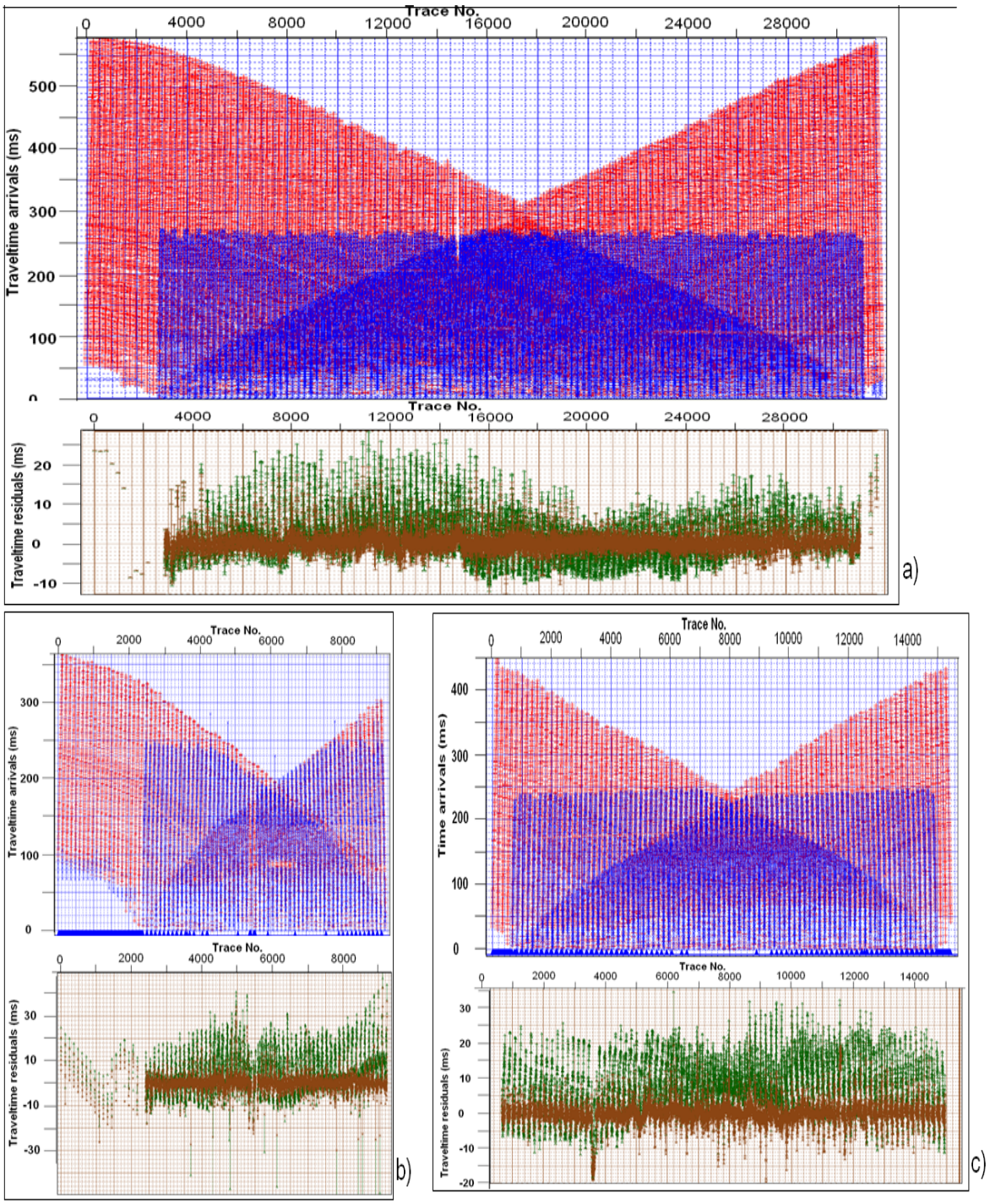

Figure 4.5 *P-wave predicted time arrivals after ray tracing (blue), picked time arrivals (red), residual times before inversion (green) and after inversion (brown) for profiles a) P-1, b) P-2, and c) P-3.*

The predicted time arrivals are subtracted from the actual picks to produce residual travel times (misfits). Positive residual travel time means the starting velocity model is too fast, negative means it is too slow. These residual travel times are used later for tomographic inversion.

Figs. 4.5 and 4.6 show the picked travel time arrivals from the data (red points), predicted travel times after ray tracing (blue points), residual times before inversion (green points) and

after inversion (brown points) for the three P-wave profiles and for the shot gather examples in Fig. 4.3, respectively.

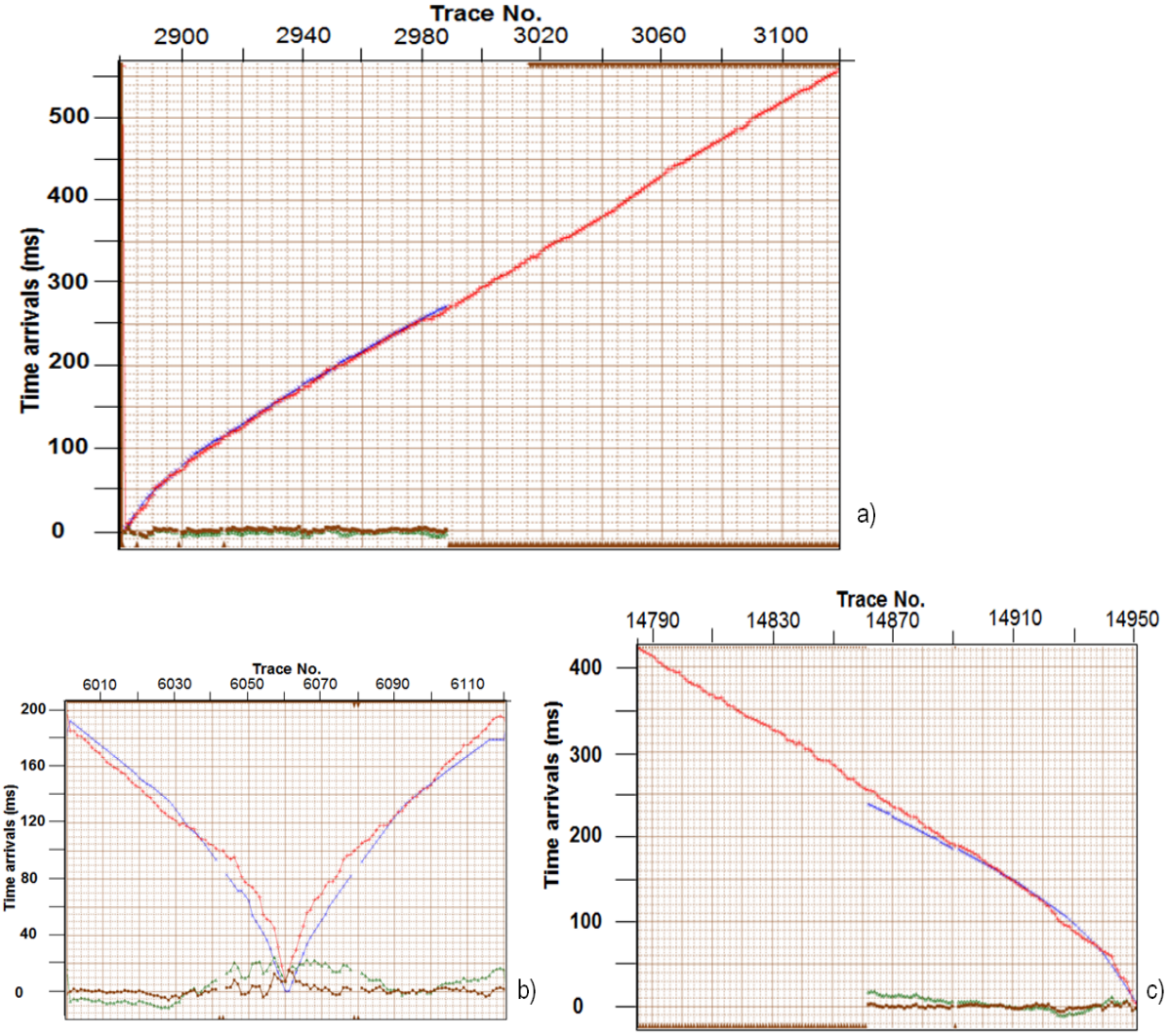

Figure 4.6 *P-wave predicted time arrivals after ray tracing (blue), picked time arrivals (red), residual times before inversion (green) and after inversion (brown) for the shot gathers in Fig. 4.3; a) from P-1, b) P-2, and c) P-3.*

In the velocity inversion (tomography) process, the initial velocity/slowness model is adjusted in order to minimize the travel time residuals as shown in Fig. 4.2. Using all the ray paths and travel time residuals in a sparse matrix inverse, the slowness or velocity field is adjusted to best reduce the travel time residuals by using equation 4.24. The inversion is run several times using different parameters such as by changing horizontal and vertical smoothing, the damping factor, limit to the maximum residual travel times to use in the inversion, and the number of iterations.

Five inversions are run for each profile using horizontal and vertical smoothing starting with 25 m by 9 m and finally with the minimum cell size 5 m by 3 m (Table 4.1). The output residual travel times are analyzed to see how well the model response (the predicted travel time arrivals) matched the observed data (picked travel time arrivals). In each inversion step the number of iterations are eight and the maximum residual travel times used are limited to less than the absolute value of 40 ms for the first inversion and up to less than 5 ms for the final inversion. The RMS (root mean square) error changed from 57%, 63%, and 127% at the beginning of the inversion (for the starting model) into 4.4%, 4.3%, and 6.6% in the final inversion for profiles P-1, P-2, and P-3, respectively (Table 4.1). Fig. 4.7 shows the P-wave velocity model of the study area obtained from the final inversion results for the three profiles.

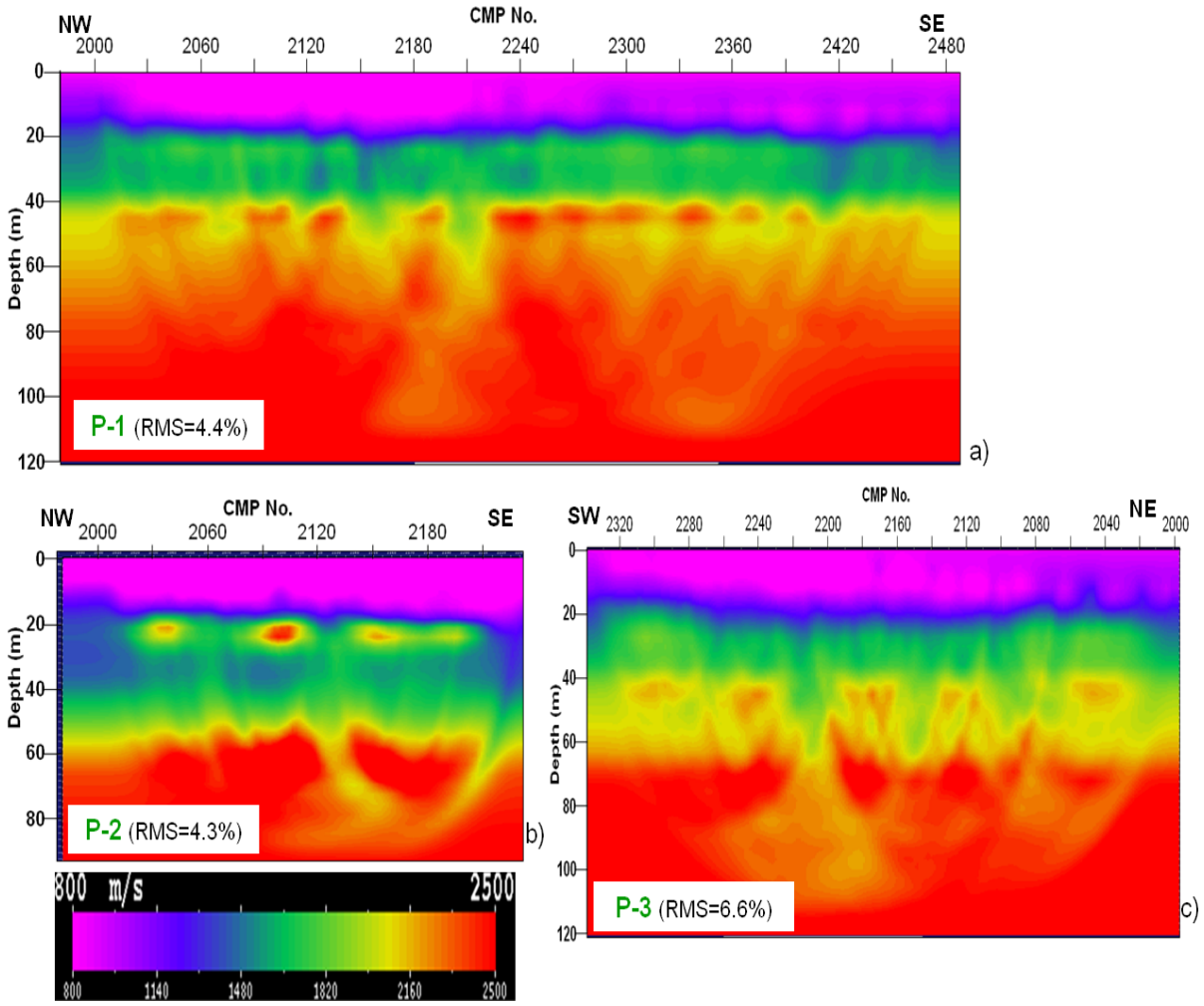

Figure 4.7 *P-wave velocity field obtained from the tomography inversion along profiles P-1(a), P-2 (b), and P-3 (c).*

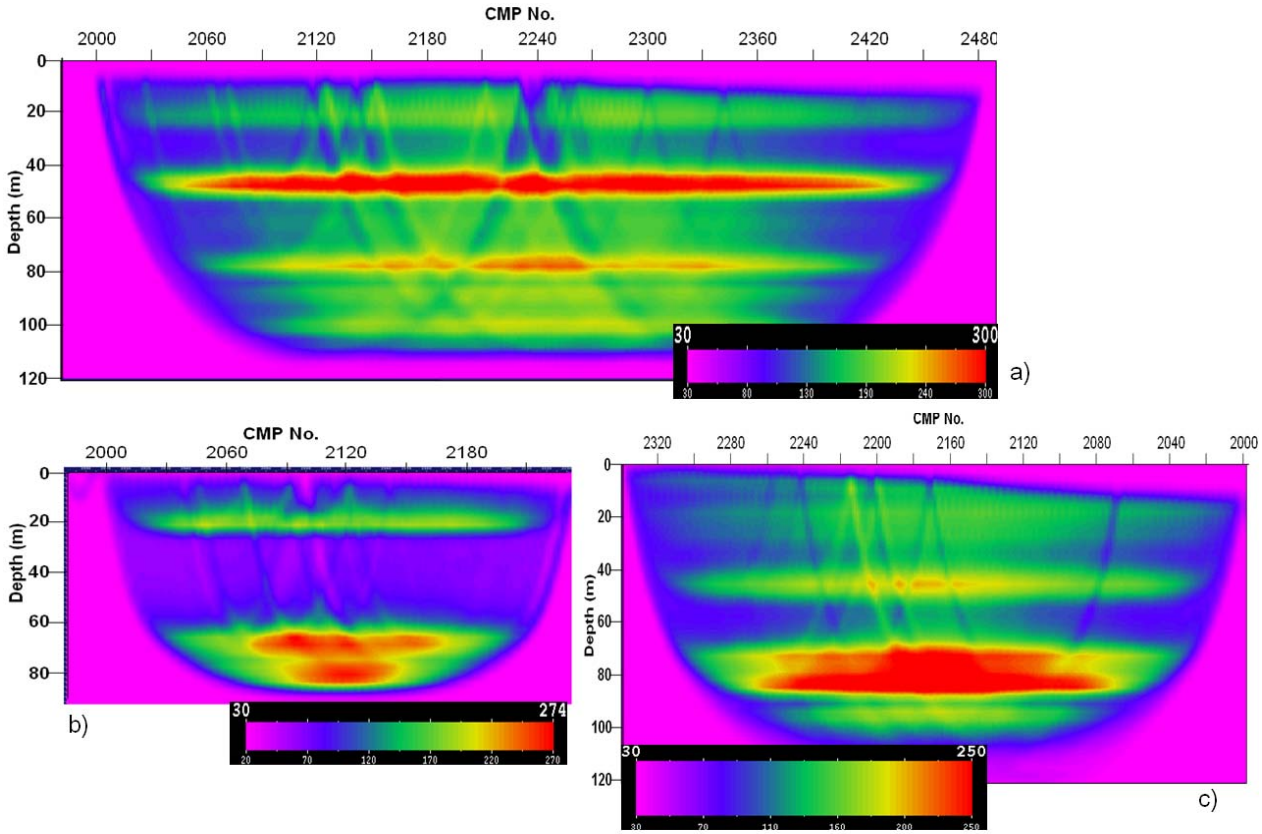

Figure 4.8 *P-wave ray density from the final tomography inversion along profiles P-1(a), P-2 (b), and P-3 (c).*

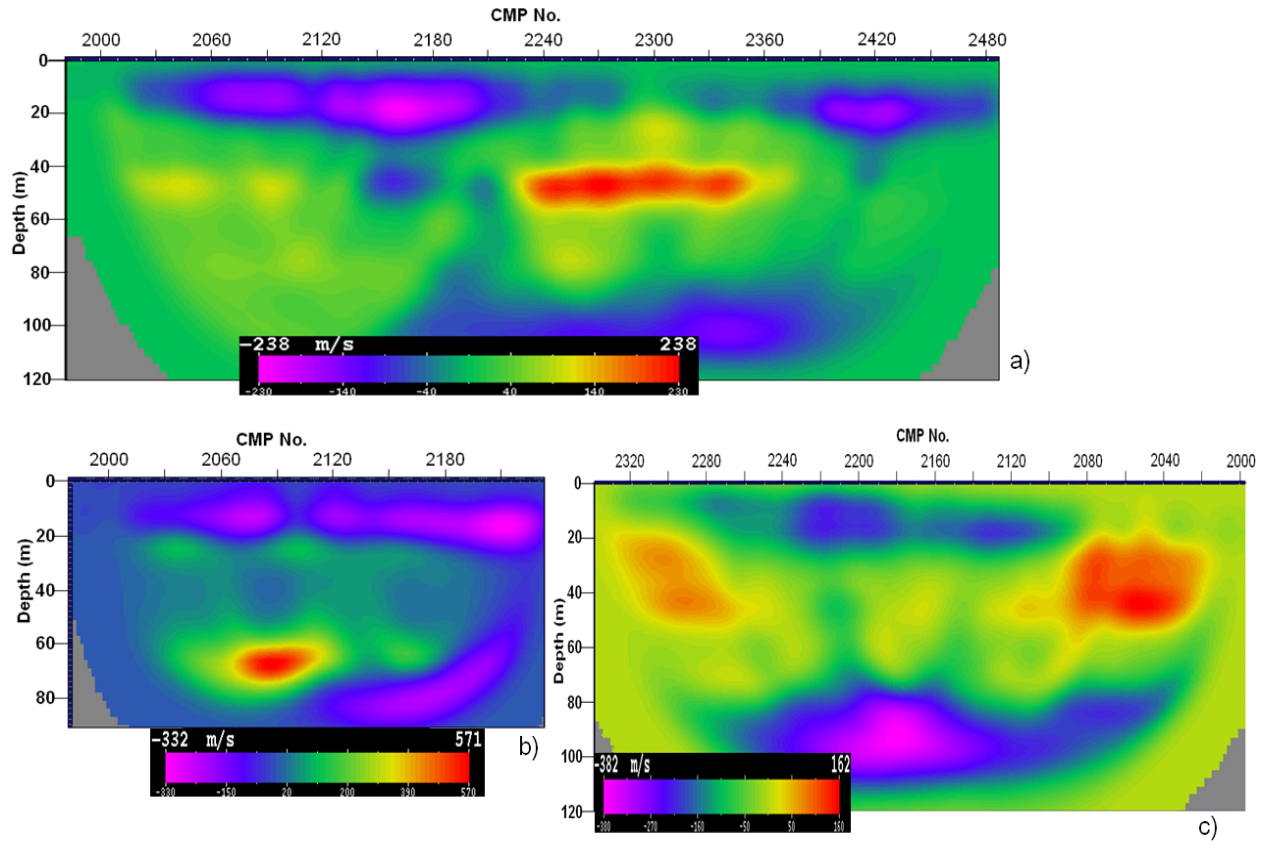

Figure 4.9 *P-wave velocity changes after the first tomography inversion for profiles P-1(a), P-2 (b), and P-3 (c).*

The ray density is also analyzed after each inversion to see whether the ray coverage had holes or not and how effective the inversion was in depth. As shown in Fig. 4.8 the maximum effective depth is up to 110 m for P-1 and P-3 profiles and 90 m for P-2. In each step, the inversion is damped by 50% in areas with a number of rays less than 30 (Table 4.1).

The output velocity field change is checked after each inversion to see whether the inversion was too aggressive or too light and to see trends of geologic features or artefacts (Fig. 4.9).

Profile	Inversion	No. of iterations	Smoothing (m)		Maximum residual travel time (ms)	Damping factor (in No. of rays)	**RMS (%)**
			Horizontal	Vertical			
P-1	1st	8	25	9	25	30	**26.3**
	2nd	8	25	6	20	30	**18.6**
	3rd	8	15	9	15	30	**14.5**
	4th	8	15	6	15	30	**12.3**
	5th	8	5	3	10	30	**8.0**
	6th	8	5	3	5	30	**4.4**
P-2	1st	8	25	9	40	30	**29.2**
	2nd	8	25	6	30	30	**15.9**
	3rd	8	15	9	20	30	**11.4**
	4th	8	15	6	18	30	**8.8**
	5th	8	5	3	15	30	**6.6**
	6th	8	5	3	10	30	**4.3**
P-3	1st	8	25	9	30	30	**23.7**
	2nd	8	25	6	20	30	**16.0**
	3rd	8	15	9	20	30	**14.3**
	4th	8	15	6	20	30	**12.8**
	5th	8	5	3	15	30	**9.9**
	6th	**8**	**5**	**3**	**10**	**30**	**6.6**

Table 4.1 *P-wave velocity inversion processing parameters.*

4.2.2 S-wave data processing

Travel time first arrival picking was performed manually for about 22080 traces of the S-wave data for the two seismic profiles along S-1 and S-2. Similar to the P-wave data, the first arrival time for the S-wave data was picked after correlation with the sweep signal and stacking of the two shots for each station. Fig. 4.10 shows examples of shot gathers with the picked first arrivals from the two S-wave profiles.

The single interval velocities derived from the stacking velocities (Fig. 3.36) were used first as a starting velocity model for the tomography inversion by modifying the interval velocities down to 100 m depth with a gradual increase in velocity gradient to stabilize the ray tracing. After some inversions, velocity models are created again by taking a single average interval velocity of the inversion results as shown in Fig. 4.11.

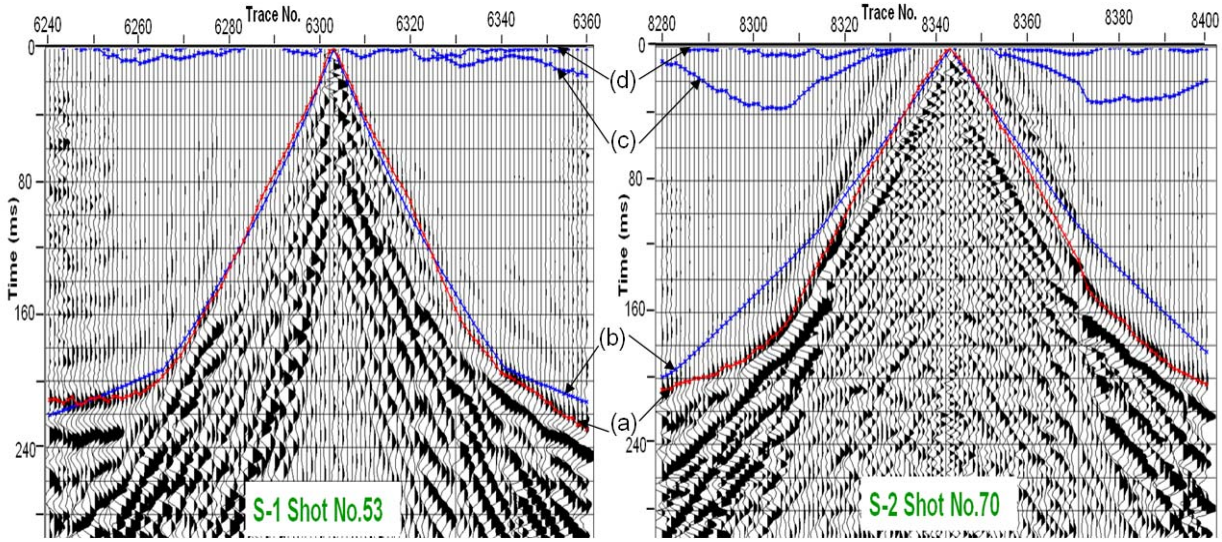

Figure 4.10 *Examples of S-wave shot gathers with picked first arrivals (a), predicted time arrivals by forward modeling (b), and the residual times before inversion (c) and after inversion (d) from profiles S-1and S-2.*

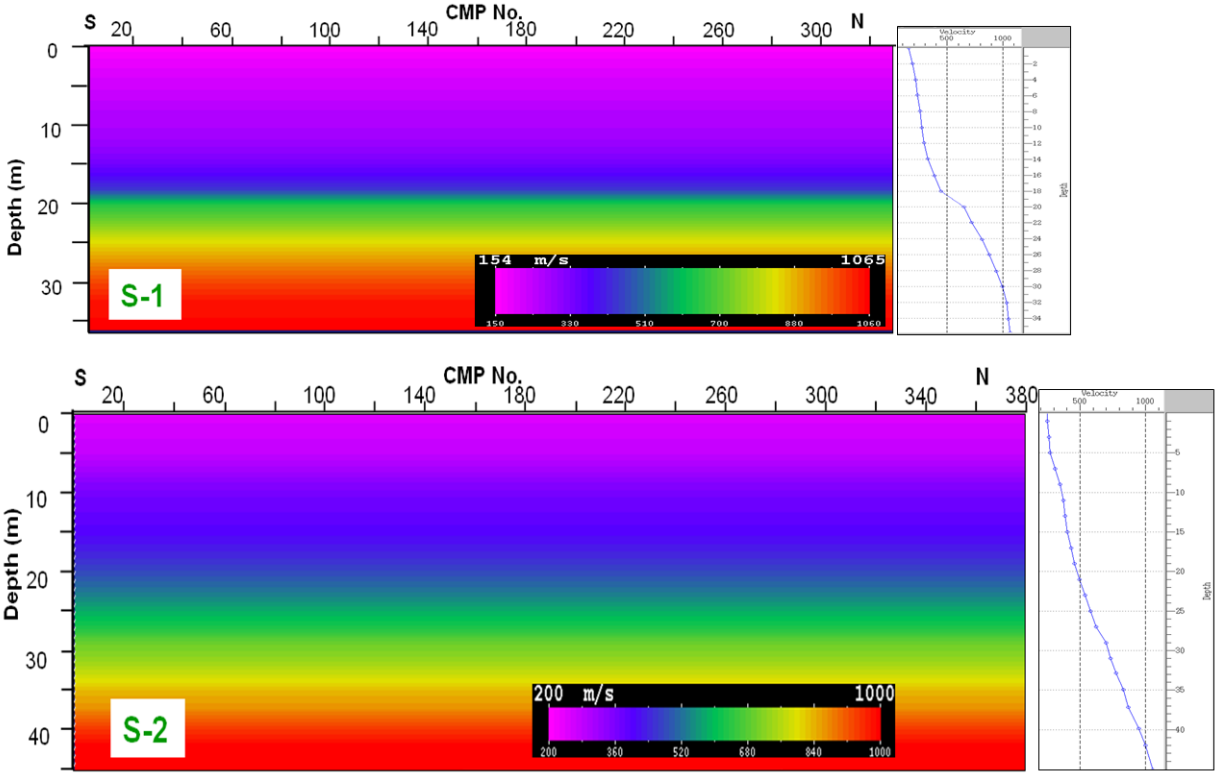

Figure 4.11 *S-wave starting velocity models used for ray tracing for profiles S-1 and S-2.*

Since the trace/geophone spacing is 1 m for the S-wave data, rays are traced by shooting methods from the source to the receivers through a gridded starting velocity model with a horizontal and vertical cell size of 1 m by 1 m in order to resolve the smallest feature of interest. The predicted time arrivals are subtracted from the actual picks after ray tracing to compute for the residual travel times. Fig. 4.12 shows the S-wave picked time arrivals, predicted time arrivals after ray tracing, residual times before inversion and after inversion for profiles S-1 and S-2.

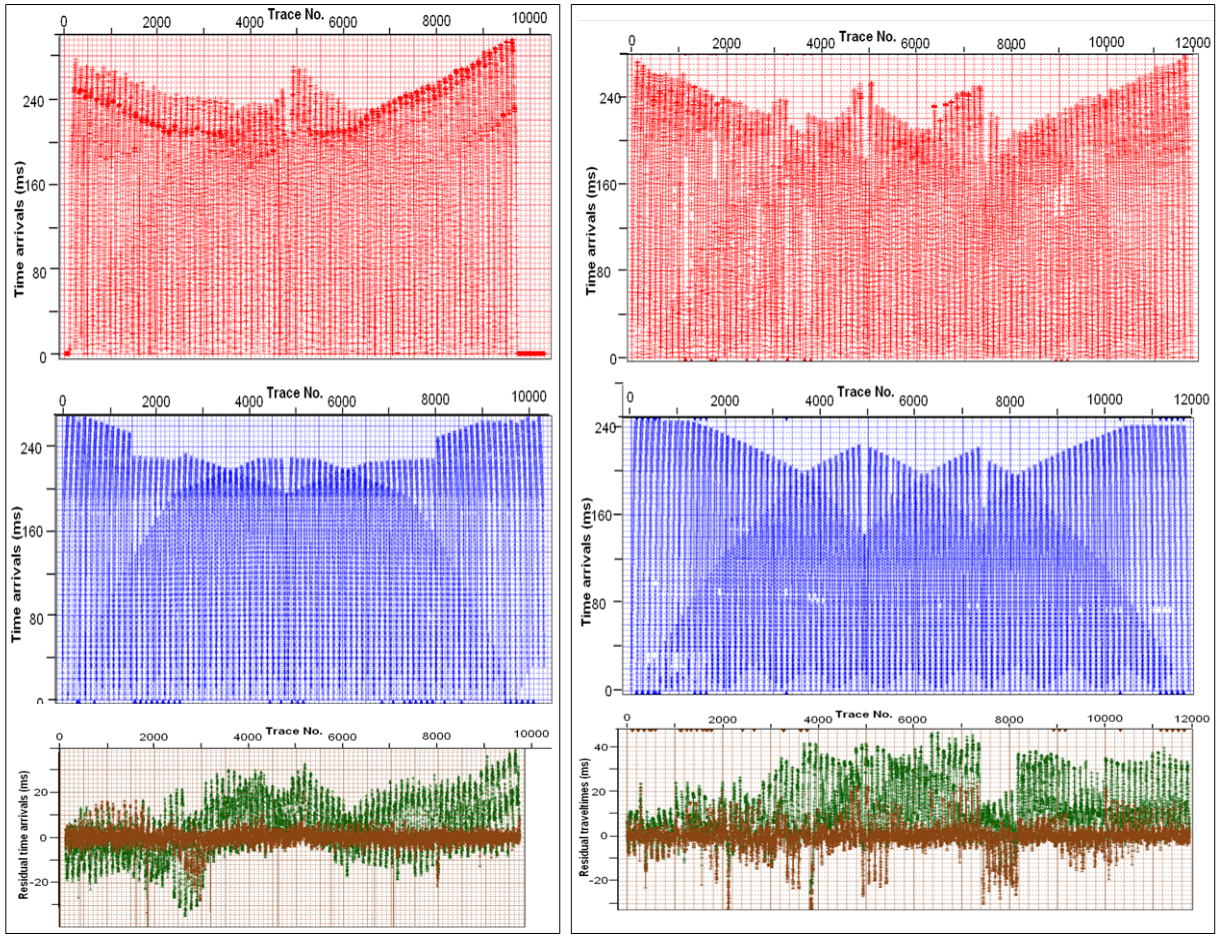

Figure 4.12 *S-wave picked time arrivals (red), predicted time arrivals after ray tracing (blue), residual times before inversion (green) and after inversion (brown) for profiles (a) S-1 and (b) S-2.*

Four inversions are run for each profile using horizontal and vertical smoothing of 3 m by 2 m, 2 m by 1 m, 3m by 1 m, and finally the minimum cell size 1 m by 1 m (Table 4.2). The output residual travel times are analyzed after each inversion to see how well the predicted travel time arrivals matched the picked travel time arrivals. In each inversion step the number of iterations are eight and the maximum residual travel times used are limited to less than the

absolute value of 40 ms for the first inversion and up to less than 5 ms for the final inversion. The RMS (root mean square) error changed from 144% and 300% at the beginning of the inversion for the starting model into 5.7% and 4.0% in the final inversion for profiles S-1 and S-2, respectively (Table 4.2). Fig. 4.13 shows the S-wave velocity model of the study area obtained from the final inversion results for the two profiles.

Profile	Inversion	No. of iterations	Smoothing (m)		Maximum residual travel time (ms)	Damping factor (in No. of rays)	**RMS (%)**
			Horizontal	Vertical			
S-1	1st	8	3	2	40	10	**12.3**
	2nd	8	2	1	30	10	**10.8**
	3rd	8	3	1	20	10	**10.1**
	4th	8	1	1	10	10	**5.7**
S-2	1st	8	3	2	40	10	**43.3**
	2nd	8	2	1	25	10	**36.9**
	3rd	8	3	1	20	10	**32.9**
	4th	8	1	1	10	10	**11.1**
	5th	**8**	**1**	**1**	**5**	**10**	**4.0**

Table 4.2 *S-wave velocity inversion processing parameters.*

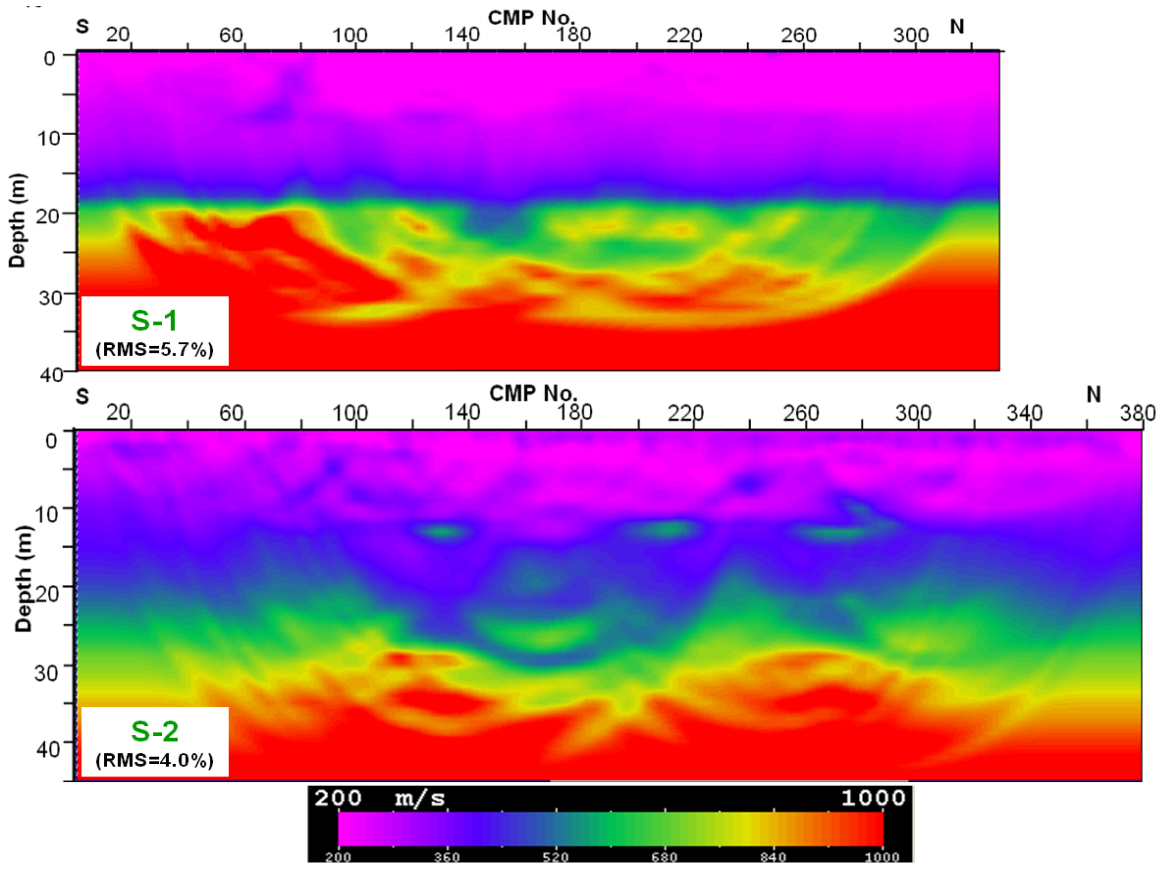

Figure 4.13 *S-wave velocity field obtained from the tomography inversion along profiles S-1 and S-2.*

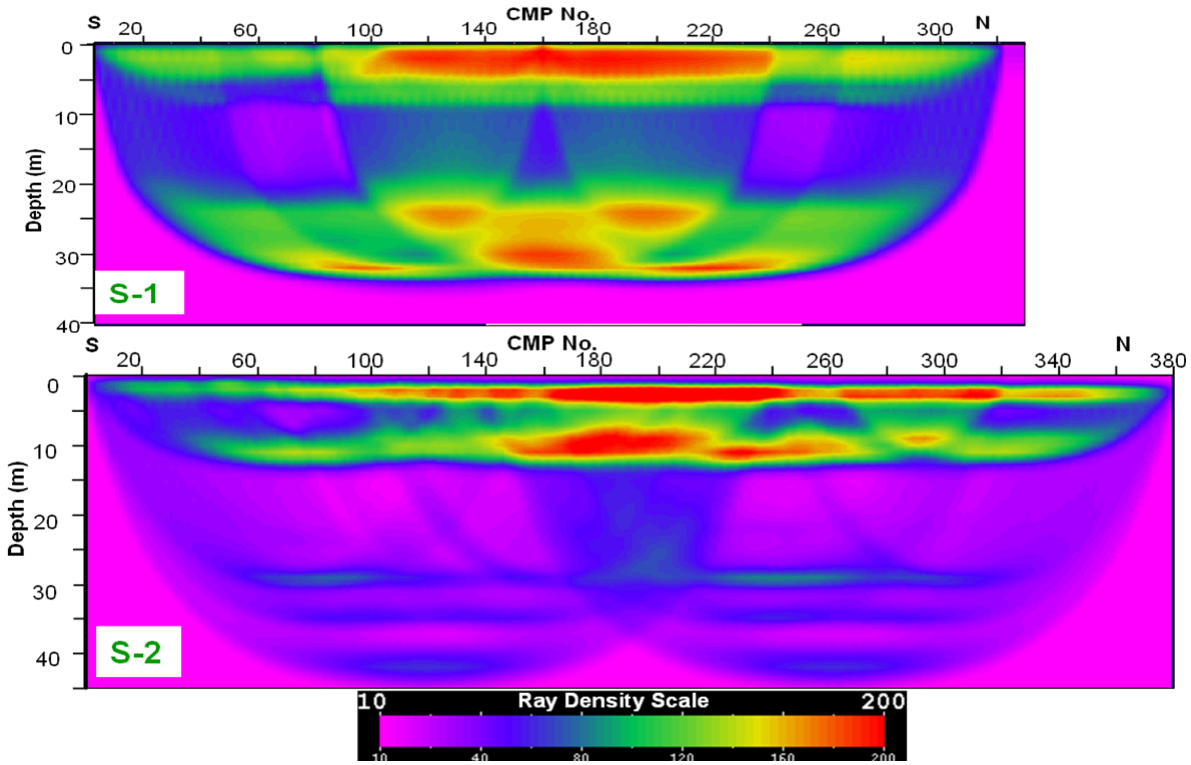

Figure 4.14 *S-wave ray densities from the final tomography inversion along profiles S-1and S-2.*

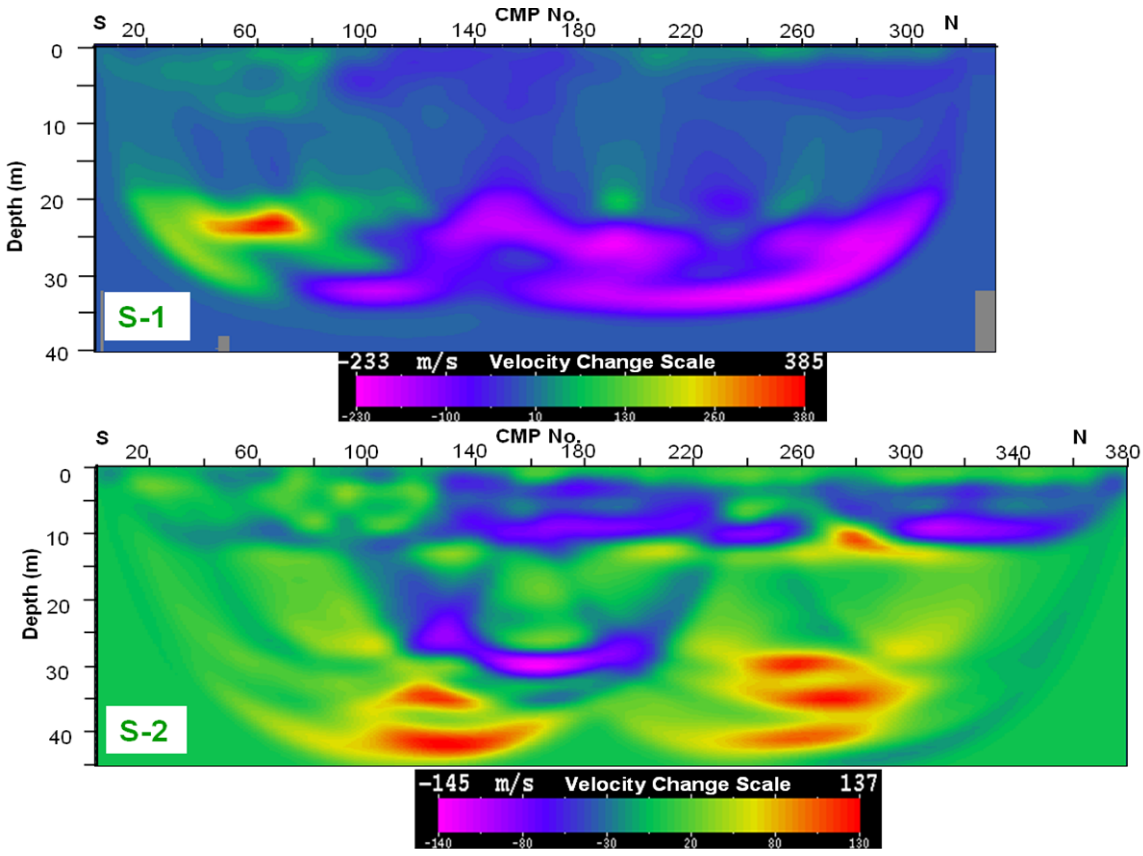

Figure 4.15 *S-wave velocity changes after the first tomography inversion along profiles S-1 and S-2.*

The ray density is also analyzed after each inversion to see whether the ray coverage had holes or not and how effective in depth was the inversion. As shown in Fig. 4.14 the

maximum effective depth is up to 35 m for S-1 and 45 m for S-2. In each inversion step, the inversion is damped by 50% in areas with a number of rays less than 10.

The output velocity field change is checked after each inversion to see whether the inversion was too aggressive or too light and to see trends of geologic features or artefacts (Fig. 4.15).

4.3 Results and interpretations of seismic refraction tomography

Before interpreting the results, it is important to critically anticipate artifacts that may be caused by lack of ray coverage. Also smoothing of the data is very important. A single average interval velocity in depth is derived from the 2D tomography section to interpret the number of velocity layers in the study area (Figs. 4.16 and 4.17).

According to the P-wave tomography results, five velocity layers are interpreted by comparing the three P-wave profiles (Fig. 4.16). The first layer reaches down to 15 m depth and has P-wave velocities ranging from 618 – 909 m/s. The second layer shows small thickness ranging from 15 – 21 m depth and exhibits P-wave velocities ranging from 1021 – 1317 m/s. The third layer from 21 – 42 m depth has P-wave velocities ranging from 1395 – 1892 m/s. The fourth layer from 42 – 63 m depth has P-wave velocities ranging between 1657 m/s and 2382 m/s. Finally, the fifth layer is below 63 m depth which exhibits P-wave velocities ranging from 2171- 2736 m/s.

In a similar way, four velocity layers are interpreted from the S-wave tomography results (Fig. 4.17). The first layer extends down to 16 m depth (S-1) and has S-wave velocities ranging from 152 – 309 m/s. The second layer is from 12 m (S-2) to 20 m depth, and has S-wave velocities between 354 m/s and 444 m/s. The third layer from 20 m to 40 (from S-2) m depth has S-wave velocities ranging from 475 - 942 m/s. A fourth layer S-wave velocity contrast is observed below 40 m depth from S-2 profile ranging between 1009 m/s and 1063 m/s.

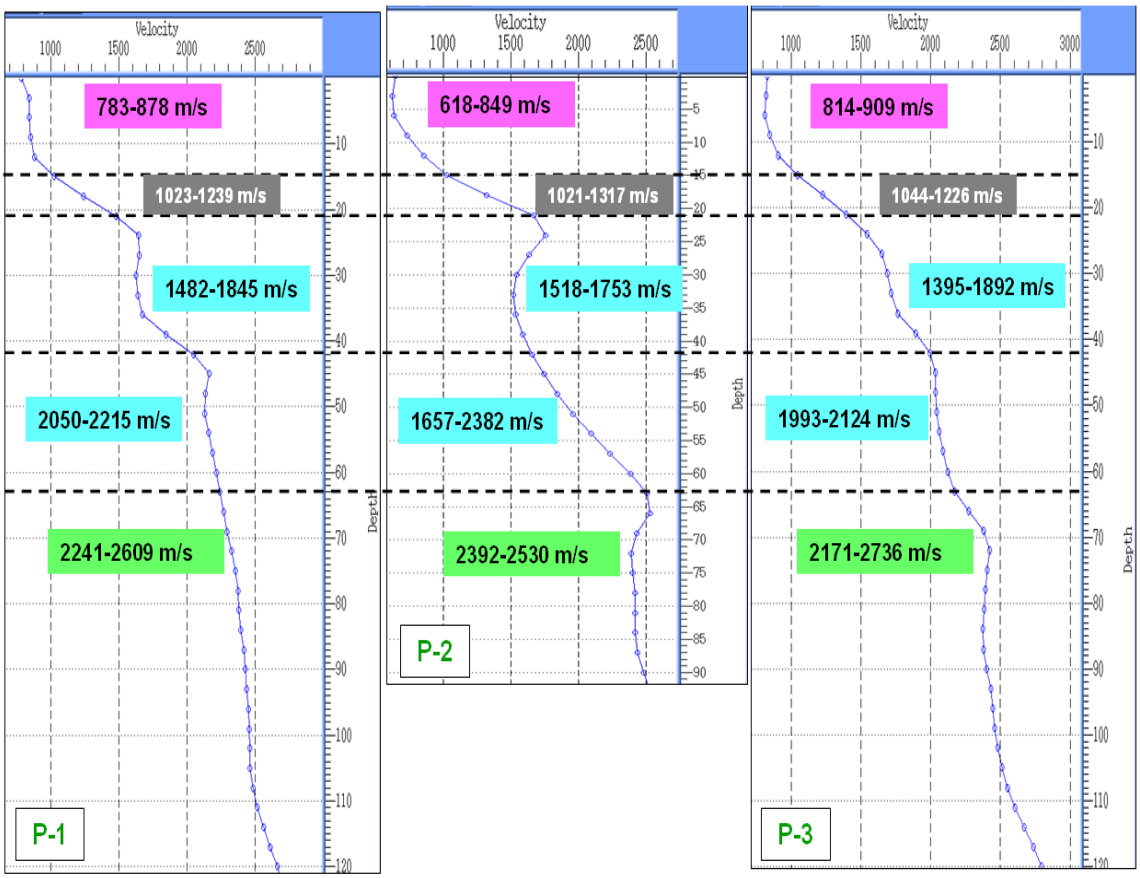

Figure 4.16 *P-wave single average interval velocities in depth after the final inversion for layer interpretation along the three profiles P-1, P-2, and P-3.*

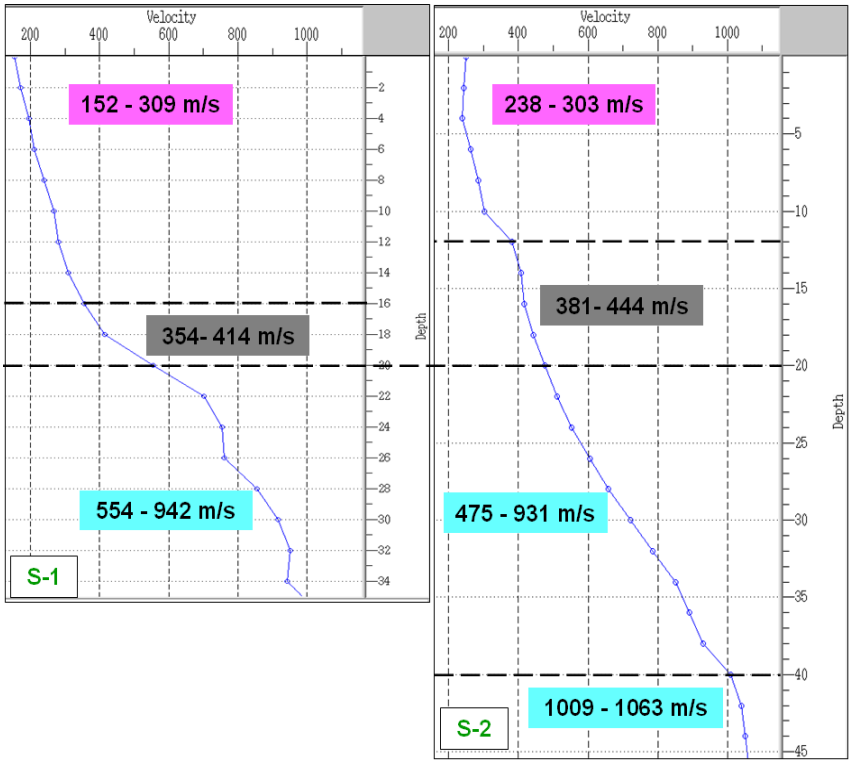

Figure 4.17 *S-wave single average interval velocity in depth after the final inversion for layer interpretation along profiles S-1 and S-2.*

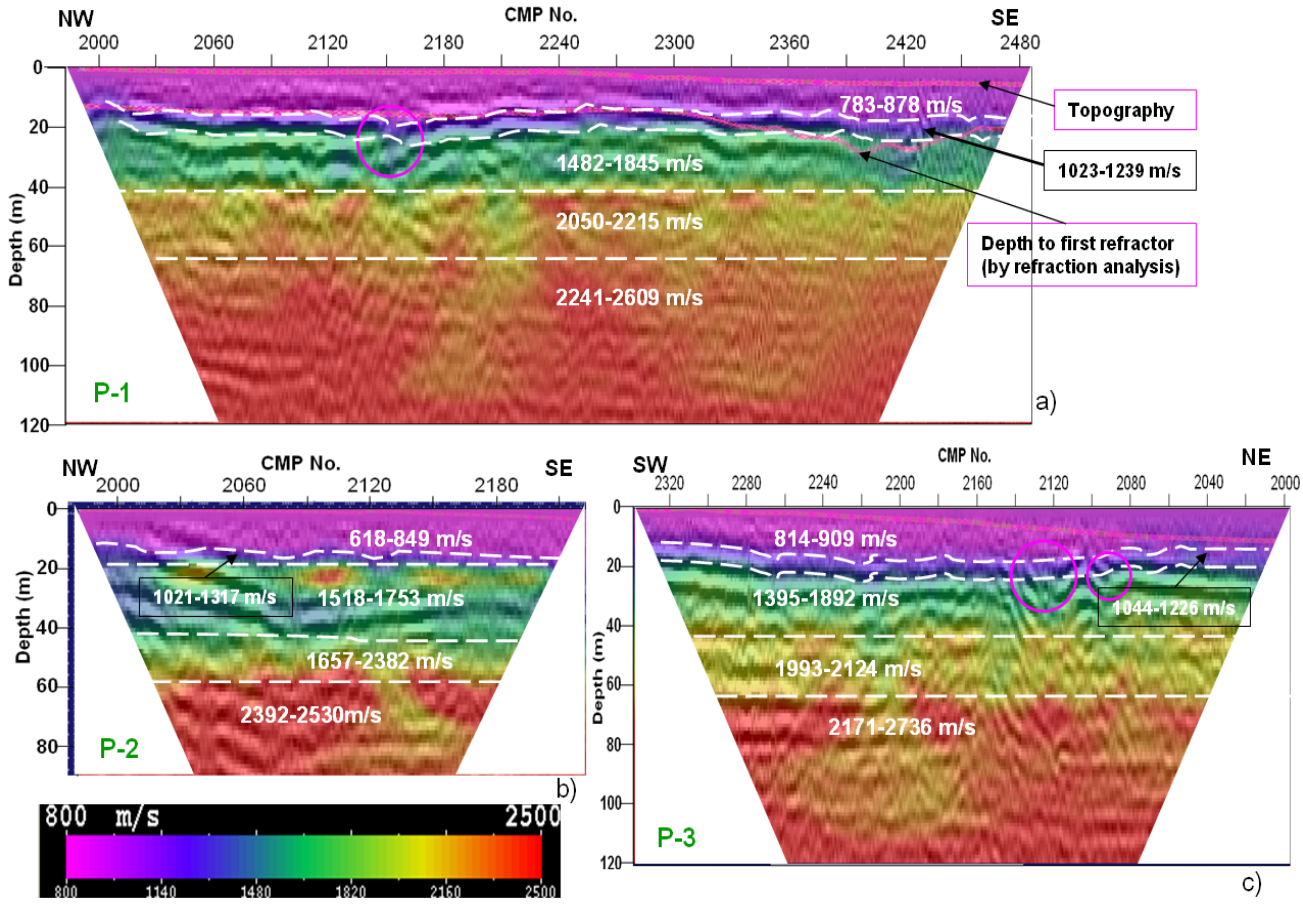

Figure 4.18 *P-wave velocity field interpreted results obtained from the tomography inversion over the 2D reflection section along profiles; (a) P-1, (b) P-2 and (c) P-3. Purple ellipses show the reflection discontinuities.*

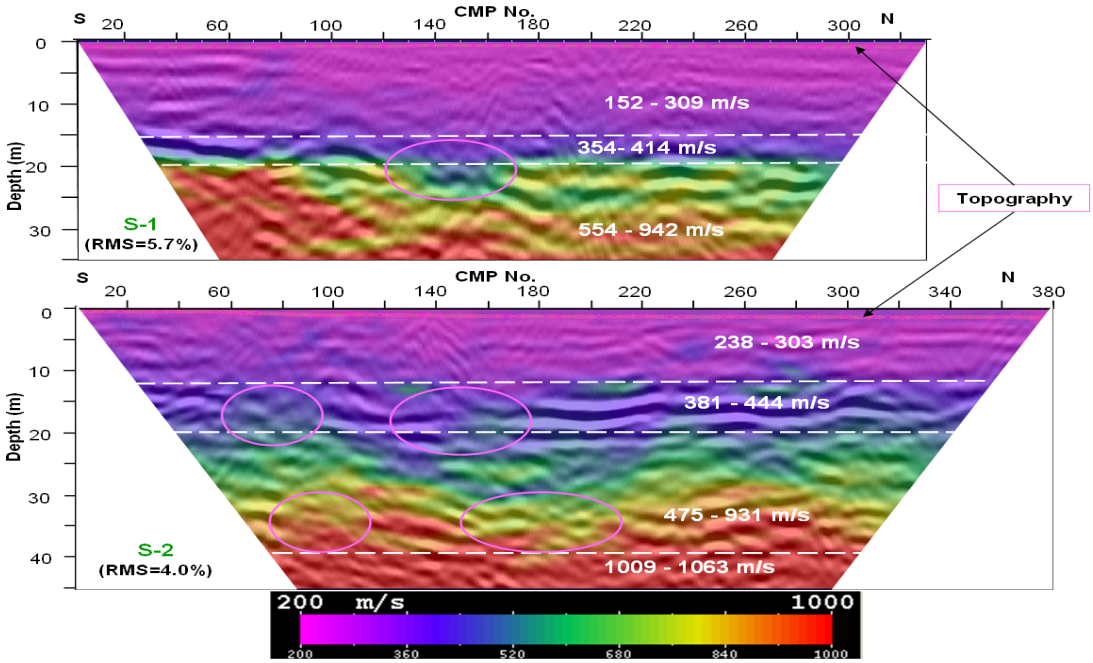

Figure 4.19 *S-wave velocity field interpreted results obtained from the tomography inversion over the 2D reflection section along profiles S-1 and S-2. Purple ellipses show the reflection discontinuities.*

From the P- and S-wave 2D tomography sections strong velocity contrasts are observed at about 20 m depth and interpreted as the top of the upper Cretaceous chalk layer, which is overlain by the Quaternary sediments. Relatively low velocity zones are observed laterally on top of the upper Cretaceous chalk layer that coincides to the reflection discontinuities (Figs. 4.18 and 4.19). This low velocity zones could be due to the collapse of the till/clay layer into the soluble chalk layer or clay filled chalk dissolution zones.

Based on the geology and integrated results of the reflection sections and velocity tomography for both the P- and S-waves the five layers are interpreted as sandy dominant sediments, till/clay rich sediments, the top of the upper Cretaceous chalk (less compacted), hard (compacted) chalk, and salt water intrusion inside the chalk layer. Table 4.3 summarizes the depth interpretations and velocity distributions of both P- and S-waves for each lithologic layer.

Layer	Depth	P-wave velocity (m/s)	S-wave velocity (m/s)	Lithology
1	0 - 15	618 - 909	152 - 309	Sandy sediments
2	15 - 20	1021 - 1317	354 - 444	Till/clay
3	20 - 40	1395 - 1892	475 - 942	Soft chalk
4	40 - 63	1657 - 2382	1009 - 1063	Hard chalk
5	> 63	2171 - 2736		Chalk + saline water

Table 4.3 *Summary of P- and S-wave velocities and lithologic interpretation.*

5 ELECTRICAL RESISTIVITY IMAGING

DC resistivity surveys are often the most suitable geophysical methods for solving environmental and engineering problems, which are frequently related to 2D or 3D geologic features. The aim of a 2D resistivity survey at the earth surface is to provide detailed information about the lateral and vertical resistivity distribution in the ground. Since the principles applied are similar to those of computer tomography in medicine or seismic tomography in seismology, such resistivity investigations are also called electrical resistivity imaging (tomography).

5.1 Fundamentals of DC resistivity

The principle of electrical resistivity imaging is based on the injection of a direct current (DC) to the earth's subsurface and measurement of the induced potential difference or voltage. Electric current (the flow of electric charges) is pumped to the ground by a driving force called voltage (potential difference) from a battery or generator. When both the positive and negative terminals of the DC source voltage are attached to the ground using conductive wires (called electrodes), electrons start to flow through the earth's subsurface from the negative terminal to the positive terminal of the DC source (conventionally the current direction is the reverse). A measure of the material (earth) to oppose the passage of the electric current is called electrical resistance and like any other semi conductor materials, the earth is acting as a resistor.

Ohm's law

According to Ohm's law, the current (I) through a conductor between two points is directly proportional to the potential difference or voltage (V) across the two points, and inversely proportional to the resistance (R) between them. Mathematically,

$$I = \frac{V}{R} \tag{5.1}$$

Suppose the resistor is made from a rectangular bar of length L and square cross-sectional area A. We can represent the electric current flowing through this resistor by a uniform

distribution of charges moving along parallel paths from one end to the other. The resistance R of this resistor is described in terms of the length L of the path followed by a charge, the cross sectional area A over which the charges are uniformly distributed, and the resistivity ρ, which is a physical property of the substance used to make the resistor

$$R = \rho \frac{L}{A} \tag{5.2}$$

Lengthening the resistor so that charges must travel longer paths through it can increase the resistance and decreasing the cross-sectional area can also impede the movement of charges by crowding them into a smaller volume.

Suppose that we make up an electric circuit in which the earth is a homogeneous resistor. Because the resistivity is assumed to be uniform, current moves away from the source, radiating outward and uniformly in all directions through a hemispherical zone. At a distance r from the source, the current has moved across the area of $2\pi r^2$, which is the surface of the hemisphere. According to Eq. (5.2), the resistance R can be expressed by the product of resistivity and the distance r that the current has travelled divided by the area $2\pi r^2$ across which it must flow:

$$R = \rho \frac{r}{2\pi r^2} = \frac{\rho}{2\pi}\left(\frac{1}{r}\right) \tag{5.3}$$

Let us connect electrodes at two different locations of the earth's surface to the battery terminals as shown in Fig 5.1. The electrode connected to the positive terminal is called the source (C_1), and the electrode connected to the negative terminal is the sink (C_2). Because of the difference in potential between these electrodes, current is compelled to flow along paths leading from the source to the sink. To determine the pattern of three-dimensional current flow in the earth, let us begin by considering the effects of the source and the sink separately and combine them later.

The source electrode is positively charged. Therefore, it repels positive electric charges, pushing them outward into the ground. The implication is that electric current flows outward

from the source into the ground. The change in potential resulting from the flow of current through the hemispherical resistor can be found from Ohm's law as

$$V = IR = \frac{I\rho}{2\pi}\left(\frac{1}{r}\right) = V_o - V_r \tag{5.4}$$

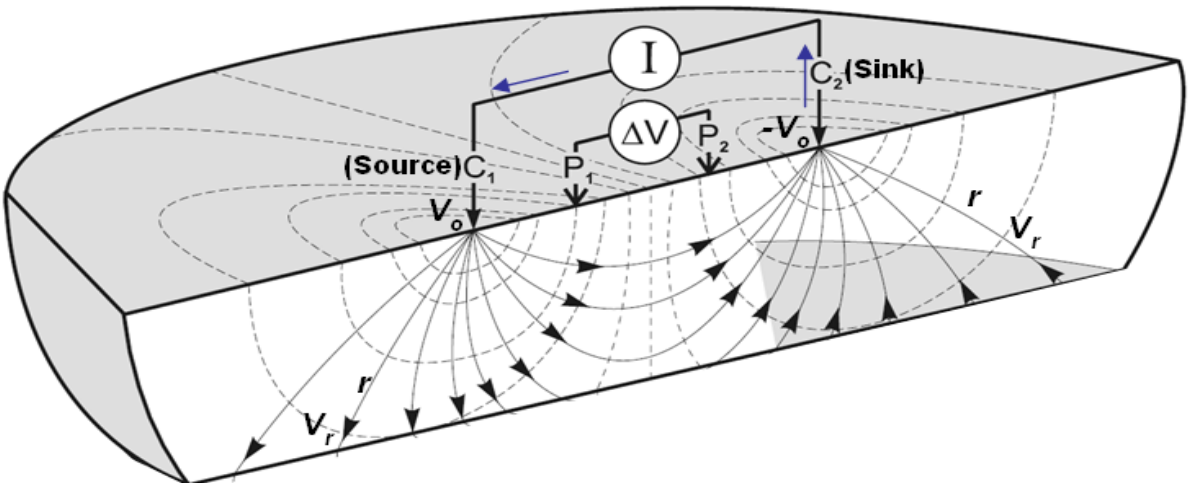

Figure 5.1 *Current flow (solid lines) radiating out from a source electrode (C_1) and converging on a sink electrode (C_2) and equipotential surfaces (dashed lines) at P_1 and P_2. Modified after Knödel et al. (2007).*

Equation (5.4) expresses the difference between the electric potential V_o at the source and the electric potential V_r at any point in the ground at distance r from the source. The electric potential related to current flowing from the source is the same everywhere on the surface of the hemisphere of radius r, which is called an equipotential surface.

If the potential at the source is V_o, the potential at the sink will be $-V_o$, for it is connected to the negative terminal of the battery. Similarly, the potential difference due to the effect of the sink electrode (C_2) between the electric potential $-V_o$ of the sink and the potential V_r at all points at distance r away from the sink, is

$$-V = IR = \frac{I\rho}{2\pi}\left(\frac{1}{r}\right) = V_r - V_o \tag{5.5}$$

Equations (5.4) and (5.5) describe the effects of the source and the sink separately by ignoring interference of the other. But to find the electric potential V at a point in the ground, we must combine the contributions of the source and sink because they are the positive and negative current sources. For example, the potential value at P_1 in the medium (Fig. 5.1) from the pair of electrodes using equations 5.4 and 5.5, is given by

$$V_{p1} = \frac{I\rho}{2\pi}\left(\frac{1}{r_{c1p1}} - \frac{1}{r_{c2p1}}\right) \tag{5.6}$$

where r_{c1p1} and r_{c2p1} are the distances to the point P_1 from the source electrode (C_1) and the sink electrode (C_2) as shown in Fig. 5.1.

The resistivity measurements are normally made by injecting current into the ground through two current electrodes C_1 and C_2, and measuring the resulting voltage difference (ΔV) at two potential electrodes P_1 and P_2 as shown in Fig 5.1. The potential difference is then given by

$$\Delta V = V_{p1} - V_{p2} = \frac{I\rho}{2\pi}\left(\frac{1}{r_{c1p1}} - \frac{1}{r_{c1p2}} - \frac{1}{r_{c2p1}} + \frac{1}{r_{c2p2}}\right) \tag{5.7}$$

Rearranging Eq. (5.7) for the resistivity, it becomes

$$\rho_a = K\frac{\Delta V}{I} \tag{5.8}$$

where $K = \left[\frac{2\pi}{\frac{1}{r_{c1p1}} - \frac{1}{r_{c1p2}} - \frac{1}{r_{c2p1}} + \frac{1}{r_{c2p2}}}\right]$ is called the geometric factor which depends on the arrangement of the four electrodes. After arranging the distances between the current and potential electrodes according to some well-known configurations one can determine the resistivity of the ground. The actual field surveys are invariably conducted over a layered earth (inhomogeneous medium) therefore the resulting resistivity obtained using Eq. (5.8) for any of the different types of configurations is called apparent resistivity (ρ_a) that constitutes a weighted average of the true resistivity.

Electrode configurations (arrays)

The most common electrode arrays used in resistivity surveying are Wenner (alpha, beta, and gamma types), Schlumberger, dipole-dipole, pole-pole, or pole-dipole (Fig. 5.2). In Wenner electrode array the spacing between all electrodes is equal and conventionally denoted by the letter ``a``. Thus the geometric factor, for example, for the Wenner-alpha becomes $K=2\pi a$. In the case of Schlumberger array, a symmetrical distribution of current and potential electrodes

about a central point is employed. But the potential electrodes are spaced much more closely than the current electrodes. In the dipole-dipole arrangement, the potential electrodes and the current electrodes function independently. Both sets tend to be fairly closely spaced with a significant distance between the sets. Since cable lengths between the electrodes may be short, it is much easier to place the potential electrodes at large distances from the current electrodes, thereby facilitating deep investigations.

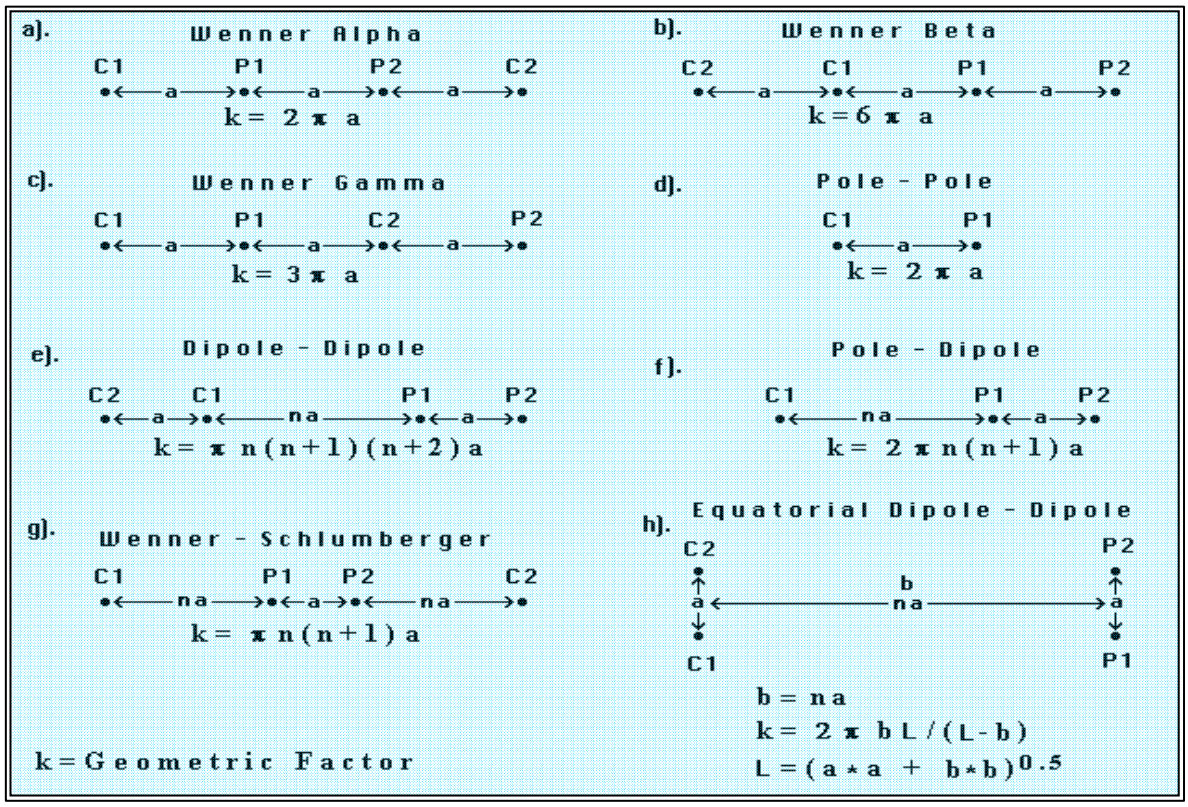

Figure 5.2 *Common arrays used in resistivity surveys and their geometric factors from Loke (2004).*

The dipole-dipole, pole-dipole and Wenner-Schlumberger arrays have two parameters, the dipole length "a" and the dipole separation factor "n". While the "n" factor is commonly an integer value, non-integer values can also be used.

Electrical resistivity surveying procedures

Electrical resistivity surveys could be 1-D, 2-D or 3-D. The 1-D resistivity method has its origin in the 1920's due to the work of the Schlumberger brothers and for approximately the next 60 years, vertical electrical sounding (VES) were normally used for quantitative interpretation (Loke, 2004). In this method, the centre point of the electrode array remains

fixed, but the spacing between the four electrodes is increased (Schlumberger array) to obtain more information about the deeper sections of the subsurface. The greatest limitation of the resistivity sounding method is that it does not take into account lateral changes in the layer resistivity. Another classical survey technique is the profiling method. In this case, the spacing between the four electrodes remains fixed, but the entire array is moved along a straight line (Wenner array). This gives some information about lateral changes in the subsurface resistivity, but it cannot detect vertical changes in the resistivity. The interpretation of data from profiling surveys is mainly qualitative and if values are obtained along several parallel profiles, a contour map of apparent resistivity can be prepared.

At present, field techniques and equipment to carry out 2D and 3D resistivity surveys are fairly well developed. 2D electrical imaging/tomography surveys are usually carried out using a large number of electrodes connected to a multi-core cable along a single survey line. Relative to the 1D, a more accurate model of the subsurface is a 2D model where the resistivity changes in the vertical direction as well as in the horizontal direction along the survey line can be observed. In this case, it is assumed that resistivity does not change in the direction that is perpendicular to the survey line. For surveys over geological bodies, 3D effects induce artefacts in 2D resistivity images. Therefore, a 3D resistivity survey and interpretation model is more accurate. However, at the present time, 2D surveys are the most practical economic compromise between obtaining very accurate results and keeping the survey costs down (Dahlin 1996; Loke, 2004).

The measured apparent resistivity values can be shown as a pseudo-section, which involves an arbitrary allocation of the position of the apparent resistivity data points. The pseudo-section does not reflect the actual resistivity distribution in the subsurface, because the potential fields are deformed due to heterogeneity and topographical effects. Therefore, 2D and 3D inversion algorithms are used to calculate a true resistivity model from the apparent resistivity data.

5.2 Inversion of 2D DC resistivity data

In electrical resistivity imaging, the aim of inversion is to reconstruct a true resistivity distribution in the subsurface by creating a resistivity model, which has a model response that is similar to the measured apparent resistivity data. To minimize non-linearity and to impose

positivity, the model parameters $\mathbf{m}_j$ and data $\mathbf{d}_i$ are the logarithms of the true resistivities and the apparent resistivities, respectively.

That is, $\mathbf{d}_i = (log\rho_{a1}, log\rho_{a2}, log\rho_{a3}, ..., log\rho_{aN})^T$ for N number of observed data and $\mathbf{m}_j = (log\rho_1, log\rho_2, log\rho_3, ..., log\rho_M)^T$ for M number of model parameters. According to Günther (2004) for large contrasts an improved convergence is observed for logarithms, however, for small contrasts the inversion of resistivity or the logarithm yields similar results.

Like any other geophysical data, the basic requirements for the inversion of the apparent resistivity data set are a fast forward algorithm for calculating theoretical apparent resistivity data from input model parameters (the true resistivities), and a technique for calculating derivatives of the data with respect to the model parameters (known as the Jacobian or sensitivity matrix, **G**).

The 2D resistivity forward modelling in the inversion routine is performed using the finite difference (Dey and Morrison, 1979) or finite element (Sasaki, 1994) numerical techniques developed to solve the potential distribution about a point source of current located in or on the surface of a half-space containing two-dimensional conductivity (resistivity) distribution.

Finite difference (FD) or finite element (FE) methods are typically used, where a continuous conductivity distribution is approximated by a mesh of individual cells or elements, each with constant conductivity or resistivity. The potential is then calculated at discrete points (nodes of the mesh) by solving a linear system of equations derived from the discretized differential equation and boundary conditions. Then, the theoretical (predicted) apparent resistivity data (ρ_{ac}) are computed in order to compare with the observed apparent resistivity (ρ_a^{obs}) values within a desired target misfit. Details on the use of FD and FE methods to solve the DC resistivity problem are well documented in the literature (e.g., Dey and Morrison, 1979; Sasaki, 1994; Spitzer, 1995; and Rücker et al., 2006).

The Jacobian matrix **G** is the matrix of partial derivatives calculated during the solution of the forward problem computed based on Eq. 4.4 (section 4.1.1) as

$$\mathbf{G} = \begin{pmatrix} \frac{\partial \log \rho_{ac1}}{\partial \log \rho_1} & \frac{\partial \log \rho_{ac1}}{\partial \log \rho_2} & \frac{\partial \log \rho_{ac1}}{\partial \log \rho_3} & \cdots\cdots & \frac{\partial \log \rho_{ac1}}{\partial \log \rho_M} \\ \frac{\partial \log \rho_{ac2}}{\partial \log \rho_1} & \frac{\partial \log \rho_{ac2}}{\partial \log \rho_2} & \frac{\partial \log \rho_{ac2}}{\partial \log \rho_3} & \cdots\cdots & \frac{\partial \log \rho_{ac2}}{\partial \log \rho_M} \\ . & & & & \\ . & & & & \\ . & & & & \\ \frac{\partial \log \rho_{acN}}{\partial \log \rho_1} & \frac{\partial \log \rho_{acN}}{\partial \log \rho_2} & \frac{\partial \log \rho_{acN}}{\partial \log \rho_3} & \cdots\cdots & \frac{\partial \log \rho_{acN}}{\partial \log \rho_M} \end{pmatrix} \quad (5.9)$$

where $\boldsymbol{\rho_{aci}}$ *(i=1,2,...,N)* are the calculated apparent resistivities called model responses and $\boldsymbol{\rho_j}$ *(j=1,2,...,M)* are the model resistivities called model parameters.

Since inversion of DC resistivity data is non-linear, it can be solved based on iteratively updating of the model parameters in the well-known regularized normal equations, for example, using Gauss-Newton least-squares method (Eq. 4.18 section 4.1.1) as

$$\mathbf{\Delta(\log\rho^k) = \left[G^T C_d^{-1} G + \lambda C_m^{-1}\right]^{-1}\left[G^T C_d^{-1}\left[\log\rho_a^{obs} - \log\rho_{ac}^k\right] - \lambda C_m^{-1}\left[\log\rho^k - \log\rho^0\right]\right]} \quad (5.10)$$

where $\Delta(\log \rho^k) = \log \rho^{k+1} - \log \rho^k$ is the logarithmic resistivity update after **k** number of iterations, $\log \rho_a^{obs} - \log \rho_{ac}^k$ the difference between the observed and calculated logarithmic apparent resistivity data, and ρ^0 is the resistivity of the starting model.

In the Gauss-Newton least-squares method, the Jacobian/sensitivity matrix (Eq. 5.9) is recalculated for all iterations (Loke and Dahlin, 2002). The finite-difference method or finite-element method which is used to calculate the predicted apparent resistivity can also be used to calculate the Jacobian/sensitivity matrix.

Calculating the Jacobian/sensitivity matrix for all iterations is the most time-consuming step of the inversion process. In order to reduce the computing time, Loke and Barker (1996) suggested estimation of the Jacobian matrix values by a quasi-Newton formulation using Broyden´s update formula (Eq. 5.11). A homogeneous earth model, for which the Jacobian matrix values can be calculated analytically, is used as the starting model. In each iteration, the Jacobian matrix is estimated by the following updating equation:

$$\mathbf{G}^{\mathbf{k+1}} = \mathbf{G}^{\mathbf{k}} + \frac{\left[\Delta \mathbf{d}_{\mathbf{c}}^{\mathbf{k}} - \mathbf{G}^{\mathbf{k}} \Delta \mathbf{m}^{\mathbf{k}}\right]}{\left[\Delta \mathbf{m}^{\mathbf{k}}\right]^{\mathbf{T}} \left[\Delta \mathbf{m}^{\mathbf{k}}\right]} \left[\Delta \mathbf{m}^{\mathbf{k}}\right]^{\mathbf{T}} \tag{5.11}$$

Here in $\Delta \mathbf{m}^{\mathbf{k}} = \Delta(\log \boldsymbol{\rho}^{\mathbf{k}}) = \log \boldsymbol{\rho}^{\mathbf{k+1}} - \log \boldsymbol{\rho}^{\mathbf{k}}$ is the model parameter update, and $\Delta \mathbf{d}_{\mathbf{c}}^{\mathbf{k}} = \log \boldsymbol{\rho}_{\mathbf{a}c}^{\mathbf{k+1}} - \log \boldsymbol{\rho}_{\mathbf{a}c}^{\mathbf{k}}$ is the change in the model response (in this case the change in calculated apparent resistivities) after the k[th] iteration.

Based on Eqs. 4.20a and 4.20b, the misfit between the observed and calculated data is provided by the normalized χ^2*(chi-square) and RMS* misfit functions defined by

$$chi - squared(\chi^2) = \frac{1}{N} \sum_{i=1}^{N} \left(\frac{\log \rho_{a,i}^{obs} - \log \rho_{ac,i}^{k}}{\log(1 + \frac{\varepsilon_i}{\rho_{a,i}^{obs}})} \right)^2 \tag{5.12a}$$

$$RMS = \sqrt{\frac{1}{N} \sum_{i=1}^{N} \left(\frac{\log \rho_{a,i}^{obs} - \log \rho_{ac,i}^{k}}{\log \rho_{a,i}^{obs}} \right)^2} \tag{5.12b}$$

where ρ_a^{obs} is the observed apparent resistivity, ρ_{ac}^{k} the calculated (model response) apparent resistivity for the k[th] iteration, and ε_i are the observed data uncertainties (or weights). An inversion solution fits the data to the level of the noise when $\chi^2 = 1$.

5.3 2D DC resistivity data acquisition

The aim of the 2D electrical resistivity survey was primarily to investigate clay filled chalk dissolution zones and secondary to differentiate the till/clay layer from the sand and chalk layers of the subsurface by interpreting in terms of the resistivity distributions, geometry and depth of the anomalies.

Before going to the field, forward modeling of the expected geology has been processed in the office to determine the most suitable electrode spacing and arrays. According to the results of the forward modeling and by compromising the number of field days, three survey lines (near to the observed sinkholes) were planned with 2 m electrode spacing and two survey lines planned with 5 m electrode spacing for a maximum depth of investigation up to 100 m. Both

Wenner-alpha and Wenner-beta arrays were selected for each survey line by considering the resolution and depth of investigations. The Wenner-alpha array has a good vertical resolution and it is an attractive choice for surveys in a noisy area due to its high signal strength. The Wenner-beta, which is a special case of the dipole-dipole array (Fig. 5.2), was a suitable choice for good lateral resolution. But due to the presence of noise (for example, wire fences and power lines) in the study area and the limited sensitivity of our resistivity meter for higher depths, more emphasis was given to the Wenner-alpha array.

The surveys were conducted at Münsterdorf from April 20 to 24, 2009 along five profiles using Wenner-alpha and Wenner-beta configurations (Fig. 5.3). The three profiles along the eastern and western sides of the football area which are 264 (R-1), 320 (R-2), and 222 (R-5) meters long are with electrode spacing of 2 meters and the two profiles (R-3 and R-4) are with electrode spacing of 5 meters and each 715 meters long.

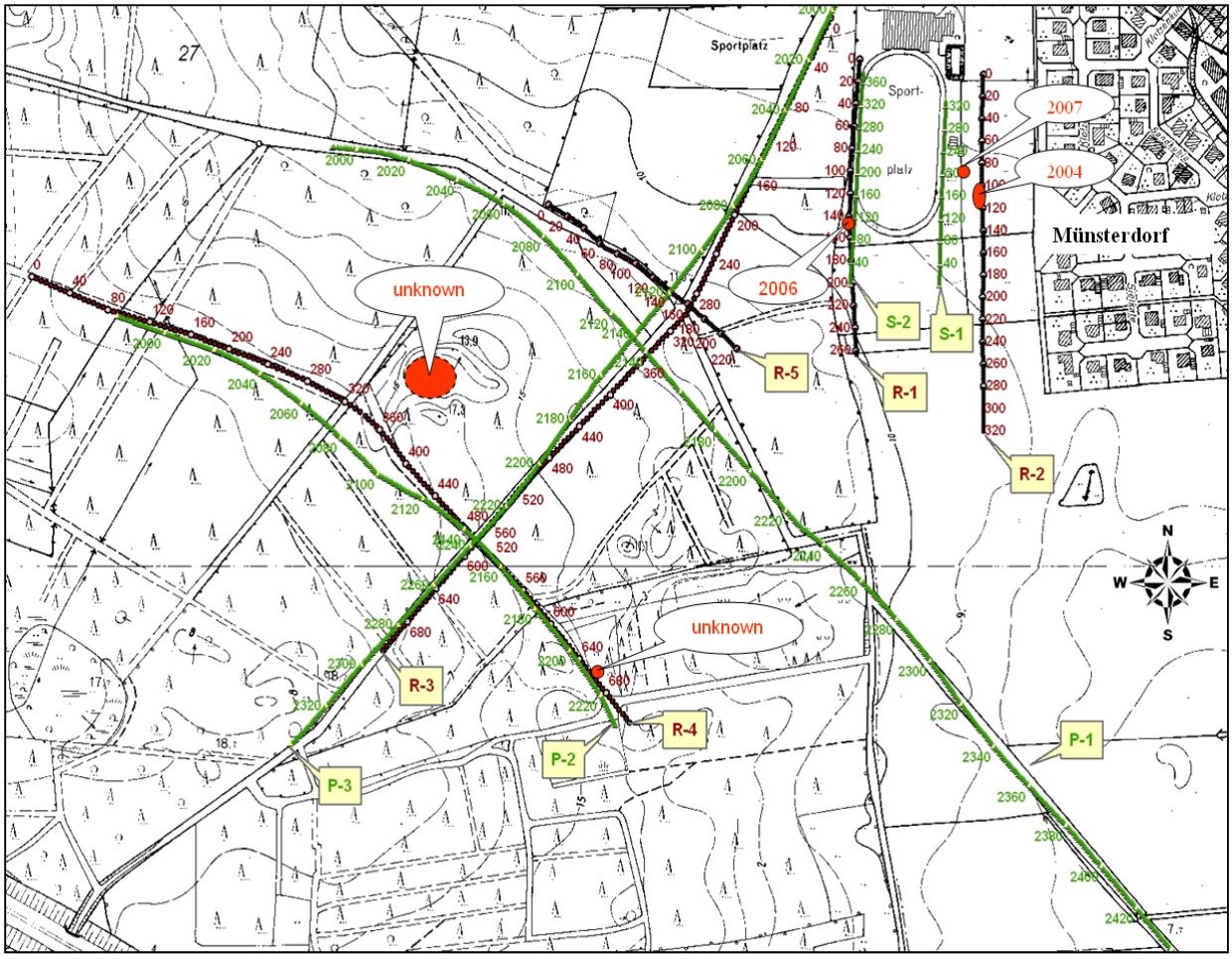

Figure 5.3 *Resistivity (R in m) and seismic (P and S in CMP) survey lines at Münsterdorf. The red circles are locations of sinkholes with year of occurrence. The numbering of the profiles is based on the data acquisition date.*

Instruments

The instruments used for these surveys include a PC controlled multi-electrode and multi-channel measuring device, decoders (switching boxes) to activate electrodes individually, stainless steel electrodes which are durable and have fairly low self-potentials, multi-core cables for connecting the electrodes, and a power supply battery. The measuring device was RESECS (RES6P), a PC controlled 8-channel DC resistivity meter system manufactured by GeoServe with a power supply of 1.2 KW battery pack. It measures both the transmitted current and voltage and stores these quantities together with the resistivity data. This instrument has measuring software and can also be able to record the chargeability however, with poor data quality. Boxes with 16 decoders (DEC16B) are used for the 2m electrode spacing surveys and 8 decoders integrated in a cable reel (DEC8R) for the 5m electrode spacing surveys**.** The electrodes location and elevation were measured by GPS. Fig. 5.4 shows the different instruments used for the 2D DC electrical resistivity survey.

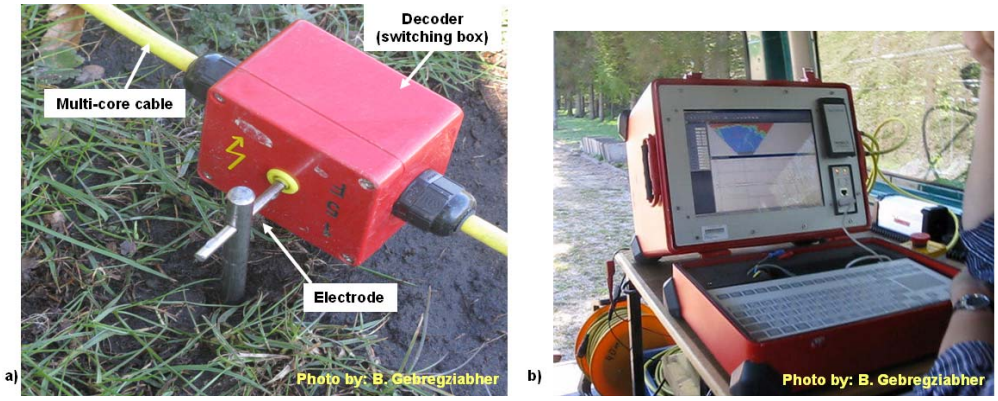

Figure 5.4 *Instruments for DC electrical resistivity survey; a) electrode attached to a decoder and multi-core cable, b) measuring device (RESECS).*

Field survey

Data acquisition begun after the electrodes were positioned with equal spacing along the profile and the multi-core cables with the switching box were connected to each electrode. The electrode contacts have been checked and the measurements were controlled by the microprocessor-driven resistivity meter inside a car. Stability and precision of each measurement has been done in terms of standard deviation by making repeated readings every 1 millisecond for each data point over a measurement time window of 1024 milliseconds (for 2 m electrode spacing) and 2048 milliseconds (for 5 m electrode spacing). In each time window a current is injected with positive, negative and zero polarities. Measurement started

after 176 milliseconds (for 2 m electrode spacing) and 400 milliseconds (for 5 m electrode spacing) of the current injection. Several depth levels were measured by increasing the electrode spacing stepwise as shown in Fig. 5.5.

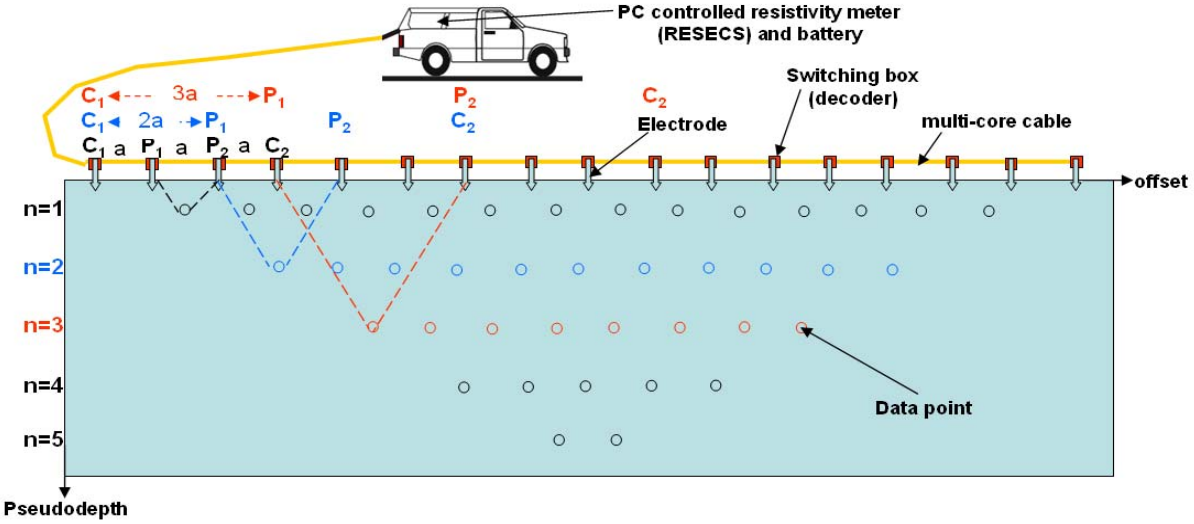

Figure 5.5 *Setup for a 2D resistivity measurement with a Wenner-alpha electrode array having a spacing `a`.*

The apparent resistivity data are plotted as a function of location along the profile and electrode separation (pseudo-section). For the Wenner electrode array, the location on the profile is given by the center of the array and the depth (pseudo-depth) is given by the spacing of the current electrodes. Based on Edwards (1977), the pseudo-depth corresponds to the depth of investigation (≈ na/2), where `n` is the electrode separation factor.

Generally the weather was warm and dry; however, a sudden rainfall occurred during the data acquisition of line R-3.

5.4 2D DC resistivity data processing

The collected data are plotted in the form of pseudo-sections which can provide an initial picture of the subsurface geology (Figs. 5.6 and 5.7). However, a 2D inversion of the measured data is necessary for the final interpretation by transforming the apparent resistivities and pseudo-depths into a 2D resistivity model. In recent years, several computer programs have been developed to carry out such inversions (e.g., Loke and Barker, 1996 and Günther, 2004). Our data is processed by applying a smoothness-constrained inversion using a Finite-Differences based software DC2DInvRes vs.2.12 (Günther, 2004) in order to create 2D subsurface resistivity models.

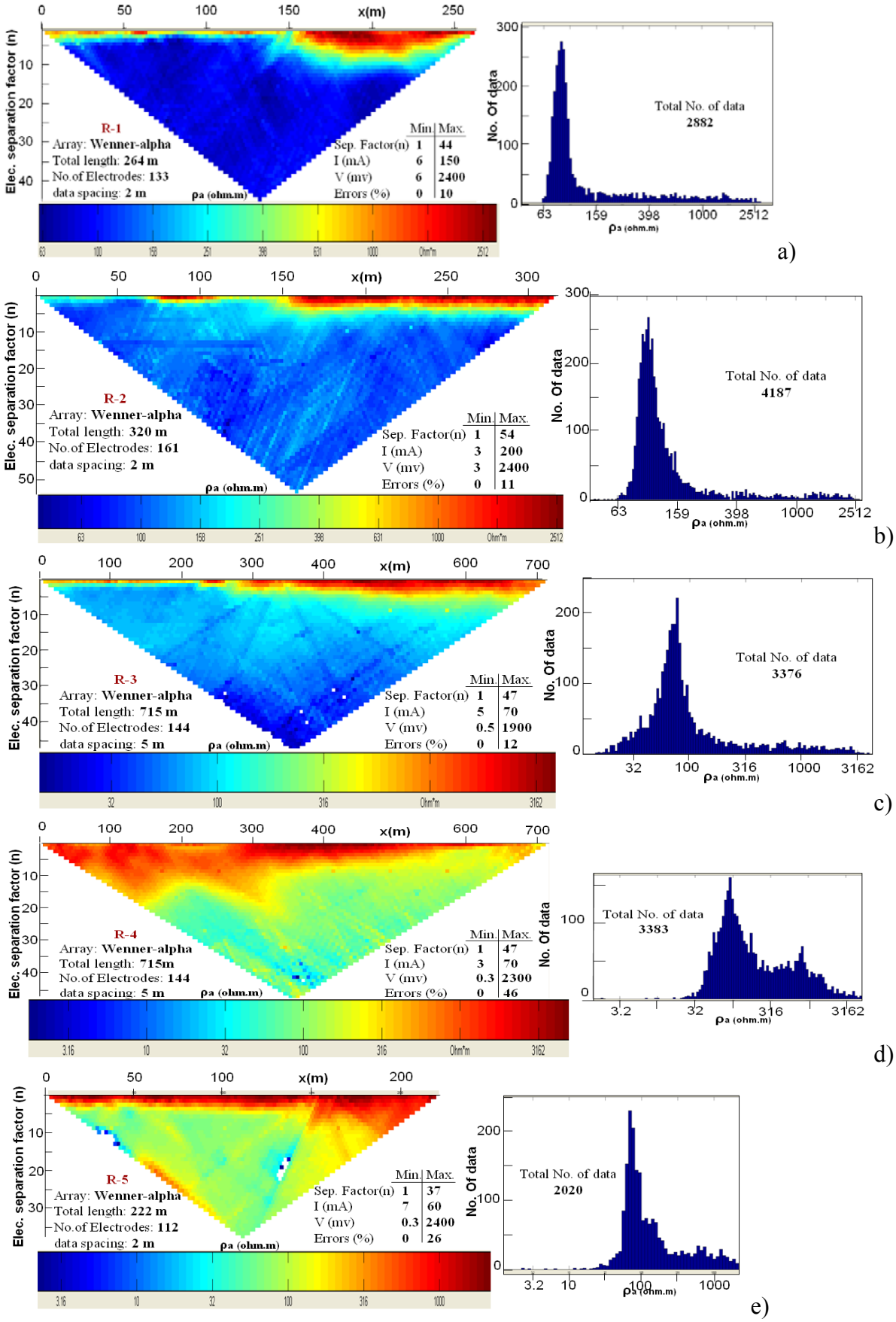

Figure 5.6 *Pseudo-sections and histograms for the raw data collected using Wenner-alpha array along profiles R-1(a), R-2(b), R-3(c), R-4(d), and R-5(e).*

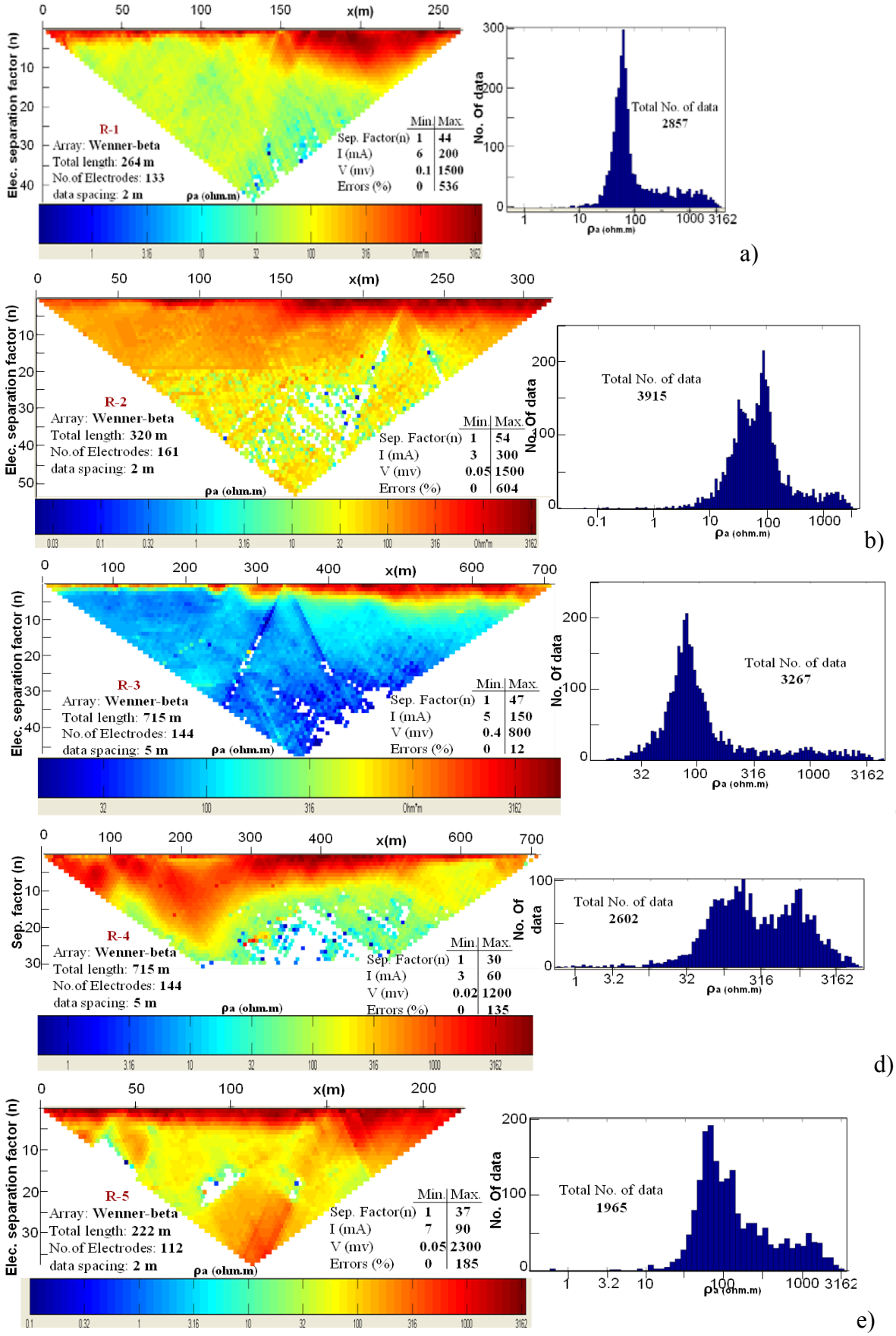

Figure 5.7 *Pseudo-sections and histograms for the raw data collected using Wenner-beta array along profiles R-1(a), R-2(b), R-3(c), R-4(d), and R-5(e).*

The final model is calculated in an iteration process which includes step-by-step forward modeling and inversion. After an initial resistivity model is chosen and parameterized, the model responses (apparent resistivities) are calculated using the forward modeling in order to compare them with the measured apparent resistivities. The program compares the forward modeling results with the measured data, the quality of the fit is determined and the parameter values for the next iteration step are specified. Then, the initial model is modified in each iteration using different algorithms (for example, using Gauss-Newton as shown by Eq. 5.10) to minimize the misfits between the calculated and measured apparent resistivities. This process is continued until a selected error (misfit) is reached for the maximum number of iterations. When the misfit is minimized with a lower RMS error (Eq. 5.12b) or the chi-squared is converged to one (Eq. 5. 12a), the inversion stops and outputs the final resistivity model. Figure 5.8 shows the work flow of an iterative nonlinear inversion of our DC resistivity data processing.

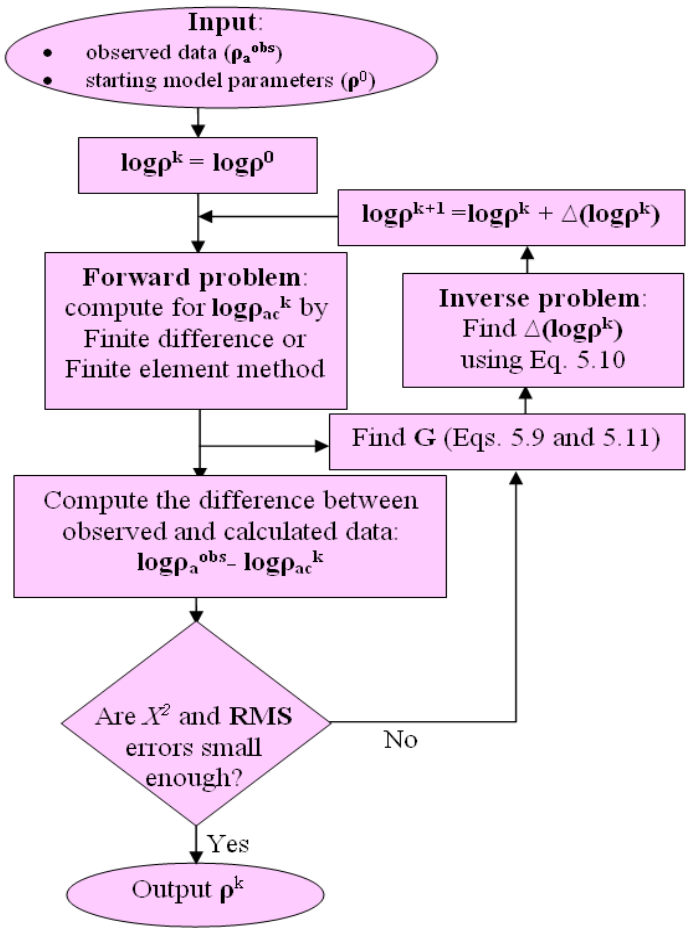

Figure 5.8 *A flow chart of an iterative nonlinear inversion for DC resistivity data. Where* $\boldsymbol{\rho^0}$ *is the starting model resistivity,* $\boldsymbol{\log\rho_a^{obs}}$ ***and*** $\boldsymbol{\log\rho_{ac}^k}$ *are the observed and calculated logarithmic apparent resistivities respectively, and* $\boldsymbol{\Delta(\log\rho^k) = \log\rho^{k+1} - \log\rho^k}$ *is the logarithmic resistivity update after* $\boldsymbol{k}$ *number of iterations.*

Data quality

The raw data are imputed with their measurement errors for each measurement cycle during the data acquisition. Before starting the inversion, each pseudo-section is visually checked to remove bad data and improve the data quality because higher noise leads to worse inversion results and lower information content for a given data set. In general, the data accuracy assessed by the measurement equipment for the surveys conducted by Wenner-beta array (Fig. 5.7) showed relatively higher noise level than the ones conducted by the Wenner-alpha array (Fig. 5.6). This could be due to the higher geometric factor for the Wenner-beta than for the Wenner-alpha. According to Günther (2004), the maximum relative error of apparent resistivity can be predicted as the sum of the relative errors of the configuration factor K (geometrical error) and the potential difference ΔV due to minimum accuracy of the measuring device (instrumental error).

Some erroneous data are clearly visible as randomly distributed in most of the pseudo-sections and some are due to electrode problems probably due to a wire fence near to the electrodes, for example, at x = 226 and 228 meters of profile R-2 (Fig. 5.7b) and a buried pipe, for example, at x = 335 and 340 meters of profile R-3 (Figs. 5.6c and 5.7c). In the pseudo-sections, they are seen as inverted ´´v´´-shaped patterns of bad data points with the two legs originating from an electrode.

Outliers of apparent resistivity data less than 10 ohm.m and with errors of higher standard deviations are removed to improve the data quality. Table 5.1 summarizes the improvement of data errors after editing and deleting the outliers. After editing (Figs. 5.9 and 5.10), the Wenner-alpha and Wenner-beta data sets are also combined to a single data for each profile with the aim to make a joint inversion. The data noise is estimated at a rate of 3 % plus a voltage accuracy of 0.01 mV for each inversion.

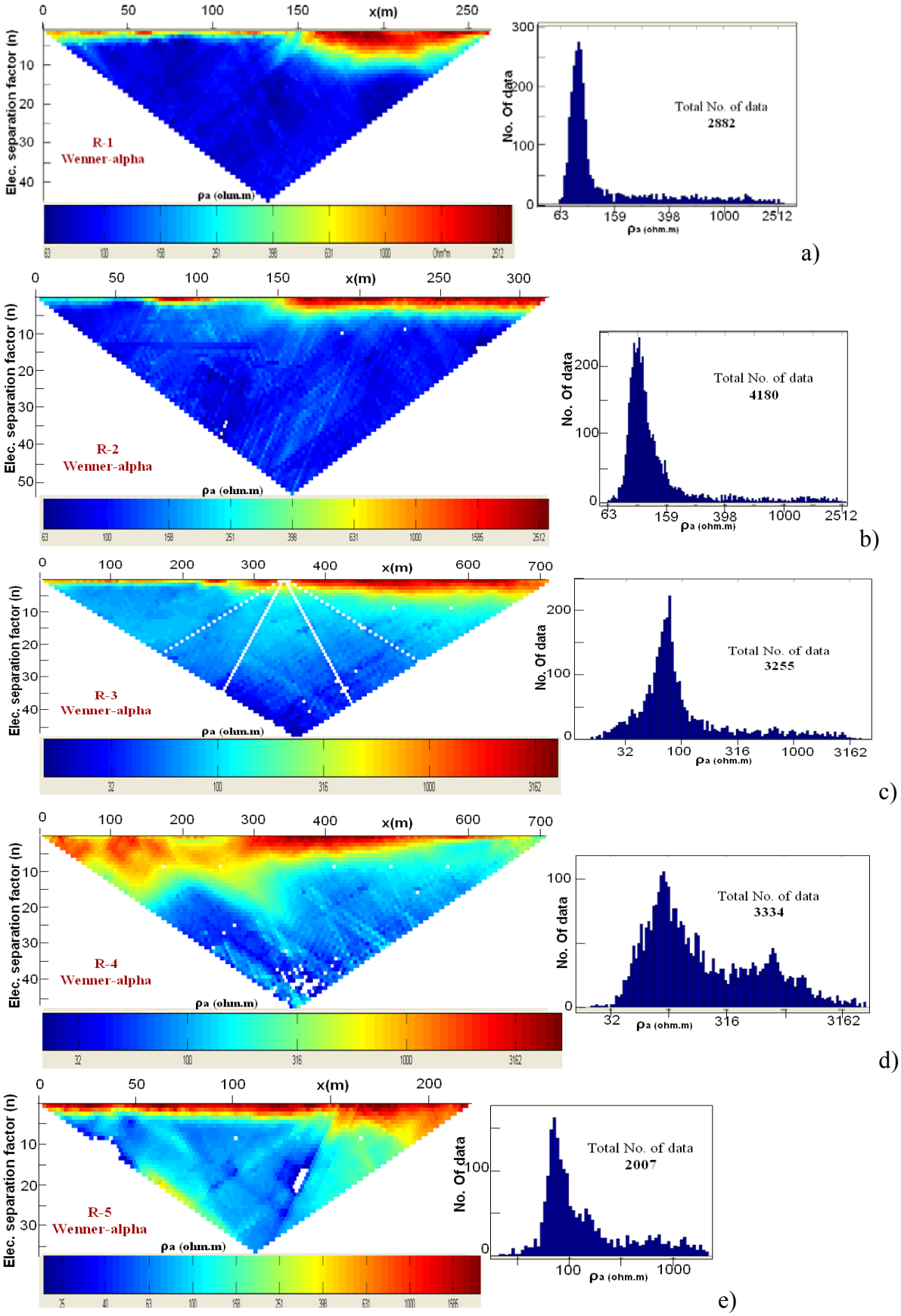

Figure 5.9 *Pseudo-sections and histograms for the edited data collected using Wenner-alpha array along profiles R-1(a), R-2(b), R-3(c), R-4(d), and R-5(e).*

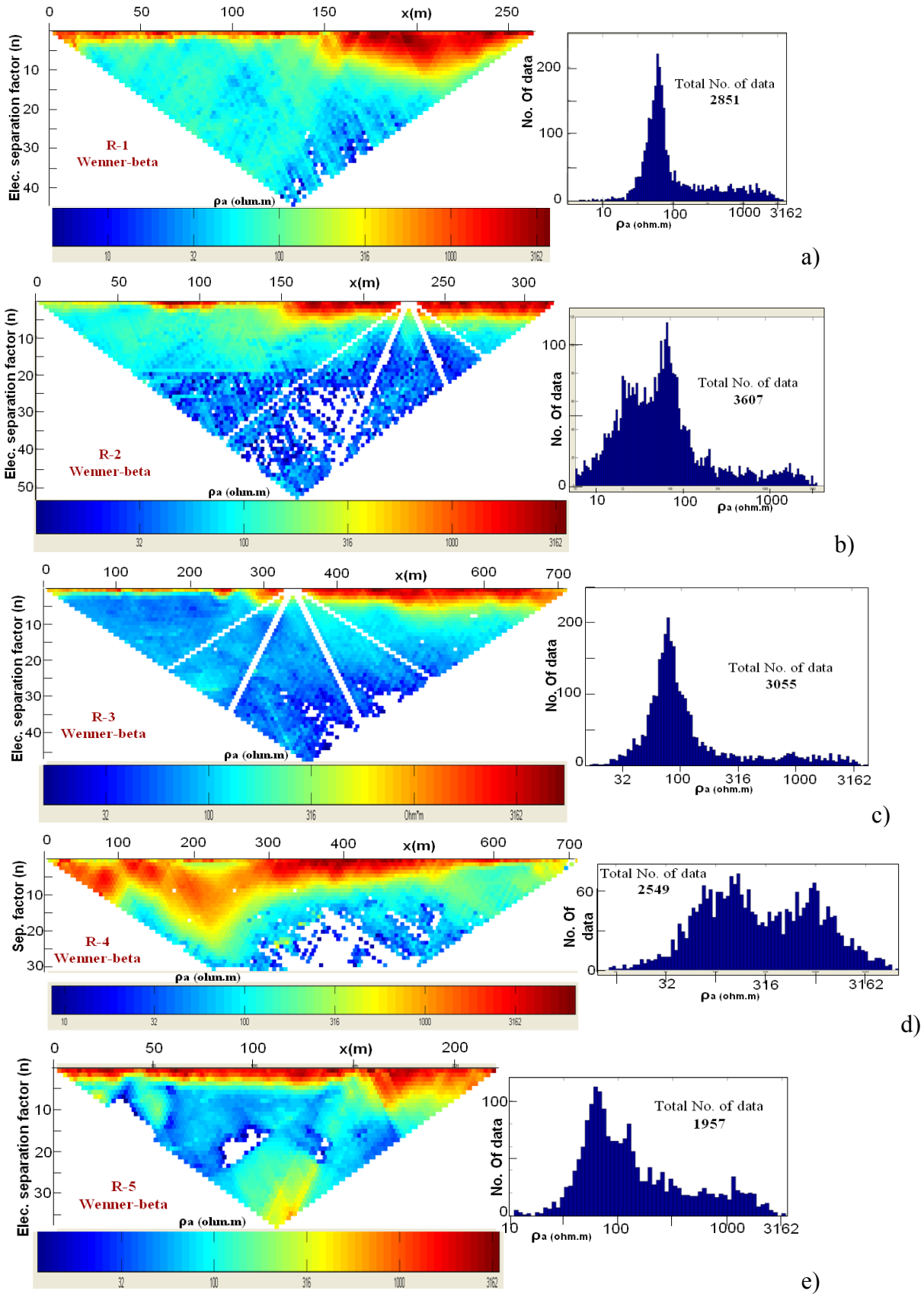

Figure 5.10 *Pseudo-sections and histograms for the edited data collected using Wenner-beta array along profiles R-1(a), R-2(b), R-3(c), R-4(d), and R-5(e).*

Profile	Array type	Total Length (m)	No. of electrodes	Spacing (m)	Electrode separation factor 'n'	Max. current Used (mA)	Before editing		After editing		No. of data deleted
							Total No. of data	Max. data error (%)	Total No. of data	Max. data error (%)	
R-1	W-α	264	133	2	1-44	150	2882	10	2882	10	0
	W-β	264	133	2	1-44	200	2857	536	2851	69	6
R-2	W-α	320	161	2	1-54	200	4187	11	4180	11	7
	W-β	320	161	2	1-54	300	3915	604	3607	46	308
R-3	W-α	715	144	5	1-47	70	3376	12	3255	12	121
	W-β	715	144	5	1-47	150	3267	12	3055	12	212
R-4	W-α	715	144	5	1-47	70	3383	46	3334	10	49
	W-β	715	144	5	1-30	60	2602	135	2549	49	53
R-5	W-α	222	112	2	1-37	60	2020	26	2007	6	13
	W-β	222	112	2	1-37	90	1965	185	1957	21	8

Table 5.1 *Summary of DC resistivity data quantity and quality for the profiles R-1, R-2, R-3, R-4, and R-5.*

Model parameterization

A starting model is parameterized into rectangular cells with a horizontal dimension equal to the electrode spacing and a logarithmically increasing thickness of a maximum model depth. The maximum depth is determined by 1D sensitivity analysis from the data automatically by the program, which shows higher depths for the Wenner-alpha than the Wenner-beta data (Fig. 5.11). The initial resistivity model is set to a homogenous half-space of the median resistivity value of the observed data. The number of layers and model cells are determined by considering the number of data points so that each model consists of a number of cells greater than or equal to the number of observed data. The size of the cells increases with increasing depth due to decreasing sensitivities.

In the inversion code, the finite difference method is used without considering the topography effect for forward modeling. The program calculates the Jacobian/sensitivity matrix for the first iteration, and then updates using the Broyden method (Eq. 5.11). The accuracy of the forward procedure affects the quality of the inversion results and can be assessed by considering the reciprocity standard deviation of the forward response.

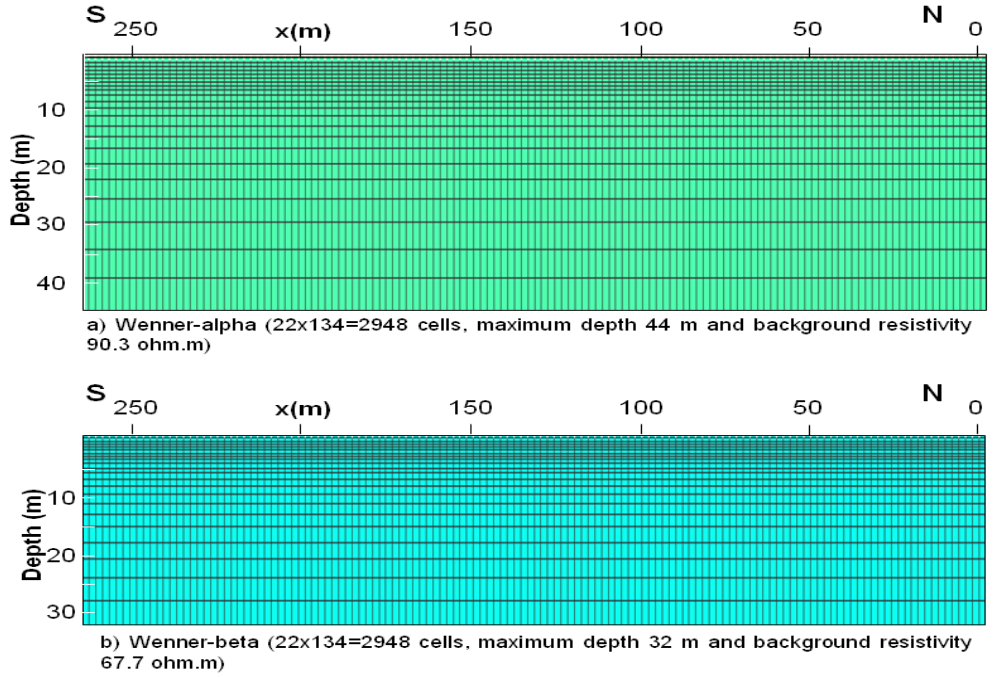

Figure 5.11 *Maximum depths by 1D sensitivity and median resistivity values of the starting models along R-1; (a) for the Wenner-alpha and (b) Wenner-beta data sets.*

Data inversion and resolution analysis

The DC2DInvRes software offers the possibility to choose between different inversion algorithms such as Gauss-Newton, truncated singular value decomposition (TSVD), simultaneous iterative reconstruction technique (SIRT), and truncated least squares (TLS) inversion options. However, based on Günther's (2004) recommendations, the Gauss-Newton method using global (for better resolution properties) smoothness constraints of second order (better handling of boundaries) with line search and a fixed regularization parameter (λ) are used for processing our data. Logarithmic resistivities without lower bounds are used for both the data and model parameters.

The sharpness of the model resolution is affected by the regularization strength. The regularization parameter weights the model constraints against the data misfit (Eq. 5.10). According to Günther (2004), for logarithmically increasing λ the resolution decreases nearly linearly. Moreover, the resolution decreases drastically with depth and outside the electrodes. Before deciding the optimum λ for processing our data, we made some tests using different values as shown in Fig. 5.12. Accordingly, small values of λ produce a highly structured model with high parameter contrasts whereas large λ values result in simple models.

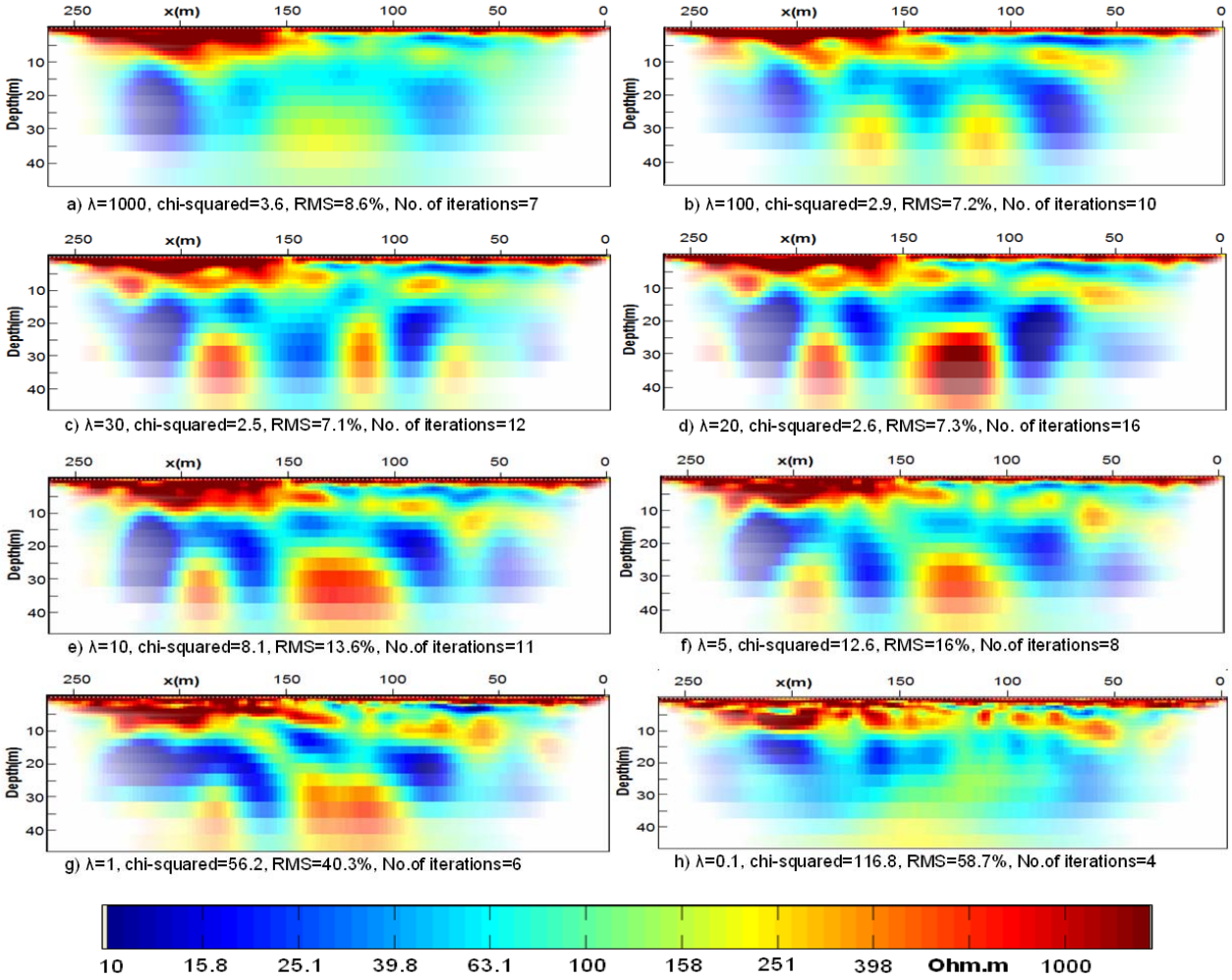

Figure 5.12 *Inversion results using different regularization parameters for R-1 Wenner-alpha data.*

For large λ (Figs. 5.12a and 5.12b) the inversion converged but the models are too smooth to see the anomalies due to increasing the influence of the smoothness constraints. As λ decreases, more and more complexities may be observed due to artifacts resulting from errors (Figs. 5.12e-h). I tried also to determine the regularization parameter using the L-curve method (Hansen and O'Leary, 1993) automatically by the software and found for example, λ = 4.72 for optimum regularization of the R-1 data. Using this method, I found a reasonable resistivity model in terms of geology along this profile but in terms of the misfits (RMS=17%) the best value is at λ = 20 (Fig. 5.13). Therefore, based on Günther (2004) recommendations, first a global minimization using fixed λ = 30 is carried out until the inversion stops. If chi-square (χ^2) does not converge to ≈1, λ is decreased step by step until the chi-square starts to increase. By compromising the model roughness/resolution and the misfits, I select the optimum regularization parameter to get a reasonable model without artifacts for the different data sets as shown in Table 5.2.

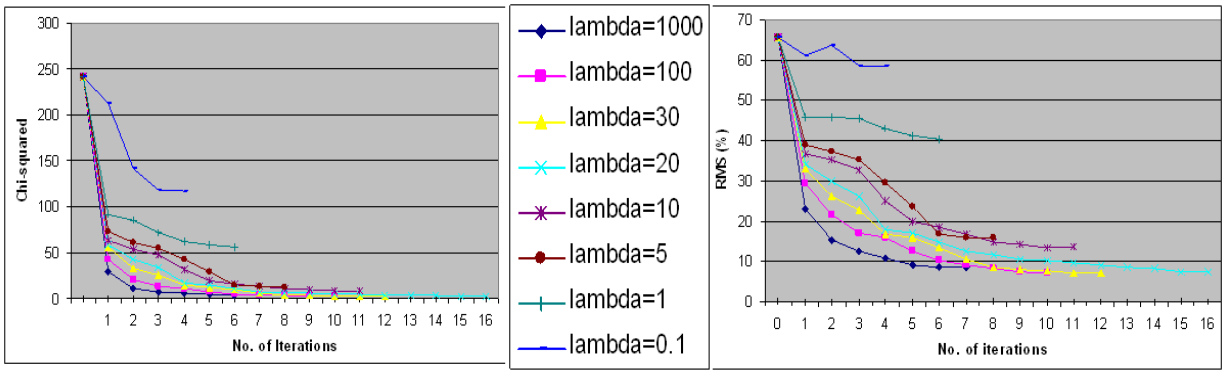

Figure 5.13 *Data misfits for eight selected values of regularization parameters; chi-squared (left) and root mean squared, RMS (right).*

Another inversion parameter is the z-weight parameter which is the ratio of vertical to horizontal smoothness (Constable et al., 1987). This helps to fine-tune the smoothness constraint by giving greater weight to vertical or horizontal structures in the inversion model. By default it is given as 1 by assuming equal weights for the vertical and horizontal smoothness. In this case better resolution is found in terms of the geology for z-weight equal to 0.5, however, with slightly higher values in the RMS and chi-squared values. Based on the aim, a reasonable resistivity model in terms of geology is more important than an excellent data fit. Therefore, I chose the z-weight parameter of 0.5 for most of our data sets (Table 5.2).

Line	Array Type	Max. Depth in m by 1D sensitivity	No. of Model layers	Total No. of cells	Initial resistivity (ohm.m)	Inversion parameters		Before Inversion		After Inversion		Total No. of Iteration
						Damping factor (λ)	z-weight	Chi-square	RMS error (%)	Chi-square	RMS error (%)	
R-1	W-α	44	22	2948	90.3	20	0.5	871.8	41.5	0.6	7.5	21
	W-β	32	22	2948	67.7	30	0.5	563.0	61.6	0.6	16.0	16
	W-α+W-β	44	22	2948	85	20	0.5	1063.7	67.9	0.7	14.7	21
R-2	W-α	59	29	4669	110	20	1	521.3	34.2	0.7	9.5	10
	W-β	32	11	1771	120	10	0.5	1141.3	53.1	0.7	10.0	13
	W-α+W-β	49	22	3542	110	20	0.5	746.8	40.1	0.8	13.0	19
R-3	W-α	131	23	3335	75.2	30	0.1	992.3	70.8	0.8	11.0	20
	W-β	83	17	2465	84	20	0.5	1175.3	57.3	0.7	18.5	26
	W-α+W-β	108	23	3335	80	30	1	411.5	69.3	0.7	17.0	14
R-4	W-α	131	23	3335	140.5	30	1	1276.0	95.1	0.8	12.9	17
	W-β	63	18	2610	252.4	30	1	1158.0	196.6	0.8	16.0	20
	W-α+W-β	99	23	3335	180	30	1	1242.7	135.3	0.7	16.0	20
R-5	W-α	40	18	2034	94.5	20	0.5	1090.0	61.9	0.8	10.8	27
	W-β	24	18	2034	100	20	0.5	1271.9	102.0	0.8	22.0	22
	W-α+W-β	35	18	2034	98.4	20	0.5	1175.6	86.1	0.8	20.0	22

Table 5.2 *Summary of inversion parameters for DC resistivity data along profiles R-1, R-2, R-3, R-4, and R-5.*

The inversion is continued again using the robust (L_1-norm) method by giving less weight to the outliers. As explained in section 4.1.1, the major weakness to the least-squares method (L_2-norm) is its sensitivity to outliers. The robust inversion (absolute value changes) is powerful to minimize the chi-squared into one. However, based on a personal communication with Thomas Günther, the RMS error can be increased because of the effect of the outliers and as shown also in Figs. 5.14 and 5.15. The robust inversion stops when the chi-squared is converged to one.

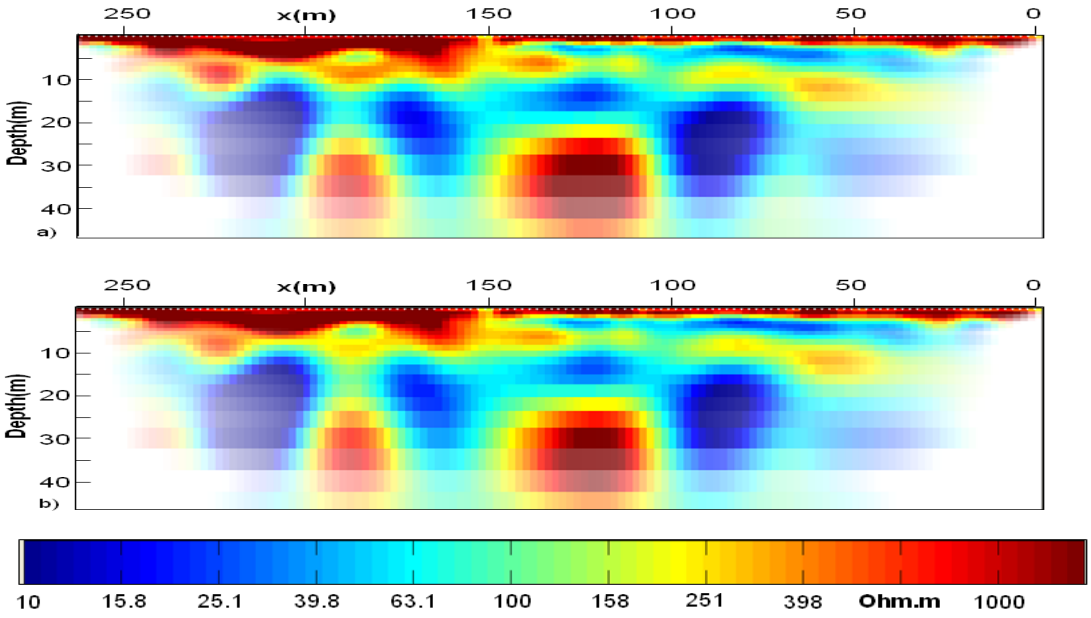

Figure 5.14 *Inversion results for R-1 Wenner-alpha data using a selected regularization parameter (λ=20); a) after least-squares method (chi-squared=2.6 and RMS=7.3%) and b) after robust inversion (chi-squared=0.8 and RMS=7.7%).*

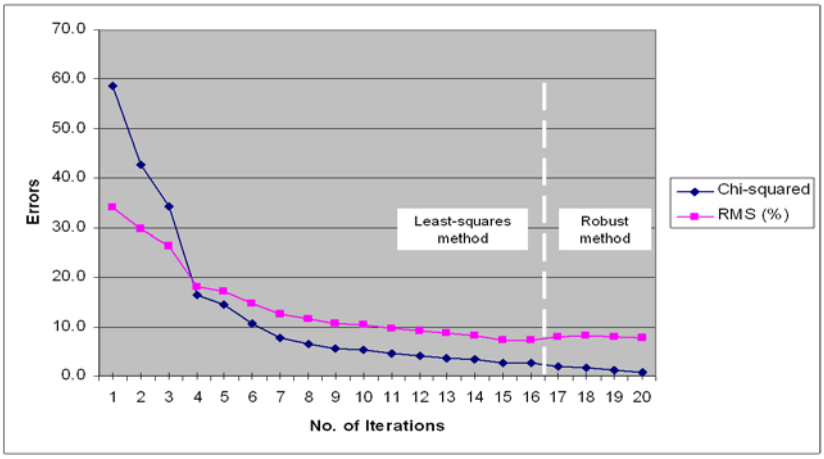

Figure 5.15 *Chi-squared and RMS values for selected regularization parameter (λ=20) before and after robust inversion.*

After the inversion stops, the model response (calculated data) and the misfits between the observed and calculated data are analyzed and the process is continued again by deleting the erroneous data points or outliers (Fig. 5.16). The calculated data can be displayed in the same way like the measured data as shown in Fig. 5.16b. The data misfit, which is the difference between the measured and calculated data divided by the measured data in percent, helps to see how the observed data are fitted by the model. As shown in Fig. 5.16c, the data misfit is plotted for each data point according to the offset and the median depth of investigation. Some inverted v-shaped traces of bad data misfit show a sign of noise for a single electrode. The misfits displayed in the histogram form (Fig. 5.16d) shows almost a Gaussian distribution, which is essential for successful least-squares inversion.

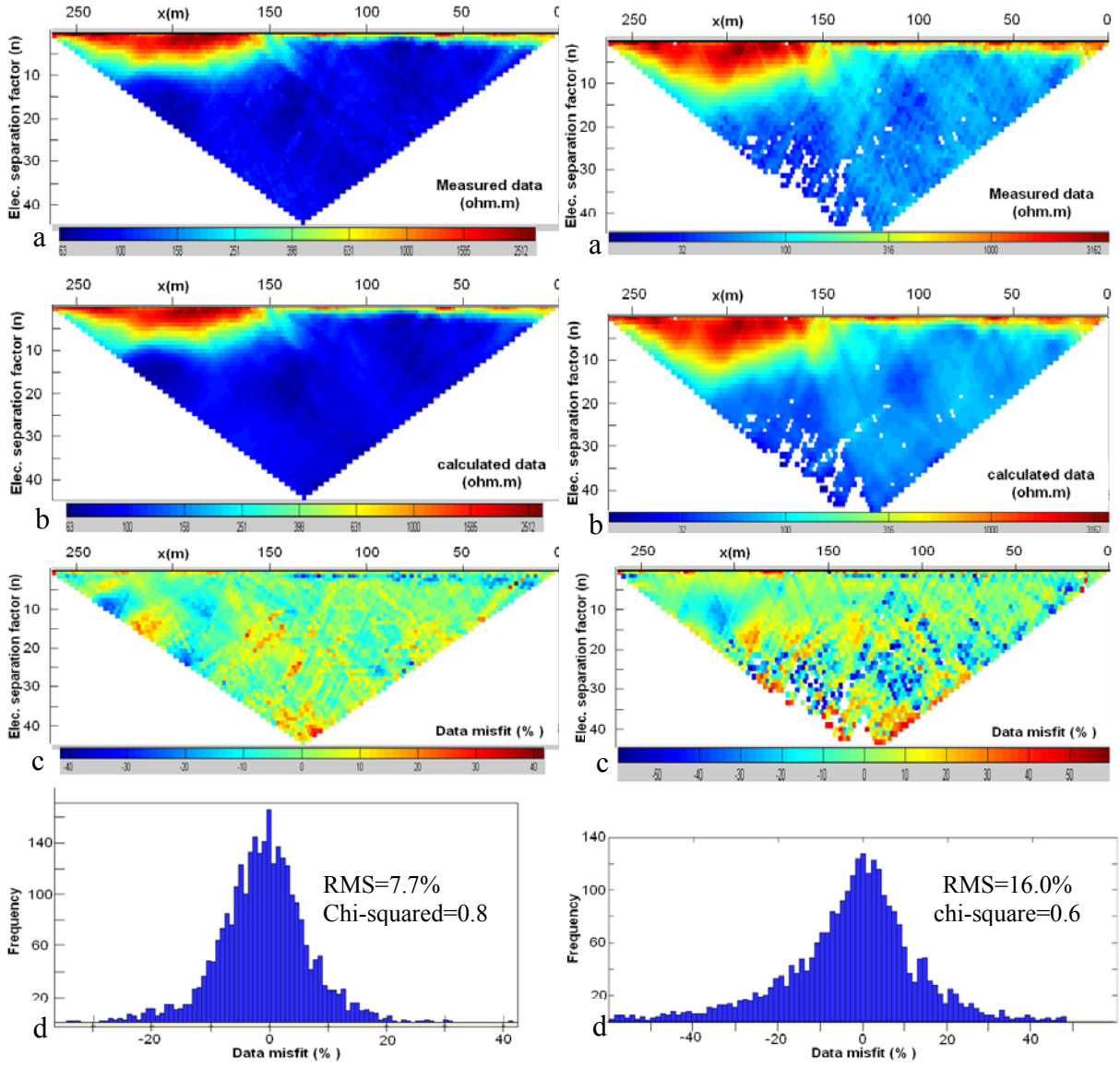

Figure 5.16 *Comparison of (a) observed data, ρ_a^{obs},(b) model response, ρ_{ac} , and (c) misfits as pseudo-section and (d) as histogram for the inverted models of R-1 data sets collected using Wenner-alpha (left) and Wenner-beta (right) arrays.*

According to Günther (2004), another method to estimate how well the data are fitted can be the misfit per error. It represents the difference between the measured data and forward response, weighted by the estimated errors. Ideally, the misfit per error (chi-square) is randomly distributed and near +/- 1 at the end of the inversion process. Fig. 5.17a shows the percentage errors of each datum point and Fig. 5.17b the misfit per error after the inversion of R-1 data sets.

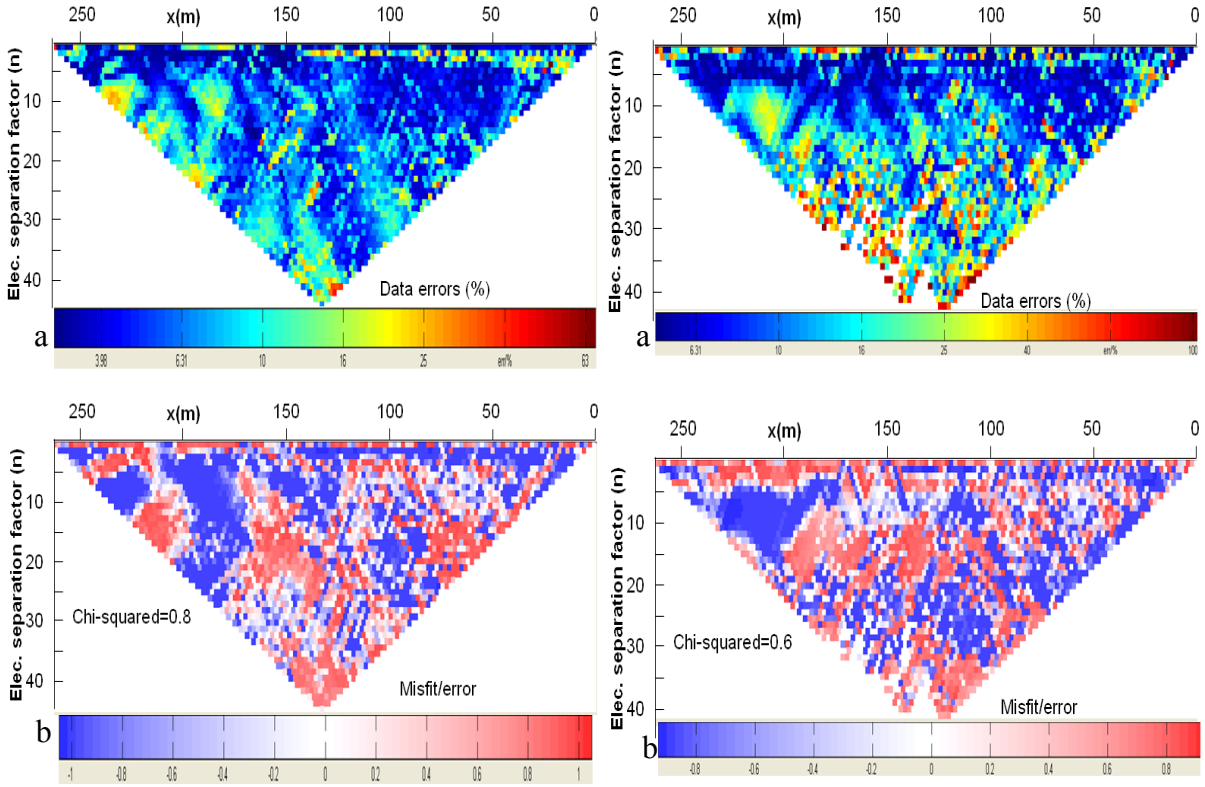

Figure 5.17 *a) Error percentage of each datum points and b) error-weighted misfits as pseudo-section form for R-1 data sets using Wenner-alpha (left) and Wenner-beta (right) arrays.*

The detectability and resolveability of the subsurface model can also be analyzed by displaying the sensitivity (Fig. 5.18a) and model cell resolution (Fig. 5.18b) for every single datum point. The sensitivity quantifies the information contained for the data set in each model cell resistivity. It is relatively higher near the surface and decreases rapidly with depth due to the reduced number of measurements over the larger subsurface volume in deeper areas. Accordingly, higher sensitivity values stand for higher reliability of the model resistivity values.

The model reliability can also be increased by denser data coverage. The coverage, which is the sum of the absolute sensitivity values over all measurements, can be displayed like a

model section as shown in Fig. 5.18c. Similar to the ray density in seismic refraction tomography, the coverage gives information how well the model cells are covered by the data set. The data coverage decreases with depth as the spacing between electrodes increases. It is also important to consider the dimension of the model cell resolution by analyzing the resolution radius section (Fig. 5.18d). The resolution radius increases from the minimum electrode spacing at shallower depth up to 12 m in higher depths.

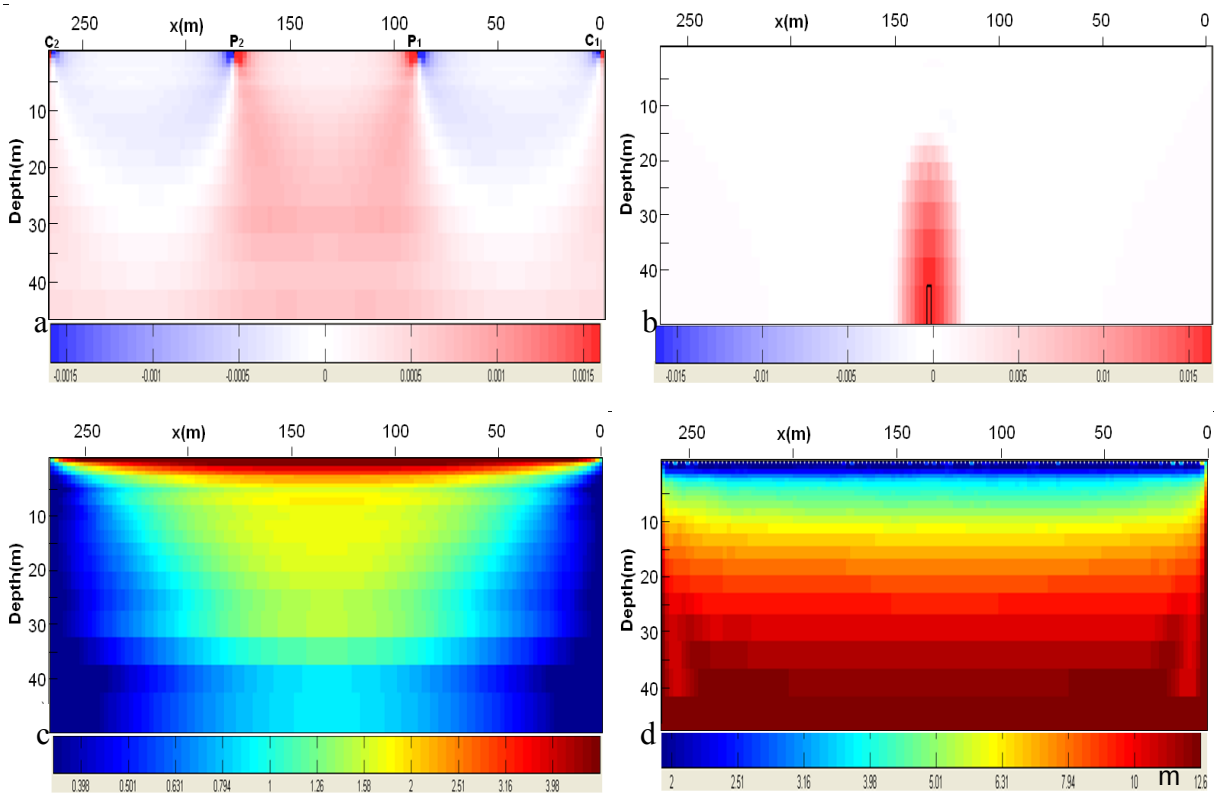

Figure 5.18 *a) Data sensitivity for the maximum electrode separation data No. 2882, b) model cell resolution for model cell 2882, c) data coverage, and d) resolution radius for the inverted model in Fig. 5.14b of profile R-1.*

The final inverted models are displayed with their respective data misfits separately for the data sets collected using Wenner-alpha (Fig.5.19) and Wenner-beta arrays (Fig.5.20). Generally, the magnitude of the data misfit error is comparatively larger for the data sets collected using the Wenner-beta array. Moreover, the data sets collected using the Wenner-alpha and Wenner-beta arrays are also combined to a single data set for each profile by a joint inversion as shown in Fig. 5.21. In most cases the data misfits for the combined inversion are better than the Wenner-beta results but not as good as the Wenner-alpha results especially at higher depth of the models. This could be because of the accuracy problem of the measuring instrument using the Wenner-beta array for higher depths due to the higher geometric factor.

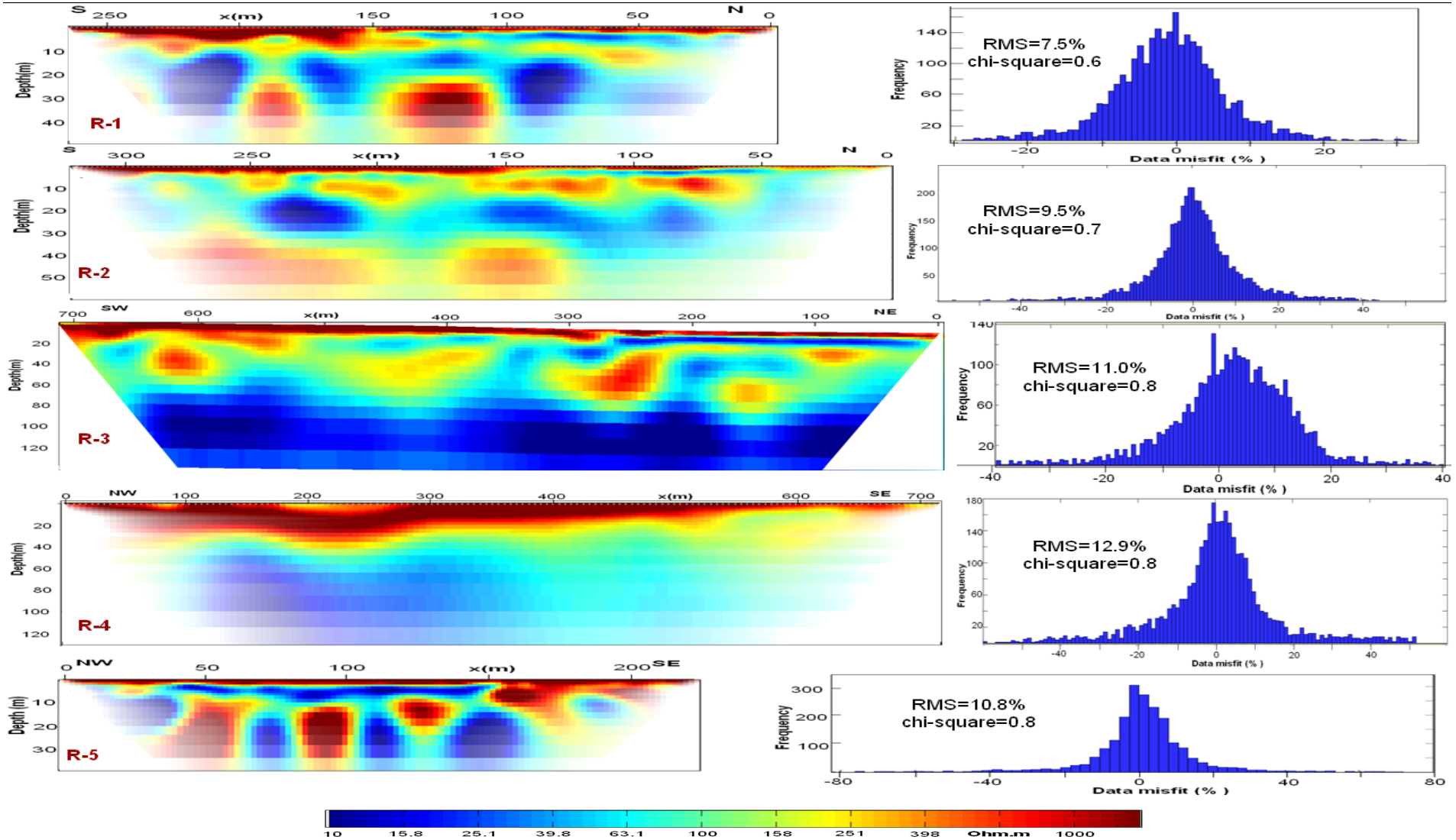

Figure 5.19 *2D electrical resistivity inverted models for the data sets collected using Wenner-alpha array (left) and the data misfit histograms (right) for each profile.*

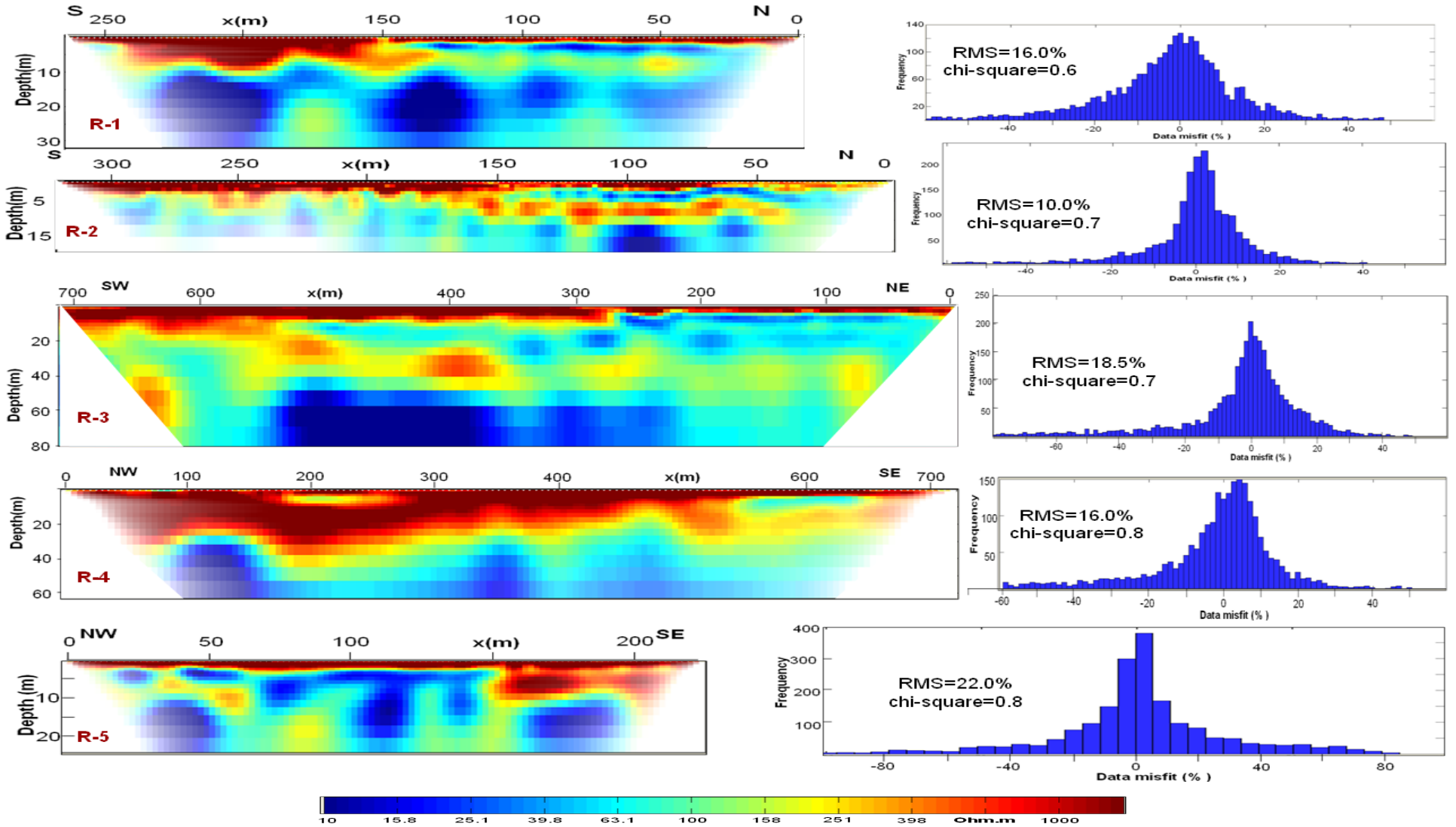

Figure 5.20 *2D electrical resistivity inverted models for the data sets collected using Wenner-beta array (left) and the data misfit histograms (right) for each profile.*

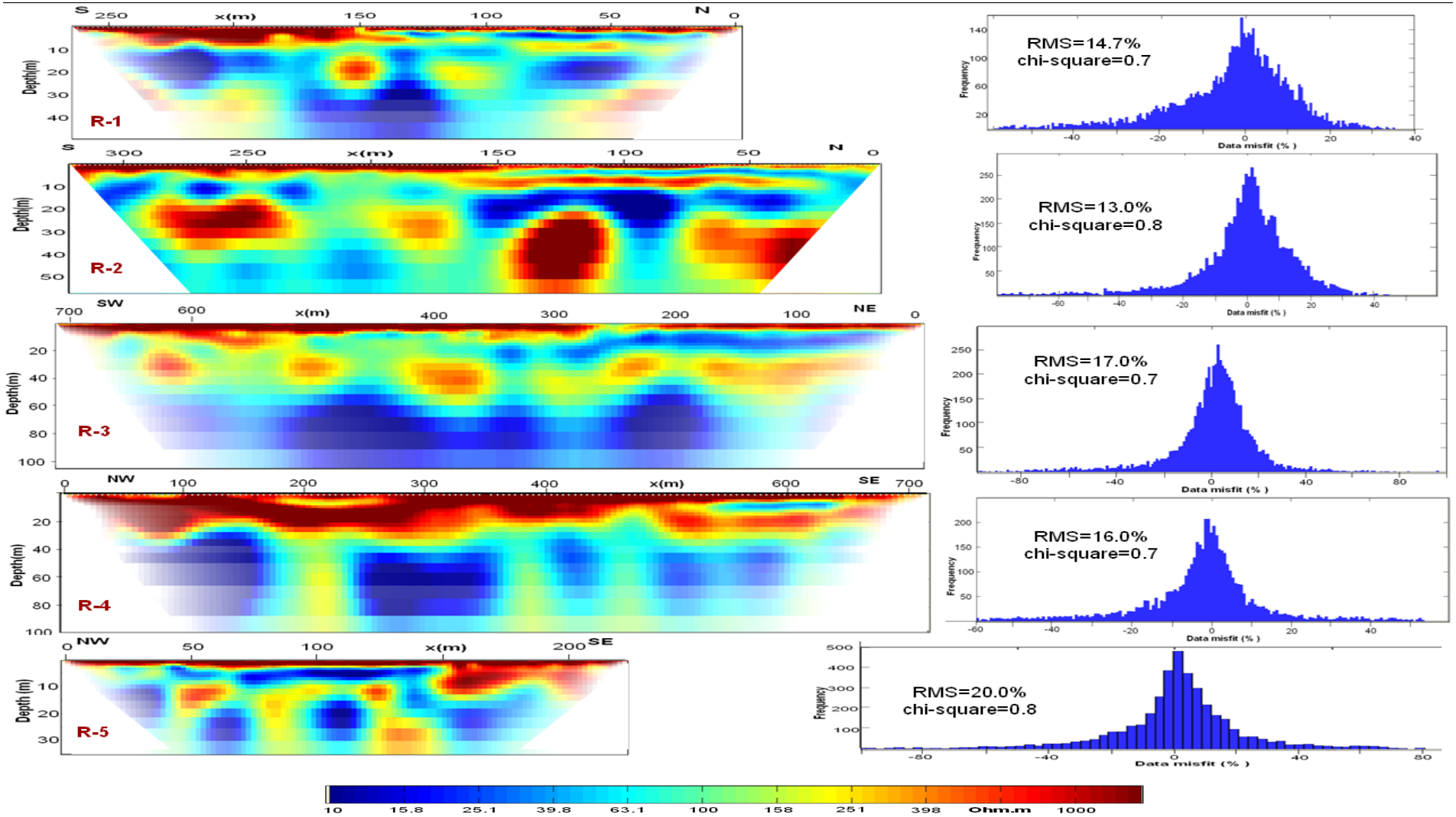

Figure 5.21 *2D electrical resistivity inverted models for the combined data sets collected using Wenner-alpha and -beta arrays (left) and the data misfit histograms (right) for each profile.*

5.5 Results and interpretations of DC resistivity imaging

The final results of a 2D resistivity survey are cross-sections of the calculated rock resistivity models along the profile lines as shown in Figs. 5.19-5.21. These cross-sections should be assessed in terms of the lithological and structural interpretation of the resistivity data. The assessment of inversion results is ambiguous due to the limited number of values and precision of the data. This ambiguity is influenced by the data coverage (density), the errors in the data, sensitivity of the electrode configuration, and the degree of misfits between the observed and predicted data.

The 2D electrical resistivity investigation has improved our understanding of the relationships between the dissolution features, the chalk layer and the Quaternary deposits. All the inversion results show a resistivity contrast between the high resistive dry sand, the saturated sand, the low resistive till/clay and clay filled chalk dissolution zones, and the chalk layers (Fig. 5.22). Moreover, low resistivity layers less than about 30 ohm.m are observed at depths below 60 to 70 m from profiles R-3 and R-4. This might be due to saltwater intrusion inside the upper Cretaceous chalk layer. Therefore, based on the 2D electrical resistivity results five lithologic layers are interpreted as dry sand, saturated sand, clay/till, freshwater and saline water saturated chalk layers.

Interpretations of the inverted models for the Wenner-alpha, Wenner-beta, and the combined resistivity data sets along profiles R-1 and R-3 are discussed by including all available information from boreholes and the seismic reflection results (Fig. 5.22a) to reduce ambiguity. As shown in Fig. 5.22, at shallow depths (less than 10 m) all the models of each profile show the same results that coincide to the lithologic boreholes. Whereas at the center and higher depths the inverted model of the Wenner-alpha data sets (Fig. 5.22b) show better results. This might be due to higher depth of investigation, higher sensitivity, less data errors and misfits when compared to the Wenner-beta data sets. The possible chalk dissolution zones interpreted from the resistivity results (broken circles) show a horizontal misfit with the seismic reflection discontinuities (purple circles) by +/- 10 m which could be a location problem due to the topographical survey.

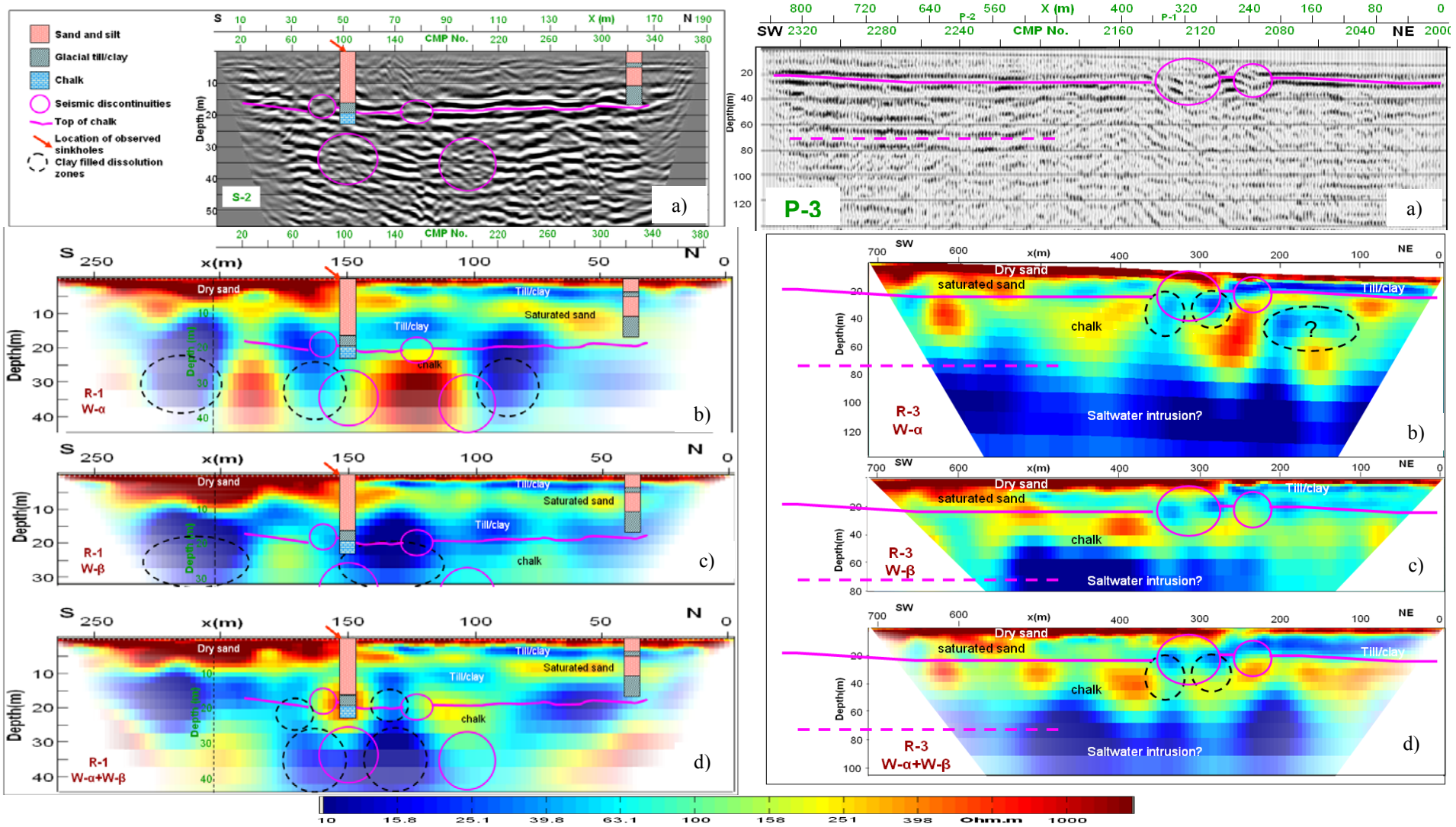

Figure 5.22 *Seismic reflection sections (a) and 2D resistivity interpreted models for the Wenner-alpha (b), Wenner-beta (c), and the combined (d) data sets along profiles R-1(left) and R-3 (right).*

The information for the left and right sides of the inverted models is best obtained from the results of the Wenner-beta and the combined data sets. For example, the till/clay column from the borehole along profile R-1 at x = 40 m and z = 15 to 17 m, exactly matches to the low resistivity layer from the inverted models of the Wenner-beta and the combined data sets as shown in Figs. 5.22c and 5.22d, respectively. This shows us the Wenner-alpha array has a good vertical resolution and is less sensitive to noises whereas the Wenner-beta has better lateral resolution but with poor data quality and misfits. Thus, the inverted models for the combined data sets show good compatibility both in vertical and lateral ways despite the misfits in position of the dissolution anomalies (≈ 10 m) from the seismic reflection discontinuities.

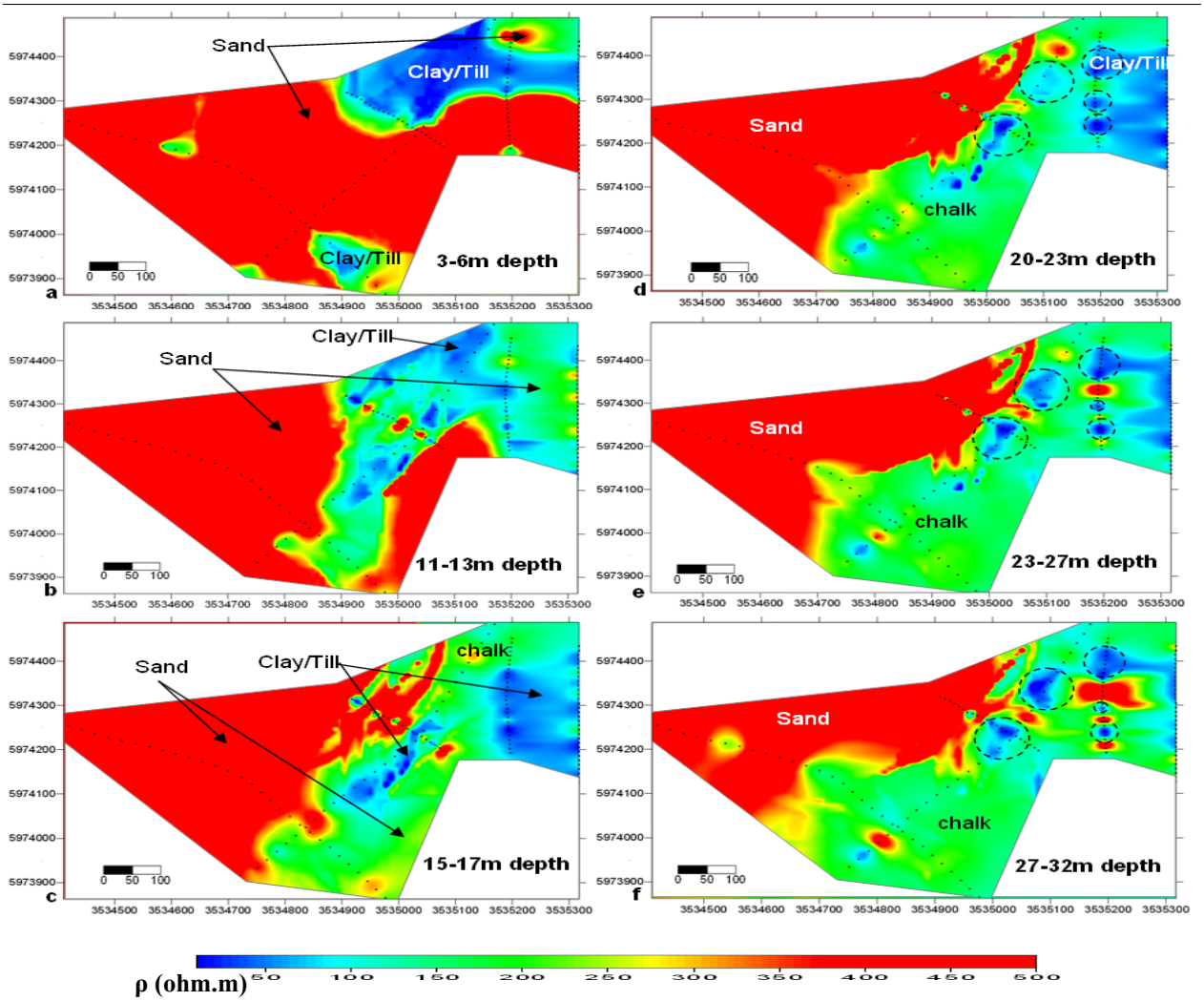

Figure 5.23 *Horizontal resistivity sections at different depths derived from the 2D inversion results. Dot lines and broken circles indicate the survey lines and the clay filled chalk dissolution zones, respectively.*

Horizontal resistivity sections for different depths can also be derived from the data of the 2D profiles (Fig. 5.23). Accordingly, the lithologies interpreted from the resistivity values are

mapped at depths of 3 – 6 m, 11 – 13 m, 15 – 17 m, 20 – 23 m, 23 – 27 m, and 27 – 32 m. At shallow depths the study area is mainly covered by the high resistive dry sand and low resistive till/clay sediments (Fig. 5.23a). According to the geology (Fig. 2.7), this could be correlated to the Pleistocene glaciofluvial (dominant on the south and western parts) and glacial sediments (dominant on the north and eastern parts), respectively. At higher depths, the thickness of the resistive sand decreases towards south. The upper Cretaceous chalk is exposed at 15 m depth towards north (Fig. 5.23c) whereas at higher depth (about 20m) in the east and southern parts (Fig. 5.23d). The clay infill dissolution zones provide good contrasts in electrical properties with the chalk, allowing detection using the 2D electrical resistivity imaging (Figs. 5.23d-f).

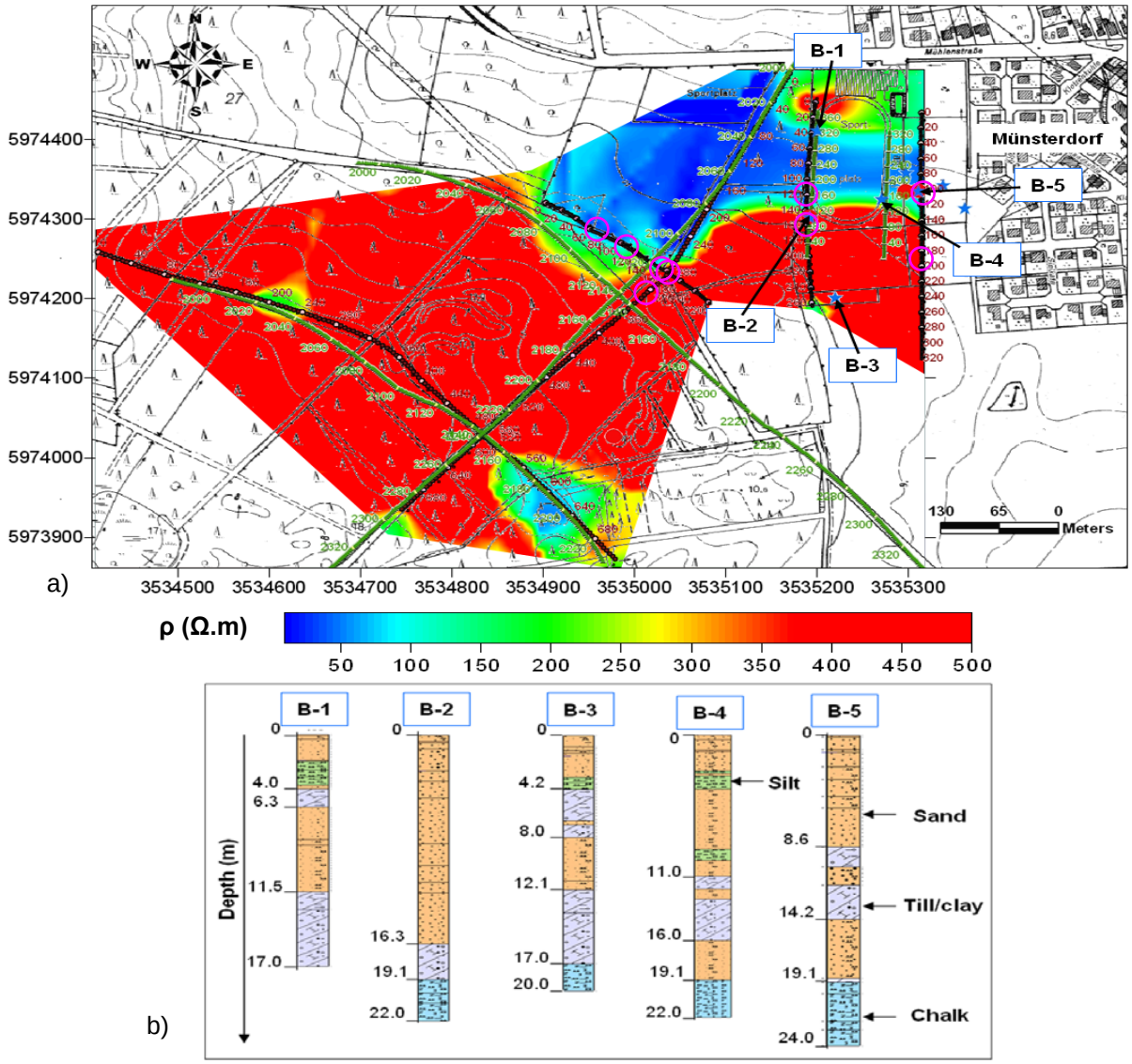

Figure 5.24 *(a) Horizontal resistivity section at the surface and (b) borehole information (after LLUR). Purple circles indicate resistivity discontinuities, blue stars are borehole locations, and red filled circles are locations of observed sinkholes.*

As shown in Fig. 5.24a, most of the observed sinkholes and the resistivity discontinuities (clay filled chalk dissolution zones) are located on the contact zone between the high resistive sand and the low resistive till/clay layers. The 2-D resistivity and the lithology from boreholes (Fig. 5.24b) confirm also sandy sediments are dominant on top of the chalk instead of till/clay near to the observed sinkholes and the clay filled chalk dissolution zones. Therefore, the occurrences of the sinkholes may be mainly dependent on the presence of adjacent impermeable till/clay layers, whereas groundwater flow through the chalk is strongly influenced by the lithologic boundary (contact zones).

Synthetic test

In order to test the effect of the inversion on the interpreted resistivity results, I produced synthetic data using the same types of geometry, separation factor, and the spacing and number of electrodes with profile R-1 of Wenner-alpha array. The input resistivity model, for producing the synthetic apparent resistivity data, is based on vertical electrical sounding (VES) results from LLUR (Fig. 5.25).

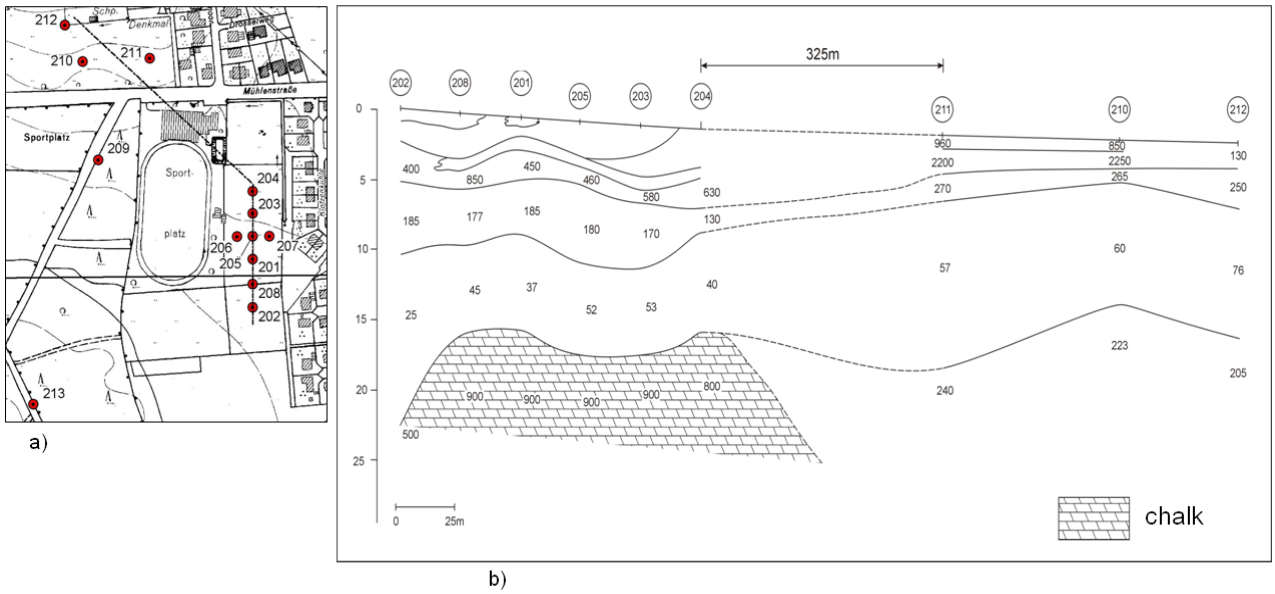

Figure 5.25 *a) Location map with vertical electrical soundings (VES) and b) the 1D inverted electrical resistivity results at different depths for each VES in Ωm (from LLUR).*

The model (Fig. 5.26a) includes a resistivity of 1500 to 2600 ohm.m for the dry sand, 40 ohm.m for the till/clay layer, 175 ohm.m for the saturated sand, and 900 ohm.m for the chalk below 20 meters depth. The two low resistivity zones with 10 ohm.m represent a clay filled

chalk dissolution zone and their location is based on the seismic reflection discontinuities from profile S-2.

The synthetic data is generated from the model using 133 equally spaced surface electrodes at the positions x = 0, 2, 4, …, 266 m similar to the field layout along profile R-1. The forward calculation is made using the finite difference method by discretizing in x from -2 to 266 m and z increases logarithmically up to 22 model layers. A total number of 2882 synthetic apparent resistivity data are produced from the given model by adding a noise of 3% for a minimum voltage of 0.01 mV at 100 mA (Fig. 5.26b).

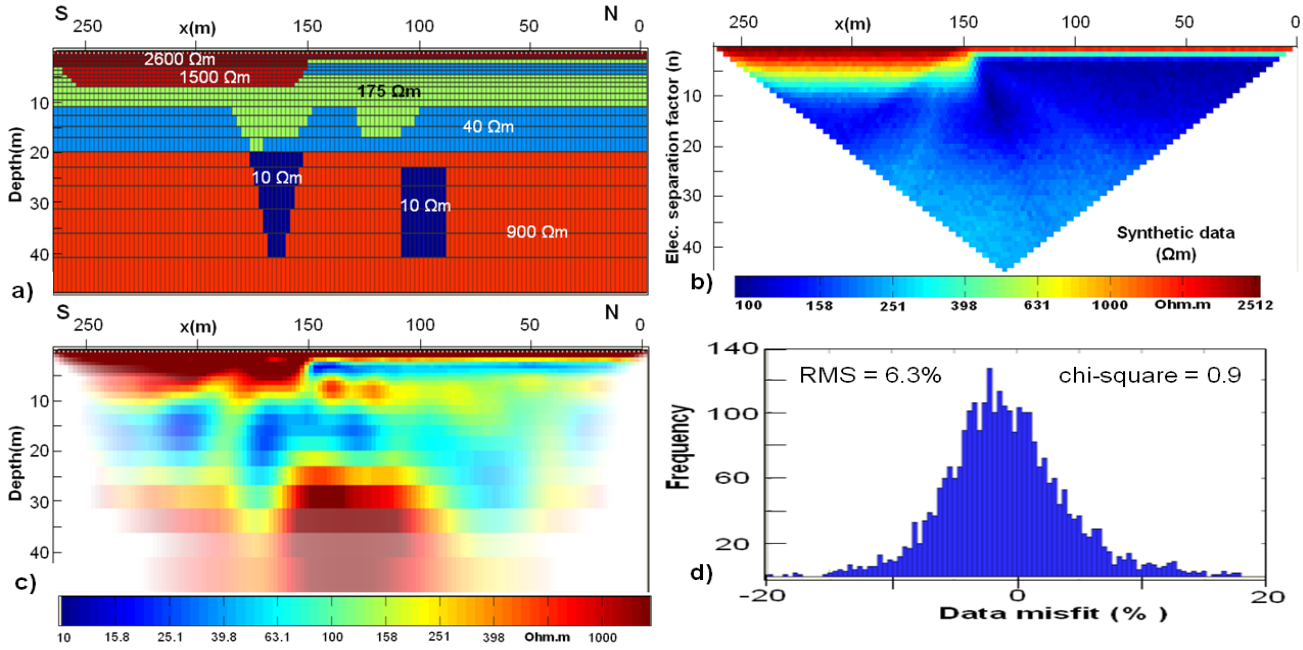

Figure 5.26 *a) Hypothetical resistivity model for producing synthetic data, b) synthetic data, c) final inverted model from the synthetic data, and d) the data misfit histogram after the final inversion.*

Inversion continuous using the Gauss-Newton global algorithm of second order smoothness constraints using a fixed regularization parameter, $\lambda = 20$, and z-weight parameter 0.5. Similar to the field data, the synthetic data is inverted first using a least-squares method then followed by robust method. The inverted final model result (Fig. 5.26c) indicates the dissolution zone anomalies but with a little displacement both in x and z directions. Both dissolution zone anomalies are located at shallower depth than that in the model. The dissolution zone at $x \approx 100$ m in the true model is found displaced in the inverted model to about $x \approx 60$ m. From this we can conclude that the mismatches for the location of the interpreted clay filled dissolution zones from the 2D resistivity sections and the seismic reflection discontinuities could also be

due to inversion effects. Moreover, the saturated sand layer at the right side of the inverted model seems to be larger in thickness and the till layer can not be identified well. A similar misfit appears to occur between our Wenner-alpha data and the borehole information at x = 40 m of profile R-1 which could be due to the poor lateral sensitivity of the Wenner-alpha array.

6 JOINT INVERSION OF SEISMIC AND RESISTIVITY DATA

Integrated geophysical interpretation using multiple geophysical methods is often used in order to decrease an ambiguity inherent in each of the methods. These days, the limitations and ambiguity of individual techniques can be significantly reduced by adopting joint inversion schemes. Different measured quantities can be integrated into a joint inversion if the measured data are influenced by a subset of common subsurface parameters or if they are structurally similar (e.g., Hertrich and Yaramanci, 2002; Gallardo and Meju, 2004 and Günther and Rücker, 2006).

In our case, a joint inversion of the seismic refraction and DC resistivity data was carried out along two selected profiles (S-2/R-1 and P-3/R-3) in order to yield structurally similar results. The two profiles are selected for joint inversion based on the location or overlapping of the seismic and resistivity survey lines, the data quality, and considering the types of the seismic data to include from both S- and P-wave data.

6.1 Principles of joint inversion

As already explained in section 4.1.1, inversion means the determination of model parameters from observed data using a starting model and then minimizing the misfits between the model response and observed data. Based on Eq. 4.6, the misfit can be quantified by constructing an objective function $\mathbf{\Phi(m)}$, consisting of a weighted sum of data misfit $\mathbf{\Phi}_d\mathbf{(m)}$ and regularization terms $\mathbf{\Phi}_m\mathbf{(m)}$, that is to be minimized as,

$$\mathbf{\Phi(m)} = \mathbf{\Phi}_d\mathbf{(m)} + \lambda\, \mathbf{\Phi}_m\mathbf{(m)} \longrightarrow \text{minimum} \tag{6.1}$$

$$\text{where } \mathbf{\Phi}_d\mathbf{(m)} = \| \mathbf{D}\,(\mathbf{d}_{obs} - \mathbf{f(m)}) \|^2 = \sum_{i=1}^{N}\left(\frac{d_i - f_i(\mathbf{m})}{\varepsilon_i}\right)^2 \text{ with } \mathbf{D} = \text{diag}\left(\frac{1}{\varepsilon_i}\right) \tag{6.1a}$$

$$\text{and } \mathbf{\Phi}_m\mathbf{(m)} = \| \mathbf{C}(\mathbf{m} - \mathbf{m}^0) \|^2. \tag{6.1b}$$

Joint inversion is based on the strategy of optimizing a model $\mathbf{m}$ for data sets of $\mathbf{d}_1^{obs}$ and $\mathbf{d}_2^{obs}$ from measurements with two geophysical methods. Their corresponding model responses are expressed as $f_1(\mathbf{m}) = \mathbf{G}_1\mathbf{m}$ and $f_2(\mathbf{m}) = \mathbf{G}_2\mathbf{m}$.

The individual errors or misfit functions, $\mathbf{\Phi}_1(\mathbf{m})$ and $\mathbf{\Phi}_2(\mathbf{m})$, for the two data sets are combined to a joint error function which is to be minimized with respect to the model parameters:

$$E = w_1\mathbf{\Phi}_1(\mathbf{m}) + w_2\mathbf{\Phi}_2(\mathbf{m}) \longrightarrow \text{minimum}$$

The weighting factors w_1 and w_2 allow different weights to be assigned to the error functions, corresponding to the significance of the data sets for the model.

Unlike to separate inversion, the joint inversion is quite difficult in least-squares inversion schemes because it is hardly possible to determine the matrix of partial derivatives of two different linear operators simultaneously (Knödel et al., 2007). Such inversions are only possible if the observed data depend on the same model parameter or if the model parameters are interconnected by some petrophysical relationship (e.g., Hertrich and Yaramanci, 2002). However, for seismic velocity and electrical resistivity such a relationship does not exist so far except for similar structures or anomalies in the resulting models.

Gallardo and Meju (2004) and Günther and Rücker (2006) developped joint inversion techniques for a combined inversion of independent physical parameters, e.g., seismic velocity and electrical resistivity, by exchanging structural information in order to allow for structural similarities. Gallardo and Meju (2004) developped the technique by minimizing the cross-gradients of both models whereas Günther and Rücker (2006) developped a new joint inversion approach based on the ideas of robust modeling i.e., by weighting the individual data and model updates.

In this thesis the minimization and regularization procedures of Günther and Rücker (2006) is discussed briefly since we used this approach for processing our data.

According to Günther and Rücker (2006), the model function in Eq. 6.1b is built by three matrices:

$$\mathbf{\Phi}_m(\mathbf{m}) = \| \mathbf{W}_c\mathbf{C}\mathbf{m}\|^2 \text{ with a constraint weighting matrix } \mathbf{W}_c = \text{diag}\,(w_i^c). \qquad (6.2)$$

The constraint matrix C is generally a first order, second order or zeroth order (identity matrix) derivation matrix of the roughness vector along x and z directions in 2D case. The individual elements, w_i^c, describe penal factors for the different model cell boundaries, for example, the model characteristic with respect to horizontal and vertical structures. Very small values are used for sharp boundaries.

Robust modeling is usually applied to data weighting (Clearbout and Muir, 1973) but can also be applied to the model gradients (Günther and Rücker, 2006). Let $\mathbf{c} = \mathbf{C}\mathbf{W}_m(\mathbf{m}-\mathbf{m}^0)$ be the roughness vector. The weighting matrix $\mathbf{W}_m = \mathrm{diag}(w_l^c)$ and the weighting term w_l^c is determined in the l_1 and l_2-Norm as

$$w_l^c = \frac{\frac{|c_l|^1}{\|c\|_1^1}}{\frac{|c_l|^2}{\|c\|_2^2}} = \frac{\frac{|c_l|}{\sum|c_i|}}{\frac{c_l^2}{\sum c_i^2}} = \frac{\sum c_i^2}{|c_l|\sum|c_i|} \tag{6.3}$$

To allow for strong contrasts step-by-step, all $w_l{}^c>1$ are set to 1 and give models with more contrasts.

In the joint inversion, instead of using the structure of $\mathbf{m}^k$ for $\mathbf{m}^{k+1}$, a parameter vector $\mathbf{P}$ is determined to introduce structural information. The parameter distribution $\mathbf{p}(r)$ is discretized by M basis functions $\boldsymbol{\psi}_j$ and their coefficients $\mathbf{m}_j$,

$$\mathbf{p(r)} = \sum_{\mathbf{j=1}}^{\mathbf{M}} \mathbf{m_j}\boldsymbol{\psi}_\mathbf{j} \tag{6.4}$$

Thus, the weights $w_l{}^c$ for determining $\mathbf{P}^{k+1}$ are calculated after Eq. 6.3 from $\mathbf{c} = \mathbf{C}\mathbf{W}_c(\mathbf{m}^k-\mathbf{m}^0)$. Simultaneously, the gradients of $\mathbf{P}^k$ are used to obtain the constraint weights for $\mathbf{m}^{k+1}$.

The iterative joint inversion scheme for combined seismic refraction and DC resistivity data is presented in Fig. 6.1 after a little modification from Günther and Rücker (2006). From both data sets a mesh incorporating topographical information is created with geophones/shot points and electrode positions as node points. After choosing the starting models V^0 and ρ^0, an appropriate constraint matrix C is created to derive the first iteration models V^1 and ρ^1 independently. Then, a smoothness matrix for the velocity inversion (C_v) is created using the resistivity model after the 1st iteration (ρ^1). Similarly, the smoothness matrix for resistivity

inversion (C_ρ) is built up based on the velocity model after the 1st iteration (V^1). This process is repeated for a number of k iterations until the misfit is converged into a reasonable target (Fig. 6.1).

Since the gradients of one parameter facilitate the development of gradients in the other without enforcing it, in the presence of boundaries or anomalies that can be seen by both methods, the joint inversion produces sharp contrasted models.

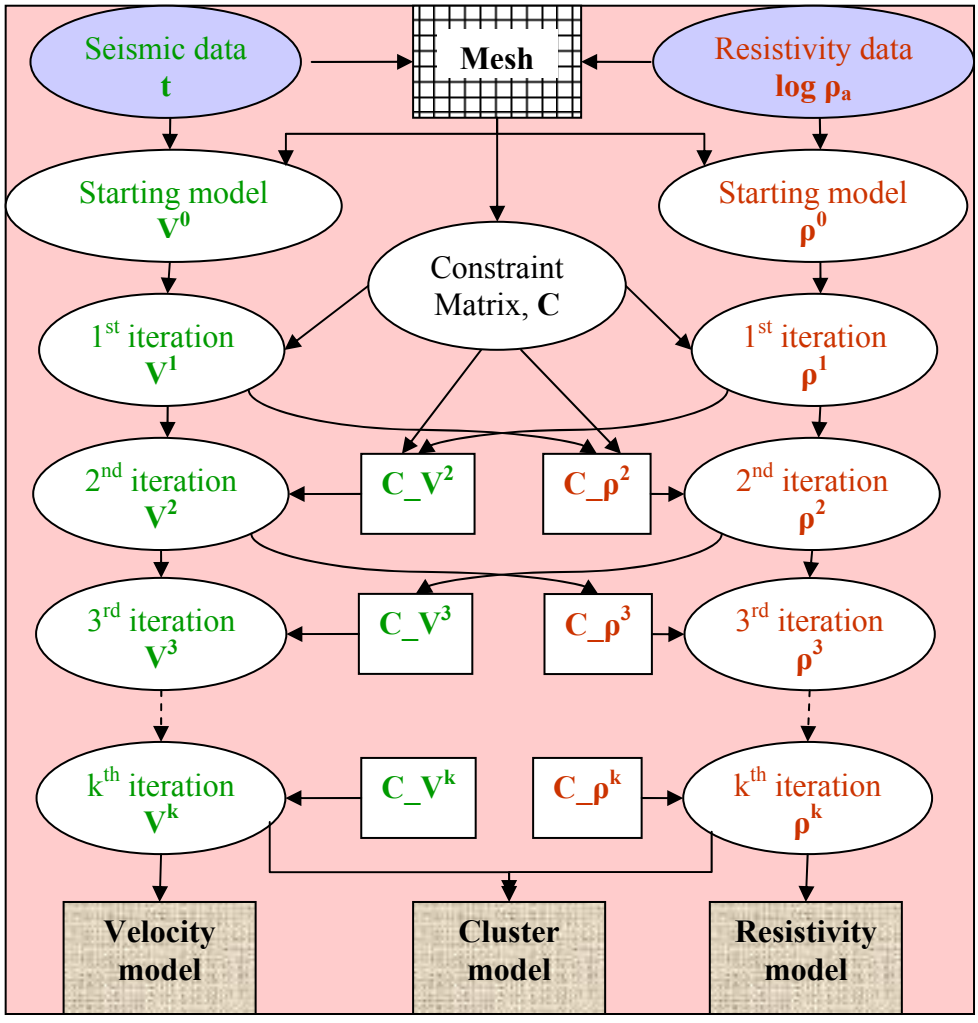

Figure 6.1 *Iterative scheme of the joint inversion procedure for combined seismic refraction and DC resistivity data modified after Günther and Rücker (2006), where t = traveltime arrival, V = velocity, ρ_a = apparent resistivity, and ρ = resistivity.*

6.2 Data processing using joint inversion

The data of the seismic refraction were the first arrival travel times and for the DC resistivity it was the logarithms of the apparent resistivities collected using Wenner-alpha as already

discussed in chapters 4 and 5, respectively. The model parameters are the logarithms of the cell velocities and resistivities. To solve the forward problem, a shortest path algorithm (Dijkstra, 1959) is used for the seismic part and the techniques of Rücker et al. (2006) for the resistivity part.

In order to perform the joint inversion, the subsurface model has been divided into triangular cells using a software package called GIMLi (Geophysical Inversion and Modeling Library, which is developed in LIAG). It can work for three types of joint inversions: one-parameter, petrophysical, and structural joint inversions.

In our case we use the structural joint inversion called structurally coupled cooperative inversion, by coupling structurally the two models in order to yield structurally similar results based on a rectangular mesh. The mesh is refined by dividing each rectangle into four triangles and the sizes of the cells are determined by the position of the velocity/resistivity interfaces. Then the inversion is run in an iterative way based on the joint inversion scheme in Fig. 6.1 until the final models for the velocity and resistivity are obtained within a desired misfit target as shown in Figs. 6.2 and 6.3.

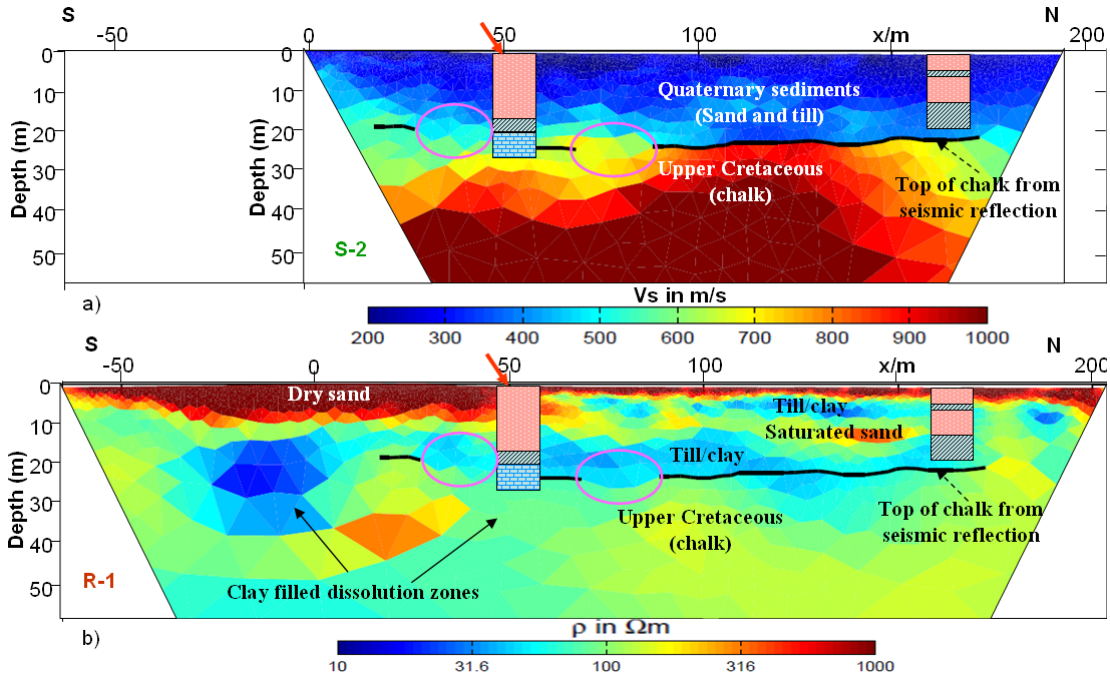

Figure 6.2 *Separate images of (a) S-wave velocity and (b) resistivity sections after joint inversion of profile S-2/R-1. The red arrow indicates the location of an observed sinkhole and purple circles are seismic reflection discontinuities.*

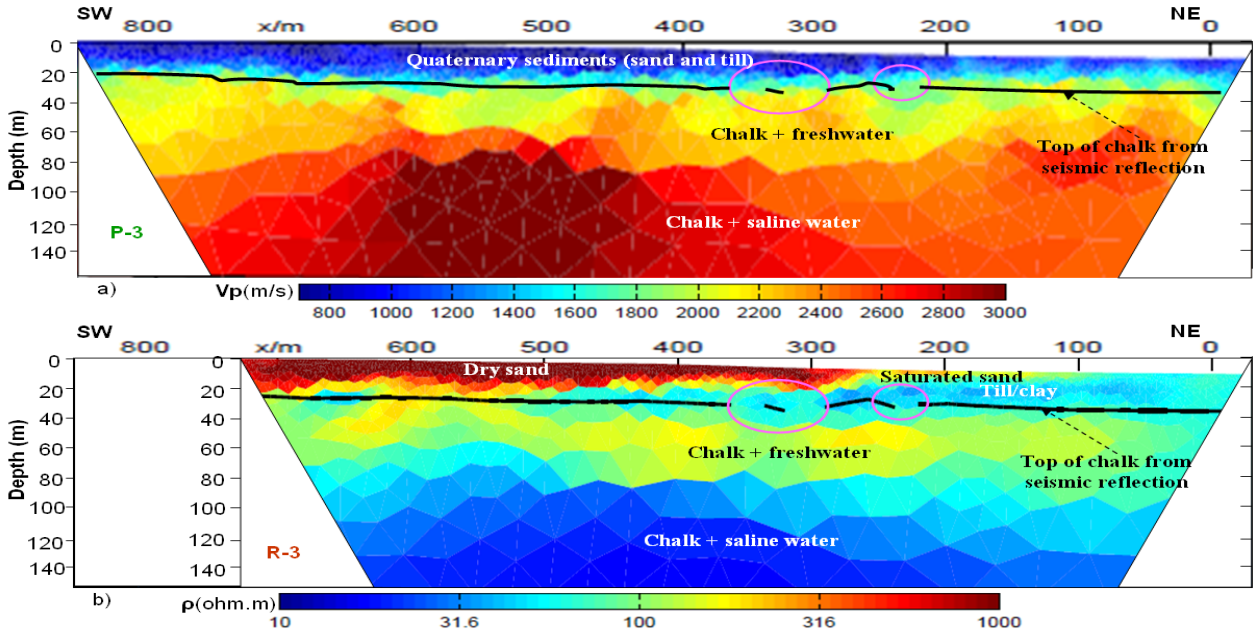

Figure 6.3 *Separate images of (a) P-wave velocity and (b) resistivity sections after joint inversion of profile P-3/R-3. Purple circles refer to discontinuities in the seismic reflection section.*

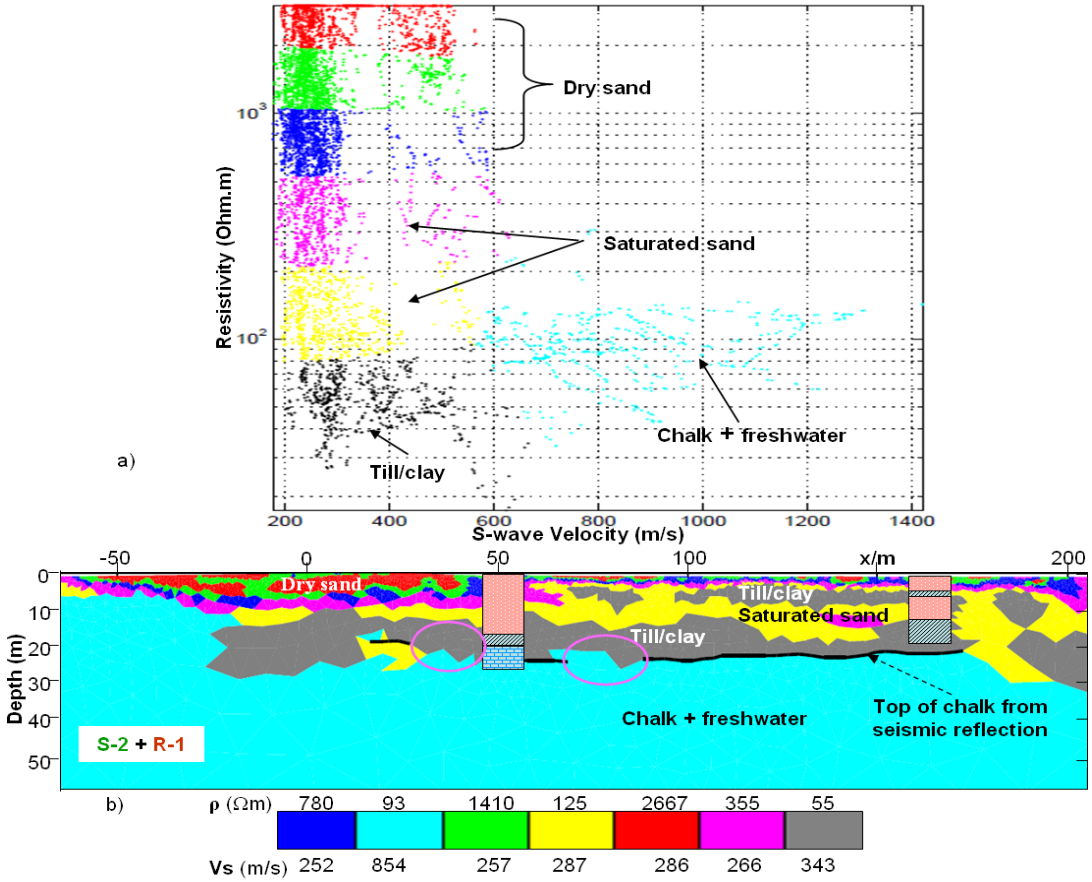

Figure 6.4 *(a) Data plots on velocity vs. resistivity and (b) a 2D combined image of velocity and resistivity model after cluster analysis for profile S-2/R-1. Purple circles are seismic reflection discontinuities. The negative x-coordinates are only verified by resistivity data.*

Furthermore, a combined image of the subsurface is obtained by a cluster analysis because it helps to map the geologic features that cannot be seen using individual inversions and reduces the ambiguity of the final stratigraphic model. The clustering technique works by minimizing the Euclidean distances of each data set and restricting to a number of layers (Th. Günther, pers. comm.). In our case, the clustering analysis is done by restricting the number of layers to 7 as shown in Figs. 6.4 and 6.5.

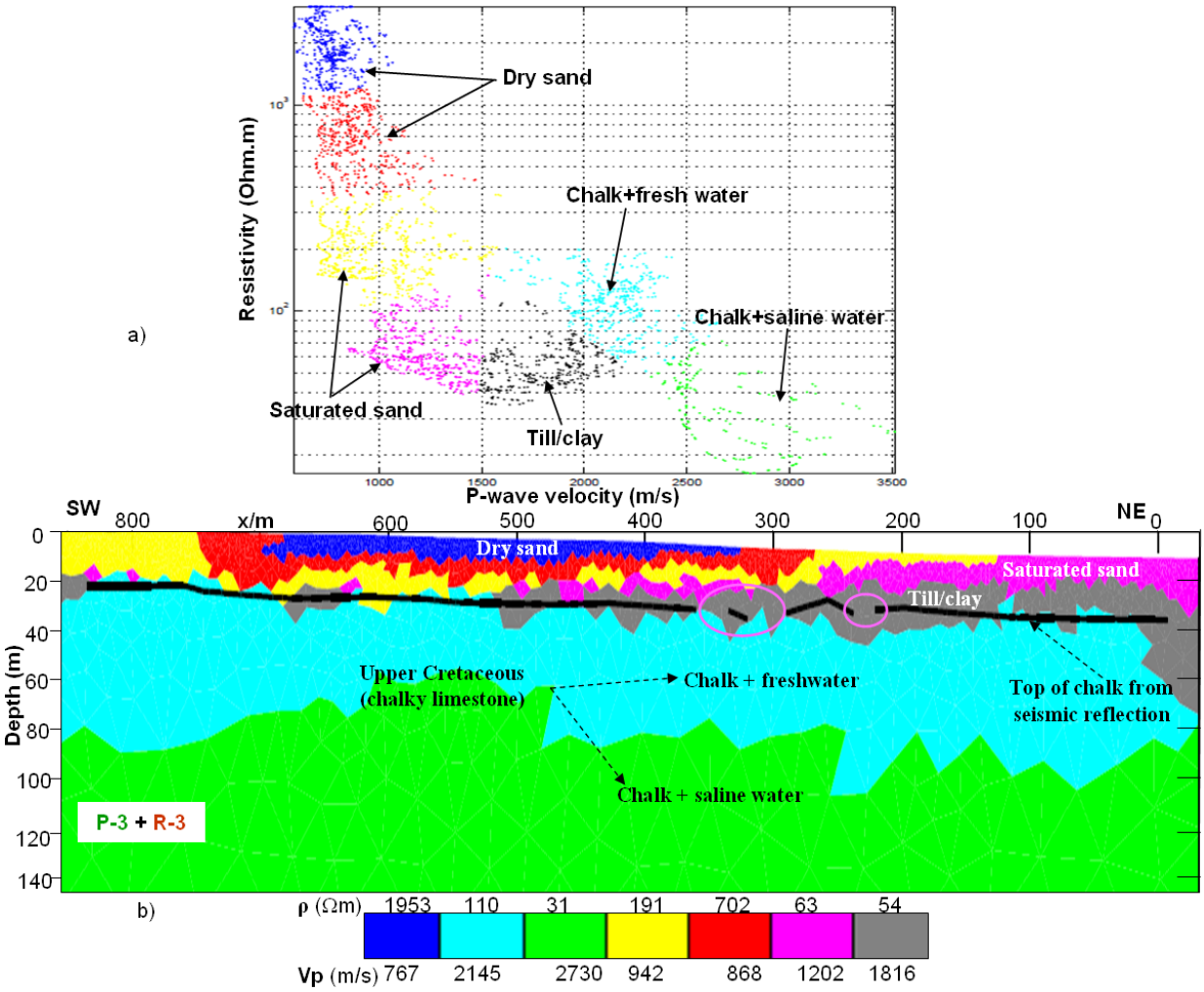

Figure 6.5 *(a) Data plots on velocity vs. resistivity and (b) a 2D combined image of velocity and resistivity model after cluster analysis for profile P-3/R-3. Purple circles are seismic reflection discontinuities. x-coordinates >715 m are only verified by velocity data.*

6.3 Joint inversion results and interpretations

The joint inversion results of the 2D seismic refraction tomography are compared with results of the 2D electrical resistivity tomography (Figs. 6.2 and 6.3). They show sharp contrasted models when the boundary can be seen by both methods. For example, a good compatibility is

found at about 20 meters with a strong velocity contrast that is interpreted as the top of the upper Cretaceous chalk layer (Figs. 6.2a and 6.3a). According to Figs. 6.2b and 6.3b, two low resistivity layers at about 5 and 15 meters depth are clearly seen and interpreted as the till/clay layers that also coincide to borehole logs. Some discontinuities with low resistivity below 20 meter depth are also observed which could be due to clay filled dissolution zones in the chalk layer.

Generally, the results from cluster analysis of the joint inversions of the two profiles (Figs. 6.4 and 6.5) indicate five velocity and resistivity layers in the study area. These are interpreted as dry sand, saturated sand, till/clay, fresh water saturated chalk and saline water saturated chalk layers.

The cluster model of S-2/R-1 (Fig. 6.4) shows that the subsurface section of the study area consists of four layers up to a total depth of 50 m. The first shows small thickness ranging from 1 - 5 m corresponding to the dry sand deposits and exhibits large variations of the resistivity values between 780 – 2667 ohm.m and S-wave velocities between 252 and 286 m/s. The second layer represents saturated sand about 5 m thick and exhibiting resistivity values between 125 and 355 ohm.m. The S-wave velocity for the saturated sand layer is about 266 – 287 m/s and thus almost similar to the dry sand layer. The third layer with resistivity about 55 ohm.m represents thin till/clay layer with S-wave velocity of about 343 m/s. The fourth layer below 20 meters depth has a resistivity value about 93 ohm.m, S-wave velocity of 854 m/s and corresponds to the upper Cretaceous saturated chalk layer.

In a similar way from the cluster model of the P-3/R-3 profile (Fig. 6.5), the above four layers are interpreted using P-wave velocities and resistivities plus one more layer at a depth of greater than 60 m, which has higher velocity (Vp= 2730 m/s) but low resistivity (<31 ohm.m) that might be due to salt water intrusion inside the chalk layer.

Table 6.1 summarizes the velocity (for both P- and S-waves) and resistivity distributions of the five interpreted geologic layers in the study area. The P- and S-wave velocity distributions of the interpreted layers are well-matched to the velocity distributions of different sediments and fluids as shown in Table 3.1 after Fertig (2005).

Depth (m)	Vp (m/s)	Vs (m/s)	Vp/Vs ratio	Poisson´s ratio	Resistivity (ohm.m)	Lithology
0-5	767-868	252-286	3.0	0.44	780-2667	Dry sand
5-10	942	287	3.3	0.45	125-181	Saturated sand
10-18	1816	343	5.3	0.48	54-55	Till/clay
18-60	2145	854	2.5	0.41	93-110	Chalk+freshwater
>60	2730				<31	Chalk+saline water

Table 6.1 *Velocity, Poisson's ratio and resistivity distributions for interpreted geologic layers at Münsterdorf. The colors are analog to Figs. 6.4 and 6.5.*

Moreover, the Vp/Vs and Poisson's ratio, which are calculated by extrapolating the P- and S-wave velocity data from the two profiles, show agreeable results for the interpreted lithologic layers. According to many authors (e.g., Hamilton, 1979), several conclusions can be drawn from measurements of Poisson's ratios for sediments and rocks. Unconsolidated, shallow, (brine) saturated sediments tend to have very high Poisson's ratios of 0.40 and greater as we can see also from our data. Since Poisson's ratios tend to decrease as porosity decreases and when the sediments become more consolidated, the chalk layer shows a relatively lower value (Table 6.1).

7 INTEGRATED RESULTS AND DISCUSSIONS

The most important objectives in this thesis are the investigations of the geology and of the sinkhole conditions. Therefore, the structures in the subsurface, lithology, and dissolution zones are investigated using integrated geophysical methods such as the seismic reflection, seismic refraction tomography, and electrical resistivity imaging surveys by incorporating information also from boreholes and regional geology.

From previous regional studies (e.g., Baldschuhn et al., 2001), we know that in the underground of Münsterdorf the Permian salt dome Krempe-Lägerdorf is situated. Due to its uplifting, upper Cretaceous carbonate layers normally deep seated at about 1000 meter were moved to a near-surface position up to 20 meters depth. The geology in the near surface consists of Quaternary sediments deposited during the Pleistocene glaciations and the underlying upper Cretaceous carbonate (chalky limestone) layers. The Pleistocene sediments mainly consist of glaciofluvial sands and marly to clayey glacial tills. The topography is characterized by a slowly varying gentle slope consisting of glaciofluvial sand and plains of till (chapter 2).

Seismic reflection surveys for both P- and S-wave data were collected to detect deep faults, fracture zones, and karstic features that may lead to the formation of the linearly aligned sinkholes; to locate the depth to carbonate layers and the salt dome and to determine the lateral and vertical situation of the leachable horizons that lead to hazards of sinkhole collapse (chapter 3). For near surface (e.g., shallower than 20 m) velocity and resistivity information, the first break arrivals of the seismic wave data of both the P- and S-waves were used for 2D seismic refraction tomography (chapter 4) and DC electrical resistivity data were measured for 2D electrical resistivity inversion (chapter 5). Moreover, by combining the seismic and DC resistivity data, a joint inversion was carried out along two selected profiles (chapter 6) for site investigation to delineate the subsurface expression of this growing chalk dissolution induced sinkholes and assess the risk for future development of the study area.

The success of the integrated geophysical investigation depends on the data coverage, data quality, penetration depth, reliability and validation in physical properties and resolution contrasts of each method. In this chapter, each geophysical method we used and their integrated results will be discussed in such perspectives.

Are the data coverage and qualities appropriate to provide enough information?

Enough data coverage is important for the resolution of the resulting models since some anomalies can be missed using sparse data sets.

In the case of seismic reflection survey the data coverage is expressed in terms of the CMP folds (Eq. 3.27). Based on Steeples (2005) recommendation, the fold should range between 6 and 60 for near surface investigations because the data quality or signal-to-noise ratio increases as the square root of the CMP fold. Moreover, the quality of the velocity analysis also depends on the fold. As already shown in Tables 3.4 and 3.5, the maximum folds are even more than 60 up to 120 for the P-wave data and up to 46 for the S-wave data. Thus, the data quality for profile P-1 is relatively higher than the other profiles. Generally, the S-wave data are poor in signal-to-noise ratio comparing to the P-wave data due to the complex data acquisition technique and the effects of the surface waves. Since the survey lines are not asphalted or concrete, most of the reflection amplitudes for the S-waves are obscured by the surface L-wave amplitudes.

The travel time first arrival picking for the seismic refraction analysis was performed manually for both the P- and S-wave data. Since the type of seismic data was collected using vibroseis and correlated with the sweep (see section 3.3), determining the first arrival time picks was difficult. To avoid such difficulty, we compared with samples of traces collected using hammer sources at the same location for the P-wave data. Accordingly, time picking was made at the positive peak of the first break arrival time for each trace. Comparatively, picking of the first arrival travel times is more difficult from the S-waves than the P-waves. Thus, the data quality for the P-waves is better than for the S-waves. The ray density or coverage is enough to make confidential interpretations based on the inverted results.

The DC resistivity data were collected using both Wenner-alpha and Wenner-beta arrays. In general, the data accuracy assessed by the measurement equipment for the surveys conducted by Wenner-beta array showed relatively higher noise level than the ones conducted by the Wenner-alpha array. This could be due to the higher geometric factor for the Wenner-beta than for the Wenner-alpha. According to Günther (2004), the maximum relative error of apparent resistivity can be predicted as the sum of the relative errors of the configuration factor (geometrical error) and the potential difference due to minimum accuracy of the

measuring device (instrumental error). The Wenner-alpha array has a good vertical resolution and it is an attractive choice for surveys in a noisy area due to its high signal strength. Whereas the Wenner-beta was a suitable choice for good lateral resolution and coverage. Thus, due to the presence of noise (for example, wire fences and power lines) in the study area and the limited sensitivity of our resistivity meter for higher depths, the Wenner-alpha data are found better in quality than the Wenner-beta data. However, in terms of coverage, the combination of both arrays is appropriate to provide enough information.

Are the depths of investigations appropriate enough according to our objectives?

The seismic reflection is better to see deeper than the refraction tomography and resistivity imaging. However, better interpretations are given from the velocity and resistivity information for the near surface.

For a seismic reflection survey with n number of geophones and a maximum depth of interest z, the geophone spacing interval would be ≈ z/n and the smallest offset is often < z/n (Steeples, 2005). This implies that the shot and geophone intervals must be proportional to the reflector depth of principal interest. At the study area Münsterdorf a maximum number of 240 geophones (profile P-1) were planted for P-wave survey with 5 m spacing on a fixed spread in order to attain a maximum depth of investigation down to ≈ 1200 m. This enables us to see down to the Permian salt dome at 800 m depth. Similarly, for the S-wave survey 120 geophones were used with 1 m spacing which could aim at a depth target up to ≈ 120 m using enough energy sources. However, thinking of the micro vibrator (Elvis-4) we used to collect our SH-wave data and the noise from surface waves due to unconsolidated soil cover, more emphasis is given to the upper ≈ 50 m depth by removing (muting) the late arrival data during data processing.

The maximum depth of investigation for the seismic refraction survey is about 1/3 of the spread length. Thus, the depth of investigation for the P-wave refraction tomography could go up to ≈ 400 m maximum depths given that there are refraction arrivals to this offsets. However, we give more emphasis down to 120 m depth by limiting the starting model for ray tracing to see detailed structures and smaller anomaly zones near to the surface (Figs. 4.5 and 4.6). For the S-wave refraction tomography the maximum depth of investigation is down to ≈ 40 m.

In the case of electrical resistivity survey, three profiles (R-1, R-2, and R-5) are conducted with 2 m electrode spacing and the two profiles (R-3 and R-4) are with 5 m electrode spacing using a maximum number of 161 electrodes (R-2). Both Wenner-alpha and Wenner-beta arrays are selected for each survey line by considering the resolution and depth of investigations. By 1D sensitivity analysis (Edwards, 1977), the maximum depth of investigation goes down from 44 m (for R-1) to 130 m (for R-3 and R-4) for the Wenner-alpha data. Similarly, for the Wenner-beta data it goes down to 32 m (R-1) and 83 m (R-3) of maximum depths.

How reliable and valid are the results in terms of the physical properties of the sediments and interpreted geology?

The application of different geophysical methods can reveal features or anomalies in the subsurface depending on their physical properties. Accordingly, the seismic reflection method is better to interpret deeper structures and depositional facies from the reflection discontinuities due to changes in impedances. The refraction tomography looks to the bed rocks and weak zones based on velocity variations. The clay infill dissolution zones provide good contrasts in electrical properties with the chalk, allowing detection through 2D electrical resistivity imaging. Moreover, the joint inversion results of the seismic refraction and the DC resistivity data investigate well the characteristics of the sand and tills of the Quaternary sediments shallower than 20 m depth with respect to the Vp/Vs, Poisson's ratio and their resistivity values.

Since no borehole data is available below 20 meters depth in the study area, the stratigraphic and lithological conditions that create seismic reflections are identified by correlation with the regional geology (chapter 2). According to the results from the 2D seismic reflection sections five major geologic units are interpreted, from the oldest to the youngest, as salt dome (Permian), claystone/sandstone (Jurassic), claystone/marl (lower Cretaceous), chalky limestone (upper Cretaceous), and the Quaternary sediment layers (Fig. 3.38). The top of the salt dome is detected at a depth of about 600 to 800 meters and is overlain by horizontally stratified Mesozoic sedimentary rocks. Although it is not common to find Jurassic layers on top of the salt domes in north Germany because of denudation (see section 2.1.1 and Fig. 2.9) some Jurassic rock layers are interpreted from the results of the new seismic sections at depths from 600 to 800 meters which might be remnants due to a massive Palaeo-sinkhole that

subsided over the salt layer before the erosion period. Their bedding is tilted hence the subsidence occurred after deposition of the sediments. A very interesting issue here is that these rocks are economically important hydro-carbon source rocks in north Germany. From this we may see some advantages of palaeo-sinkholes namely to preserve treasures from erosion. This layer is sealed by impermeable claystone/marl intercalations (lower Cretaceous) at depths 500 to 600 meters and between 20 and 500 meters depth the upper Cretaceous chalky limestone is interpreted. Although the seismic method can be used to map the geology in 2D imaging with certain degree of success, in this thesis it was initially applied to detect tectonic faults and seismic discontinuities for the interpretation of sinkholes. In fact, from the results no major fault zones are identified except for a few discontinuities on top of the upper Cretaceous (chalk) layer. These discontinuities are observed along P-1, P-3, S-1, and S-2 profiles (Figs. 3.38 and 3.40). Although there is no major fault detected, the locations of the seismic reflection discontinuities are close to the observed sinkholes and still aligned linearly as shown in Fig. 3.41.

From the seismic reflection method information about the Quaternary sediments in the very near surface that is shallower than 20 meters depth is scarce. Relatively, the S-wave sections are better than the P-wave results for the resolution of the upper 20 meters depth. The enhanced ability to resolve shallow subsurface structures in a medium using S-waves is due to their low propagation velocity and shorter wavelength and data density with CMP spacing of 0.5 m. This is much better than the P-waves with CMP spacing of 2.5 m.

To fill the lack of information at near surface and to image velocity variations of the subsurface the first travel time arrivals of both the P- and S-wave seismic data were used for 2D velocity modeling. According to the P-wave tomography results, five velocity layers are interpreted from the three P-wave profiles (Fig. 4.16). The first layer is up to 15 m depth and has P-wave velocities ranging from 618 – 909 m/s. The second layer shows small thickness ranging from 15 – 21 m depth and exhibits P-wave velocities ranging from 1021 – 1317 m/s. The third layer from 21 – 42 m depth has P-wave velocities ranging from 1395 – 1892 m/s. The fourth layer from 42 – 63 m depth has P-wave velocities ranging between 1657 m/s and 2382 m/s. Finally, the fifth layer is below 63 m depth which exhibits P-wave velocities ranging from 2171- 2736 m/s (see Tables 4.3 and 6.1).

In a similar way, four velocity layers are interpreted from the S-wave tomography results (Fig. 4.17). The first layer is up to 16 m depth (S-1) and has S-wave velocities ranging from 152 – 309 m/s. The second layer is from 12 m (S-2) to 20 m depth, with S-wave velocities between 354 m/s and 444 m/s. The third layer from 20 m to 40 m (from S-2) depth has S-wave velocities ranging from 475 - 942 m/s. A fourth layer S-wave velocity is observed below 40 m depth from S-2 profile ranging between 1009 m/s and 1063 m/s (see Tables 4.3 and 6.1).

From the P- and S-wave 2D tomography sections strong velocity contrasts are observed at about 20 m depth compatible to both the P- and S-wave seismic reflection results and interpreted as the top of the upper Cretaceous chalk layer. Relatively low velocity zones are observed laterally on top of the upper Cretaceous chalk layer that coincides to the reflection discontinuities (Figs. 4.18 and 4.19). This low velocity zones could be due to the collapse of the till/clay layer into the soluble chalk layer or clay filled chalk dissolution zones.

Based on the geology and integrated results of the reflection sections and velocity tomography for both the P- and S-waves the five layers are interpreted as sandy dominant sediments, till/clay rich sediments, the top of the upper Cretaceous chalk (less compacted), hard (compacted) chalk, and salt water intrusion inside the chalk layer as already summarized in Table 4.3.

The aim of the 2D electrical resistivity survey was primarily to investigate clay filled chalk dissolution zones and secondary to differentiate the till/clay layer from the sand and chalk layers of the subsurface by interpreting in terms of the resistivity distributions, geometry and depth of the anomalies. Accordingly, the final inversion results of the 2D resistivity surveys (Figs. 5.19-5.21) can be assessed in terms of the lithological and structural interpretation of the resistivity data. The assessment of inversion results could be ambiguous due to the limited number of values and precision of the data. This ambiguity is influenced by the data coverage (density), the errors in the data, sensitivity of the electrode configuration, and the degree of misfits between the observed and predicted data. For example, the interpretations of inverted models for the Wenner-alpha, Wenner-beta, and the combined resistivity data sets along profile R-1 and R-3 (Fig. 5.22) are discussed by including all available information from boreholes and the seismic reflection results to reduce the ambiguity. Thus, at shallow depths (less than 10 m) all the models of each profile show the same results that coincide to the

lithologic boreholes. Whereas at the center and higher depths the inverted model of the Wenner-alpha data sets show better results. This might be due to higher depth of investigation, higher sensitivity, less data errors and misfits than the Wenner-beta data sets. The information for the left and right lateral sides of the inverted models is better to interpret from the results of the Wenner-beta and the combined data sets. For example, the lithologic borehole along R-1 profile at x = 40 m exactly matches to the inverted models of the Wenner-beta and the combined data sets as shown in Figs. 5.22c and 5.22d, respectively. This shows us the Wenner-alpha array has a good vertical resolution and is less sensitive to noises whereas the Wenner-beta has better lateral resolution but with poor data quality and misfits. Thus, the inverted models for the combined data sets of Wenner-alpha and Wenner-beta show more reliable and valid results both in vertical and lateral ways to the available boreholes and seismic information. In general, the 2D electrical resistivity investigation has improved our understanding of the relationships between the dissolution features, the chalk layer and the Quaternary deposits. All the inversion results show a resistivity contrast between the high resistive dry sand, the saturated sand, the low resistive till/clay, and the chalk layers. Moreover, low resistivity layers less than about 30 ohm.m are observed at depths below 60 to 70 meters from profiles R-3 and R-4. This might be due to saltwater intrusion inside the upper Cretaceous chalk layer. Therefore, based on the 2D electrical resistivity results five lithologic layers are interpreted as dry sand, saturated sand, clay/till, freshwater and saline water saturated chalk layers.

Horizontal resistivity sections for different depths can also be derived from the data of the 2D profiles. Accordingly, the lithologies interpreted from the resistivity values are mapped at depths of 3 - 6 m, 11 – 13 m, 15 -17 m, 20 – 23 m, 23 – 27 m, and 27 -32 m as shown in Fig. 5.23. At shallow depths the study area is mainly covered by the high resistive dry sand and low resistive till/clay sediments (Fig. 5.24a). From the geology (Fig. 2.7) this could be correlated to the Pleistocene glaciofluvial (dominant on the south and western parts) and glacial sediments (dominant on the north and eastern parts), respectively. At higher depths, the thickness of the resistive sand decreases towards south. The upper Cretaceous chalk is exposed at 15 m towards north (Fig. 5.23c) whereas at higher depth (about 20m) in the east and southern parts (Fig. 5.23d). The clay infill dissolution zones provide good contrasts in electrical properties with the chalk, and exactly match with the discontinuities from the seismic reflection results despite of a little misfit (≈ ±10 m) in horizontal positions. This could

be a location problem due to topographical survey or due to the effects of inversion as shown using the synthetic test in Fig. 5.26.

The joint inversion results of the 2D seismic refraction tomography are compared with results of the 2D electrical resistivity tomography for profiles S-2/R-1 and P-3/R-3 (Figs. 6.2 and 6.3) and show sharp contrasted models when the boundary can be seen by both methods. For example, a good compatibility is found at about 20 meters with a strong velocity contrast and interpreted as the top of the upper Cretaceous chalk layer (Figs. 6.2a and 6.3a) that agree with the seismic reflection results. According to Figs. 6.2b and 6.3b, two low resistivity layers at about 5 and 15 meters depth are clearly seen and interpreted as the till/clay layers that also coincide to borehole logs. Some discontinuities with low resistivity below 20 meter depth are also observed which could be due to clay filled dissolution zones in the chalk layer.

Generally, the cluster analysis of the joint inversions (Figs.6.4 and 6.5) map the geologic features that cannot be seen using individual inversions or the seismic reflection results and reduce the ambiguity of the final stratigraphic models especially for the near surface Quaternary sediments. The results indicate five velocity and resistivity layers in the study area. These are interpreted as dry sand, saturated sand, till/clay, fresh water saturated chalk and saline water saturated chalk layers.

The cluster model of S-2/R-1 shows (Fig. 6.4) that the subsurface section of the study area consists of four layers up to a total depth of 50 m. The first shows small thickness ranging from 1 - 5 m corresponding to the dry sand deposits and exhibits large variations of the resistivity values between 780 – 2667 ohm.m and S-wave velocities between 252 and 286 m/s. The second layer represents saturated sand about 5 m thick and exhibits resistivity values between 125 and 355 ohm.m. The S-wave velocity for the saturated sand layer is about 266 – 287 m/s and thus almost similar to the dry sand layer. The third layer with resistivity about 55 ohm.m represents thin till/clay layer with S-wave velocity of about 343 m/s. The fourth layer below 20 meters depth has resistivity values about 93 ohm.m, S-wave velocity of 854 m/s and corresponds to the upper Cretaceous saturated chalk layer. In a similar way from the cluster model of profile P-3/R-3 (Fig. 6.5), the above four layers are interpreted using P-wave velocities and resistivities plus one more layer at a depth of greater than 60 m, which has higher velocity (Vp = 2730 m/s) but low resistivity (<31 ohm.m) that might be due to salt water intrusion inside the chalk layer which is common in north Germany. For example,

according to Iwanoff (1998), saline water is ascending from deeper parts of the chalk and infiltrates into pits due to the relief of hydraulic pressure during mine water pumping in the Lägerdorf quarry sites which is located at southeastern part of the study area.

Table 6.1 summarizes the velocity (for both P- and S-waves) and resistivity distributions of the five interpreted geologic layers in the study area. The P- and S-wave velocity distribution of the interpreted layers is well-matched to the velocity distributions of different sediments and fluids as shown in Table 3.1 after Fertig (2005). Moreover, the Vp/Vs and Poisson's ratio, which is calculated by extrapolating the P- and S-wave velocity data from the two profiles, show agreeable results for the interpreted lithologic layers. According to many authors (e.g., Hamilton, 1979), several conclusions can be drawn from measurements of Poisson's ratios for sediments and rocks. Unconsolidated and shallow sediments tend to have rather high Poisson's ratios of 0.40 and greater as we can see also from our data. Since Poisson's ratios tend to decrease as porosity decreases and when the sediments become more consolidated, the chalk layer shows lower values (Table 6.1).

The physical properties of the sediments and the contrasts of the geologic models from all the integrated geophysical methods clearly show that the results are reliable and valid to make the given interpretations and conclusions by calibrating with the borehole data.

How are the sinkhole or dissolution conditions related to the geology in the study area?

Although all methods can give accurate and detailed information of the subsurface interfaces, their results must be integrated to draw some conclusions about the cause and location of the sinkhole vulnerable area.

Thus, from all the methods, most of the observed sinkholes and the seismic discontinuities are located on the contact zone between the glaciofluvial sand and the marly to clayey glacial till layers (Fig. 7.1). The 2D resistivity and the lithology from boreholes confirm sandy sediments are dominant on top of the chalk instead of till/clay near to the observed sinkholes and the reflection discontinuities.

According to Farrant (2001), geological mapping of the upper Cretaceous chalk of southern England has demonstrated, karst features are more widespread than previously recognized and

most of them are distributed close to the contact with overlying Palaeogene strata and Quaternary deposits, where extensive point recharge is concentrated. The karst features are dissolution pipes that occur as conical, sediment filled cavities that developed from the surface and extend down into the chalk. Large caves are rare, despite the capacity of the chalk to support significant roof spans. However, mixing of highly saturated water from diffuse flow through the porous chalk with less saturated water flowing through open fractures and bedding planes will generate zones of enhanced dissolution by producing a sponge-work pattern of voids along bedding partings.

Based on the geophysical investigations in this thesis, a similar situation is happening in north Germany particularly at the study area (Münsterdorf) with the same geologic settings of the upper Cretaceous chalk which is pushed up to near surface (about 20 meters depth) by the Permian salt dome and overlain by the Quaternary sediments. Thus, mapping of the Quaternary deposits allows us a better prediction of where dissolution features could occur.

In most of the study area, there is an unconfined sand aquifer underlain by an irregularly discontinuous aquiclude of marly to clayey glacial till layer at 12 to 18 meters depth just over the upper Cretaceous chalk (Fig. 7.1). This thin layer may prevent the infiltration of rainwater into the chalk and separate the chalk aquifer from the shallow sandy aquifer above it. But at the north and northeast of the site, the shallow sand aquifer is confined between a nearly E-W striking thin till/clay layer at 3 to 5 meters depth and a similar layer at 12 to 18 meters depth over the chalk.

From borehole measurements near to the football area, the surface water table is found at about 2 m depth or 6 m above sea level. Based on Iwanoff (1998), the shallow sand aquifers are affected by dewatering due to hydraulic connections to the chalk layer caused by mine pumping in the open quarries of chalk at Lägerdorf (see section 2.2.3). Therefore, groundwater movements in the chalk strata due to dewatering could also influence the recharge zones in the overburden Quaternary sediments (for example, through the geologic boundaries) and also increase the dissolution rate of the chalk. When the bedrock water table inside the chalk layer declines rapidly, the dissolution zones or cavities may collapse due to loss of fluid-pressure support inside them as shown in Fig. 7.1.

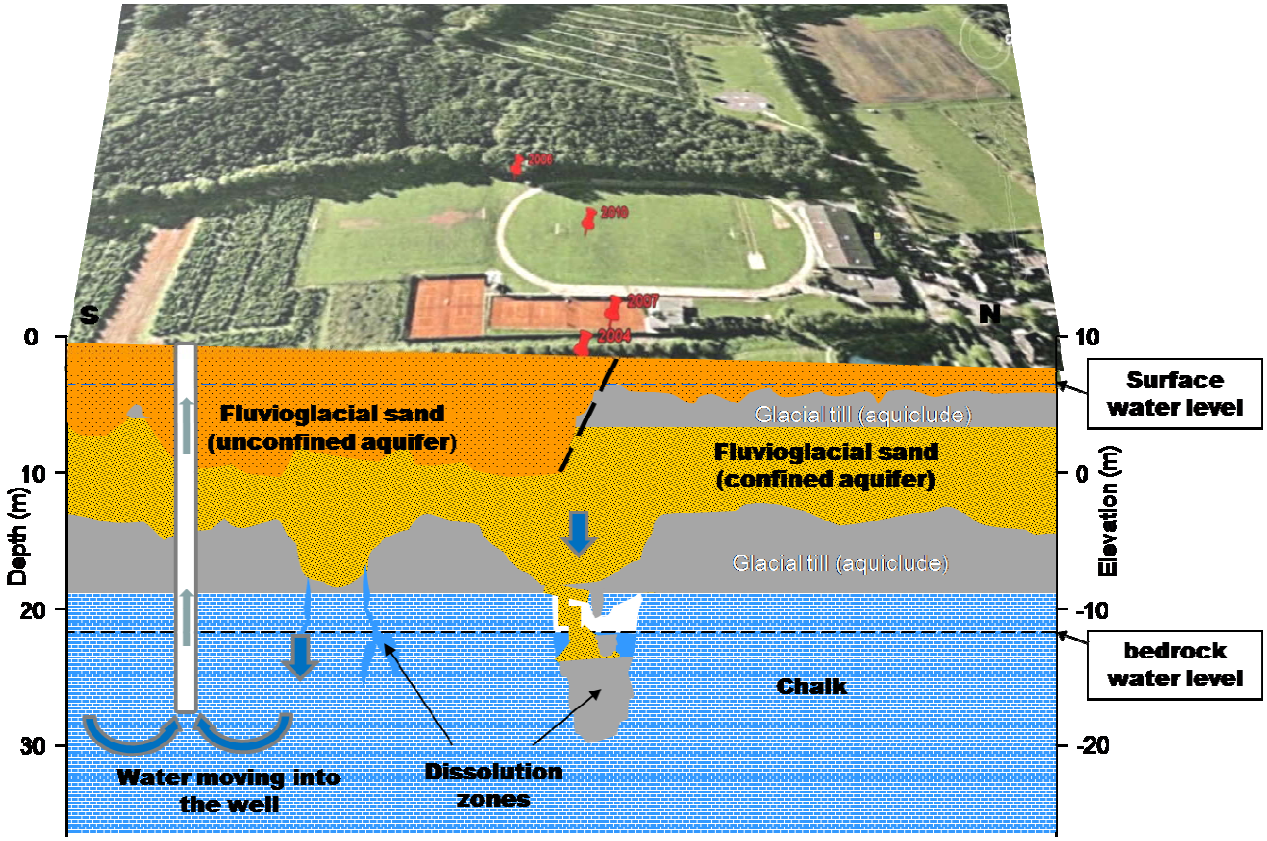

Figure 7.1 *A 2D sketch along the football area that indicates the possible geologic, groundwater and sinkhole conditions.*

Accordingly, the occurrences of the Münsterdorf sinkholes may be mainly dependent on the presence of discontinuous impermeable till/clay layers, whereas groundwater flow through the chalk is strongly influenced by the lithologic boundary (contact zones) between the confined and unconfined sand aquifers.

From all our results and reasonings, the sinkhole vulnerable site in the study area is mapped finally as shown in Fig. 7.2. Clearly, the observed sinkholes and all the anomalies from geophysical methods are located in areas near to the lithologic boundary (contact zone) between the glaciofluvial sand and the glacial till/clay layers where there may be concentrated recharge. Moreover, the shallow glacial till/clay layer might cause geotechnical problems at the adjacent margin with the sand by swelling and shrinking when the surface water level fluctuates, since the clay minerals are capable of absorbing water in between the silicate layers held by weak bonds.

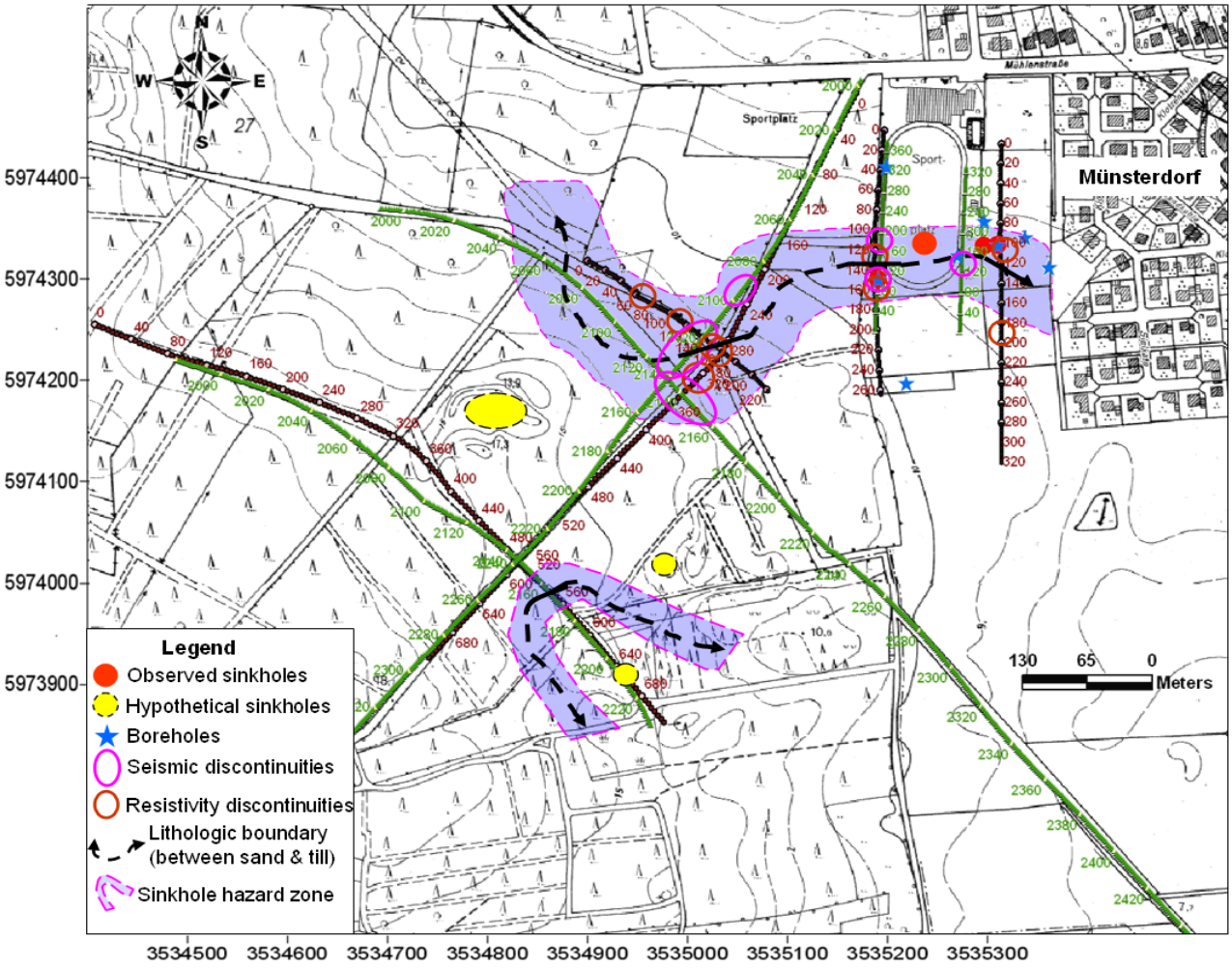

Figure 7.2 *A map of sinkhole vulnerable zone at Münsterdorf interpreted from the integrated geophysical results.*

8 CONCLUSIONS AND RECOMMENDATIONS

8.1 Conclusions

All the geophysical methods and their integrated results can give rather accurate and detailed information of the subsurface interfaces to draw some conclusions about the cause and location of the sinkhole vulnerable area. Therefore, based on the objectives and the results from the geophysical investigations, the following conclusions are drawn about the sinkhole conditions at Münsterdorf-Lägerdorf area.

1. The methods we used are adequate for the investigation of sinkholes and the integrated geophysical results give a clear picture of the distribution of the physical properties.

2. The occurrence of the sinkholes in the study area appears to be due to the dissolution of the carbonate chalk layer at about 20 m depth. The Krempe-Lägerdorf salt dome detected at 600 to 800 meters depth is not directly involved in the occurrence of the sinkholes but indirectly by having pushed up the carbonate chalk layer from about 1000 m depth towards the near surface up to 20 m depth.

3. No prominent faults or tectonic structures are observed near to the aligned sinkholes. But in the seismic reflection sections some discontinuous zones in the near surface are detected on the top of the chalk layer, which are also aligned linearly with the observed sinkholes and might hint to dissolution zones. Moreover, from the resistivity and seismic refraction tomography sections, lower resistivity and velocity zones are detected near to the seismic reflection discontinuities and below the observed sinkholes on top part of the chalk and this might also be a hint to clay filled chalk dissolution zones.

4. Mapping of the Quaternary sediments that cover the chalk layer allows better prediction of where dissolution features may occur. Most of the observed sinkholes and the interpreted dissolution zones from the geophysical anomalies seem to be located on a geologic boundary or contact zone between the fluvioglacial sand and the glacial till/clay layers at the surface.

5. In most part of the study area, the chalk is covered by an irregularly discontinuous aquiclude of marly to clayey glacial till layer at 12 to 18 meters depth. But, permeable sandy sediments are dominant on top of the chalk instead of the impermeable till/clay near to the observed sinkholes and the dissolution zones, which might be due to erosion. Thus, where the cover is sand a high density of dissolution features in the chalk may be expected. In areas of more cohesive cover (such as the till/clay layer) the density of dissolution features tends to be less.

6. Groundwater movements in the chalk strata due to dewatering could also influence the recharge zones in the overburden Quaternary sediments (for example, through the geologic boundaries) and also increase the dissolution rate of the chalk. When the bedrock water table inside the chalk layer declines rapidly, the dissolution zones or cavities may collapse due to loss of fluid-pressure support inside them.

7. The occurrences of the sinkholes at Münsterdorf may be mainly dependent on the presence of permeable sand on top of the chalk due to erosion of the impermeable glacial till layer at 12 to 18 meters depth and the presence of adjacent impermeable till/clay to the permeable sand layers at the surface, whereas groundwater flow through the chalk is strongly influenced by the geological boundary or contact zones. In other words, in areas of concentrated groundwater recharge along the geological boundary, conduits or dissolution zones will develop. Therefore, the discontinuous till/clay impermeable margins at 12 to 18 meters depth on top of the chalk and/or contact zones between the permeable fluvioglacial sand and adjacent impermeable glacial till/clay layers at 3 to 6 meters depth are the potential sinkhole hazards in the study area.

8. Moreover, the shallow glacial till/clay layer at 3 to 6 meters depth might cause geotechnical problems at the adjacent margin with the sand by swelling and shrinking when the surface water level fluctuates. This is because the clay minerals are capable of absorbing water between the silicate layers held by weak bonds and increase its volume.

8.2 Recommendations

Based on the outcomes of this study, the following recommendations are forwarded.

1. As the chalk is found near to the surface in the town, a good understanding of the geohazards and risks associated with the dissolution zones is essential to prevent hazards and costly engineering works. Therefore, further investigation should be made to map the contact zone between the impermeable glacial till and the permeable fluvioglacial sand in the whole town.

2. Pumping groundwater at the contact zone should be avoided since it enhances the groundwater flow between the confined and unconfined shallow aquifers and facilitates the dissolution rates of the chalk.

3. Borehole geophysics is needed for further validation of the velocity and resistivity data and to better characterize the physical properties and to derive some empirical relationships between the velocities and the resistivities with regard to the porosity, permeability**,** transmissivity, and hydraulic conductivity nature of the sediments in the study area.

4. Further processing of the P-wave seismic reflection data by giving more weight to the higher depths from 600 to 800 m is recommended for searching of hydro-carbon rich rocks or bright spots in the palaeo-sinkhole.

5. The chalk layer below 60 m depth is saturated with salt water. If mining of the chalk for cement and lime production (e.g., Lägerdorf) extends below this depths, the waste water salinity has to be considered as it may have a negative impact for the environment.

Bibliography

Aki, K. and Richards, P. (1980) Quantitative seismology: Theory and methods. 557pp., Freeman, San Francisco.

Al-Zoubi, A., Abueladas, A-R., Camerlynck, C., Al-Ruzouq, R, Al-Rawashdeh,S., Ezersky, M., and Ali, W. (2007) Use of 2D multi electrodes resistivity imagining for sinkholes hazard assessment along the eastern part of the Dead Sea, Jordan., American Journal of Environmental Sciences 3(4), 229-233.

ASTM (1999) Standard Guide for Selecting Surface Geophysical Methods, Designation D-6429. American Society for Testing and Materials, Philadelphia, 11pp.

Baker, G.S. (1999) Processing near-surface seismic-reflection data- a primer. Course notes series, no. 9. SEG.

Baldschuhn, R., Binot, F., Fleig, S., and Kockel, F. (2001) Tectonic atlas of Northwest Germany and the German North sea sector - structures, structural development and Palaeogeography. Geol. Jb., A 153: 88 S., 3 CD's; Hannover.

Beck, B.F. (1984) Sinkholes: Their geology, engineering and environmental impact: Proceedings of the first multidisciplinary conference on sinkholes and the environmental impacts of karst, Orlando, FL, October 15-17, 1984.

Beck, B.F. and Herring, J.G. (2001) Geotechnical and Environmental Applications of Karst Geology and Hydrology. Taylor and Francis, ISBN 90 5809 1902.

Beck, B.F. (2003) Sinkholes and the engineering and environmental impacts of karst. Geotechnical special publication No. 122. American society of civil engineers.

Belka, Z. and Narkiewicz, M. (2008) Devonian. In: McCann, T. (eds.) The Geology of Central Europe. Volume 1: Precambrian and Palaeozoic. Geological Society, London, 383-410.

Bell, F.G. (1992) Salt mining and associated subsidence in mid-Cheshire, England, and its influence on planning. Bulletin Association Engineering Geologists, 29, 371-386.

Bell, F. G. (2007) Engineering geology, 2nd edition. Elsevier

Benson, R.C. and Yuhr, L.B. (1987) Assessment and long term monitoring of localized subsidence using ground penetrating radar. In: Beck, B.F. and Wilson, W.L. (eds.), Karst hydrogeology: Engineering and environmental applications, pp. 161-169. Balkema, Rotterdam.

Benson, R. C., Yuhr, L.B., and Kaufmann, R. D. (2003) Assessing the risk of karst subsidence and collapse. In: Beck, B.F. (eds.) Sinkholes and the engineering and environmental impacts of karst. Geotechnical special publication No. 122, 31-39. American society of civil engineers.

Beres, M., Luetscher, M., and Olivier, R. (2002) Integration of ground-penetrating radar and microgravimetric methods to map shallow caves. J. Appl. Geophys, 46 pp.249–262.

Berryman, J.G. (1991) Nonlinear inversion and tomography: Lecture notes. Earth resource laboratory, MIT.

Bishop, I., Styles, P., Emsley, S.J., and Ferguson, N.S. (1997) The detection of cavities using the microgravity technique: Case histories from mining and karstic environments. Geological society special publication, 12, 155-168.

Black, R., Steeples, D., and Miller, R. (1994) Migration of shallow reflection data. Geophysics, v.59, 402-410.

Bonila, C., Rehwoldt, E.B., and Dunscomb, M.H. (2004) Geophysical testing for voids caused by non-compacted backfill, in Proceedings of the Symposium on Engineering Geology and Geotechnical Engineering, 39, p. 197-205.

Bosak, P. and Benes, V. (2003) Geophysical characteristics of epikarst; case studies from Zagros Mts. (Iran) and the Koneprusy region (Czech Republic), Acta Carsologica, 32;2, p. 255-267.

Brune, G. (1965) Anhydrite and gypsum problems in engineering geology. Bulletin Association Engineering Geologists, 3, 26-38.

Brzostowski, M. and McMechan, G. (1992) 3-D tomographic imaging of near-surface seismic velocity and attenuation. Geophysics, 57, 396-403.

Carpenter, P. J., Higuera-Diaz, I. C., Thompson, M. D., Atre, S., and Mandell, W. (2003) Accuracy of seismic refraction tomography codes at karst sites, geophysical site characterization: Seeing beneath the surface, proceedings of a symposium on the application of geophysics to engineering and environmental problems, San Antonio, Texas, April 6-10, pp.832-840.

Chabert, C. (1981) Les Grandes cavite´s Francaises, 154pp. Federation Francaise de Speleologie : Paris.

Claerbout, J.F. and Muir, F. (1973) Robust modeling with erratic data. Geophysics, 38, 826–844.

Constable, S.C., Parker, R.L., and Constable, C.G. (1987) Occam's inversion: A practical algorithm for generating smooth models from electromagnetic sounding data. Geophysics, 52, 289-300.

Dahlin, T. (1996) 2D resistivity surveying for environmental and engineering applications. First break, 14, 275-284.

Debeglia, N., Bitri, A., and Thierry, P. (2006) Karst investigations using microgravity and MASW: application to Orl´eans, France Near Surf. Geophys. 4 215–225.

Deceuster, J., Delgranche, J., and Kaufmann, O. (2006) 2D cross-borehole resistivity tomographies below foundations as a tool to design proper remedial actions in covered karst. Journal of App. Geophysics, 60, 68-86.

Dey, A. and Morrison, H.F. (1979) Resistivity modeling for arbitrarily shaped two-dimensional structures. Geophysical prospecting, 27, 106-136.

Dijkstra, E. W. (1959) A note on two problems in connexion with graphs. Numerische Mathematik, 1:269–271.

Dix, C. (1955) Seismic velocities from surface measurements. Geophysics 20, 68–86.

Dobecki, T. L. and Upchurch, S. B. (2006) Geophysical applications to detect sinkholes and ground subsidence. Leading Edge 25 336–341.

Drew, D. (1985) Karst processes and landforms, 240pp. Macmillan, London.

Edwards, L.S. (1977) A modified pseudosection for resistivity and induced-polarization. Geophysics, 42, 1020-1036.

Ehrmann, W.U. (1986) Zum Sedimenteintrag in das zentrale nordwesteuropäische Oberkreidemeer. Geologisches Jahrbuch A 97, pp. 3–139.

Eissmann, L. (1995) Sachsen. In: Benda, L. (eds.) Das Quartär Deutschlands. 148–198, Berlin, Stuttgart.

Eppelbaum, L., Ezersky, M., Al-Zoubi, A., Goldshmidt, V., and Legchenko, A. (2008) Study of the factors affecting the karst volume assessment in the Dead Sea sinkhole problem using microgravity field analysis and 3D modeling. Advances in Geosciences, Vol. 18: 1-19. www.adv-geosci.net/18/1/2008.

Ezersky, M., Legchenko, A., Kamerlynck, C., and Al-Zoubi, A. (2008) Identification of sinkhole development mechanism based on a combined geophysical study in Nahal Hever South area (Dead Sea coast of Israel), Environmental Geology, doi 10.1007/s00254-008-1591-7 (in-press).

Farrant, A.R. (2001) Karst development in the southern English chalk. In: Beck, B.F. and Herring, J.G. (eds.), Geotechnical and Environmental Applications of Karst Geology and Hydrology, pp.77-82. Taylor and Francis, ISBN 90 5809 1902.

Feist-Burkhardt, S., Götz, A.E., Szulc, J., Borkhataria, R., Geluk, M., Haas, J., Hornung, J., Jordan, P., Kempf, O., Michalik, J., Nawrocki, J., Reinhardt, L., Ricken, W., Röhling, H.-G., Rüffer, T., Török, A., and Zühlike, R. (2008) Triassic. In: McCann, T. (eds.) The Geology of Central Europe. Volume 2: Mesozoic and Cenozoic. Geological Society, London, 749-822.

Fertig, J. (2005) Geschwindigkeits- und Dichtewerte in Sedimenten. In: Knödel, K., Krummel, H., and Lange, G. (eds.) Handbuch zur Erkundung des Untergrundes von Deponien und Altlasten, vol. 3, Geophysik. Springer, Berlin.

Foose, R.M. (1969) Mine dewatering and recharge in carbonate rocks near Hershey, Pennsylvania. In: Kiersch, G.A., Cleaves, A.B., Adams, W.M., Pincus, H.J., and Ferguson, H.F. (eds.) Legal aspects of geology in engineering practice: Geological Society of America, Engineering Geology Case Histories no. 7, pp. 46-60.

Foose, R.M., and Humphreville, J. A. (1979) Engineering geological approaches to foundations in the karst terrain of the Hershey Valley: Bulletin of the Association of Engineering Geologists, v. 16, no. 3, pp. 355-381.

Ford, D.C. and Williams, P.W. (2007) Karst Hydrology and Geomorphology : London, Wiley Chichester, 2nd ed., 576 p.

Gadallah, M. and Fisher, R. (2009) Exploration geophysics. 274pp., Springer, Berlin.

Gallardo, L. A. and Meju, M. A. (2004) Joint two-dimensional dc resistivity and seismic travel time inversion with cross-gradients constraints. J. Geophys. Res., 109:03311.

Garetzky, R.G., Ludwig, A.O., Schwab, G., and Stackebrandt, W. (2001) Neogeodynamics of the Baltic Sea depression and adjacent areas, results of IGCP project 346. Brandenburgische Geowissenschaftliche Beiträge, 8.

Garotta, R. (1999) Shear waves from acquisition to interpretation: Distinguished instructor series, No. 3. SEG, Tulsa, OK USA.

Gebregziabher, B., Günther, T. and, Wiederhold, H. (2010) Joint inversion of seismic refraction and electrical resistivity tomography to investigate sinkholes. Extended abstract, EAGE Near Surface 2010, 06. – 08.09.2010; Zürich, Switzerland.

Gerardi, J. (2009) Forschungsverbundvorhaben ``Dynamik abgesoffener oder gefluteter Salzbergwerke und ihres Deckgebirgsstockwerks``. Exkursionsführer und Veröffentlichungen der Deutsche Gesellschaft für Geowissenschaften (EDGG), Hannover.

Glennie, K.W. and Underhill, J.R. (1998) Origin, development and evolution of structural styles. In: Glennie, K.W. (eds.) Petroleum Geology of the North Sea. Blackwell Scientific Publications, Oxford in press.

Grandjean, G. and Leparoux, D. (2004) The potential of seismic methods for detecting cavities and buried objects: experimentation at a test site. J. Appl. Geophys. 56 93–106.

Günther, T. (2004) Inversion methods and resolution analysis for the 2D/3D reconstruction of resistivity structures from DC measurements. PhD thesis, University of Mining and Technology Freiberg. Available at http://fridolin.tu-freiberg.de.

Günther, T. and Rücker, C. (2005) A triple-grid technique for the 3d inversion of dc resistivity data incorporating arbitrary topography. Extended abstract, EAGE Near Surface Conference, Palermo, Italy.

Günther, T. and Rücker, C. (2006) A new joint inversion approach applied to the combined tomography of DC resistivity and seismic refraction data. Extended abstract, 19. EEGS annual meeting (SAGEEP), 02. – 06.04.2006; Seattle, USA.

Gutierrez, F. and Cooper, A.H. (2002) Evaporite dissolution subsidence in the historical city of Calatayud, Spain: Damage appraisal and prevention. Natural Hazards, 25, 259-288.

Hamilton, E.L. (1979) Vp/Vs and Poisson's ratio in marine sediments and rocks. J. Acoust. Soc. Am., 66(4):1093-1101.

Hansen, P.C. and O´Leary, D.P. (1993) The use of the l-curve in the regularization of discrete ill-posed problems. SIAM J. Sci. Comput., 14, 1487-1503.

Harrison, H.D. and Hiltunen, D.R. (2003) Characterization of karst terrane via SASW seismic wave method. American society civil engineers geotechnical special publication 122, 519-528.

Hertrich, M. and Yaramanci, U. (2002) Joint inversion of Surface Nuclear Magnetic Resonance and Vertical Electrical Sounding, Journal of Applied Geophysics, 50, 179-191.

Hiltunen, D.R., Hudyma, N., Quigley, T.P., Samakur, C. (2007) Ground truthing seismic refraction tomography for sinkhole detection in Florida. Florida department of transport.

Hoover, R.A. (2003) Geophysical choices for karst investigations. American Society Civil Engineers Geotechnical Special Publication 122, 529-538.

Hubral, P., Schleicher, J., Tygel, M., and Hanitzsch, C. (1993) Determination of Fresnel zones from travel time measurements. Geophysics 58, 703–712.

Iwanoff, A. (1998) Environmental impacts of deep opencast limestone mines in Lägerdorf, north Germany. Mine water and the environment, 17, 52-61, DOI: 10.1007/BF02687244.

Jaritz, W. (1969) Epirogenese in Nordwest-Deutschland im höheren Jura und in der Oberkreide. -Geol. Rundschau, 59, 114-124.

Jaritz, W. (1987) The origin and development of salt structures in Northwest Germany. In: Lerche, I. and O´Brian, J. (eds.) Dynamical geology of salt and related structures. Academic Press, Orlando, FL, 479-493.

Johnson, K.S. and Neal, J.T. (2003) Evaporite karst and engineering/environmental problems in the United States. Oklahoma Geological Survey Circular, 109, 353pp.

Kaiser, A., Reicherter, K., Hübscher, C., and Gajewski, D. (2005) Variation of the present-day stress field within the North German Basin-insights from thin shell FE modeling based on residual GPS velocities. Tectonophysics, 397, 55-72.

Kearey, P., Brooks, M., and Hill, I. (2002) An introduction to geophysical exploration. 3rd eds., Blackwell, UK.

Kirsch, R. (2006) Groundwater geophysics: A tool for Hydrogeology, 500pp., Springer Berlin.

Kirsch, R., Liebsch-Dörschner, T., Wiederhold, H. (2004) Wenn der Boden einbricht-Erdfälle in Schleswig-Holstein. –Landesamt für Natur und Umwelt Schleswig-Holstein, Jahresbericht 2004, 201-210.

Kleywegt, R.J. and Enslin, J.F. (1973) The application of gravity method to the problem of ground settlement and sinkhole formation in dolomite on the far west Rand, south Africa. International Association Engineering Geology, Proceedings Hannover symposium on sinkholes and subsidence, T301-315.

Knapp, R. and Steeples, D. (1986) High resolution common-depth-point seismic reflection profiling: Instrumentation. Geophysics, 51, 276-282.

Knödel, K., Yaramanci, U. and, Lange, G. (2007) Joint Inversion. In: Knödel, K., Lange, G. and Voigt, H.-J. (eds.), Environmental Geology: Hand-book of field methods and case studies, pp. 1159-1163. Springer, Berlin.

Kockel, F. (1995) Structural and palaeogeographical development of the German North Sea sector. Beiträge zur regionalen Geologie der Erde, 26, 1-96.

Kozary, M.T., Dunlap, J.C., and Humphrey, W.E. (1968) Incidence of saline deposits in geologic time. Geological Society America Special Paper 88, 43-57.

Krawczyk, C.M., McCann, T., Cocks, L.R., England, R., McBride, J., and Wybraniec, S. (2008) Caledonian Tectonics. In: McCann, T. (eds.) The Geology of Central Europe. Volume 1: Precambrian and Palaeozoic. Geological Society, London, 303-381.

Kroner, U., Mansy, J.-L., Mazur, S., Aleksandrowski, P., Hann, H.P., Huckriede, H., Lacquement, F., Lamarche, J., Ledru, P., Pharaoh, T.C., Zedler, H., Zeh, A., and Zulauf, G. (2008) Variscan tectonics. In: McCann, T. (eds.) The Geology of Central Europe. Volume 1: Precambrian and Palaeozoic. Geological Society, London, 599-664.

Kruse, S., Grasmueck, M., Weiss, M., and Viggiano, D. (2006) Sinkhole structure imaging in covered Karst terrain. Geophysical Research Letters 33: L16405. DOI: 10.1029/2006GL026975.

Kuniansky, E.L. (2005) U.S. Geological Survey Karst Interest Group proceedings, Rapid City, South Dakota, September 12-15, 2005: U.S. Geological Survey Scientific Investigations Report 2005-5160, 296 p.

Langer, W.H. (2001) Potential Environmental Impacts of Quarrying Stone in Karst—A Literature Review U.S. Geological Survey Open-File Report OF-01-0484, p.17.

Lay, T. and Wallace, T. (1995) Modern global seismology. International geophysics series, v.58, 534pp., Academic press, USA.

Legchenko, A.M., Ezersky, M., Boucher, M., Camerlynck, C., Al-Zoubi, A., and Chalikakis, K. (2008) Pre-existing caverns in salt formations could be the major cause of sinkhole hazards along the coast of the Dead Sea. Geophys. Research Letters, 35, L19404, doi:10.1029/2008GL035510, American Geophysical Union.

Leucci, G. (2003) Evaluation of karst cave stability using integrated geophysical methods. GeoActa, 2, p. 75-88.

Litt, T., Schmincke, H.-U., Frechen, M., and Schlüchter, C. (2008) Quaternary. In: McCann, T. (eds.) The Geology of Central Europe. Volume 2: Mesozoic and Cenozoic. Geological Society, London, 1287-1340.

Liu, Z. Yuan, D., and Dreybrodt, W. (2005) Comparative study of dissolution rate-determining mechanisms of limestone and dolomite. Environ. Geology 49 274-279.

Loke, M.H. (2004) Tutorial: 2-D and 3-D electrical imaging surveys. Unpublished lecture notes. Online, www.geo.phys.ualberta.ca.

Loke, M.H. and Barker, R.D. (1996) Rapid leas-squares inversion of apparent resistivity pseudosections by a quasi-Newton method. Geophysical prospecting, 44, 131-152.

Loke, M.H. and Dahlin, T. (2002) A comparison of the Gauss-Newton and quasi-Newton methods in resistivity imaging inversion. Journal of applied geophysics, 49, 149-162.

Lowe, D.J. (1992) Chalk caves revisited. Cave science, 19, 55-58.

Martinez, J.D., Johnson, K.S., and Neal, J.T. (1998) Sinkholes in evaporite rocks. American Scientist, 86, 38-51.

Maystrenko, Y., Bayer, U., and Wenderoth, M.S. (2006) 3D reconstruction of salt movements within the deepest post-Permian structure of the Central European Basin System-the Glueckstadt Graben. Netherlands Journal of Geosciences-Geologie en Mijnbouw, 83, 181-196.

McCann, T. (2008) The Geology of Central Europe. Volume 1 and 2. Geological Society, London, 1449pp.

McCann, T., Kiernowski, H., Krainer, K., Vozarova, A., Peryt, T., Oplustil, S., Stollhofen, H., Schneider, J., Wetzel, A., Boulvain, F., Dusar, M., Török, A., Haas, J., Tait, J., and Körner, F. (2008) Permian. In: McCann, T. (eds.) The Geology of Central Europe. Volume 1: Precambrian and Palaeozoic. Geological Society, London, 531-598.

McDowell, P.W. (1989) Ground subsidence associated with doline formation in chalk areas of southern England. In: Beck, B.F. (eds.), Engineering and environmental impacts of sinkholes and karst, pp. 129-134. Balkema, Rotterdam.

McDowell, P.W., Barker, R.D., Butcher, A.P., Culshaw, M.G., Jackson, P.D., McCann, D.M., Skipp, B.O., Matthews, S.L., and Arthur, J. (2002) Geophysics in engineering investigations. Geological society engineering geology special publication 19, 252pp. London.

Menke, W. (1989) Geophysical data analysis: Discrete inverse theory. Academic press, New York.

Miller R.D. and Xia J. (2002) High-resolution seismic reflection investigation of a subsidence feature on US highway 50 near Hutchinson, Kansas. Presented at the Symposium on the Application of Geophysics to Engineering and Environmental Problems, SAGEEP, paper 13CAV6, published on CD.

Newton, J.G. (1976) Induced sinkholes – A continuing problem along Alabama highways, in International Association of Hydrologic Sciences, Land Subsidence Symposium: Proceedings of the Second International Symposium on Land Subsidence held at Anaheim, California, IAHS-AISH Publication no. 121, pp. 453-463.

Newton, J.G. (1987) Development of sinkholes resulting from man's activities in the eastern United States. US Geological Survey Circular 968, 54pp.

Osazuwa, I.B., and Chinedu, A.D. (2008) Seismic refraction tomography imaging of high-permeability zones beneath an earthen dam, in Zaria area, Nigeria: Journal of Applied Geophysics, 66, 44–58.

Parker, R.L. (1994) Geophysical inverse theory. Princeton university press, Princeton.

Patterson, D.A., Davey, J.C. Cooper, A.H., and Ferris, J.K. (1995) The investigation of dissolution subsidence incorporating microgravity geophysics at Ripon, Yorkshire. Quarterly Journal Engineering Geology, 28, 83-94.

Polom, U., Arsyad, I., Wiyono, S., Krawczyk, C. (2007) Classification of earthquake site effects by shallow reflection seismics using a shear-wave land-streamer system. Abstract, AGU fall meeting.

Pugin, A.J.-M., Pullan, S.E., Hunter, J.A., and Oldenborger, G.A. (2009) Hydrogeological prospecting using P- and S-wave landstreamer seismic reflection methods. Near Surface Geophysics 7, 315-328.

Rabbel, W. (2006) Seismic method. In: Kirsch, R. (eds.) Groundwater geophysics: A tool for Hydrogeology, 23-84, Springer Berlin.

Rawlinson, N. and Sambridge, M. (2003) Seismic traveltime tomography of the crust and lithosphere. Advances in Geophysics, 46, 81-197.

Reicherter, K., Froitzheim, N., Jarosinski, M., Badura, J., Franzke, H.-J., Hansen, M., Hübscher, C., Müller, R., Poprawa, P., Reinecker, J., Stackebrandt, W., Voigt, T., von Eynatten, H., and Zuchiewicz, W. (2008) Alpine tectonics north of the Alps. In: McCann, T. (eds.) The Geology of Central Europe. Volume 2: Mesozoic and Cenozoic. Geological Society, London, 1233-1286.

Robinson, E. and Coruh, C. (1988) Basic exploration geophysics. 562pp., John Wiley & sons, New York.

Rode, W. and Cramm, S. (2006) Schwingungserzeuger für seismische Anwendungen: Offenlegungsschrift DE 10 2006 055 457.4, Bundesrepublik Deutschland Deutsches Patent- und Markenamt, 24.07.2008.

Roth, M.J.S., Mackey, J.R., Mackey, C., and Nyquist, J.E. (2002) A case study of the reliability of multielectrode earth resistivity testing for geotechnical investigations in karst terrains. Engineering Geology, 65;2-3, p. 225-232.

Rücker, C., Günther, T., and Spitzer, K. (2006) 3-D modeling and inversion of dc resistivity data incorporating topography – part I: Modeling. Geophys. J. Int.

Sasaki, Y. (1994) 3-D resistivity inversion using the finite-element method. Geophysics, 59, 1839-1848.

Scheck-Wenderoth, M., Krzywiec, P., Zühlke, R., Maystrenko, Y., and Froitzheim, N. (2008) Permian to Cretaceous tectonics. In: McCann, T. (eds.) The Geology of Central Europe. Volume 2: Mesozoic and Cenozoic. Geological Society, London, 999-1030.

Schuck, A. and Lange, G. (2007) Seismic methods. In: Knödel, K., Lange, G. and Voigt, H.-J. (eds.), Environmental Geology: Hand-book of field methods and case studies, pp. 1159-1163. Springer, Berlin.

Sheehan, J.R., Doll, W.E., Mandell, W.A., and Watson, D.B. (2005) Detecting Cavities with Seismic Refraction Tomography: Can it be done? Extended abstract, Symposium on the Application of Geophysics to Engineering and Environmental Problems, Atlanta, GA, April 3-7, 2005.

Sheriff, R. (1977) Limitations on resolution of seismic reflections and geologic detail derivable from them. In: Payton (eds.), Seismic Stratigraphy: Application to Hydrocarbon Exploration, AAPG-Memoir No. 26, AAPG, Tulsa, p. 3–14.

Sloan, S.D., Steeples, D.W., and Tsoflias, G.P. (2009) Ultra-shallow imaging using 3D seismic-reflection methods. Near Surface Geophysics 7, 307-314.

Smith, D.V. (2005) The State of the Art of Geophysics and Karst: A General Literature Review. In: Kuniansky, E.L. (eds.) U.S. Geological Survey Karst Interest Group proceedings, Rapid City, South Dakota, September 12-15, 2005: U.S. Geological Survey Scientific Investigations Report 2005-5160, 296 p.

Spitzer, K. (1995) A 3-D finite-difference algorithm for DC resistivity modeling using conjugate gradient methods. Geophys. J. Int., 123, 903-914.

Steeples, D. W. and Miller, R. D. (1987) Direct detection of shallow subsurface voids using high-resolution seismic-reflection techniques. In: Beck, B. F., Wilson, W. L., and Balkema, A. A. (eds.) Karst Hydrogeology; Engineering and Environmental Applications, 179-183.

Steeples, D. W. and Miller, R. D. (1990) Seismic reflection methods applied to engineering, environmental and groundwater problems. In: Ward, S. (eds.) Geothechnical and Environmental Geophysics, volume 1, pp. 1-29, SEG.

Steeples, D. W. and Miller, R. D. (1998) Avoiding pitfalls in shallow seismic reflection surveys. Geophysics, 63, 1213-1224.

Steeples, D.W. (2005) Near-surface geophysics 75 years of progress. The leading edge 24 582-585.

Stefani, J.P. (1995) Turning-ray tomography. Geophysics, 60, 1917-1929.

Tamiru, G. (2009) Lithological relevance of near-surface seismic velocity model. Ph.D. thesis, Leibniz Universität Hannover.

Tarantola, A. (1987) Inverse problem theory: Methods for data fitting and model parameter estimation. Elsevier, Amsterdam.

Tejero, A., Chavez, R. E., Urbieta, J., and Flores-Marquez, E. L. (2002) Cavity detection in the southwestern hilly portion of Mexico city by resistivity imaging. J. Environ. Eng. Geophys.7 130–9.

Torsvik, T.H., Carlos, D., Mosar, M., Cocks, L.R., and Malme, T. (2002) Global reconstructions and North Atlantic paleogeography 440 Ma to Recent. In: Eide, E.A. (eds.) BATLAS—Mid Norway Plate Reconstruction Atlas with Global and Atlantic Perspectives. Geological Survey of Norway, Trondheim, 18–39.

Van Schoor, M. (2002) Detection of sinkholes using 2D electrical resistivity imaging, Journal of Applied Geophysics, V. 50, No. 4.

Veeken, P. (2007) Seismic stratigraphy, basin analysis and reservoir characterisation: Seismic exploration, v.37. Elsevier, the Netherlands.

Verdier, J.P. (1996) The Rotliegend sedimentation history of the southern North Sea and adjacent countries. In: Rondeel, H.E., Batjes, D.A., and Nieuwenhuijs, W.H. (eds.) Geology of gas and oil under the Netherlands. The Royal Geological and Mining Society of the Netherlands-KNGMG, 45-56.

Voigt, S., Wagreich, M., Surlyk, F., Walaszczyk, I., Ulicny, D., Cech, S., Voigt, T., Wiese, F., Wilmsen, M., Niebuhr, B., Reich, M., Funk, H., Michalik, J., Jagt, J.W., Felder, P.J., and Schulp, A.S. (2008) Cretaceous. In: McCann, T. (eds.) The Geology of Central Europe. Volume 2: Mesozoic and Cenozoic. Geological Society, London, 923-998.

Waltham, A.C., Simms, M.J., Farranat, A.S., and Goudie, H.S. (1997) Karst and caves of Great Britain (Geology conservation review series, 12), 358pp. Chapman and Hall, London.

Waltham, T., Bell, F., and Culshaw, M. (2005) Sinkholes and subsidence: karst and cavernous rocks in engineering and construction. Springer, UK.

Widess, M. (1973) How thin is a thin bed? Geophysics 38, 1176-1180.

Wiederhold, H., Buness, A.H., and Bram, K. (1998) Glacial structures in northern Germany revealed by a high-resolution reflection seismic survey. Geophysics, 63, 1265-1272.

Wiederhold, H., Gebregziabher, B., and Kirsch, R. (2008) Geophysical investigation of a sinkhole feature in Schleswig-Holstein. Extended abstract, EAGE Near Surface 2008, 15. – 17.09.2008; Krakow, Poland.

Wilson, M., Neumann, E.-R., Davies, G.R., Timmerman, M.J., Heeremans, M., and Larsen, B.T. (2004) Permo-Carboniferous magmatism and rifting in Europe. Geological Society, London, Special publications, 223.

White, D. (1989) Two-dimensional seismic refraction tomography. Geophys. J., 97, 223-245.

Xia, J. and Miller, R.D. (2007) Integrated geophysical survey in defining subsidence features on a golf course. J. Geophys. Eng., 4, 443.

Xu, C. and Butt, S. D. (2006) Evaluation of MASW techniques to image steeply dipping cavities in laterally inhomogeneous terrain. J. Appl. Geophys. 59 106–116.

Xu, W. and Zhao, G. (1988) Mechanism and prevention of karst collapse near mine areas in China. Environmental Geology Water Science, 12, 37-42.

Yilmaz, O. (1987) Seismic data processing. SEG, Tulsa, Oklahoma.

Yilmaz, O. (2001) Seismic data analysis-processing, inversion and interpretation of seismic data. SEG, (V.1&2) 2027pp. Tulsa, OK USA.

Yuan, D. (1987) Environmental and engineering problems of karst geology in China. In: Beck, B.F. and Wilson, W.L. (eds.), Karst hydrogeology: Engineering and environmental applications, pp. 1-11. Balkema, Rotterdam.

Zhang, J. and Toksöz, M. (1998) Nonlinear refraction traveltime tomography. Geophysics, 63, 1726-1737.

Zhou, W., Beck, B.F., and Adams, A.L. (2002) Selection of an effective electrode array to map sinkholes in karst terranes using electrical resistivity tomography. Abstract, Geological society of America, 34:2, p. 16.

Ziegler, P.A. (1975) Geologic evolution of the North Sea and its tectonic framework. Am. Assoc. Petrol. Geol., 59, 1073-1097.

Ziegler, P.A. (1990) Geological atlas of western and central Europe, 2nd eds. Shell Internationale Petroleum Maatschappij B.V.

Résumé

Berhanu Gebregziabher Gared
P.O.Box 231
Mekelle University, Ethiopia
Tel.: +251-913011765
+31-207707739
Email: brishg2000@fastmail.fm
brishg2000@yahoo.com

Date and place of birth: 19 February 1977, Ethiopia
Sex: Male
Nationality: Ethiopian
Marital status: Married

Educational Background

- PhD candidate at Leibniz Institute for Applied Geophysics, LIAG and Leibniz University of Hannover, Germany, since 2007. Dissertation topic: ***´´Environmental and Engineering Geophysical Studies for Sinkhole Problems Using Seismic Reflection, Refraction Tomography, Electrical Resistivity Imaging, and Joint Inversions´´***.

- MSc. in Applied Geophysics, Department of Earth Science, Addis Ababa University from 2001 to 2003. Dissertation topic: ***´´Integrated Geophysical methods to investigate geological structures and hydrostratigraphic unit at Aynalem, SE Mekelle´´***.

- BSc. in Geology, Department of Earth Science, Addis Ababa University from 1996 to 2000.

- Completed Secondary School at Atse Yohannes Secondary School, Mekelle, Tigray in 1996.

- Completed Elementary School at Haik Elementary School, Haik, S. Wollo in 1990.

Work Experiences

- From 2003 to 2006 Lecturer in Mekelle University Department of Earth Sciences and teaching Exploration Geophysics, Environmental Science, and Geology courses. Moreover, head of the registrar office for the Faculty of Science and Technology.

- From 2000 to 2001 Graduate Assistant in Mekelle University department of Earth Sciences and teaching Environmental Science and Geomorphology courses and assisting field terrain mapping.

Publications

- ***Joint inversion of seismic refraction and electrical resistivity tomography to investigate sinkholes.*** B. Gebregziabher, T. Günther, & H. Wiederhold (2010),

Extended abs., European Association of Geoscientists & Engineers (EAGE) - Near Surface 2010, Sep. 6 – 8, Zurich, Switzerland.

- ***Electrical resistivity and seismic refraction tomography applied for sinkhole investigations at Münsterdorf, North Germany.*** B. Gebregziabher, T. Günther, & H. Wiederhold (2010), Poster Abs., 70 Jahrestagung der Deutschen Geophysikalischen Gesellschaft (DGG70), 15-18 March 2010, Bochum, Germany.

- ***Sinkhole investigations using P- and S-wave reflection seismic in Schleswig-Holstein, North Germany.*** B. Gebregziabher, H. Wiederhold, & R. Kirsch (2009), Poster Abs., 69 Jahrestagung der Deutschen Geophysikalischen Gesellschaft (DGG69), 23-26 March 2009, Kiel, Germany.

References:

1. Prof. Dr. Hans-Joachim Kümpel
   Tel: +49 511-643-2101
   Email: Hans-Joachim.kuempel@bgr.de

2. Dr. Helga Wiederhold
   Tel: +49 511-643-3520
   Email: Helga.wiederhold@liag-hannover.de

3. Prof. Dr. Charlotte Krawczyk
   Tel: +49 511-643-3518
   Email: lotte@liag-hannover.de

4. Prof. Dr. Jutta Winsemann
   Tel: +49 511-762-2964
   Email: winsemann@geowi.uni-hannover.de